Bayesian Inference to Calibrate Flow Geometry in Ice Sheet Modelling of the Last Scandinavian Ice Sheet

Rosie Archer

A thesis submitted in partial fulfilment of the requirements for the
Doctor of Philosophy

The University of Sheffield
Department of Geography
May 2024

Contents

List of Figures

List of Tables

List of Abbreviations

AFDA	Automated Flow Direction Analysis tool
BIIS	British-Irish Ice Sheet
CN	Cosmogenic Nuclide dating
DEM	Digital Elevation Model
EISMINT	European Ice Sheet Modelling INiTiative
EISC	Eurasian Ice Sheet Complex
GAM	Generalised Additive Model
GLM	Generalised Linear Model
ISMIP	Ice Sheet Model Intercomparison Project
ISSM	Ice Sheet and Sea level Model
LALA	Likelihood of Accordant Lineations Analysis tool
LGM	Last Glacial Maximum
MCMC	Monte Carlo Markov Chain
MH	Metropolis-Hastings
MIS	Marine Isotope Stage
MISI	Marine Ice Sheet Instability
MSGL	Mega-Scale Glacial Lineations
OAT	One-at-a-time
OSL	Optically Stimulated Luminescence
PCA	Principal Component Analysis
PDD	Positive-Degree Day
PI	Pre-Industrial
PISM	Parallel Ice Sheet Model
PMIP	Palaeoclimate Modelling Intercomparison Project
RCP	Representative Concentration Pathways
SBKIS	Svalbard-Barents-Kara Ice Sheet
SIA	Shallow-Ice Approximation
SICOPOLIS	SImulation COde for POLythermal Ice Sheets
SIS	Scandinavian Ice Sheet
SSA	Shallow-Shelf Approximation

Funding

This PhD studentship was funded by the European Research Council (ERC) under the European Union's Horizon 2020 research and innovation programme (grant agreement No. 787263) as part of the PalGlac ERC Advanced Grant to Chris D. Clark.

Abstract

Both the Greenland and Antarctic ice sheets are experiencing increased levels of melt, contributing to potentially devastating sea level rise. Therefore, quantifying future changes to the contemporary ice sheets is imperative to understand and mitigate the risks associated with their demise. Uncertainty within projections of ice sheets under different climate scenarios is large. Palaeo-ice sheets left behind a wealth of information on past ice extents, timing and flow directions. By looking to the past and using data to validate and constrain numerical model simulations, numerical models of present-day ice sheets can be improved, and the uncertainty within projections of ice mass loss and sea level rise can be reduced.

Here, I focus on and simulate the last Scandinavian Ice Sheet between 40 and 5 thousand years ago, as well as the surrounding ice sheets over Eurasia, to find a model input parameter space that is optimised to fit the available flow geometry. In this thesis, I present a new Bayesian framework that takes an initial perturbed parameter ensemble for the last Eurasian Ice Sheet Complex, compares it to past observed flow directions and identifies an updated parameter sampling routine on a reduced parameter space so as to improve the overall model-data match of future ensembles. To quantitatively compare and score observed flow geometry from glacial landforms to model simulations in a statistically rigorous way, a new model-data comparison tool is presented: the Likelihood of Accordant Lineations Analysis (LALA) tool. This work could be used further to develop a robust simulation of the Scandinavian Ice Sheet, as well as other palaeo-ice sheets, optimised to flow geometry and to simulate data-driven spin-ups for use in ice sheet projections.

Acknowledgements

My first thanks is to my supervisor, Jeremy Ely. Thank you for meeting me when I became convinced objects can't move and helping me add fluff to my 'concise' writing style. I will always be grateful for your support when I decided to take on the world in the middle of my PhD and for agreeing to take on a Maths student in the first place.

I would also like to thank my supervisor and PI, Chris Clark, for the 'big picture' meetings and for introducing me to the world of lamb farming. I will always remember my first lamb, Percy, and will never forget the peanut pasta in Greenland. You still owe me a new toothbrush.

Thank you to all my PalGlac pals: Frances for teaching me how to make pretty maps, Ben for the Peak District fieldwork chaos and Helen for teaching me how to swim and introducing me to the world of spas in Budapest. To Bryony, thank you for taking me for coffee and hosting cosy craft nights. Thank you to my mum, dad, and Emma for supporting me in my journey as a perpetual student and for always being at the end of the phone when I need you.

Tess, you have quickly become my best friend, and I have loved having you as my dance partner, housemate, and conference buddy. I look forward to getting our nails done together for many more years to come.

Finally, to Alex. Thank you for being there for me in the hard times and pushing me when you knew I needed it. You always believed in me more than I believed in myself.

Chapter 1

Introduction

1.1 Ice sheets

An ice sheet is defined as a sufficiently large mass of ice built up by snowfall and hosted on a landmass or grounded in shallow sea and is typically defined as larger than 50,000 km^2 (on Climate Change , IPCC). Ice sheets grow and retreat over timescales of decades to millenia. Historically, there have been periods with colder climates, known as glacial periods, followed by interglacial periods that are comparatively warmer. Ice sheets are more prevalent in the glacial periods, and globally, the interglacial periods tend to have significantly less ice mass but not necessarily none. Glacial periods occurred regularly every 41,000 years until about 1.4 Ma (million years ago), where this periodicity lengthened to 100,000 years (Lisiecki and Raymo, 2007). These glacial-interglacial cycles are caused by three main states of the Earth's orbit: eccentricity, which is how elliptical the Earth's orbit is; obliquity, which is how tilted the Earth's axis is; and precession, which is the direction of the Earth's tilt (Benn and Evans, 2014*a*). In combination, these three factors cause major changes in the amount of solar radiation that reaches the Earth, leading to colder climates when the solar radiation is low and warmer climates when it is high. In the current interglacial period, known as the Holocene, trends of temperature increases are consistently being recorded and are broadly attributed to the greenhouse effect brought on by anthropogenically related increases in carbon emissions (Pörtner et al., 2022).

Whilst the Earth is experiencing an interglacial period, there are still two modern ice sheets: the Greenland Ice Sheet and the Antarctic Ice Sheet. The Greenland Ice Sheet covers approximately 80% of the island it sits on and contains 7.4 m of sea level equivalent

(Morlighem et al., 2017). It is predominantly terrestrial, meaning the ice terminates on land. The other contemporary ice sheet, the Antarctic Ice Sheet, covers 98% of the land beneath and, unlike the Greenland Ice Sheet, is marine-based, as the majority of its perimeter terminates in the ocean. The Antarctic Ice Sheet contains 61% of the Earth's freshwater and would raise the average sea level by around 58 m if it were to fully melt (Morlighem et al., 2020). Clearly, due to the amount of fresh water and potential to significantly increase sea level, the future of these ice sheets is imperative to understand. Anthropogenically induced climate change is speeding up the melting of these ice sheets and is expected to continue with increasing intensity if carbon emissions are not reduced (Pörtner et al., 2022). Rising sea levels would cause increased flooding in coastal areas worldwide, destroying infrastructure and natural habitats (Pörtner et al., 2022). Predicting the future behaviour of the current ice sheets, based on various emissions scenarios, is vital to prepare for and reduce the impacts of increased melting.

During the last glacial period (approximately 115 ka to 11.7 ka, where 1 ka represents a thousand years before 1950), there were expansive ice sheets over North America, Europe, Greenland and Antarctica, as shown in Figure 1.1 (Batchelor et al., 2019). In the Northern Hemisphere, ice sheets reached their maximums approximately between 26 and 19 ka (Clark, P., et al., 2009). These ice sheets that existed in the past are known as palaeo-ice sheets. Having already deglaciated, the evidence left behind by these palaeo-ice sheets may help us understand how ice sheets retreat. Whilst the observational record of contemporary ice sheets is only decadal in length, palaeo-ice sheets provide centennial to millennial scale records of ice sheet behaviour. Learning about past ice sheet behaviour and being able to validate that understanding increases the fidelity and confidence in predictions made about future ice sheets under the effects of climate projections.

1.2 Observational record of palaeo-ice sheets

Palaeo-ice sheets leave behind a rich observational record, giving insights into their past behaviour. This record can be broadly grouped into three types: geomorphology (landforms), sediments and relative sea level indicators. In this thesis, I will focus on the former two, as relative sea level indicators have been more commonly used in the past (Patton et al., 2017; Tarasov et al., 2012) and as the geomorphology and sediments provide an immediate and direct comparison model-data comparison compared to the relative sea level effects take several thousand years to appear. The evidence left behind by palaeo-ice sheets helps scientists reconstruct different aspects of the history of these ice sheets. It also provides a method to validate numerical ice sheet models to check their efficacy.

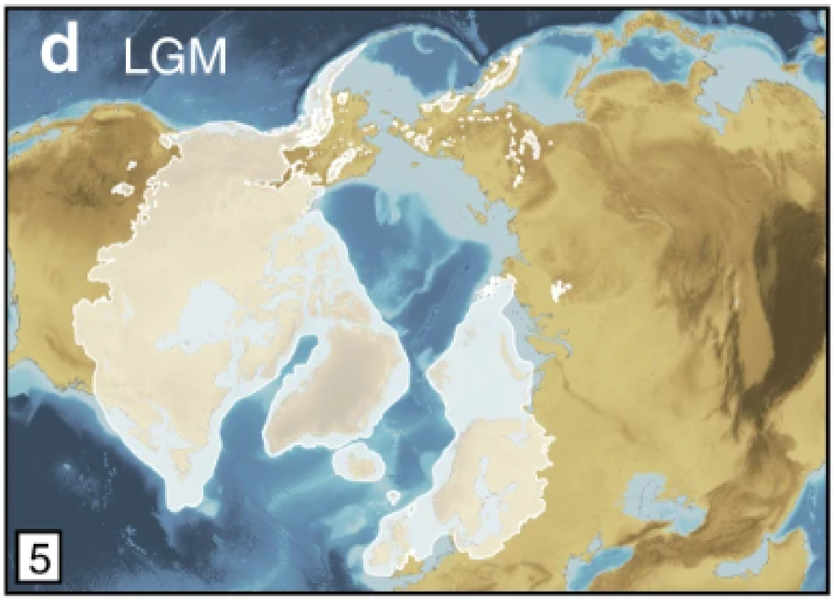

Figure 1.1: Estimated extents of Northern Hemisphere palaeo-ice sheets at the last glacial maximum, approximately 20,000 years ago (taken from Batchelor et al. (2019)).

A landform is an identifiable and discrete feature of the terrain and can be formed in many different ways, including by an ice sheet. Of the landforms left behind by ice sheets, subglacial bedforms, such as drumlins, ribs and mega-scale glacial lineations, are perhaps the most indicative of past ice conditions. The genesis of drumlins is highly debated (e.g. Boulton, 1987; Clark, 2010; Fowler, 2000; Hindmarsh, 1998; Shaw, 1983; Smalley, 1981; Smalley and Unwin, 1968), but regardless of their formation, their alignment with former ice flow direction allows us to infer past ice flow directions. Such glacial lineations can be grouped together, in flowsets, if they are spatially and directionally similar, and assumed to have formed in the same event (Clark, 1997; Hughes et al., 2014). Relative timings of lineation formation can sometimes be inferred dependent on whether or not they are found to be superimposed (knows as cross-cutting) on one another at specific locations (Clark, C.D., et al., 2009). Cross-cuttings occur if one set of lineations form on top of another and from this, the relative age order of the flowset formation can be determined. By understanding cross-cutting relationships, the flow evolution of an ice sheet can be deciphered. Unfortunately, due to the techniques available for assessing absolute ages, subglacial bedforms cannot be dated, as they were formed beneath an ice sheet, where life cannot be sustained, and light and exposure to cosmic rays required for the current dating techniques is not available.

Sediment is transported under (subglacially), within (englacially) and on the surface (supraglacially) of an ice sheet. When the location of the ice sheet margin is sustained, the transported sediment can be released to form a ridge called a moraine, making a landform record of the margin position. Moraines can also be formed by the ice mass pushing loose sediment together during an advance and leaving the ridge as the ice retreats. There are several distinct types of moraines that form at different areas of an ice sheet (Benn and Evans, 2014*b*; Bennett and Glasser, 2011). Terminal moraines, in particular, are formed at the front of an ice sheet at the maximum extent of the ice (Barr and Lovell, 2014). Any moraines formed at the front of an ice margin but behind the terminal moraine are termed recessional moraines. Hence, due to how the ridges form, moraines indicate where a former ice margin was, the extent at the time of moraine formation and the shape of an ice sheet's recession. As terminal and recessional moraines were formed in front of an ice sheet, there is the possibility of dating them and retrieving an absolute formation date.

Moraines and lineations are examples of landforms created by ice sheets that give specific information about the movements of a former ice sheet, namely the extent and flow direction. Previously, landforms were recorded in field surveys with researchers working on an area of interest. More commonly now, satellite imagery is used, allowing for remote mapping of these features. The mapping tends to be done systematically and extensively, to cover the whole area of interest. Butcher et al. (in prep) has developed a new method to map large areas systematically, without the need to map every single feature. Figure 1.2 shows the flow directions captured from this mapping (Boyes et al., 2023; Butcher et al., in prep), that will be described further in Chapter 4. Once these different observations have been collated for a specific area, whether that be on a whole ice sheet scale or more locally, the relative movements of the ice sheet can be determined (Andrews, 1982; Chandler et al., 2018; Stokes et al., 2015). This can involve filling in any gaps, working out relative timings and combining multiple forms of evidence to make inferences.

Although the geomorphological record is useful for describing past ice sheet behaviour and providing relative ages, for example, cross-cutting relations, they do not provide absolute ages for the timings of said behaviours. Samples taken from features of the observational record can be dated, and utilised to infer when it formed. There are various techniques for absolute geochronological dating, including: radiocarbon dating, Optically Stimulated Luminescence (OSL) and Cosmogenic Nuclide (CN) dating.

Carbon is an abundant element in the atmosphere and has both stable and non-stable isotopes: atoms of the same element and same number of protons, but with differing numbers of neutrons and hence varying atomic weights. Carbon-14 is a non-stable, radioactive isotope that combines with oxygen in the atmosphere and then transfers to living organisms. The amount of carbon-14 contained in an organism is fixed during its life and then begins to decay after death at a steady rate (Libby, 1954). By calculating the amount of this isotope

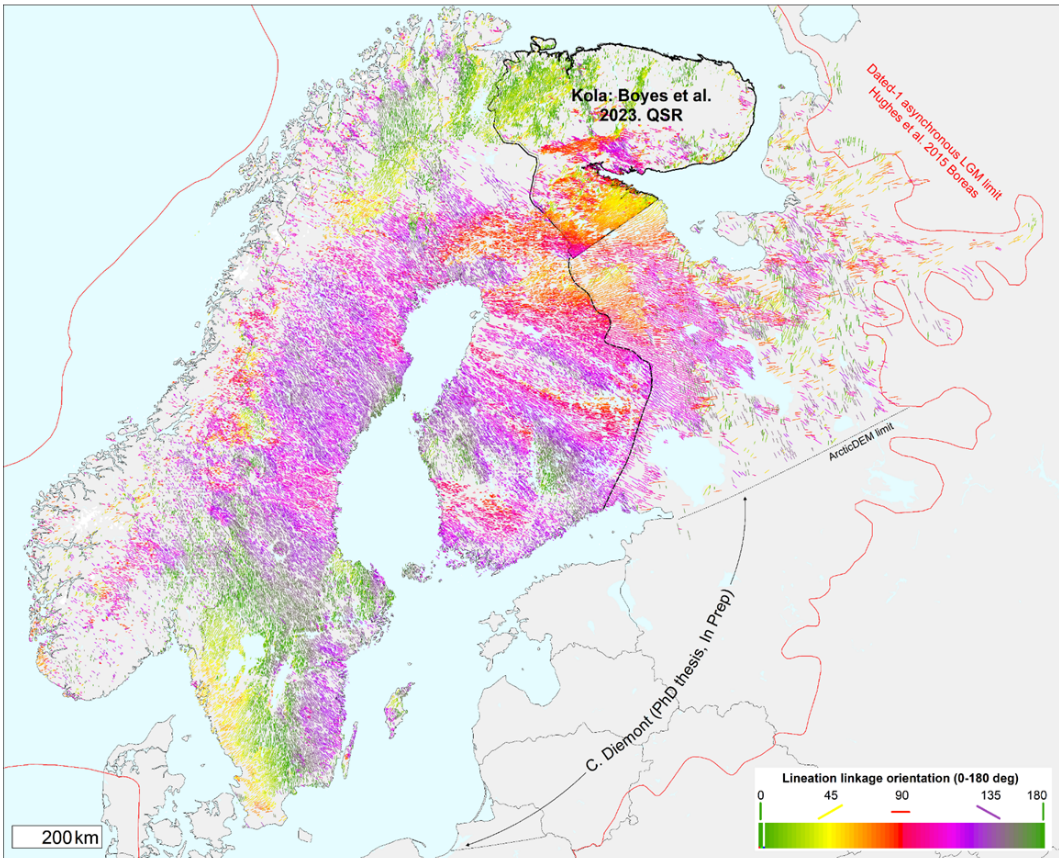

Figure 1.2: Locations and inferred directions of lineation product, taken from Butcher et al. (in prep).

remaining in an organic sample, the carbon-14 age can be found, representing the time since the organism died. The carbon-14 age must then be calibrated to give an equivalent calendar age. As the ratio of carbon-14 and carbon-12 has varied over time this calibration is not trivial. Projects such as IntCal (Reimer et al., 2020) for the Northern Hemisphere, take absolute dates which are independent from the radiocarbon samples and work out how the raw carbon-14 age relates to a useable calendar date. For dating relevant in a glacial context, samples are collected from near moraines, for example. The calculated date is then assumed to be an ice-free time as living organisms are unable to survive beneath the ice sheet. Radiocarbon dating can date organics as old as 55 ka, and so is appropriate for timings needed from the last glacial maximum (LGM) onwards.

OSL dating exploits the natural radioactivity of sediments and how this affects minerals such as quartz (Preusser et al., 2009) and feldspar (Krbetschek et al., 1996). When sediment is buried, luminescence begins to grow as the electrons in the minerals become excited due to the exposure to radiation (Duller, 2008). Due to the natural radiation, these electrons then get trapped within imperfections in the crystal lattice (Preusser et al., 2008). The longer the sample is buried, the higher the number of trapped electrons. By calculating the equivalent dose, which is the amount of radiation the sample has been exposed to, and dividing by the dose rate, which is location dependent and is the amount of radiation per thousand years the sample would have been exposed to, gives the sample age (Duller, 2008). The samples for OSL must be carefully obtained and not exposed to sunlight as this resets the signal through a process called bleaching and the age is lost. This also means that it is assumed the sample was buried at the time of interest and not re-exposed since. To calculate the number of trapped electrons in a sample, and hence the equivalent dose, a light source is applied, giving the electrons enough energy to escape as photons and this can be measured. This style of dating is used in glacial environments (Fuchs and Owen, 2008) at sites with known past ice margins where glacial sediment would have been deposited, such as pro-glacial lakes (e.g. Luethgens et al., 2011). Compared to radiocarbon dating, this method can date much older samples, up to around 100 ka.

Cosmic rays are charged, high-energy particles that are constantly entering the Earth's atmosphere. Upon doing so, when these particles hit exposed rock, a spallation reaction occurs which splits nuclei of specific elements and cosmogenic nuclides are formed. The resulting isotopes of different elements can be counted, and the ratio of one isotope to another can be used to calculate the amount of cosmogenic nuclides and hence an exposure age. There are many isotopes created in this process, each with different half-lives. Utilising this property allows relatively old and young ages to be dated with increased accuracy, up to 10 million years old. This method is known as Cosmogenic Nuclide dating. Relevant to glaciation ages, boulders from moraines and erratics can be dated, assuming they have been exposed since deposition (Small et al., 2017).

Experts often use all the available lines of evidence combined with their expert interpretation to reconstruct the former flow conditions and margin positions of a palaeo-ice sheet through time (e.g. Batchelor et al., 2019; Clark et al., 2022, 2012; Hughes et al., 2014). When absolute ages are collected, reconstructions of ice sheets can include timings at which they reached certain extents. Considering the subglacial landform record alone can provide relative chronologies, but lacks these absolute timings.

Whilst empirical reconstructions are informative to what the ice previously looked like, reconstructions achieved in this way lack a physics basis. This means that certain variables such as ice velocity and thickness, are missing and cannot be reconstructed using the observed data. In contrast, numerical ice sheet models are based on approximations of the ice physics and can be used to reconstruct past ice sheets.

1.3 Ice sheet modelling

Numerical modelling enables us to examine how different processes affect ice sheets and predict how they might behave in the future. Both contemporary and palaeo-ice sheets are important to model. Modelling contemporary ice sheets gives insights into how the Greenland and Antarctic ice sheets may respond to various climate projections by modelling into the future. By modelling palaeo-ice sheets, the plethora of data left behind by the past ice mass can be used to validate the model outputs and explore parameterisations and model set-ups that give realistic outputs based on the evidence.

Modelling of ice sheets is conducted for two purposes: prognostic and diagnostic. Prognostic modelling is used to predict the future of the current ice sheets (e.g. Davies et al., 2014; Goelzer et al., 2013, 2020), or to hindcast palaeo-ice sheets (e.g. Patton et al., 2017, 2016; Pollard et al., 2016). Prognostic modelling of the contemporary ice sheets is used to predict how they may react and change according to future climate scenarios (e.g. Davies et al., 2014; Goelzer et al., 2020; Payne et al., 2004). Diagnostic modelling, on the other hand, is used to learn about specific physical processes occurring within the ice sheet (e.g. Pollard et al., 2015; Tulaczyk et al., 2000).

Prognostic and diagnostic modelling of palaeo-ice sheets has the advantage of being validated against the observational record, which does not exist in full for the contemporary ice sheets. The record for the contemporary ice sheets relies on satellite imagery and fieldwork and is only decadal, whereas the palaeo-record consists of landforms and geochronological data which span centuries to many millennia.

To use numerical ice sheet models, a certain number of unknown parameters and boundary conditions must be first inputted by the user. For example, information containing topography or geothermal heat flux may be required. Other values, such as the exponent in the ice flow law, must be chosen as the precise values for different modelling scenarios are unknown. Estimated ranges for the input parameters are decided upon based on expert knowledge and by findings of other studies. The required parameters hold a specific uncertainty as the true value is unknown. The climate parameters have an especially high uncertainty due to the difficulty of replicating and estimating. These uncertainties need to be reduced as much as possible to improve predictive accuracy. Learning which parameters can cause the highest variation in model output is typically done using a sensitivity analysis, highlighting which parameters are more or less important to changing the model output, thus informing the user as to which parameters are the most important to target to reduce uncertainty. Conversely, the parameters that affect the variation in output the least can be discarded, reducing the parameter space considerably and speeding up model computational time. Methods to identify the most and least important parameters are discussed in Chapter 4.

Models use defined parameter values to solve the differential equations that determine the physics of the ice sheet, discussed in Chapter 2. Ice flow can be modelled using the Stokes equations, encapsulated in so-called full Stokes models. Due to computational limitations, some simplifications need to be made when solving the physics behind an evolving ice sheet (Mahaffy, 1976) and different levels of complexity of ice sheet models, shown in Figure 1.3, are available for differing contexts. The full Stokes model is the most complex and representative of all processes. This model is useful for simulating small areas and time frames but requires too much computational time and power to use in most cases. For example, modelling a small glacier over a short period of time can be feasible using a high level of sophistication, whereas modelling a whole ice sheet glaciation on a continent-wide scale would need a more basic approach. Hence, a variety of different models are needed for these various applications. The simplest models are reliant on the small depth-to-width ratio that is reasonable to assume for most ice masses and hence this approximation is called a shallow approximation. Two of the simplest ice flow models using the shallow approximation are the Shallow Ice Approximation (SIA) (Hutter, 1982) and the Shallow Shelf Approximations (SSA) (Weis et al., 1999). These only model the ice sheet or ice shelf flow, respectively. Many studies have used an SIA model to simulate ice flow (e.g. Greve, 1997; Ritz et al., 1996; Rutt et al., 2009), but studies using an SSA model alone are uncommon (e.g. MacAyeal et al., 1996).

Coupling the two shallow approximations gives a hybrid model. Together, the SIA and

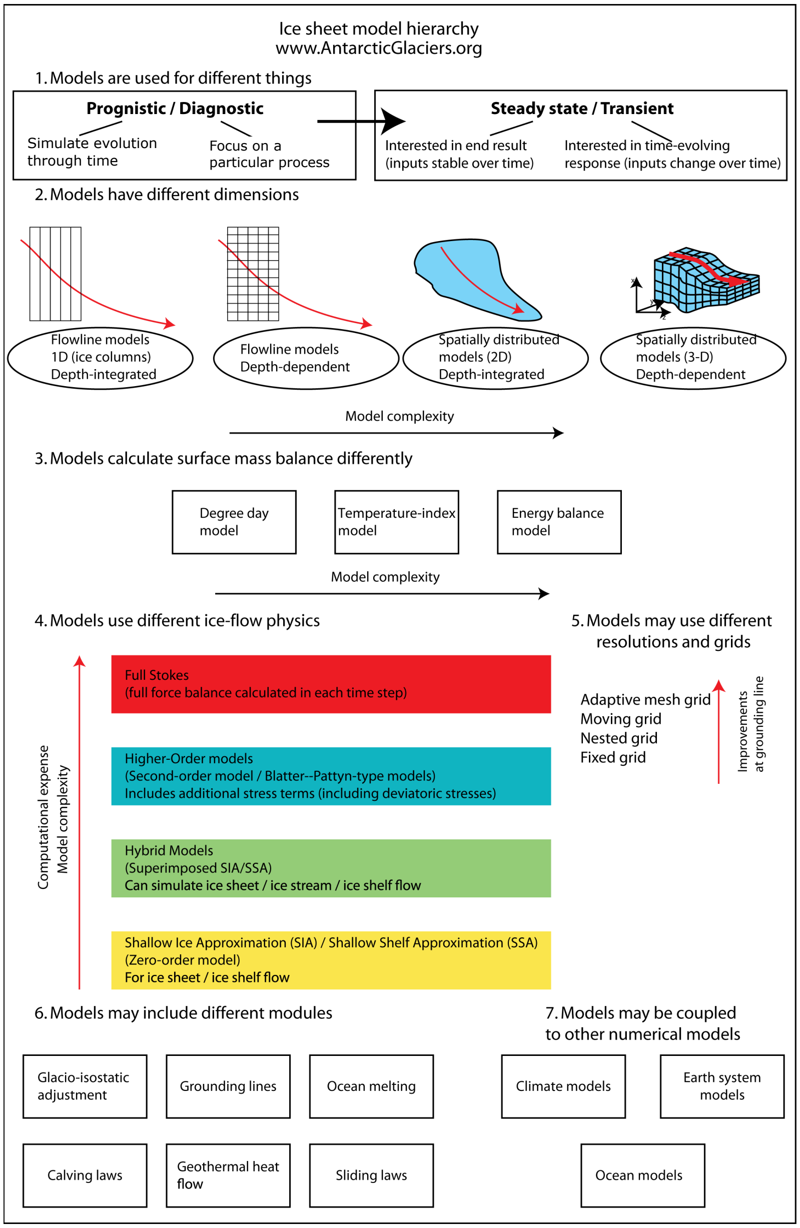

Figure 1.3: Hierarchy of numerical ice sheet models and adaptations that can be made, taken from Davies (2020).

SSA can better approximate ice flow at the grounding line. The SIA is applied to grounded ice with minimal sliding, whereas the SSA is applied to the floating shelves. A combination of both is applied around the grounding line, where ice flow velocity increases. An example of a hybrid model is the Parallel Ice Sheet Model (PISM). PISM is a popular, open-source ice sheet model that can be used for continental ice sheets over long periods of time (e.g. Bochow et al., 2023; Hill et al., 2022; Reese et al., 2023). The first papers using this model were published in 2007 (Bueler, Brown and Lingle, 2007), and there have been over 200 papers published since (the PISM authors, n.d.) (as of March 2024). PISM solves the shallow stress balance approximations, valid for small depth-to-width ratios, to calculate the updated ice dynamics as time progresses. The SIA is applied to grounded ice with minimal sliding, whereas the SSA is applied to the floating shelves. This model uses an adaptive time step method, meaning the stress balance equations are solved when a set of stability conditions are reached. The adaptive time steps reduce any unnecessary calculations and thus speed up the simulation. A combination of these factors makes PISM a good model for palaeo-ice sheets as it provides an appropriate level of detail as well as can complete simulations within computational power and time restrictions over large domains and timescales. PISM is the model chosen for this thesis, and its underpinning physics are described in detail in Chapter 2.

Higher-order models are one step up in complexity from hybrid models and contain extra stress terms and therefore require more computational time and power (Blatter, 1995; Pattyn, 2003). Work has been done to improve the computation of these models (e.g. Blatter, 1995; Colinge and Blatter, 1998; Larour et al., 2012*a*; Pattyn, 2003), as numerical stability has been historically hard to reach (e.g. van der Veen, 1989; van Der Veen and Whillans, 1989). As computational power increases, the use of higher-order models has increased, and open-source models are now available such as the Ice Sheet System Model (Larour et al., 2012*a*).

The most complex models solve the Stokes equations, outlined in Chapter 2, which are the most comprehensive representation of an ice mass and, because of this, are the most computationally expensive models. An example of these so-called full Stokes models is the Elmer/Ice model (Gagliardini, 2022). Elmer/Ice produces a highly detailed output but is only feasible to run on short timescales and small areas.

Ice sheet modelling has a long history, with work starting in the 1950s. The first studies, in both the 1950s and 1960s, constructed the basis for the physics of numerical modelling of ice flow. Glen (1955) undertook laboratory experiments to discover a proportional relationship between ice flow and stress leading to the formulation of Glen's flow law. Nye (1952) gave simplified ways to look at ice flow over bedrock, Weertman (1957) looked at how obstacles restrict sliding, and Lliboutry (1968) found equations for friction at the base of the ice mass. The first attempts of numerical modelling began in the late 1960s (e.g. Campbell and Rasmussen, 1969; Mahaffy, 1976; Rasmussen and Campbell, 1973). Since then, numerical models have undergone a huge shift in complexity due to improved understanding and increased computational capacity. In the early stages, two-dimensional models were created, mainly focussing on ice sheet extent, with perfectly plastic ice assumed and a steady state (e.g. Budd and Jenssen, 1975; Reeh, 1984). Mahaffy (1976) created one of the first three-dimensional ice sheet models that modelled ice flow and was an early example of an SIA model, based on simplifications derived in previous decades (e.g. Glen, 1955; Lliboutry, 1968; Nye, 1952; Weertman, 1957).

Models originally were basic and quite limited in their applications. By the late 80s, early 90s, the effect of ice temperature on ice flow was incorporated into numerical models with thermomechanical coupling as well as time dependence (e.g. Hindmarsh et al., 1989; Huybrechts, 1990). Limitations in computing power restricted the model resolutions (e.g. Budd and Jenssen, 1989; Huybrechts and Oerlemans, 1988). The increase in the number of models available led to the need to test their reliability and repeatability. The accuracy of these models was assessed in a series of model intercomparison projects. These projects provided a benchmark for modellers to validate their code and compare their models in a standardised way. The first inter-model comparison compared the success of five ice shelf models (MacAyeal et al., 1996). Subsequently, model intercomparison projects became an important tool to enable careful comparison between models. In its first phase, the European Ice Sheet Modelling INiTiative (EISMINT) looked at SIA models and experimented with fixed and moving ice sheet margins (Huybrechts and Payne, 1996). The second iteration of EISMINT used similar experiments to the first to investigate the effects of thermomechanical coupling (Payne et al., 2000). The Ice Sheet Model Intercomparison Project (ISMIP) followed on from EISMINT. It focussed on four key topics: higher-order models (Pattyn et al., 2008), Heinrich events (Calov et al., 2010), marine ice sheet models (Pattyn et al., 2012) and ice dynamics response to warming for contemporary ice sheet models (Seroussi et al., 2020).

By the 2000s, computational capabilities had significantly improved, which led to the emergence of open-source ice sheet models complete with documentation and user support (e.g. Bueler and Brown, 2009; Larour et al., 2012a). With the addition of support and easy access to ready-made ice sheet models, more researchers have the opportunity to complete modelling studies without the need to create a model from scratch each time. As knowledge and computer power have improved more recently, numerical modelling began to account for processes that have not previously been included (e.g. DeConto and Pollard, 2016) as well as new parameterisations (e.g. Lazeroms et al., 2018). Varying resolutions across the domain have been investigated to increase details in areas of interest, for example, the grounding line, but keeping the computational cost low by using a coarse resolution elsewhere (e.g. Cornford et al., 2013).

Ice sheet models require many unknown parameter inputs before simulations can be completed. As the exact values are not known, ranges for each parameter are tested. To explore the parameter space, perturbed parameter ensembles are used, where each parameter is changed to a different value within the set range for a set number of simulations. Once the ensemble is completed, the simulations that best match the available data should be identified. For ice sheet modellers, empirical reconstructions are a powerful resource that can be used to validate simulations. Visual comparisons between simulations and reconstructions are commonplace; however, quantitative comparisons are currently limited. In Chapter 3, I present a tool that quantitatively compares model simulations to the observed flow directions.

1.4 Eurasian Ice Sheet Complex

The EISC was made up of three separate ice sheets, which joined and separated throughout the last glacial (Hughes et al., 2016), shown in Figure 1.4. They were the British-Irish Ice Sheet (BIIS), the Scandinavian Ice Sheet (SIS) and the Svalbard-Barents-Kara Ice Sheet (SBKIS), all of which reached their maximum extents independently (Patton et al., 2016). The combined ice mass reached 5.5 Mkm^2 at its maximum (Hughes et al., 2016) and was thought to contain 20 m sea level equivalent of water (Patton et al., 2017). The EISC is the ice sheet complex focussed on in this thesis, with the most attention paid to the Scandinavian component and mainly over its core area due to the large amount of physical evidence constraining its last glaciation. With this evidence, the success of model simulations can be assessed and used to improve the model-data fit.

The oxygen isotope ratio measures the fluctuations between amounts of oxygen-18 compared to oxygen-16. These fluctuations are stored in deep ocean cores and can be assessed by laboratory analyses. The ratio is linked to changes in climate and the glacial/interglacial periods (Raymo et al., 2018; Shackleton, 1973). Based on this, as well as observations and numerical modelling efforts, it is thought that there have been ice sheets growing and melting over Europe consistently in glacial periods (Batchelor et al., 2019). The Eurasian Ice Sheet Complex (EISC) reached two maxima over the last glacial cycle. One was in Marine Isotope Stage (MIS) 4 and one after this in MIS2. The last glacial maximum, occurring at MIS2 is the focus of this thesis, so the timescale modelled in this thesis is restricted to

Figure 1.4: Outline of the maximum extent of the Eurasian Ice Sheet Complex (EISC) as determined in Hughes et al. (2016).

between 40 ka and 5 ka, encompassing ice sheet fluctuations in MIS2. Also, only simulating from 40 to 5 ka allows for a modelling study with a reasonable resolution and a more complex model than could be used otherwise.

Whilst landform mapping has been carried out in various regions across the domain of the last EISC (e.g. Boulton et al., 2001; Bowen et al., 2002; Dongelmans, 1996; Glückert, 1974; Greenwood et al., 2016; Punkari, 1997), the approaches and outputs vary, and so model-data comparison becomes difficult. The PALGLAC project, which has funded the research for thesis, sought to reconstruct the SIS and so mapped the area in a systematic and consistent way. The data produced can therefore be used confidently to validate model simulations without having issues with inconsistent/missing data.

Previous modelling efforts have been performed on the EISC, using different levels of model complexity and with different project aims. A summary of the previous modelling studies is given in Table 1.1. The majority of past projects have a prognostic focus (Arnold and Sharp, 2002; Clason et al., 2014; Payne and Baldwin, 1999), using a model to test hypotheses of landform genesis or investigating the effect of processes that may impact the contemporary ice sheets. Prognostic modelling using the EISC or parts of the EISC has the advantage of being able to substantiate hypotheses with a wealth of evidence that is not available for the contemporary ice sheets.

The studies that use diagnostic modelling either model a part of the EISC (Clason et al., 2016; Fastook and Holmlund, 1994; Näslund et al., 2003), or model the whole area but the build-up and retreat separately (Boulton et al., 2003; Patton et al., 2017, 2016). Studies that restrict the domain to the SIS vary greatly in modelled timescales. Näslund et al. (2003) models the last 120 ka whilst Fastook and Holmlund (1994) looks specifically at the Younger Dryas. With such vastly different timescales come different goals. For example, Näslund et al. (2003) had to use a coarse model grid of 70×100 km^2 which is more computationally efficient but would not be able to capture complexities in regional areas. This approach produces an overview of the glaciation without the fine detail. Fastook and Holmlund (1994) used a higher resolution of 50×10 km^2 which was possible due to the shorter timescale considered.

As the EISC covers such a large domain, simple models tend to be the preference for work on the area (Clason et al., 2014; Forsström and Greve, 2004; Payne and Baldwin, 1999; Siegert and Dowdeswell, 2004). However, some work has been done with a more complex ice sheet model in Patton et al. (2016) and Patton et al. (2017). Patton et al. (2016) set out to model the growth of the EISC from 37 to 19 ka using a Blatter-Pattyn model (Blatter, 1995; Pattyn, 2003). Blatter-Pattyn models more closely represent the Stokes equations than either SIA or SSA, but are still relatively computationally efficient. The use of this model

Table 1.1: Summary of previous modelling attempts of the whole EISC or solely the SIS.

Reference	Model type	Purpose	Notes
Fastook and Holmlund (1994)	Finite-element	Diagnostic	Modelled the SIS around the Younger Dryas (approximately 12.9 ka to 11.7 ka), finding that the Baltic ice stream was important to match the model to the evidence. Achieved by changing the basal conditions.
Payne and Baldwin (1999)	Thermomechanically coupled 3D model	Prognostic	Explaining certain formation of observed landforms. The simple model set-up was used as the aim was to test a hypothesis and not to accurately replicate the ice sheet.
Arnold and Sharp (2002)	2D, time-dependent with hard-bed basal hydrology	Prognostic	Aims to replicate complex patterns of past flow directions not normally captured by modelling.
Näslund et al. (2003)	From Fastook and Chapman (1989)	Diagnostic	Modelled the SIS over the Weichselian glaciation (approximately 120 ka to present). Rose diagrams were used to compare modelled and observed flow directions.
Boulton et al. (2003)	Thermomechanically coupled 3D model	Diagnostic	Simulated the last glacial cycle (from 120 ka) and focussed on the formation and effect of ice streaming.
Forsström and Greve (2004)	SICOPOLIS from Greve (1997)	Diagnostic	Early sensitivity analysis, making one change per simulation and comparing output to a default simulation.
Siegert and Dowdeswell (2004)	SIA coupled with a basal sediment deformation model	Diagnostic	The climate input was changed until the modelled LGM extent matches the geological evidence.
Clason et al. (2014)	SICOPOLIS	Prognostic	Uses the SIS as a proxy to the Greenland ice sheet to test the impacts of the surface meltwater effect.
Patton et al. (2016)	Blatter-Pattyn model	Diagnostic	Models the build-up of the last EISC and qualitatively compares the output to the data.
Patton et al. (2017)	Blatter-Pattyn model	Diagnostic	Models the deglaciation of the last EISC, starting from the LGM modelled in Patton et al. (2016).
Gudlaugsson et al. (2017)	SICOPOLIS	Prognostic	Investigates model sensitivity of the last EISC to the subglacial hydrology.
Åkesson et al. (2018)	ISSM	Diagnostic	Regional model with high-resolution (1 km) grid on the grounding line and coarser resolution elsewhere (10 km). Finds a warming ocean input triggers the retreat of the grounding line in several fjords but cannot be attributed to the full retreat.

allowed Patton et al. (2016) to simulate the EISC over a long time with a 10 km resolution. Model simulations were performed with different parameter values, and a simulation that was deemed optimal based on empirical evidence was chosen. This optimal model was then used in Patton et al. (2017) with updated parameter values and continued to simulate the deglaciation of the ice sheet, from 23 to 8 ka. This simulation was validated against a range of observations, e.g. lineations, geochronological data and relative sea level metrics. In my study, I will attempt to model the whole glaciation, keeping the parameters constant between the glaciation and deglaciation (differing from the approach of Patton et al. (2016) and Patton et al. (2017)), hoping to find an optimal parameter set.

A couple of the studies (Clason et al., 2014; Forsström and Greve, 2004) use the SImulation COde for POLythermal Ice Sheets (SICOPOLIS) model (Greve, 1997), which is a simple SIA implementation of ice flow. Using this model will take a shorter amount of time and less computer power but with less detail. Getting the balance of detail and computational efficiency is important and depends on the research question being considered.

One thing all of these studies (outlined in Table 1.1) have in common is that the analysis is mostly qualitative when comparing the simulations to the observational record, visually comparing the model to the data. Some studies perform a more quantitative comparison, using the currently published tools (e.g. the Automated Flow Direction Analysis (AFDA) tool) (e.g. Patton et al., 2017, 2016).

In this thesis, the full build-up and deglaciation will be modelled without changing parameters at the LGM, as was the case in Patton et al. (2017). Model-data comparisons will take a quantitative approach with statistical backing (see below), which is so far underutilised in ice sheet modelling (Chapter 3).

1.5 Bayesian inference

Statistics is broadly split into two ways of thinking, frequentist and Bayesian, both of which can be useful in different situations (e.g. Fornacon-Wood et al., 2022). Frequentist statistics keep parameters at fixed values; probabilities are seen as frequencies. In contrast, Bayesian statistics considers parameters to be their own random variables; they are not fixed and are subjective (O'Hagan, 2008). Frequentist statistics also assumes that the data is repeatable, whereas Bayesian sees data as fixed. Bayesian inferences provide a distribution for the parameters, i.e. how likely each probability is. For example, consider a die unknown to be fair or not, where in this context a fair dice would mean rolling any number has equal probability. A frequentist statistician would assign the probability of rolling a 6, say, as the frequency of a 6 appearing as the die is rolled a lot of times. A Bayesian statistician could start by assigning a flat probability distribution to the rolling of a 6, so that rolling a 6 is thought to be any probability. As the die was rolled, this data would be incorporated into the probability distribution and continuously updated as more data becomes available.

The root of Bayesian statistics is Bayes' Theorem, where for two events E and F,

$$P(E|F) = \frac{P(F|E)P(E)}{P(F)}. \tag{1.1}$$

Bayes' theorem describes how conditional probabilities are related, which proves useful when deriving conditional distributions used in Bayesian statistics. When approaching a problem where Bayesian inference will be used, with data X and parameter vector $\boldsymbol{\theta}$, first, a prior distribution is set. A prior distribution, $p(\boldsymbol{\theta})$, considers any knowledge or beliefs the statistician may have before any data is observed. If no prior information is available, an uninformative prior can be chosen instead. Once the data has been collected, the likelihood of the data given certain parameters, $p(X|\boldsymbol{\theta})$, can be calculated. The aim of Bayesian inference is to find the posterior distribution, $p(\boldsymbol{\theta}|X)$, which calculates the distribution of the parameters given the observed data. Using Bayes' Theorem (Equation 1.1), the posterior distribution can be derived as

$$\begin{aligned} p(\boldsymbol{\theta}|X) &= \frac{p(X|\boldsymbol{\theta})\, p(\boldsymbol{\theta})}{p(X)} \\ &\propto p(X|\boldsymbol{\theta})\, p(\boldsymbol{\theta}) \end{aligned} \tag{1.2}$$

where proportionality can be used as $p(X) = \int p(\boldsymbol{\theta})\, p(X|\boldsymbol{\theta})\, d\boldsymbol{\theta}$ has no dependence on the parameter vector $\boldsymbol{\theta}$.

Bayesian statistics provides flexibility: the probability distributions can be easily updated as more or new data becomes available and allows inference even with data that cannot be repeated. Therefore, this type of inference is good for this context, as new data is regularly published and data, such as individual landforms, are not repeatable, so the location and orientation cannot be reobserved in the same way as a dice can be reobserved if rerolled. Thus far, Bayesian approaches have rarely been combined with ice sheet modelling, although they have started to become more common (e.g. Edwards et al., 2021; Pollard et al., 2016). In other fields, however, it is commonplace to see. Engineering, medicine and computer science have been using Bayesian statistics in studies since the 1960s (e.g. Borko and Bernick, 1964; Florentin, 1962; Talbot and Harrison Jr, 1966).

Bayesian inference is a useful tool and the underpinning of several Chapters in this thesis (Chapters 3, 4 and 5). Ice sheet modelling often has a high-dimensional parameter space where the effect of each parameter, and how the parameters may affect the model output in combination is largely unknown and needs to be explored. If certain parameters do not largely affect the model output, they could be discarded to reduce the dimensionality of the parameter input space (Chapter 4). Model surrogates, such as emulators, can fill in gaps by predicting the model output given a specified parameter input (Chapter 5).

1.6 Aims and objectives

1.6.1 Aim of thesis:

Combine ice sheet modelling with Bayesian inference to simulate the flow of the last Scandinavian Ice Sheet.

1.6.2 Objectives:

1. Create a statistically rigorous model-data comparison tool to compare model-simulated and inferred past ice flow direction.
2. Run a perturbed ensemble of simulations of the Eurasian Ice Sheet complex using the Parallel Ice Sheet Model.
3. Complete a sensitivity analysis to determine which model input parameters are the most important for influencing ice flow directions judged against empirical observations of flow. Explore and determine which parameters can be discarded to reduce the dimensionality of the parameter space.
4. Use a Gaussian process emulator to optimise the parameter sampling design and identify model simulations that best explain the documented flow geometries.
5. Run new simulations to find an optimal model to fit the collated data on ice flow.

1.7 Thesis structure and relation to published work

The field of palaeo-glaciology suffers from a lack of statistical rigour and could better use Bayesian inference methods. This thesis seeks to address this gap by outlining a workflow that can optimise the parameter space according to a model-data match. Here, the aim is to improve the flow geometry model match over the Eurasian Ice Sheet complex, but the methods outlined could also be applied to other domains and other types of evidence left behind by palaeo-ice sheets. Chapter 2 starts by describing the equations used to model ice flow and how PISM makes simplifications so that simulations over long timescales and large domains are computationally feasible. The design of the initial perturbed parameter ensemble is described. Then, Chapter 3 outlines a new model-data comparison tool, the Likelihood of Accordant Lineations Analysis (LALA) tool, for past and modelled flow directions. This work is published in Archer et al. (2023) and uses data from Ely et al. (2024). The results of the initial ensemble are presented in Chapter 4, and then the scores of the simulations using LALA are calculated. The sensitivity of the model input parameters to various outputs is then investigated. Chapter 5 builds a Gaussian process emulator and uses a history matching process to find input parameter sets that score highly using LALA, without testing all parameter combinations within PISM. Chapter 6 outlines a perturbed parameter ensemble calibrated to the flow geometry with an updated parameter sampling routine, compares the two ensemble results and discusses the implications of this work. Finally, Chapter 7 summarises and concludes the thesis.

Chapter 2

Experimental design and setup of the Parallel Ice Sheet Model and initial testing

2.1 Introduction

As the climate continues to warm, the need to understand how ice sheets react to this anthropogenically caused warming becomes imperative (Pörtner et al., 2022). Numerical ice sheet models can be used to predict future ice sheet behaviour based on different climate scenarios (e.g. DeConto and Pollard, 2016; Kopp et al., 2017). However, the uncertainty in predictive models is large (Bamber et al., 2019), and it is difficult to verify the results. One method for reducing this uncertainty is to validate models by simulating palaeo-ice sheets. Palaeo-ice sheets have left behind a geological record of past ice dynamics (Stokes et al., 2015). This means that when modelling past ice sheets, the model results can be compared to the observed data to assess the success of the model. In this thesis, the focus is to look at modelling palaeo-ice sheets in order to learn more about the important mechanisms driving different parts of past ice masses (Chapter 1). This in turn could help improve the predictive capabilities of forward modelling. Throughout this thesis, I have used a numerical ice sheet model, the Parallel Ice Sheet Model (PISM) (Bueler and Brown, 2009; Winkelmann et al., 2011) to produce simulations of the last Eurasian Ice Sheet Complex (EISC) across the last 40 ka. Numerical models take a range of approximations of ice flow. The approach in PISM is that of a hybrid model, combining shallow-shelf and shallow-ice approximations, the details of which are described in Section 2.2. Numerical models require certain boundary conditions and parameter inputs to solve the underlying ice flow equations. Often, the exact values of these parameters are unknown, and a range of values need to be sampled. An ensemble of model simulations is used in this thesis to explore the parameter space, by perturbing the parameter values for each ensemble member.

In this chapter, I start by deriving the underlying physics used within PISM to simulate ice flow (Section 2.2). Then, I describe the input parameters and boundary conditions this thesis explores (Section 2.3). I report results from the initial ensemble experiment, which were qualitatively checked against observations to ensure the model was working effectively (Section 2.4). This led to the development of a parameterization for the precipitation to account for continentality, described in Section 2.4.2. Finally, Section 2.5 describes the perturbed ensemble design methods used in this project and outlines how many simulations will be run in each chapter. The list of parameters and ranges that will be explored for each is also summarised in this section.

2.2 Ice flow physics in PISM

Flow of an ice mass is described by the Stokes equations, which are derived from the Navier-Stokes equations. First, we define $\boldsymbol{u} = (u, v, w)^T$ to be the velocity vector, where u, v represent the horizontal velocities and w represents the vertical velocity, ρ is the density of ice, $\boldsymbol{g}$ is the acceleration due to gravity, p is pressure and η is viscosity. The Navier-Stokes equations for mass and momentum for Newtonian fluids are

$$\nabla \cdot \boldsymbol{u} = \boldsymbol{0}, \quad \rho \frac{D\boldsymbol{u}}{Dt} = \rho \boldsymbol{g} - \nabla p + \eta \nabla^2 \boldsymbol{u}, \tag{2.1}$$

respectively.

For ice sheets, we can estimate the likely orders of magnitudes for the terms in Equation 2.1. Calculating the Reynolds number, which is the ratio of inertial to viscous forces, indicates whether the flow of a fluid is turbulent or laminar, i.e. moving in layers. In this case, the Reynolds number is very small, suggesting ice flows in a laminar manner, and so the Navier-Stokes equations can be simplified by removing the terms relevant to inertial stresses. From this, the Stokes equations (Stokes, 1843) can be derived and are given as

$$\nabla \cdot \boldsymbol{u} = \boldsymbol{0}, \quad \boldsymbol{0} = \rho \boldsymbol{g} - \nabla p + \nabla \cdot \boldsymbol{\tau}. \tag{2.2}$$

where $\boldsymbol{\tau}$ is the deviatoric stress tensor which defines the amount of deformation in each direction.

Solving the underlying physics of how ice and ice sheets flow is extremely complex and requires a lot of computer power and time. There are ice sheet models which solve all of the Stokes equations (e.g. Gagliardini, 2022). However, due to their computational expense, these 'Full-Stokes' models can only be implemented for short time scales or small glaciers. Several approximations can be made to simplify the Stokes system, meaning larger areas and time scales can feasibly be modelled numerically.

The main approximation relies on an ice mass's relatively small depth-width ratio. The model approximations following this concept are called shallow approximations for this reason. First, a shallow-ice approximation (SIA) can calculate the velocity of grounded ice. In particular, an SIA model works well in areas where basal sliding is at a minimum. The second shallow approximation is a shallow-shelf approximation (SSA), which is used in areas where side stresses are more of a focus. This approximation is especially important in fast-flowing areas like ice streams, and for ice shelves where the ice is not grounded and the SIA is ill-posed. PISM combines these two shallow approximations to effectively calculate the velocities across different portions of an ice sheet, which the approximations on their own would be unable to do. This combination is why PISM is often referred to as a hybrid model.

2.2.1 Mass continuity

One important concept that PISM uses is that mass must be conserved. In this case, the stronger condition of the mass having a continuous flow must be upheld and so a mass continuity equation can be derived. Bueler and Brown (2009) gives the kinematic equations at the surface and the base of an ice sheet; in other words, how the surface and base of each ice column change over time. We define $\boldsymbol{x} = (x, y, z)^T$ to be the direction vector, where x, y are the horizontal directions and z is the vertical direction. Let h represent the surface elevation and b represent the bed elevation. Let M be the accumulation and S be the basal melt rate. Then,

$$\begin{aligned} \frac{\partial h}{\partial t} &= M + w_h - \begin{pmatrix} u_h \\ v_h \end{pmatrix} \cdot \nabla h, \\ \frac{\partial b}{\partial t} &= S + w_b - \begin{pmatrix} u_b \\ v_b \end{pmatrix} \cdot \nabla b. \end{aligned} \tag{2.3}$$

We define the ice thickness to be $H = h - b$. Then, to calculate how the ice thickness changes over time, we use

$$\frac{\partial H}{\partial t} = \frac{\partial h}{\partial t} - \frac{\partial b}{\partial t}. \tag{2.4}$$

Substituting in Equations 2.3 into Equation 2.4 gives

$$\frac{\partial H}{\partial t} = (M - S) + (w_h - w_b) - \left(\begin{pmatrix} u_h \\ v_h \end{pmatrix} \cdot \nabla h + \begin{pmatrix} u_b \\ v_b \end{pmatrix} \cdot \nabla b \right). \tag{2.5}$$

To simplify the equation further, we use the incompressibility property of ice. This property ensures that the density of the ice is kept constant. Incompressibility can be written succinctly as $\nabla \cdot u = \frac{\partial u}{\partial x} + \frac{\partial v}{\partial y} + \frac{\partial w}{\partial z} = 0$. By integrating this condition vertically, we get

$$\int_b^h \frac{\partial w}{\partial z}\, dz = -\int_b^h \left[\frac{\partial u}{\partial x} + \frac{\partial v}{\partial y}\right] dz$$

$$w_h - w_b = -\left(\frac{\partial}{\partial x}\int_b^h u\, dz - u_h\frac{\partial h}{\partial x} + u_b\frac{\partial h}{\partial x} + \frac{\partial}{\partial y}\int_b^h v\, dz - v_h\frac{\partial h}{\partial y} + v_b\frac{\partial h}{\partial y} \right)$$

$$w_h - w_b = -\left(\frac{\partial}{\partial x}(H\bar{u}) + \frac{\partial}{\partial y}(H\bar{v}) - \begin{pmatrix} u_h \\ v_h \end{pmatrix} \cdot \nabla h + \begin{pmatrix} u_b \\ v_b \end{pmatrix} \cdot \nabla b \right).$$

This can then be simplified by setting $H\bar{\boldsymbol{u}}$ to be the horizontal ice flux, $\boldsymbol{Q}$ and $\begin{pmatrix} u_. \\ v_. \end{pmatrix} = \boldsymbol{u}_.$, leaving us with the equation

$$w_h - w_b = -\nabla \cdot \boldsymbol{Q} + \boldsymbol{u}_h \cdot \nabla h - \boldsymbol{u}_b \cdot \nabla b. \tag{2.6}$$

Substituting the above (Equation 2.6) into Equation 2.5 gives

$$\frac{\partial H}{\partial t} = M - S - \nabla \cdot \boldsymbol{Q}. \tag{2.7}$$

In PISM, this is how the ice thickness is calculated numerically over the spatial domain at each time point.

2.2.2 Energy conservation

There are three sources of energy transfer arising from ice flow which for the purposes of PISM can be combined into a single equation defining the conservation of energy; advection, conduction and the heat transferred through strain. Advection is the transfer of heat

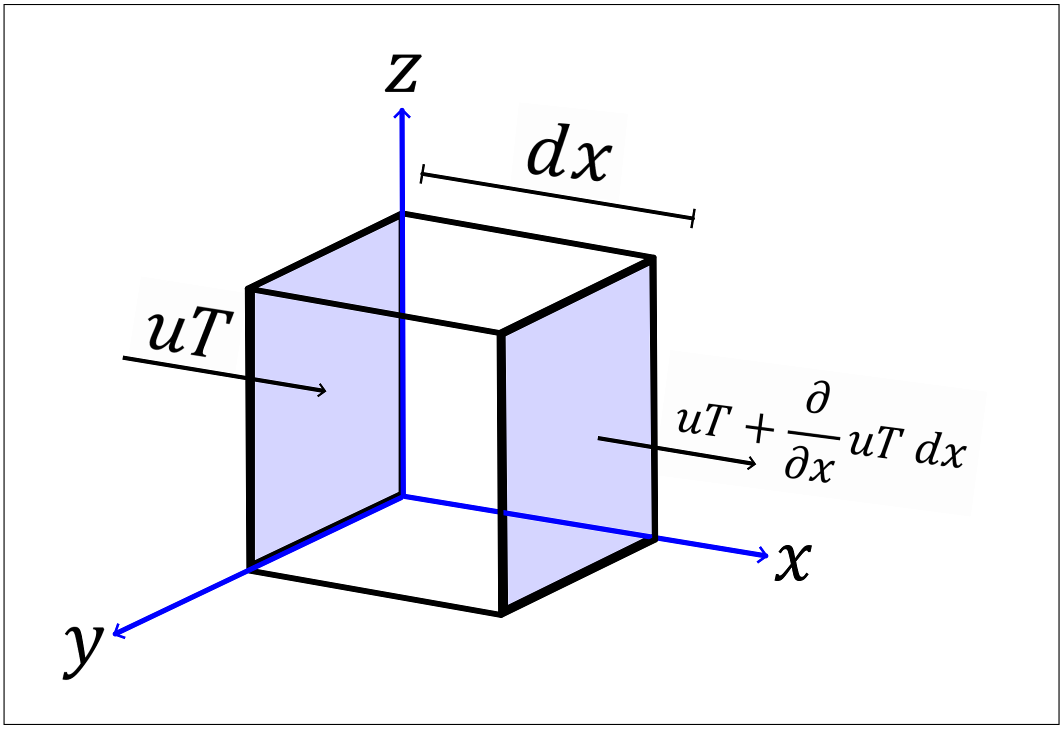

Figure 2.1: Depiction of a grid box in an ice column and the advection flux that occurs in the x direction.

caused by the ice moving and conduction is the transfer of heat caused by atoms vibrating and colliding with other atoms, passing on heat. Firstly, the values for the advection and conduction in the x direction, with the y and z directions calculated using the same procedure, will be derived. The advection flux through one column of ice is

$$Advection_x = \rho c_p \left(uT - (uT + \frac{\partial}{\partial x} uT\,dx) \right) \tag{2.8}$$

$$= -\rho c_p \frac{\partial}{\partial x} uT\,dx, \tag{2.9}$$

where c_p is the specific heat capacity of ice and T is the ice temperature. An illustration of this flux for one ice column in the x direction is shown in Figure 2.1.

For the flux of the conductivity,

$$Conduction_x = k \frac{\partial T}{\partial x}\,dx, \tag{2.10}$$

where k is the conductivity of the ice. We define FD_x, FD_y, FD_z and Σ_x, Σ_y, Σ_z be the total flux deficit and the heat transferred by strain in each direction x, y, z respectively. Then

$$FD_x = -\rho c_p \frac{\partial}{\partial x} uT\, dx + k \frac{\partial T}{\partial x}\, dx + \Sigma_x\, dx. \tag{2.11}$$

Combining the flux deficits in each direction, the conservation of energy in one column of ice, can be derived

$$\begin{aligned} \frac{\partial}{\partial t}(\rho c_p T\, dx\, dy\, dz) &= FD_x\, dy\, dz + FD_y\, dx\, dz + FD_z\, dx\, dy \\ \frac{\partial T}{\partial t}\rho c_p &= FD_x + FD_y + FD_z \end{aligned}$$

$$\begin{aligned} \frac{\partial}{\partial t}(\rho c_p T\, dx\, dy\, dz) = -\rho c_p \left(\frac{\partial}{\partial x} uT\, dx + \frac{\partial}{\partial y} vT\, dy + \frac{\partial}{\partial z} wT\, dz \right) \\ + \left(\frac{\partial^2 T}{\partial x^2}\, dx + \frac{\partial^2 T}{\partial y^2}\, dy + \frac{\partial^2 T}{\partial z^2}\, dz \right) + \Sigma, \end{aligned}$$

where $\Sigma = \Sigma_x + \Sigma_y + \Sigma_z$. Simplifying further,

$$\frac{\partial}{\partial t}(\rho c_p T\, dx\, dy\, dz) = -\rho c_p (\boldsymbol{u} \cdot \nabla T) + k \nabla^2 T + \Sigma. \tag{2.12}$$

In PISM, Equation 2.12 is simplified again omitting the second order partial derivatives in the conduction term in the x and y directions due to the shallow approximation. Also, the calculation for Σ is simplified compared to a Full Stokes model using the same approximation. Hence, in PISM, the equation accounting for the conservation of energy is

$$\frac{\partial T}{\partial t}\rho c_p = -\rho c_p (\boldsymbol{u} \cdot \nabla T) + k \frac{\partial^2 T}{\partial z^2} + \Sigma. \tag{2.13}$$

2.2.3 Basal melt

The standard melting point for ice is defined to be 273.15 K in PISM. However, when ice is under pressure, the melting point is altered. The more pressure applied, the freezing point lowers, and therefore the ice melts more easily. In PISM, the pressure melting point is a linearly decreasing function subtracting ice thickness multiplied by a parameter representing the dependence of melting point due to depth away from the normal melting point. At the base of the ice, the pressure melting point is especially important. Combined with the original ice temperature and the thickness of the ice sheet, there may be basal melting, or freeze-on in the opposite scenario. The ice melted at the base of the ice sheet is stored in the till. The basal melt rate, S, is described in PISM as

$$S\Delta t = \frac{c_p}{L}\int_b^{b+100} (\tilde{T}(t+\Delta t) - T^*)\left[0.2\frac{b+100-z}{100}\right] dz, \tag{2.14}$$

where t is time, L is the latent heat of fusion for ice, $\tilde{T}(t+\Delta t)$ is the predicted ice temperature for a small time step Δt and T^* is the pressure melting temperature for ice. The pressure-adjusted temperature is calculated at each point in an ice column, z. The equation for T^* is

$$T^* = T_0 - 8.66 \times 10^{-4}(h - z), \tag{2.15}$$

where T_0 is the melting temperature for ice and 8.66×10^{-4} K m^{-1} represents how the melting point of ice depends on depth (Bueler and Brown, 2009).

Once the basal melt rate has been calculated, the amount of meltwater stored in the substrate beneath the ice sheet can be found. PISM records this amount of stored water as a representative thickness, W. Over time, this changes as follows

$$\frac{\partial W}{\partial t} = S + K_{melt}\left(\frac{\partial^2 W}{\partial x_1^2} + \frac{\partial^2 W}{\partial x_2^2}\right). \tag{2.16}$$

Adding the right-hand term accounts for the diffusion of some of the meltwater from other columns of ice. The parameter K_{melt} is half of the square of the diffusion distance for the meltwater thickness, given to be 20 km, divided by the diffusion time for the meltwater distance, given to be 1000 years, and so has the value

$$K_{melt} = \frac{1}{2}\left(\frac{20}{1000}\right)^2 = 0.0002.$$

Equivalently, Equation 2.16 means the meltwater thickness is given by the basal melt rate with added diffusion, modelled with a Normal distribution, with mean 20 and variance 1000^2. The model then adjusts the temperature of the ice columns to be no higher than the pressure melting point.

2.2.4 SIA stress balance

As there is a small depth to width ratio with continental ice sheets, as is being studied here, the Stokes equations (Stokes, 1843) can be simplified to a shallow approximation. In the interior of an ice sheet, where the ice is grounded, the ice is very slow moving as there is little to no basal slip. For these parts of the ice sheet, the SIA stress balance is used to calculate the flow.

The SIA stress balance is given by the equation from Bueler and Brown (2009)

$$\left(\frac{\partial u_1}{\partial z}, \frac{\partial u_2}{\partial z}\right) = -2(\rho g)^{n_{SIA}} A(T^*)(h-z)^{n_{SIA}} |\nabla h|^{n_{SIA}-1} \nabla h, \tag{2.17}$$

where n_{SIA} is the flow exponent for the SIA stress balance and $A(T^*)$ is the ice softness depending on the pressure-adjusted temperature of ice. The horizontal velocity field, (u_1, u_2), given by the SIA model can be obtained by integrating the above equation vertically, giving

$$(u_1, u_2) = -2(\rho g)^{n_{SIA}} |\nabla h|^{n_{SIA}-1} \nabla h \int_b^z A(T^*)(h-\zeta)\, d\zeta. \tag{2.18}$$

In the version of PISM used in this study, the enhancement factor, E_{SIA}, is incorporated into Equation 2.18 as well (Winkelmann et al., 2011).

2.2.5 SSA stress balance

When ice begins to float, becoming ice shelves, an SSA stress balance is required as the assumptions used for the SIA are no longer valid, as drag occurs at the sides rather than at the bottom as in the previous section. The SSA stress balance is defined by the pair of equations

$$\frac{\partial}{\partial x}\left[2\bar{\nu}H\left(2\frac{\partial \nu_1}{\partial x} + \frac{\partial \nu_2}{\partial y}\right)\right] + \frac{\partial}{\partial y}\left[\bar{\nu}H\left(\frac{\partial \nu_1}{\partial y} + \frac{\partial \nu_2}{\partial x}\right)\right] + \tau_{b,1} = \rho g H \frac{\partial h}{\partial x} \tag{2.19}$$

$$\frac{\partial}{\partial x}\left[\bar{\nu}H\left(\frac{\partial \nu_1}{\partial y} + \frac{\partial \nu_2}{\partial x}\right)\right] + \frac{\partial}{\partial y}\left[2\bar{\nu}H\left(\frac{\partial \nu_1}{\partial x} + 2\frac{\partial \nu_2}{\partial y}\right)\right] + \tau_{b,2} = \rho g H \frac{\partial h}{\partial y} \tag{2.20}$$

which are solved for the SSA horizontal velocity field (v_1, v_2), using the vertically averaged viscosity, $\bar{\nu}$,

$$\bar{\nu} = \frac{\bar{B}}{2}(E_{SSA})^{-\frac{1}{n_{SSA}}} \left[\frac{1}{2}\dot{\epsilon}_{ij}\dot{\epsilon}_{ij} + \frac{1}{2}\dot{\epsilon}_{ii}^2\right]^{\frac{1-n_{SSA}}{2n_{SSA}}}. \tag{2.21}$$

Here, $\bar{B}$ is the vertically averaged ice hardness, $\tau_{b,i}$ is the basal shear stress, n_{SSA} is the flow law exponent for the SSA stress balance and $\dot{\epsilon}$ is the strain rate tensor. The parameter E_{SSA} is the enhancement factor for the SSA model. The enhancement factors, both for the SIA and the SSA, are included to encapsulate the anisotropic property of ice, whereby the properties of ice are directionally dependent. Solving the above equations is much more computationally expensive than the SIA counterpart.

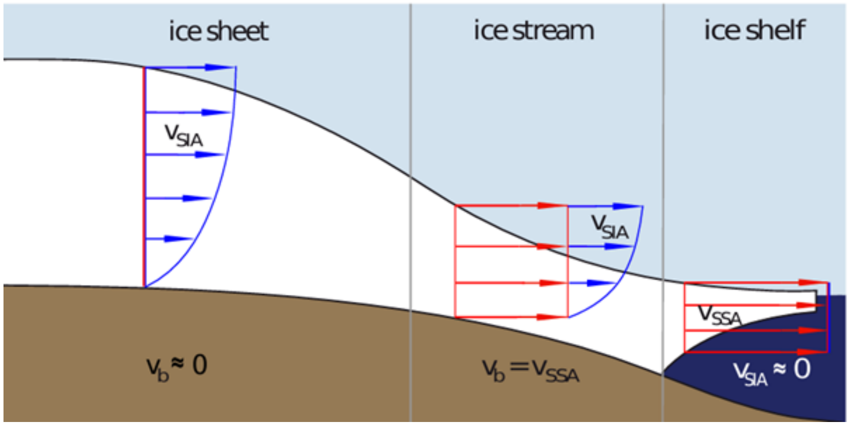

Figure 2.2: Locations where the two stress balances, shallow-ice and shallow-shelf approximation (SIA and SSA respectively), are used on their own or in combination. The red indicates the SSA component, and the blue the SIA component. Taken from Winkelmann et al. (2011).

2.2.6 Combined stress balance

At each time step and in every grid cell, both the SIA and SSA are calculated. Then, in PISM, the overall stress balance combines the SIA and SSA stress balances by simply adding them together. The different areas of an ice sheet can broadly be categorised into three areas. There is grounded ice, which for the EISC is the majority of the ice. Grounded ice near the interior of the ice sheet has negligible basal sliding, and as such, the SSA stress balance is also negligible. When sliding becomes more significant and ice velocity increases, ice streams form. Ice streams are where the importance of the SIA stress balance starts to decrease and the SSA stress balance becomes more significant. For marine-terminating areas of the ice sheet, there is the possibility for ice shelves to form. At the point the ice starts to float, the SSA stress is used as there is no basal drag and thus, the SIA stress no longer captures the relevant processes. The locations where the two stress balances are most important are shown in Figure 2.2.

2.2.7 Basal mechanics

The fast-moving sections of ice sheets achieve high velocities through basal sliding. Because of this, geology plays an important role regarding how much friction the ice sheet's base must overcome to slide, which in turn affects the ice surface elevation and thickness. The sliding law used in this study to calculate the basal shear stress, $\boldsymbol{\tau_b}$, is a power law, dependent on a velocity threshold value, $u_{threshold}$, and an exponent, q, as follows.

$$\boldsymbol{\tau_b} = -\tau_c \frac{\boldsymbol{u}}{u_{threshold}^q |\boldsymbol{u}|^{1-q}}, \tag{2.22}$$

where $u = (u_1 + v_1, u_2 + v_2)$ and τ_c is the yield stress. For the yield stress, a map of values was input into PISM with the domain area categorised. The map, from Pollard et al. (2023) outlines the sections of varying surface characteristics, obtained using satellite imagery, sediment thickness maps and geological mapping, and is shown in Figure 2.3. Five categories were identified: offshore sediment, thick sediment, thin sediment, bedrock and areas where ice streams could form. These five values, as well as the exponent q described in Equation 2.22, were also perturbed in the ensemble.

2.3 Input parameters and boundary conditions

In order to solve the ice flow equations given in Section 2.2 and simulate the growth and retreat of an ice sheet, input values must be chosen, and initial model design choices need to be determined. For the initial model simulations (outlined later in Section 2.5), a horizontal model resolution of 16 km was used with a view to performing higher resolution simulations when the parameter space has been narrowed down. Vertically, the resolution is spaced quadratically, providing a higher resolution output at the base of the ice (on the order of 10s of metres) compared to further up the ice column (in the order of 100s of metres), where changes to the basal temperature are less important. These resolutions give a good amount of detail for their purpose whilst still completing simulations in a reasonable time. The model simulations are run from 40 ka to 5 ka, giving a complete glaciation and subsequent deglaciation. Spatial outputs, such as ice velocity and thickness per grid cell, are produced every 100 years, and one-dimensional outputs, such as total ice volume across the whole area, are produced every 10 years. Often, only one of either the advance or retreat of an ice sheet is simulated (e.g. Gandy et al., 2021; Patton et al., 2017, 2016), so this study aimed to see if both could be modelled successfully in one simulation. The input datasets for boundary conditions and parameter ranges for specific processes are described in the following sections.

2.3.1 Climate forcing

Climate input is one of the most important and most uncertain boundary conditions when modelling palaeo-ice sheets (Stokes et al., 2015). Climatic conditions determine the mass-balance of the ice sheet (Section 2.3.2), and thus govern its size and extent. To calculate mass balance, precipitation levels as well as air temperature both need to be considered.

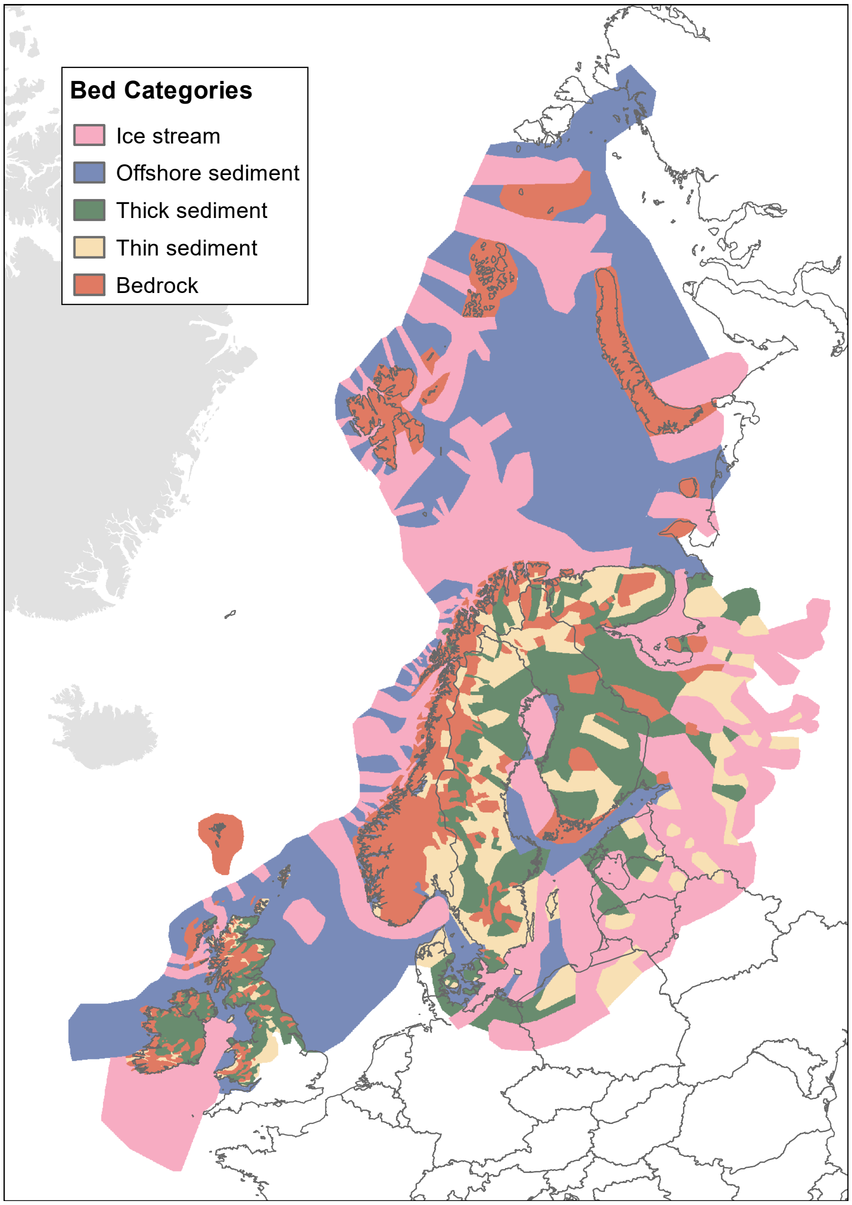

Figure 2.3: Categorisations of land types for assigning basal shear stress, across the model domain, data from Pollard et al. (2023). The default values used for the basal shear stresses and the ranges which are perturbed in the ensemble are given in Table 2.2. Modern country outlines are shown in grey.

The Palaeo-climate Modelling Intercomparison Project Phase 3 (PMIP3) created snapshot climate datasets using various orbital configurations and concentrations of greenhouse gases for both temperature and precipitation (Braconnot et al., 2012). From this, monthly snapshots are derived, showing the two metrics at the LGM, taken to be 21 ka in PMIP3, and at 1850 AD, which is preindustrial (PI) or the time before anthropogenic carbon emissions were produced. There are nine different simulations available for the LGM alone. To encapsulate each of these simulations in our ensemble, a weighted average could be used for both temperature and precipitation inputs at the PI and LGM snapshots. Using a weighted average input would require 36 weighting parameters to account for the nine different models at two snapshots and for each of the precipitation and temperature inputs. This adds a huge amount of extra model simulations to fill the parameter space adequately.

Two methods were used to sample the modelled climates from PMIP3 efficiently. First, we consulted Niu et al. (2019), who simulated the ice cover at 21 ka for the Northern Hemisphere, which is approximately the LGM for the EISC, and considered output from nine of the PMIP3 models. Figure 2.4, taken from Niu et al. (2019), shows these results. From this output, it can be seen that some of the climate models make either far too much or far too little ice cover over Europe. The climate models that create unrealistic amounts of ice cover are ignored for this study. The models kept for this study are COSMOS-ASO (Budich et al., 2010; Raddatz et al., 2007; Roeckner et al., 2003, 2004; Valcke et al., 2006; Wetzel et al., 2004), IPSL-CM5A-LR (Kageyama et al., 2013a,b), MIROC-ESM (Ohgaito et al., 2013; Sueyoshi et al., 2013) and MPI-ESM-P (Giorgetta et al., 2013; Jungclaus et al., 2013; Man et al., 2014) from the Freie Universitaet Berlin, Institute for Meteorology, the Institut Pierre-Simon Laplace, the Japan Agency for Marine-Earth Science and Technology, Atmosphere and Ocean Research Institute (The University of Tokyo) and National Institute for Environmental Studies, and the Max-Planck-Institut für Meteorologie, respectively. Only considering these four simulations reduces the initial number of weighting parameters from 36 down to 16.

The second approach to further reduce the dimensionality within the climate input, was to perform a Principal Component Analysis (PCA). This considered the spatial variation of temperature and precipitation between the four model outputs considered. PCA reduces the input parameter space whilst still containing a large percentage of the variation between the model simulations. A PCA projects the original datasets into a new coordinate system, so each component is independent. These components are ordered by the amount of variance each contains. Depending on the proportion of variance required, some of the components may be found to contribute very little and can be discarded without losing too much of the total information contained by the original data.

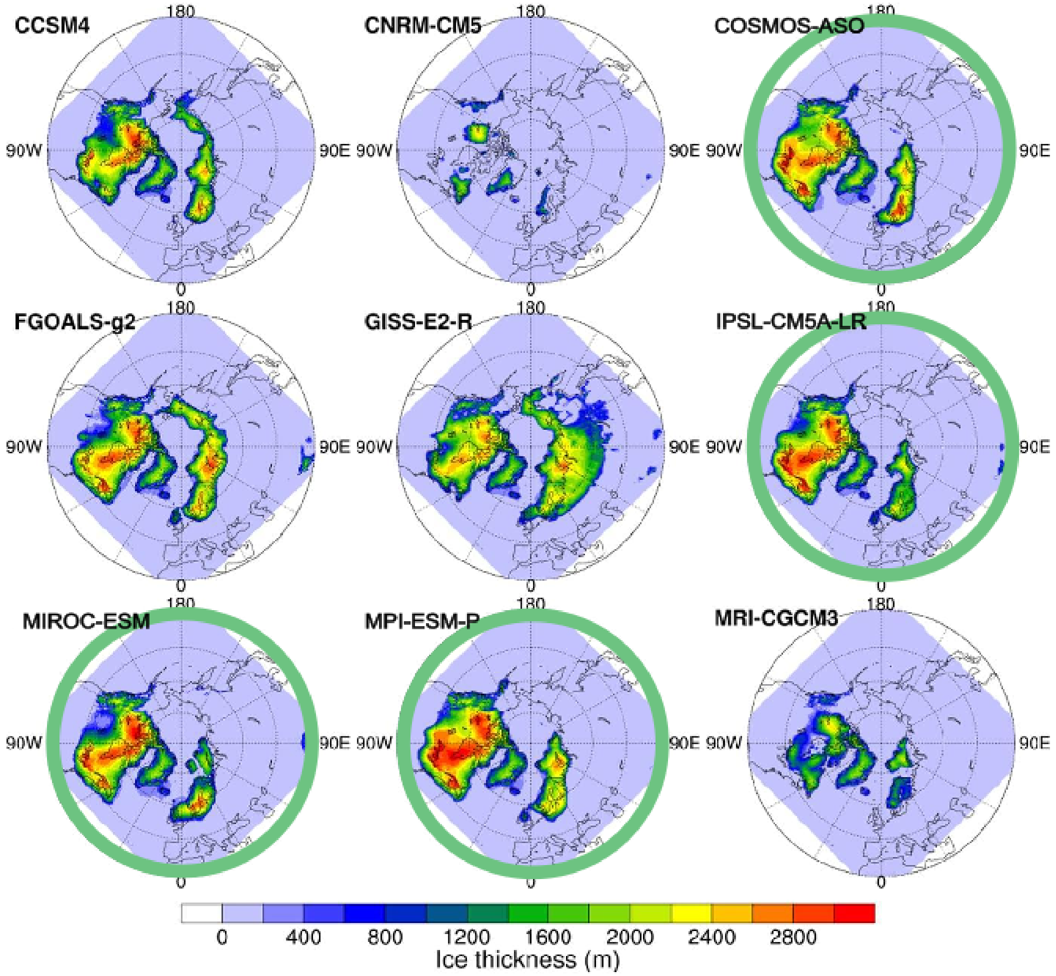

Figure 2.4: Adapted from Niu et al. (2019), showing modelled ice thickness in the Northern Hemisphere at 21 ka driven by nine different climate models. The COSMOS-ASO, ISPL-CM5A-LR, MIROC-ESM and MPI-ESM-P climate models, circled in green, produce a reasonable level of ice cover over Europe at this time, so these four are kept and the remaining PMIP3 simulations are discarded for this study.

A weighted average of the climate models is required, represented by

$$a_1M_1 + a_2M_2 + a_3M_3 + a_4M_4$$

where each a_i is the weighting of the model, M_i, for $i \in \{1, \dots, 4\}$. After the PCA is carried out, a model of the form

$$\alpha_1P_1 + \cdots + \alpha_kP_k$$

will be used where the P_i are the principal components and the α_i are the new weightings, with $i \in \{1, \dots, k\}$ where $k < 4$ is the number of principal components needed to retain an appropriate proportion of the variance. This technique has been shown to work similarly in Turner (2020).

Four PCAs were performed for both the precipitation and temperature data at both the LGM and PI times. The outcome of the PCAs was that only seven principal components are needed to retain around 73% of the total variance, outlined in Table 2.1. Without the PCA, 16 weighting parameters would have to be included in the parameter study, four for each snapshot and type of data. More parameters require more model simulations to explore the unknown parameter space properly, thus the PCA approach appears to be a promising method for reducing computational costs.

Whilst the PMIP3 simulations are a useful starting point, they only provide a monthly snapshot for the LGM and PI periods, whereas the model simulations need a climate input for every year between these snapshots as well. To interpolate between these values, a glacial index approach was implemented. This approach utilises an ice core, specifically GRIP (Anderson and Leng, 2004), which indicates the ratio (δ^{18}O) of Oxygen-18 (^{18}O) to Oxygen-16 (^{16}O) isotopes over time. An ice core contains trapped bubbles of air, frozen at different points in time. The air bubbles provide a record of δ^{18}O throughout time and can be used as a climate proxy. The GRIP core was used as it is the nearest available record to the study area over the time period in question (Figure 2.5). At each point in time, the

Table 2.1: Summary of climate principal components and the variance they capture, perturbed in the initial experiments.

Climate input	Number of Principal Components	Percentage of Variance Captured (%)
LGM Precipitation	2	78
PI Precipitation	2	78
LGM Temperature	2	84
PI Temperature	1	51

glacial index, $I(t)$, is calculated using the following equation

$$I(t) = \frac{\delta^{18}\text{O}(t) - \delta^{18}\text{O}_{PI}}{\delta^{18}\text{O}_{LGM} - \delta^{18}\text{O}_{PI}}, \tag{2.23}$$

for $t \in [40, 5]$ ka. The index is then used to adjust the temperature and precipitation rates for the time steps of interest each month to account for seasonal climate variation. Let $T_{mon}(t, x, y)$ and $P_{mon}(t, x, y)$ represent the monthly temperature and precipitation rates at each time, t, and location, x, y. Then, using equations from Niu et al. (2019)

$$T_{mon}(t, x, y) = T_{mon}(PI, x, y) + \frac{T_{mon}(LGM, x, y) - T_{mon}(PI, x, y)}{I_{LGM} - I_{PI}} I(t) \tag{2.24}$$

and

$$\begin{aligned} P_{mon}&(t, x, y) \\ &= \max\left\{P^*_{mon}(PI, x, y) + \frac{P_{mon}(LGM, x, y) - P^*_{mon}(PI, x, y)}{I_{LGM} - I_{PI}} I(t), 0\right\}, \end{aligned} \tag{2.25}$$

where

$$P^*_{mon}(PI, x, y) = P_{mon}(PI, x, y) e^{\beta h(t,x,y)}$$

which undoes the elevation correction at present day, described below.

In general, precipitation levels are reduced as elevation increases. PISM corrects for this using a decay rate parameter, β, to adjust the precipitation based on the surface elevation, h. The corrected monthly precipitation levels, $P^{cor}_{mon}(t, x, y)$, are given as

$$P^{cor}_{mon}(t, x, y) = P_{mon}(t, x, y) e^{-\beta h(t,x,y)}.$$

Similarly, we use a lapse rate γ_T to adjust the temperature given a certain elevation (Hinck et al., 2022). This reduces the calculated temperature by a linear factor of the change in elevation, where the factor is the lapse rate. The glacial index calculations are performed automatically in an extended version of PISM created and documented in Hinck et al. (2022).

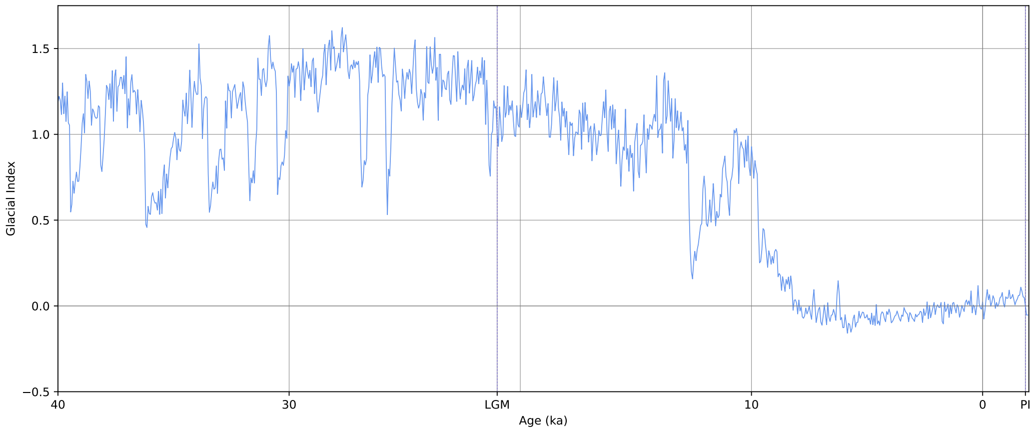

Figure 2.5: Glacial index $I(t)$ from the GRIP core over the time frame used within this study. The times at which there are PMIP3 simulations are marked on in blue, at 21 ka and 1850 AD.

2.3.2 Positive-degree day model

An ice sheet's size is primarily determined by the surface mass balance. The surface mass balance of an ice sheet describes the amount of ice being added, or accumulated, compared to the amount of ice being lost, or ablated. Surface accumulation occurs when precipitation falls as snow or when water freezes onto the ice sheet. Surface ablation occurs through melting and then the surface meltwater can either runoff or can refreeze back onto the ice mass. To calculate the surface mass balance, the snowfall as well as the melt need to be calculated. For this study, a positive-degree day (PDD) model is used for this purpose.

The precipitation input has already been defined using the PMIP3 simulations as described in Section 2.3.1. However, the mass balance, the difference between accumulation and ablation, also needs to be determined. For times when the prescribed temperature is over 2°C, any precipitation falls as rain, and at times where the temperature is below 0°C, precipitation falls as snow. Between these temperatures, a linear relationship is used to determine the amounts of each precipitation. For example, if the temperature is 1°C, half the precipitation will fall as snow, and the other half will fall as rain. To account for daily variability, a small addition to the temperature is included based on the standard deviation of the temperature input. A Normal distribution with this standard deviation is sampled, and this value is used as the added temperature variability.

The original PDD model was formulated by Reeh (1991). This yields a double integral, integrating over both temperature and time. When this PDD model was first implemented into ice sheet models, it was assumed that it had to be solved numerically. This added a large computational expense to running simulations. Calov and Greve (2005) proved that the temperature integral could, in fact, be solved analytically and therefore only the remaining time integral needed to be solved numerically. This sped up the computation of the PDD model significantly, estimated at a 90% increase in efficiency (Calov and Greve, 2005). The formulation used in PISM comes directly from Calov and Greve (2005) and is written as

$$PDD = \int_0^A \frac{\sigma}{\sqrt{2\pi}} \exp\left(\frac{-T_{ac}^2}{2\sigma^2}\right) + \frac{T_{ac}}{2} \mathrm{erfc}\left(\frac{-T_{ac}}{\sigma\sqrt{2}}\right) dt, \tag{2.26}$$

where σ is the standard deviation of temperature, T_{ac} represents the seasonal temperature changes over a year, and A is the time period to evaluate the PDD model over. The final term includes a complementary error function that Calov and Greve (2005) define to be

$$\mathrm{erfc} = \frac{2}{\sqrt{\pi}} \int_0^\infty e^{-x'}\, dx'.$$

Every week in the model simulation, the total snow accumulation and the number of days with temperatures over freezing are summed, called the positive-degree days. Once these values have been obtained, the new snow depth can be calculated

$$\mathrm{SnowDepth}_{t+1} = \mathrm{SnowDepth}_t + \mathrm{Accumulation}.$$

From these values, the snow melt and ice melt can be calculated using two parameters, F_s and F_i respectively, that are varied in the ensemble that define how much melt occurs per PDD

$$\mathrm{SnowMelt}_{max} := PDD \times F_s.$$

If the maximum snow melt is less than the current snow depth, then the calculated melt of snow is removed and none of the below ice is melted. If the maximum snow melt is more than the current snow depth, all the snow is melted and the ice melt is computed as follows

$$\mathrm{IceMelt} := \left(PDD - \frac{\mathrm{SnowMelt}_{max}}{F_s}\right) F_i.$$

PISM also allows for a specified proportion of the melted ice and snow, kept at a constant 60% for all simulations (Ritz, 1997), to refreeze rather than all running off. Through this process the runoff and the surface mass balance are both updated within the simulation. The runoff is the total snow and ice melt with the refreeze subtracted and the surface mass balance is simply the difference between the accumulation and the runoff.

2.3.3 Grid definition and initial conditions

There are several input files provided to PISM to start the simulation. These inputs are often of varying resolutions and are also sometimes incomplete. Before any transient calculations are performed, PISM bootstraps the input files, ensuring all are at the correct resolution as well as interpolating for any missing variables. To specify the resolution that we want the output to be calculated at, there are several parameters that have to be defined. These will stay the same for each member in an ensemble, but the resolution will change between experiments.

We can isolate the domain we wish to simulate, but this needs converting into a grid compatible with a computer model. To do this we define a grid that represents the domain with different dimensions depending on the level of detail needed, an example of this is shown in Figure 2.6. The model grid requires four directions to be specified, x and y giving the horizontal dimensions, and z and bz representing the vertical directions, from the bed upwards and the bed downwards, respectively. Both dimensions are in metres in each direction (defined as L_x, L_y, L_z and L_{bz}), as well as the number of grid cells (defined as M_x, M_y, M_z and M_{bz}) to determine the model resolution. Figure 2.7 shows the domain considered for this project. The domain is specified with L_x as 3696 km, and L_y as 5600 km. The corresponding number of grid cells are 231 for M_x, and 350 grid points for M_y. These values were chosen for the initial simulations to have a 16 km horizontal resolution. Vertically, we create 51 quadratically spaced layers above the bed, M_z, of which the maximum ice thickness cannot exceed 10000 m, L_z. Below the bed, 11 equally spaced layers, M_{bz}, span 2000 m, L_{bz}.

The model simulations all start at 40 ka, which is thought to be a relatively ice-free time over Europe. However, there is evidence that there was a small ice mass across the Scandinavian Mountains in Norway around this time (e.g. Lambeck et al., 2010), so this is included in the initial PISM inputs to account for this. The initial ice thickness of this Norwegian ice mass is taken from a perfectly-plastic ice sheet model (Gowan et al., 2016) conducted by Ely et al. (2024) and Bradley et al. (2023).

2.3.4 Topography and glacio isostatic bed depression

Ice flow is also dependent upon basal topography. Basal topography for this study was taken from GEBCO Bathymetric Compilation Group (2019). The dataset was gridded to a horizontal resolution of 1 km, but this resolution was regridded to match the resolution of different model experiments throughout this thesis to increase computational efficiency. The model domain spans $46^{\circ}N$ to $90^{\circ}N$ and $-15^{\circ}E$ to $110^{\circ}E$, outlined in Figure 2.7.

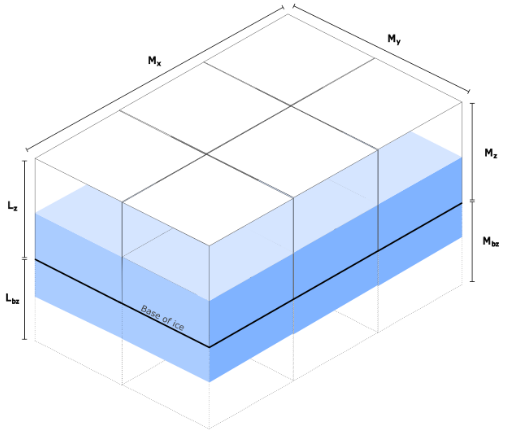

Figure 2.6: An example model grid scheme that can be used within PISM. In this example, $M_x = 3$, $M_y = 2$ and $M_z = M_{bz} = 1$. The values for L_z and L_{bz} are given in metres and set the vertical resolution. The base of the ice is identified by the thick black line.

As an ice sheet increases in size, the mass causes the bed to depress and the local sea level to rise. Conversely, if the ice sheet then shrinks, the ground experiences uplift, and the local sea level will fall. A bed deformation model is included within PISM to account for these effects. The Lingle-Clark bed deformation model, described in Lingle and Clark (1985), considers two layers below the bed, the lithosphere and the upper mantle and calculates how ice of a certain mass deforms the bed. The model uses the flexural rigidity or force needed to bend the lithosphere and the viscosity and density of the upper mantle. Classically, a simpler model is used, one that does not take into account the viscosity of the asthenosphere, however the Lingle-Clark model does not decrease computational efficiency (Bueler, Lingle and Brown, 2007) as a fast Fourier transform can be used for quick computation.

Ice sheets around the globe have two effects on the sea level around our modelled ice sheet. First, the overall sea level is affected by the total size of all ice sheets. The bigger the total mass of ice sheets, the less water in the oceans and therefore, the worldwide sea level is lower. When the ice sheets are smaller, the opposite is true. Secondly, other ice sheets (e.g. Antarctica and the Laurentide ice sheets) create a gravitational attraction around the ice, pulling water towards them. As PISM is not run on a global scale, these effects are not included. To account for these processes, model data from Bradley et al. (2023) is used with the EISC removed from the model to include these sea level changes.

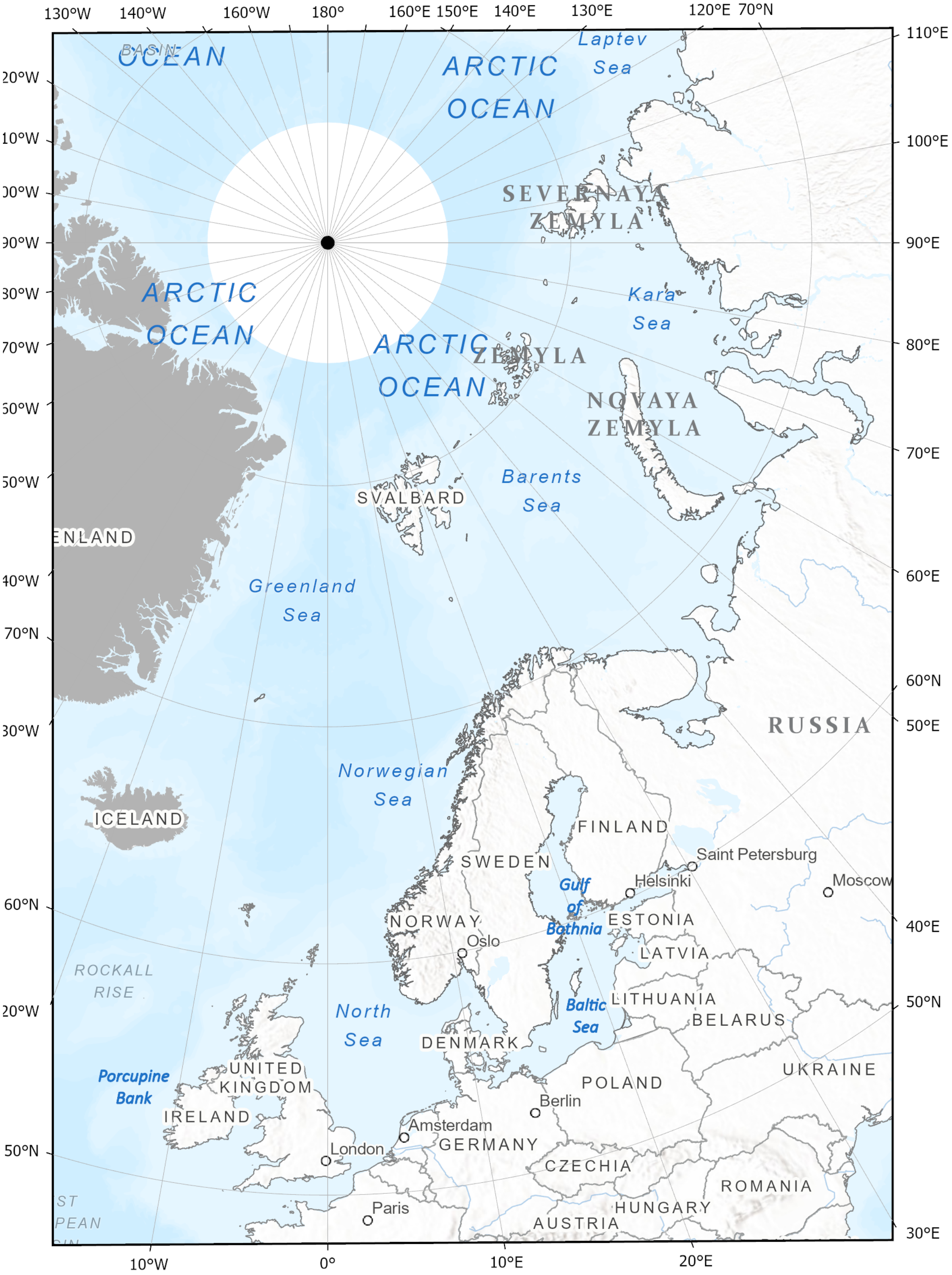

Figure 2.7: Domain considered for model experiments.

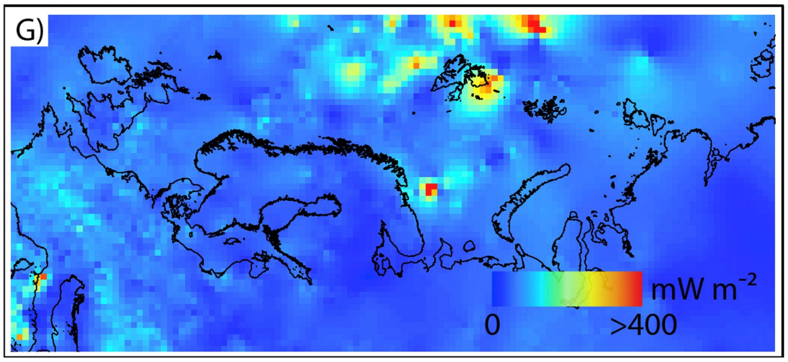

Figure 2.8: Geothermal heat flux input, taken from Patton et al. (2016), data originally from Pollack et al. (1993).

2.3.5 Basal shear stress at the ice sheet bed

When the basal shear stress applied by the ice sheet, $\boldsymbol{\tau_b}$, exceeds the basal yield stress, τ_c, the ice sheet starts to slip. As outlined in Section 2.2.7, five different basal yield stress categories were determined, shown in Figure 2.3, and assigned values, given in Table 2.2. The default values were chosen to ensure the ice stream areas had the lowest value, and were therefore the slippiest, and the areas identified as bedrock had the highest value, and were the hardest parts for the basal shear stress to exceed the yield stress. In each simulation, each of the five categories are perturbed, such that the categories have the same value, i.e. all ice streams across the domain have the same yield stress. The yield stress values that are perturbed in the ensemble are given in Table 2.2.

2.3.6 Basal heat flux

Convection allows heat from the Earth's mantle to reach the surface, which is called geothermal heat flux. The amount of geothermal heat varies across the world (Pollack et al., 1993). A heat flux map is an important input to include as areas with higher geothermal heat will melt the ice much faster than areas with lower flux. The input for this was taken from Patton et al. (2016), originally gridded from Pollack et al. (1993), and is shown in Figure 2.8.

2.3.7 Marine terminating areas of the ice sheet

Marine terminating ice sheets can also lose mass through melt at the terminus. Two factors that are pivotal for determining this melt are ocean temperature as well as salinity. A higher ocean temperature can increase the melt rate of ice shelves, and high ocean salinity causes ice to float more easily.

The amount of heat flux, Q_{heat}, between the ocean and the ice depends on the difference in temperature between the ocean and the temperature required for the ocean to freeze at a certain depth below the surface, $T_o - T_f$, as well as the ocean density, ρ_o, the specific heat capacity of the ocean, c_{p_o}, the thermal exchange velocity, U, and a tuning parameter, F_{melt}. These are combined to calculate heat flux as

$$Q_{heat} = \rho_o c_{p_o} U F_{melt} (T_o - T_f) \tag{2.27}$$

The tuning parameter has been included in order for the heat flux to match observed data (Martin et al., 2011) and will be varied in the ensemble (see Table 2.2 described later).

Within PISM, there is a set of four options commonly used together, especially by researchers at the Potsdam Institute. These have been shown to work well for Antarctica and have also been used in this study. The conditions remove icebergs that cause computational issues (`kill_icebergs`, see Winkelmann et al. (2011)), allow ice shelves to grow across a portion of a grid cell (`part_grid`, see Albrecht et al. (2011)), calculate basal melt around the grounding line (`subgl`, see Feldmann et al. (2014)) and on an ice shelf edge uses a stress boundary condition (`cfbc`, see Winkelmann et al. (2011)).

Marine ice sheets flow into the ocean and under certain conditions, ice can begin to grow out over the water and become a floating ice shelf. When the salinity of the ocean is high, the freezing and melting points of ice are lowered, making an ice shelf harder to form. The thinner the floating ice, the more likely it is to break off the main ice sheet and become an iceberg. This is called calving. Many processes drive calving, e.g., from melting under an ice shelf and crevasse propagation, across different settings, e.g. land and marine (Benn et al., 2007). Due to a lack of understanding behind the mechanics of these processes, the parameterisations used within numerical models do not fully encapsulate the complexities calving is thought to contain (e.g. Choi et al., 2018). In this study, I have chosen to use a thickness-based parameterisation of calving. While more complex calving laws are available in PISM, this choice was made for simplicity, and that this thesis does not directly focus on understanding such processes. This approach sets a value, H_{cr}, that specifies the minimum thickness (in metres) that an ice shelf can be without it being removed. The values chosen for the ensemble experiment are based on observations of marine-terminating ice masses that found that ice shelves experiencing calving rarely have a thickness of less than 200 m (Albrecht et al., 2011) and the range of values explored for H_{cr} are given in Table 2.2.

2.3.8 Ice flow parameters

The ice flow equations, described in Section 2.2, require several parameters namely the enhancement factor (described in Section 2.2.5) and the exponent in both the flow law for the SIA (Equation 2.18) and the SSA (Equation 2.21) stress balances, as well as the exponent in the sliding law (Equation 2.22). When varying the stress balance parameters, the values for the SIA and SSA are kept the same within a simulation but varied across the ensemble (Table 2.2).

2.4 Initial experiments

2.4.1 Results

With all of the parameters outlined in previous sections, 21 have been identified to change within the ensemble experiments. After running 42 preliminary test simulations, both the modelled southern margin and to the east in the Barents Sea were consistently too big, extending around 400 km beyond limits known from geological evidence (Figure 2.9). Interestingly, the southern extent rarely changed with different parameter combinations. The percentage of the initial 42 simulations, sampled with a Latin hypercube method described in Section 2.5.2, that cover the domain at 21 ka is shown in Figure 2.9 and is compared to the reconstructed margins for the same time from Hughes et al. (2016). From this, it was suspected that a key process was not being represented in the current model setup. As there was too much ice growing, it seemed likely that there was a problem with the precipitation input and it was found that previous studies modelling the BIIS found similar results, (e.g. Boulton and Hagdorn, 2006). As a test to confirm whether the precipitation input was the cause of the invariably large extent, the model was run with half the original precipitation. Whilst this altered input did not solve the whole extent problem, it did go some way to reduce it. Given that the southern margin is furthest from the main source of moisture, the Atlantic Ocean, the effects of continentality were expected to be important, as discussed below.

2.4.2 Accounting for continentality

The equilibrium line depicts the point where the accumulation and ablation levels are equal, i.e. no ice mass is gained or lost. The altitude of the equilibrium line increases for ice masses further inland (Chorlton and Lister, 1968, 1971). This effect is called continentality. To account for this effect within the model, a curve is used to represent precipitation decay

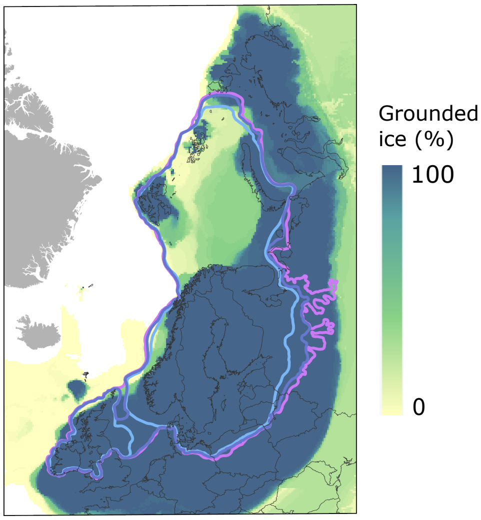

Figure 2.9: The percentage ice cover at 21 ka summarised from a preliminary 42 member Latin hypercube ensemble, overlaid with the minimum, maximum and most-credible (in blue, purple and pink respectively) LGM extents derived by Hughes et al. (2016), based on geological evidence. Note that these simulations predict ice extent considerably exceeding the southern and eastern margins of the known ice sheet.

dependent on distance away from the continental shelf break in the Norwegian Sea. The equation of the curve is

$$y = \frac{80}{1 + \exp(mx - 5)} + 20 \tag{2.28}$$

with m being the gradient of the curve, and x being the calculated distance, shown in Figure 2.10. This curve was chosen so that the reduction in precipitation never exceeds 80% and decays at an appropriate rate over the distances considered. Three boxes, separating the three ice sheets (BIIS, SIS and SBKIS), are being considered with different decay rates outlined in Figure 2.11.

An initial experiment was run to ensure the new parameters were having the desired effect of reducing the ice extent. The ice thickness output at 21 ka of this initial experiment is provided in Figure 2.12 and shows the reduced ice extent compared to the original ensemble seen in Figure 2.9. Hence, the four planned parameters for the precipitation PCA can be removed and replaced with the three new parameters from the precipitation decay approach to account for continentality. This reduces the parameter space from 21 parameters to 20.

Figure 2.11 shows the ranges of decay gradients considered for each of the areas. In the large ensemble, the three gradient parameters have ranges: $m_{brit} \in [9, 30]$, $m_{scandi} \in [5, 10]$ and $m_{barents} \in [0.5, 2]$.

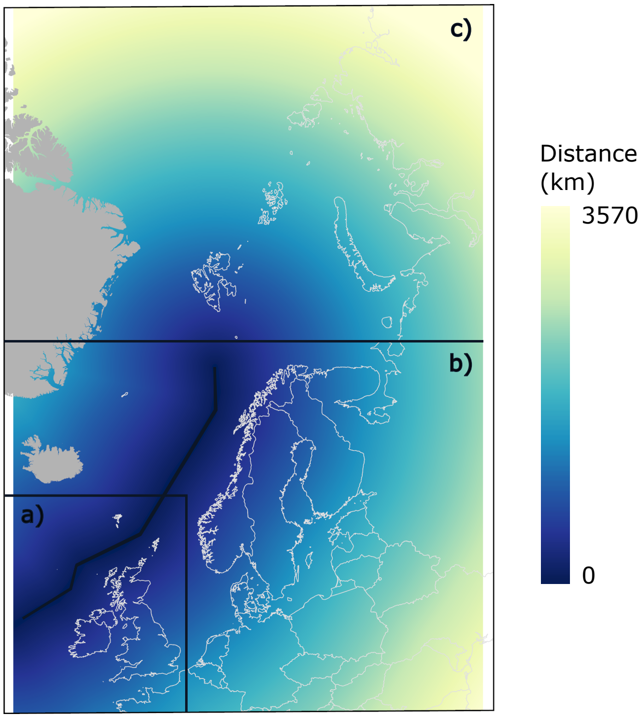

Figure 2.10: The blue to yellow gradient shows the distance from the continental shelf break, represented by the grey line north of Britain and Norway. The continental shelf break is drawn up until the inferred influence of the thermohaline circulation. The domain is split into three areas roughly matching the three ice sheets being modelled, the British-Irish Ice Sheet, the Scandinavian Ice Sheet and the Svalbard-Barents-Kara Sea Ice Sheet indicated by **a**, **b** and **c**, respectively.

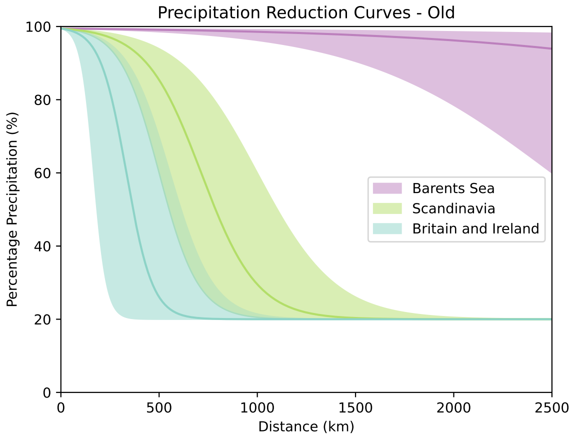

Figure 2.11: Subdomains for applying the continentality effect. The lines within each of the three sections represent the default gradient given in Table 2.2.

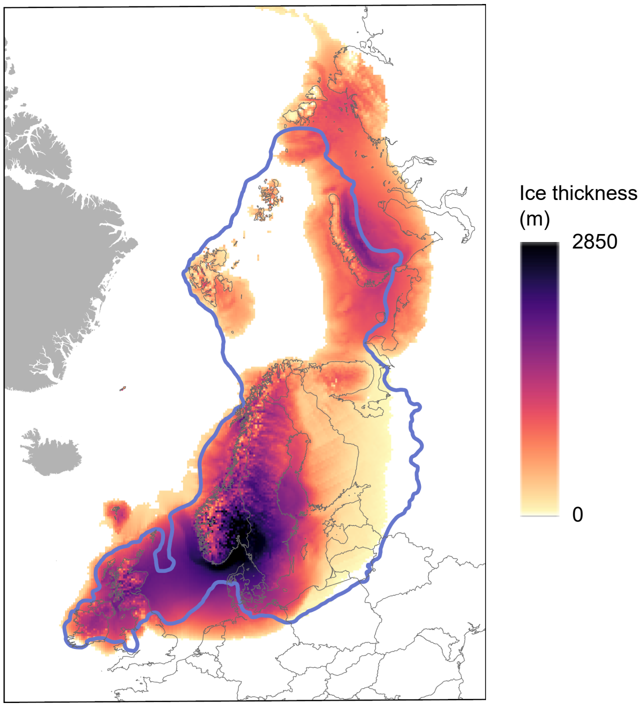

Figure 2.12: Ice thickness at 21 ka from a simulation using the default parameters (see Table 2.2) including the precipitation gradient parameters to account for the continentality effect of declining precipitation away from the ocean. The blue line shows the most credible ice extent according to Hughes et al. (2016).

Table 2.2: Parameters and ranges of interest that will be explored in the initial perturbed ensembles.

Parameter	Parameter Symbol	Range Explored	Default Value
Flow exponent	n_{SIA}/n_{SSA}	$[2, 4]$	3
Flow enhancement	E_{SIA}/E_{SSA}	$[0.5, 3]$	1.75
Sliding law exponent	q	$(0, 1)$	0.5
Calving thickness threshold	H_{cr}	$[50, 300]$	175
PDD snow	F_s	$[2, 5]$	3.5
PDD ice	F_i	$[5, 10]$	7.5
Thin till yield stress	τ_c	$[60, 100]$	80
Thick till yield stress		$[30, 70]$	50
Offshore sediment yield stress		$[10, 30]$	20
Bedrock yield stress		$[100, 150]$	125
Ice stream yield stress		$[5, 20]$	12.5
Principal component weightings for temperature (see Table 2.1)	α_i	$[-1, 1]$	0
Precipitation decay gradients	m_{brit}	$[9, 30]$	15
	m_{scandi}	$[5, 10]$	7
	$m_{barents}$	$[0.5, 2]$	1
Melt factor	F_{melt}	$[0.005, 0.05]$	0.0275
Temperature lapse rate	γ_T	$[0.04, 0.09]$	0.065
Precipitation decay rate	β	$[40, 100]$	70

2.5 Ensemble design and sampling

I have identified 20 parameters that need to have a value assigned in order for the ice flow equations to be solved (Table 2.1 and Table 2.2). In the section below, I explore the parameter space that needs to be considered in the perturbed ensembles, then in Section 2.5.2, I look into different sampling techniques for creating the said ensemble and then in Section 2.5.3, I outline the ensemble I run for use throughout the rest of the thesis.

2.5.1 Parameter ranges

In Sections 2.2 and 2.3, 20 parameters have been identified to include in the perturbed ensemble. The range of values chosen for each parameter was determined by looking at a previous study that achieved reasonable results over the BIIS (Ely et al., 2024). Each of the parameters that will be perturbed in this study and the associated values are shown in Table 2.2.

2.5.2 Sampling methods

When starting to run numerical model simulations with unknown parameters, it is important to explore the parameter space to learn how the parameters affect model output and try to find the optimum parameter values. There are a number of different sampling methods available. In this thesis, two are considered; one-at-a-time sampling and Latin hypercube sampling. The former is considered a local sampling technique, and the latter is a global sampling technique. The differences between the two methods are discussed below.

One-at-a-time sampling

A common sampling method within glaciology is termed one-at-a-time (OAT) sampling. All parameters are given a set, default value and then in each simulation one parameter is changed to an extreme value, either the minimum or maximum value in the range. There are several limitations to this method, discussed fully in Chapter 4, but the main issue is that this method cannot capture the interactions that may occur between parameters.

Latin hypercube sampling

Different from the previous method, a Latin hypercube sample varies all of the parameters in every simulation (McKay et al., 1979). The method systematically samples so that the parameter space is more fully explored and investigates the effects that multiple parameters can cause when interacting. Each parameter range is split uniformly into a specified number of strata. The number of strata dividing the parameter ranges should match the number of simulations required for the sample. For every parameter range, each value in each stratum is included in exactly one sample. Figure 2.13 shows an example of a Latin Hypercube design sample in two dimensions with five input samples that comply with this design.

An extension to this sampling approach is to require the condition that the minimum distance between points is maximised. The maximin criterion ensures the sample points are spread across the parameter space in the most optimal way to explore the effects of different parameter combinations (Jones and Johnson, 2009).

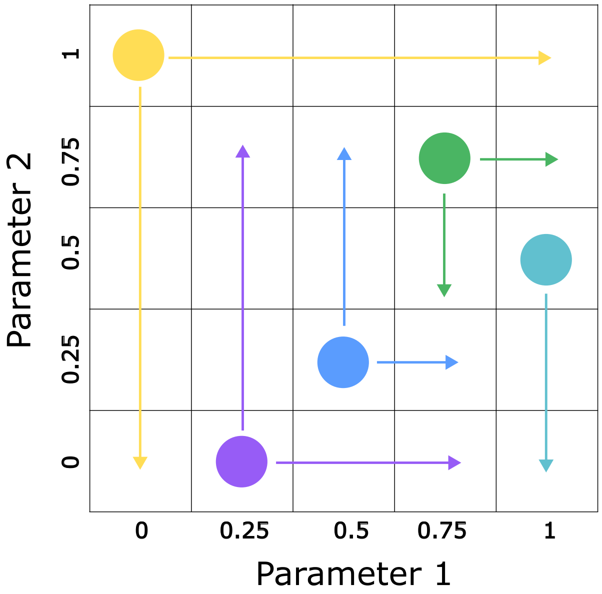

Figure 2.13: An example Latin hypercube design for sampling across a parameter space with two parameters and five input samples that comply with the design, shown as coloured circles.

2.5.3 Number of experiments

In Chapter 4, an initial ensemble will be performed. For this ensemble, 200 model simulations will be completed with parameter inputs sampled uniformly according to a maximin Latin hypercube design. Then, in Chapter 6, a further 130 simulations will be performed with a new sampling routine and a reduced parameter space, described throughout this thesis.

2.6 Summary

In this chapter, I have summarised the main components and underlying physics that make PISM run and the approximations that have been made to reduce the computational cost and time frame that simulations will take to perform. Notably, several of the parameters are poorly constrained, exemplifying the need for performing perturbation experiments to fully explore the parameter space and find the most likely parameter values and ranges. The largest uncertainty is likely the climate input. To account for this, I use a PCA for the temperature input, outlined in Section 2.3.1, and a precipitation reduction gradient based on the effect of continentality for the precipitation input, discussed in Section 2.4.2. The total number of parameters that will be explored in the large ensemble in Chapter 4 is 20. The large ensemble will be comprised of 200 simulations, and the parameters will be sampled using a Latin hypercube design. As seen in Section 2.5, a Latin hypercube design allows the parameter interactions to be investigated, as opposed to an OAT approach which is commonly used in this field.

Notation for Chapter 2

Symbol	Description
$A(T^*)$	Ice softness for ice at pressure adjusted temperature
$\bar{B}$	Vertically averaged ice hardness
b	Bed elevation
bz	Specifying the vertical direction below the bed
c_p	Specific heat capacity of ice, c_{p_o} is the specific heat capacity of the ocean
$\dot{\epsilon}$	Strain rate tensor
FD_x	Total flux deficit in the x direction
$\boldsymbol{g}$	Acceleration due to gravity
H	Ice thickness
h	Surface elevation
η	Viscosity
$I(t)$	Glacial index function
K_{melt}	Parameter calculated as half the squares value of diffusion distance
k	Conductivity of ice
L	Latent heat of fusion for ice
L_x,L_y,L_z,L_{bz}	Number of metres in directions x, y, z and bz that defines the PISM grid
M	Accumulation
M_x,M_y,M_z,M_{bz}	Number of grid points in directions x, y, z and bz that defines the PISM grid
$\bar{\nu}$	Vertically averaged viscosity
$P_{mon}(t,x,y)$	Monthly precipitation rates
p	Pressure
ρ	Density of ice, ρ_o is the density of the ocean
$\boldsymbol{Q}$	Horizontal ice flux
Q_{heat}	Heat flux
S	Basal melt rate
Σ	Heat transferred by strain
σ	Standard deviation of temperature
T	Temperature of ice, T_o is the ocean temperature and T_f is the temperature for the ocean to freeze
T^*	Temperature of ice adjusted for pressure
$T_{mon}(t,x,y)$	Monthly temperature rates
T_{ac}	Seasonal temperature changes over a year
t	Time
$\boldsymbol{\tau_b}$	Basal shear stress
$\boldsymbol{\tau} = (\tau_{ij})$	Deviatoric stress tensor
U	Thermal exchange velocity
$\boldsymbol{u} = (u,v,w)^T$	Velocity vector, where u, v are horizontal velocities and w is vertical velocity
$u_{threshold}$	Velocity threshold for sliding
W	Representative stored water thickness
$\boldsymbol{x} = (x,y,z)^T$	Direction vector

Chapter 3

Assessing ice sheet models against the landform record: The Likelihood of Accordant Lineations Analysis (LALA) tool

3.1 Introduction

The information left behind by palaeo-ice sheets provides a long-term record of ice sheet behaviour (Clark et al., 2018) which, if unlocked, has great potential to be used to improve the predictive ice sheet models essential to forecasting the fate of ice sheets in our warming world (e.g. Edwards et al., 2021; Goelzer et al., 2013; Lipscomb et al., 2021; Nowicki et al., 2020), and our reconstructions of past ice sheets (e.g. Andrews, 1982; Stokes et al., 2015). Quantitative comparisons between numerical model simulations and palaeo-ice sheet evidence are becoming more commonplace (e.g. Ely et al., 2021; Gandy et al., 2019, 2021; Tarasov et al., 2012), replacing qualitative descriptions of fit to evidence (e.g. Boulton and Hagdorn, 2006; Siegert and Dowdeswell, 2004). This shift is prompted by a need to quantify the degree-of-fit between models and evidence to assess output uncertainty, and is facilitated by an increase in computing power enabling sufficient resolution within simulations for comparison to take place. However, the use of quantitative model-data comparison tools in palaeo-ice sheet modelling experiments are far from routine. This is at least partially a consequence of the underdevelopment of model-data comparison tools.

The most abundant landform evidence left behind by palaeo-ice sheets are subglacial lineations (henceforth lineations). Often thought of as the separate categories of drumlins (e.g. Menzies, 1984), crag and tails (e.g. Dowdeswell, Todd and Dowdeswell, 2016), and mega-scale glacial lineations (MSGL) (Clark, 1993), lineations can be broadly defined as streamlined hills, formed at the ice-bed interface. Lineations are typically on the order of 100-1000 m in length, though they can reach several kilometres in the case of MSGL (Spagnolo et al., 2014). The origin of subglacial lineations, especially drumlins, has garnered much scientific debate and is an active field of research, see Ely et al. (2022). However, general agreement can be found amongst geomorphologists on two factors: i) lineations are streamlined in the direction of ice flow, and thus represent former ice flow direction at a point in time during the lifecycle of an ice sheet; and ii) lineations form under warm-based conditions, conducive to the transport of subglacial material. Two further observations help glacial geomorphologists reconstruct the past behaviour of ice sheets. First, lineations typically occur in fields of regular arrangement with similar orientation and morphology (Clark et al., 2018), although isolated examples do also exist (Evans et al., 2015). As such, lineations can be grouped into flowsets, larger regions of a palaeo-ice sheet bed thought to represent an ice sheet flow event (Clark, 1997). Second, sets of lineations can be observed to cross-cut each other, with younger forms superimposed upon those formed during older flow events (Clark, 1993). Such cross-cutting relationships enable a sequence of ice flow orientations to be deciphered. On this basis, the interpretation of lineations has provided much insight into the operation of palaeo-ice sheets (e.g. Dyke, 2008; Greenwood and Clark, 2009; Hughes et al., 2014; Stokes et al., 2009).

Despite being a pervasive and information-rich source of data on palaeo-ice sheet behaviour, lineations are underutilised in palaeo-ice sheet modelling experiments. There have been initial approaches for incorporating observed lineations into model-data comparisons, however, these lack statistical rigour. The first attempt at building a tool for comparing simulated ice flow directions and those derived from observations of lineations was developed by Li et al. (2007). The Automated Flow Direction Analysis (AFDA) tool provides a measure of the degree-of-fit between simulated and observed flow directions throughout the duration of an ice sheet simulation (Li et al., 2007). Two metrics are calculated from gridded datasets of simulated and observed flow directions. The resultant mean difference aims to provide a measure of the overall directional offset between simulation and data, whilst residual variance is used as a measure of the level of agreement between the shape of the two flows. Ely et al. (2021) subsequently developed a workflow for assessing whether cross-cutting relationships were replicated, whereby model-data agreement was declared if a simulation was able to replicate flow directions in the correct sequence.

Despite its existence, uptake of AFDA has been low. As of February 2023, a Google Scholar search indicated that Li et al. (2007) had been actively used in six studies which use the tool within ice sheet model experiments. This may reflect the tool being ahead of its time, as ice sheet simulations have only recently been able to simulate the detailed flow fields recorded in lineations. It may also be due to certain weaknesses of AFDA, which are aimed to be addressed in this work. The lack of a comprehensive and formal statistical underpinning to AFDA makes decisions about the degree-of-fit between an ice sheet simulation and observed lineation data highly subjective. A declaration of a model-data match requires user-defined thresholds in resultant mean difference and residual variance (Ely et al., 2021). This hinders comparison between simulations.

The need to run many computationally expensive simulations has started to encourage statistical surrogates to be incorporated into ice sheet modelling workflows (Edwards et al., 2021). Empirical data from ice sheets has not yet been used to refine a model parameter space to improve the model-data fit. One approach to do this is to use an emulator with a metric encapsulating the fit of each model simulation to the empirical data. Model-data comparison tools therefore became a big point of interest. The binary fit/no-fit metric of AFDA is unsuitable for emulation, which requires a more refined, continuous, and rigorous measure of fit as well as the inability to compare simulations within an ensemble directly. Hence, in this chapter, I present a novel scoring method for comparing observed lineations with numerical model output. I have created Python functions and code to run this method with typical model output, netCDF files, and include a written, worked example and the same example implemented in code. This work is published in Archer et al. (2023).

This chapter is laid out as follows. In Section 3.2 an overview of the Likelihood of Accordant Lineations Analysis (LALA) and how the tool scores a simulation against a record of observed lineations is outlined. A simple example is worked through in Section 3.2.9 to illustrate the method. A key component explored in this chapter is how to incorporate uncertainty into the scoring process. In Section 3.4, the uncertainty occurring between different people interpreting the observational record differently is investigated and then results of the experiment are discussed in Section 3.4.2. Finally, LALA is used to score an ensemble of the British-Irish Ice Sheet, in Section 3.5.

The new tool, LALA, is provided in Archer et al. (2023) as a Python script (v3.0+) along with a tutorial that works through synthetic examples of observed lineation locations and directions, and ice sheet model output that can be found at `https://github.com/rosiearcher/LALA-Tool`. It is built to handle netCDF files of ice sheet model simulations and observations of lineation formation. NetCDF files are a common format for ice sheet model output and is also the format of PISM output which is the numerical ice sheet model used in this thesis. An overview of the statistical underpinning of LALA is provided in Section 3.2 below.

In brief, LALA considers that lineations were formed under specific subglacial conditions, and aligned with the ice flow direction at the time of their formation. The likelihood that the observed lineations were formed by a prescribed ice sheet simulation is calculated, providing an assessment of that specific simulation's quality-of-fit. Typically, I expect this tool will be used to compare different simulations within a large ensemble, perhaps representing a range of hypothetical forcings and ice sheet parameter selections, to identify those simulations that are most likely and hence narrow down the plausible range of forcings and parameters. The output from LALA can, however, also be considered on a per-flowset basis, as demonstrated later in Section 3.5, where the tool is applied to simulation of the BIIS. The relative timings of lineations can be inferred from the observational record and are a valuable addition to learning about the timings of past flow directions of palaeo-ice sheets. Accounting for these cross-cutting relationships is currently beyond the scope of LALA, but would be an interesting extension to explore. In this application of LALA, only a single point in the centre of each flowset is considered, which may not represent flow across complex flowsets with curving directions. Equally, users of LALA could score each model cell a flowset covers and check for coherent temporal matches.

3.2 A probabilistic model for the likelihood of flowset formation

LALA is built upon a rigorous statistical foundation: a simple probabilistic model, based upon three initial assumptions regarding the formation of lineations, that provides a link between an ice sheet and its resultant lineations. Having constructed this probabilistic model, the LALA tool and the score for any ice sheet simulation follow directly. Suppose that observations of lineations are gridded to the scale of the ice sheet model output in question to compare, which correspond to n flowsets across the overall study region $\mathcal{X}$, a complete or partial palaeo-ice sheet bed. These flowsets are observed at locations $x_1, \ldots, x_n$ and are accompanied by estimates of their inferred directions $\theta_1, \ldots, \theta_n$. Given these observed flowsets, providing paired $(x_i, \theta_i)_{i=1}^n$ information, the aim is to score any simulated ice sheet M to assess its level of agreement with the observations across the simulated time period $\mathcal{T}$. This score is obtained by evaluating the log-likelihood of the ice sheet under consideration, $l(M|(x_i, \theta_i)_{i=1}^n)$, according to directional and locational model-data match.

Throughout this chapter, I will denote an ice sheet, M, at time t and location x as $M(x, t)$. This $M(x, t)$ is effectively output of an ice sheet simulation at a specific time step and location and might consist of many variables, e.g., ice thickness, basal and englacial velocity (speed and direction), thermal regime, and mass balance. Given an ice sheet $M(x,t)$, over locations $x \in \mathcal{X}$ and times $t \in \mathcal{T}$, three assumptions are made regarding the creation of flowsets.

The first assumption is that ice cover is required for lineation formation. At any time t when a location x is covered by ice, there is a small probability that lineations could form in that location. This probability of forming lineations may depend upon the location, the time, and the properties of the ice sheet at that time. Denote the probability of lineation formation at location x and time t as $\lambda(x,t,M(x,t))$. This will critically depend upon the properties of the ice sheet under consideration and the location x.

Secondly, assume that the formation of lineations are completely independent from one another in both space and time (conditional on the value of λ). This assumption likely holds at the scale of an ice sheet that is considered here, though note that at the scale of neighbouring lineations, interactions between lineations may occur (Ely et al., 2018).

The last assumption is that lineations align with ice flow direction. Intuitively, the lineations will align (at least approximately) with the ice flow at the point they are formed. However, from lineation morphology alone, it can be difficult to ascertain the upstream and downstream ends of a lineation (Spagnolo et al., 2011, 2010), especially in regions which experienced a complex ice flow history. Thus, the tool allows for orientations to be exactly opposite of those prescribed by the user (i.e., the lineations could record ice flow in the exact opposite direction). This assumption could be relaxed in future versions of LALA, to account for regions where ice flow direction is well known.

Under these initial assumptions, the flowsets form what is known as a marked, inhomogeneous, Poisson point process (Kingman, 1993). A Poisson point process can model the occurrence of random, independent events over a defined space. An intensity function is associated with the point process and defines the rate at which events appear in the set space. In this case, to make the tool as flexible as possible, an inhomogeneous intensity function is specified so that the intensity can be non-constant function across the space. For LALA, the intensity function will depend on the location, time and the simulation output and will be denoted as $\lambda_M = \lambda(x,t,M(x,t))$. A marked Poisson point process utilises the same idea, with the added benefit of attaching an extra piece of information to each point, in this case: direction. Here, lineations are the points, with the orientations of the lineations being the marks, and the model domain is the space where the formation of lineations is considered. The associated rate that is attached to this Poisson process is calculated from the expected number of lineations in the domain over time divided by the number of time-integrated plausible areas for lineation formation, and the inhomogeneous property allows for the rate to vary with respect to space and time. For any subregion $\mathcal{A}$ and time interval $(a, b]$ the number flowsets formed $N(\mathcal{A}, (a, b])$ will follow a Poisson distribution with mean

$$\Lambda(\mathcal{A}, (a, b]) = \int_{\mathcal{A}} \int_a^b \lambda(x, t, M(x, t))\, dt\, dx,$$

that is to say, $N(\mathcal{A}, (a, b]) \sim Po(\Lambda(\mathcal{A}, (a, b]))$.

Given a set of n observed flowsets at locations $x_1, \ldots, x_n$ and with estimated paired directions $\theta_1, \ldots, \theta_n$, the Poisson point process model can be used to calculate the log-likelihood of any particular ice sheet. This log-likelihood is the score of one simulation calculated by the LALA tool. Those ice sheets with greater log-likelihoods are more likely than those ice sheets with lower log-likelihoods in the sense that they make the observed lineations (in terms of both location and direction) more probable. The full details on constructing the log-likelihood can be found in Section 3.2.7, but an intuitive explanation of the main elements is provided below.

The study region should be restricted to those areas which have been assessed for lineations (i.e., the location has been checked, and it is known whether the location has, or does not have lineations). Those regions which have not been mapped (and hence where the existence, or absence, of lineations is unknown at an ice sheet model resolution) should not be included in the tool or form part of the study area $\mathcal{X}$. When scoring an ice sheet against the flowsets, the value of the ice sheet in this unmapped area should also be discarded.

3.2.1 Overview of scoring direction and location

The rate of lineation formation at a specific point and time, $\lambda(x, t, M(x, t))$ can, in principle, depend upon multiple variables: the location, the time, the properties of the ice sheet and properties of the sediment. However, for the initial implementation of LALA and to simplify the intuitive explanation below, the dependence on these other variables is reduced so that $\lambda(x, t, M(x, t))$ has two states: i) potential for lineation formation and ii) impossible for lineation formation.

The conditions for which the formation of lineations is possible is a debated topic (for a recent review, see Ely et al. (2024)), however, this is not a discussion to be solved in this thesis. For the purposes of this chapter, and used subsequently, a simplistic set of conditions is decided upon. The conditions for formation are that at a specified time and location, ice must be present and grounded, as well as thicker than 10 m and have a velocity higher than 10 ms^{-1}. For ease of notation, these conditions will henceforth be referred to as the set $\mathcal{S}$. Other users of LALA can change or adapt $\mathcal{S}$, based on what the user deems important for formation. In the two-state version of $\lambda(x, t, M(x, t))$, set

$$\lambda(x,t,M(x,t)) = \begin{cases} \lambda, & \text{if } (x,t,M(x,t)) \in \mathcal{S} \\ 0, & \text{otherwise} \end{cases} \tag{3.1}$$

for some constant λ. A description of how to choose the value of λ is given in Section 3.2.8. Whilst the focus will be on the two-state approach described above, a more general $\lambda(x,t,M(x,t))$ can also be used.

The final score given by LALA for each ice sheet simulation is based on likelihoods and is made up of two parts. First, the likelihood associated with the number and locations of flowsets is calculated. This accounts for the amount of time the simulated ice sheet has the correct conditions for flowset formation over the domain. The second part is the likelihood that accounts for the closeness of the orientation match of the observed and simulated flow directions. The method for calculating these two likelihoods is described below.

3.2.2 Number and locations of flowsets

The first two of the assumptions taken in this chapter (ice cover and the complete independence of lineation forming events) imply that for any ice sheet M, the number and locations of the flowsets follow an inhomogeneous Poisson point process (Kingman, 1993). Let N as the random variable representing the number of observed flowsets. Under this model, the number of flowsets for a particular ice sheet follows a Poisson distribution with mean $\int_{\mathcal{X}} \lambda_M(x)\,dx = \Lambda_M(\mathcal{X})$. To compute the likelihood of forming n flowsets in the locations $\mathbf{x} = (x_1, \ldots, x_n)^T$ where they were observed, under this model for N, first, split the likelihood up into components that are simpler to find.

$$\mathcal{L}_M(\lambda(x,t,M(x,t))\,|\,\mathbf{x}) \propto P(N=n) \times \mathcal{L}_M(N=n,\, \lambda(x,t,M(x,t)\,|\,\mathbf{x}). \tag{3.2}$$

Next, both of the above components can be calculated. Using the probability mass function of the Poisson distribution outlined above, the first component can be found directly.

$$P(N=n) = \frac{\Lambda_M(\mathcal{X})^n \exp^{-\Lambda_M(\mathcal{X})}}{n!}. \tag{3.3}$$

The second component in Equation 3.2 is effectively calculating the likelihood of one flowset forming at each location where they have been observed. Therefore,

$$\begin{aligned}
\mathcal{L}_M(N = n,\, \lambda(x, t, M(x, t) \,|\, \mathbf{x}) &\propto \frac{\Lambda(x_1)}{\int_{\mathcal{X}} \Lambda_M(x)\, dx} \times \cdots \times \frac{\Lambda(x_n)}{\int_{\mathcal{X}} \lambda_M(x)\, dx} \\
&= \prod_{i=1}^{n} \frac{\Lambda(x_i)}{\int_{\mathcal{X}} \lambda_M(x)\, dx} \\
&= \frac{1}{\Lambda_M(\mathcal{X})^n} \prod_{i=1}^{n} \Lambda(x_i).
\end{aligned} \tag{3.4}$$

Hence the locational component of the final LALA score can be calculated as

$$\begin{aligned}
\mathcal{L}_M(\lambda(x, t, M(x, t)) \,|\, x_1, \ldots, x_n) &\propto \frac{\Lambda_M(\mathcal{X})^n \exp^{-\Lambda_M(\mathcal{X})}}{n!} \times \frac{1}{\Lambda_M(\mathcal{X})^n} \prod_{i=1}^{n} \Lambda(x_i) \\
&= \left[\prod_{i=1}^{n} \Lambda_M(x_i)\right] e^{-\Lambda_M(\mathcal{X})}.
\end{aligned} \tag{3.5}$$

Here, in the simplified two-state λ case (as described above), the term $\Lambda_M(\mathcal{X})$ reduces to $\lambda A_M(\mathcal{X})$, where $A_M(\mathcal{X})$ is the total time and area that has the potential to form flowsets, in other words, meets the conditions required by the ice sheet M. The term $\Lambda_M(\mathcal{X})$ integrates these individual values over the whole study area and effectively calculates the total "time × area" rate where the ice sheet simulation has the potential to form lineations.

Given the same lineation formation rate $\lambda(x, t, M(x, t))$, larger ice sheets (covering greater areas where lineation formation is possible) will be expected to create more lineations than smaller ice sheets. Additionally, the inclusion of the term $\Lambda_M(x_i) = \lambda A_M(x_i)$ in Equation 3.5 highlights that it is more likely to see lineation formation in locations where the ice sheet has remained for longer. This will be reflected in the scores given to different ice sheet simulations. Solely in terms of scoring the location of the lineations, greater scores will tend to be given to those models where the ice sheet persists over the lineation locations and penalises simulations that extend beyond the data reconstructed glaciated area through time, as defined by the user.

3.2.3 Flowset orientation

In addition to considering the fit to the locations of the observed lineations, the tool also seeks to assess the fit between the orientations of the observed lineations and the simulated ice sheet. Suppose that there is a flowset which forms at location x_i and time $t_i^\star$. The tool assumes that the orientation of the resultant flowset aligns with the direction of ice flow in

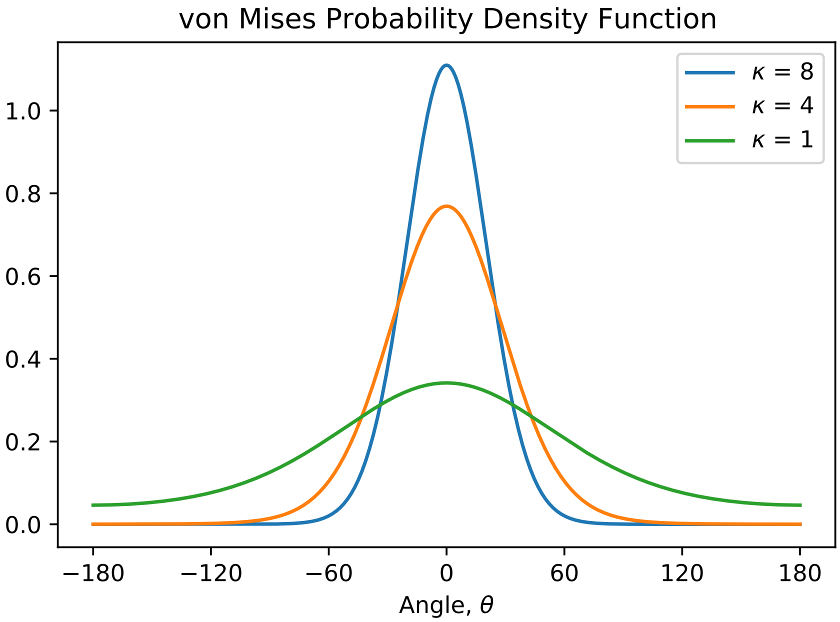

Figure 3.1: The probability density function of three various von Mises distributions with the same mean, 0, and three different shape parameter values, κ. As κ increases then the distribution becomes more concentrated around its mean. Here angles are shown in degrees (360° is 2π radians).

the location at the point of formation. Specifically, the observed orientations θ_i are modelled according to a von Mises distribution (von Mises, 1981). The von Mises distribution provides a distribution for angles that is an approximate analogue of the Normal distribution. The von Mises distribution requires two parameters to be specified, a mean that the distribution is centred around $\mu(x_i, t_i^\star)$, and a concentration parameter κ, that controls the width of the distribution. Angles used within this distribution have to be measured in radians (where 360° is 2π radians), but I have described the worked example (Section 3.2.9) in degrees for simplicity. Examples of the von Mises probability density function for different values of κ are shown in Figure 3.1 (also using degrees). The selection of κ is discussed in Section 3.4.4, but can be exploited to incorporate sources of uncertainty into the model. To formally derive the likelihood for the orientation model-data match, two sources of uncertainty need to be thought about and then formulated into the model.

The first source of uncertainty comes from how the resolution of the ice sheet model, which may be much larger than the size of a flowset, compares to the true direction a flowset it is representing, denoted as ϕ_i. Conditional on lineation formation occurring at time t and location x_i, a flowset will be created (independently of other flowsets) that has a direction related to the basal flow direction of the ice sheet at point of creation. The flowsets therefore constitute a marked Poisson point process, with the mark being their direction. Specifically, assume that ϕ, will be distributed according to a von Mises distribution as

$$f_{vonM}(\phi_i|\mu(x_i,t),\kappa_2) = \frac{\exp\left(\kappa_2\cos(\phi_i - \mu(x_i,t))\right)}{2\pi I_0(\kappa_2)}.$$

Here κ_2 denotes the concentration of the true flowset around the simulated ice flow direction, and $\mu(x_i,t)$ denotes the simulated ice flow direction at location x_i and time t.

Each flowset has an estimated direction θ_i based on mapping. Assume that the observed θ_i can either relate to the underlying angle ϕ_i of the flowset, or the opposite direction $\phi_i+\pi$. The scientist describing the flowset may equally report the direction as being upstream or downstream due to their morphology. This mapping may lead to some measurement uncertainty in the estimate θ_i and this second source of uncertainty also needs to be included in the tool. The density of $\theta_i|\phi_i$ is

$$f(\theta_i|\phi_i) = \frac{1}{2}f_{vonM}(\theta_i|\phi_i,\kappa_1) + \frac{1}{2}f_{vonM}(\theta_i|\phi_i+\pi,\kappa_1).$$

Here κ_1 relates to the accuracy of the observed past ice flow direction compared to the true past ice flow direction.

For simplicity in modelling, the observational uncertainty in lineation direction reported by the mapper is combined with the variability around the ice flow direction at time of formation, into one parameter κ. When the lineation is formed by an ice sheet M, a slight approximation leads to a final observation model for θ of:

$$f_M(\theta_i|\mu(x_i,t^\star_{x_i})) = \frac{1}{2}f_{vonM}(\theta_i|\mu(x_i,t^\star_{x_i}),\kappa) + \frac{1}{2}f_{vonM}(\theta_i|\mu(x_i,t^\star_{x_i})+\pi,\kappa) \tag{3.6}$$

where $t^\star_{x_i}$ denotes the time of the formation that led to the flowset at x_i and κ is a concentration term combining both the observational and regridding components of variability, discussed in Section 3.4.4.

Due to the morphology of lineations, LALA accounts for inferred observed directions occurring in the reported direction or the exact opposite direction. This leads to modelling the observed direction θ_i as

$$f_M(\theta_i|\mu(x_i,t^\star_i),\kappa) = \frac{1}{2}f_{vonM}(\theta_i|\mu(x_i,t^\star_i),\kappa) + \frac{1}{2}f_{vonM}(\theta_i+\pi|\mu(x_i,t^\star_i),\kappa), \tag{3.7}$$

where

$$f_{vonM}(\theta_i|\mu(x_i,t_i^\star),\kappa) = \frac{\exp\left(\kappa\cos(\theta_i - \mu(x_i,t_i^\star))\right)}{2\pi I_0(\kappa)}$$

is the probability density function of a von Mises distribution and $I_0(\kappa)$ is the modified Bessel function of order 0 that, when multiplied by 2π, ensures the distribution integrates to 1 as required.

In reality, the precise time $t_i^\star$ at which the lineations were formed in location x_i is unknown. All that is known is that it must have formed at one of the times when the ice sheet met the flowset forming conditions. To assess the overall directional fit, the tool must therefore average over all the times when lineations could be formed. Precise details are given in Equation 3.11 but, in the simplified two-state case for $\lambda(x_i,t,M(x_i,t))$, the likelihood of a particular ice sheet model M in terms of the agreement between the observed and simulated direction of flowset i is calculated as

$$\mathcal{L}(M,x_i|\theta_i) = f(\theta_i|x_i,M) = \frac{1}{T_M(x_i)}\int_{T_M(x_i)} f_M(\theta_i|\mu(x_i,t),\kappa)\,dt, \tag{3.8}$$

where $T_M(x_i)$ represents the time steps at location x_i where lineation formation is deemed possible.

Here $\mu(x_i,t)$ is the orientation of ice flow in model M at location x_i at time t, and $f_M(\theta_i|\mu(x_i,t),\kappa)$ is the mixture of the von Mises and flipped von Mises with location μ and concentration κ as described in Equation 3.7. To combine these directional components, the likelihood for each individual flowset is multiplied together, over all the n flowsets within LALA.

$$\mathcal{L}(M,\mathbf{x}|\theta_i) \propto \prod_{i=1}^{n}\left\{\int_{T_M(x_i)} f_M(\theta_i|\mu(x_i,t),\kappa)\,dt\right\}. \tag{3.9}$$

Intuitively, this directional likelihood component to LALA will provide greater scores to those ice sheets where, when lineation formation is possible at location x_i, the ice sheet flow aligns precisely with the observed direction of the lineations. Low scores will be obtained for those ice sheets that, when lineation formation is possible, have flow directions that lie at odds with the observed direction of the flowsets.

3.2.4 Log-likelihood of $\{x_i,\theta_i\}_{i=1}^n$

To calculate the log-likelihood of any hypothetical ice sheet M given the number, locations, and directions of the flowsets observed in the study region $\mathcal{X}$, the components described above are combined, and the natural logarithms are taken. In the case of the simplified two-state lineation formation model, and excluding the possibility that a lineation may have formed outside the period of study, the final log-likelihood for a simulation M becomes:

$$l(M|\{x_i, \theta_i\}_{i=1}^{n}) = \left[\sum_{i=1}^{n} \log\left\{\int_{T_M(x_i)} f_M(\theta_i|\mu(x_i,t),\kappa)\,dt\right\}\right] - \int_{\mathcal{X}} \Lambda_M(x)\,dx. \tag{3.10}$$

The first component of this log-likelihood (within the square brackets of Equation 3.10), relating to the fit of the simulated ice flow direction compared to the flowset orientation, can be used as an intuitive indicator for which flowsets are contributing the most to the final score. This can be used as a way to judge the flowsets which fit well to a simulation and which do not. This idea is explored further in Section 3.5.

3.2.5 For a generalised $\lambda(x_i, t, M(x_i, t))$

So far, a two-state version of $\lambda(x_i, t, M(x_i, t))$ has been described based on a set of conditions $\mathcal{S}$, however, a generalised version can be written. In a general case, the rate can be varied over time and space in any way and is not restricted to values of either 0 or λ. The generalised log-likelihood can therefore be written as

$$l(M|\{x_i, \theta_i\}_{i=1}^{n}) = \left[\sum_{i=1}^{n} \log\left\{\int_{\mathcal{T}} f_M(\theta_i|\mu(x_i,t),\kappa)\,\lambda(x_i,t,M(x_i,t))\,dt\right\}\right] - \int_{\mathcal{X}} \Lambda_M(x)\,dx. \tag{3.11}$$

3.2.6 Accounting for lineations that occurred outside the simulation period

I anticipate that LALA may be used for a wide range of model-data comparison experiments, with different time periods and areas. As such, some study areas may contain glacial lineations which were formed outside of the time period being simulated by the ice sheet model (e.g., during a prior glacial, or later/earlier during the same glaciation). Additionally, it is possible that lineations may have formed as a result of processes that are poorly represented in the ice sheet model, or there may be an insufficiently high temporal resolution of the simulation output to capture all lineation forming events, i.e., lineation formation occurred between simulation time steps. Without additional interpretation of the evidence, such possibilities cannot be ruled out. This possibility is accounted for in LALA by assigning a small, but statistically relevant, probability, p, that any observed lineation may be unrelated to the ice sheet simulation that is to be tested.

To allow for the possibility that some of the observed flowsets forming outside of the study an additional, independent, Poisson point process over the same region $\mathcal{X}$ but over a (pseudo)-time period $(-1, 0]$ with intensity $\lambda^\star(x)$ is introduced. Here the intensity depends only upon the location x, typically, $\lambda^\star(x) = 0$ would be expected in deep ocean locations, or where the topography is such that flowsets are impossible. LALA assumes that formation of lineations created from this additional point process lead to flowsets that lie uniformly in any direction, i.e., the true direction ϕ of any flowset created in this pseudo-time period has probability density

$$f_{out}(\phi) = \frac{1}{2\pi}.$$

This additional Poisson point process aims to represent the possibility a flowset may have been created outside the realm of the study (before the time $t = 0$ when simulations start). In any sub-region $\mathcal{A}$, the number of (unrelated) flowsets also follows a Poisson distribution with mean

$$\Lambda^\star(\mathcal{A}) = \int_{\mathcal{A}} \lambda^\star(x)\, dx.$$

Users are able to specify the probability, p, that any given lineation relates to such a pre-study ice sheet. The rate of the additional Poisson point process, $\lambda^\star(x)$, is chosen adaptively to incorporate the user-selected probability. An explanation of how to find the appropriate value $\lambda^\star(x)$ is given below.

Rather than choose a value for $\lambda^\star(x_i)$ directly, instead specify p, the prior probability that an observed flowset arises from outside the study's scope. The number of flowsets created by the ice sheet $M(x, t)$ over the study period $\mathcal{T}$ and region $\mathcal{X}$ follows a Poisson distribution with mean $\Lambda(\mathcal{X}, \mathcal{T})$. The number of flowsets created by the (pseudo-time) ice sheet to represent formation for reasons not considered in the study has a Poisson distribution with mean $\Lambda^\star(\mathcal{X})$. Therefore the chosen value of $\lambda^\star(x_i)$ is selected by setting

$$\Lambda^\star(\mathcal{X}) = \frac{p}{1-p}\Lambda(\mathcal{X}, \mathcal{T}).$$

Typically $\lambda^\star(x_i) = \lambda^\star$ is chosen for regions where lineation formation is possible, and zero otherwise. Hence $\Lambda^\star(\mathcal{X}) = \lambda^\star A_{pre}(\mathcal{X})$ where $A_{pre}(\mathcal{X})$ is the area where lineations could form within the overall study region $\mathcal{X}$ outside of the time period $\mathcal{T}$. The default is to select $p = 0.01$, meaning approximately one in every 100 pieces of lineation data may have formed outside of the chosen time period.

3.2.7 Final log-likelihood $l(M|\{x_i, \theta_i\}_{i=1}^n)$

To find the final log-likelihood, including the outlier possibility, the locational and directional components need updating. Due to their independence, the point process for ice sheet M (over times $\mathcal{T} = (0, T]$) and the outlier point process (to represent potential earlier ice sheets, over times $\mathcal{T}_{pre}$) can be combined to obtain another marked inhomogeneous Poisson point process. For this combined process, the underlying distribution for $N(\mathcal{X}, \mathcal{T} + \mathcal{T}_{pre})$ is $Po(\Lambda(\mathcal{X}, \mathcal{T}) + \Lambda(\mathcal{X})$. Hence, based on Equation 3.5, the likelihood of seeing the n flowsets in locations $x_1, \ldots, x_n$ across the study period and including the outlier process is

$$f(x_1, \ldots, x_n | M) \propto \prod_{i=1}^{n} \{\Lambda(x_i) + \Lambda^{\star}(x_i)\} \, e^{-(\Lambda(\mathcal{X}, \mathcal{T}) + \Lambda^{\star}(\mathcal{X}))},$$

where $\Lambda(x_i) = \int_0^T \lambda(x_i, t, M(x_i, t)) \, dt$.

Conditional on the flowset locations, the likelihood of the observed directions θ_i can also be calculated for $i = 1, \ldots, n$. This is achieved by first conditioning on $t^{\star}_{x_i}$ the time of the flowset formation at location x_i. Giving,

$$f(t^{\star}_{x_i} | x_i, M) = \begin{cases} \frac{\lambda(x_i, t^{\star}_{x_i}, M(x_i, t^{\star}_{x_i}))}{\Lambda(x_i) + \Lambda^{\star}(x_i)} & \text{for } t^{\star} \in (0, T] \text{, i.e., formed by an ice sheet } M; \\ \\ \frac{\lambda^{\star}(x_i)}{\Lambda(x_i) + \Lambda^{\star}(x_i)} & \text{for } t^{\star} \in (-1, 0] \text{, i.e., unrelated to the study.} \end{cases}$$

Then, conditional on the time $t^{\star}_{x_i}$ that the flowset in location x_i is formed, the distribution of θ_i is known. The updated likelihood $f(\theta_i | x_i, M)$ can be derived as

$$\begin{aligned} f(\theta_i | x_i, M) &\propto f(t^{\star}_{x_i} | x_i, M) \, f(\theta_i | t^{\star}_{x_i}, x_i, M) & (3.12) \\ &= f_{\mathcal{T}}(t^{\star}_{x_i}, x_i, M) \int_{\mathcal{T}} f_M(\theta_i | \mu(x_i, t^{\star}_{x_i})) \, dt + f_{\mathcal{T}_{pre}}(t^{\star}_{x_i} | x_i, M) \, f_{out}(\theta), & (3.13) \end{aligned}$$

where $f_M(\theta_i | \mu(x_i, t^{\star}_{x_i}))$ is given in Equation 3.6. Hence, the likelihood of $\theta_i | x_i, M$ is found to be

$$f(\theta_i | x_i, M) = \frac{1}{\Lambda(x_i) + \Lambda^{\star}(x_i)} \left[\int_0^T f_M(\theta_i | \mu(x_i, t^{\star}_{x_i})) \lambda(x_i, t^{\star}_{x_i}, M(x_i, t^{\star}_{x_i})) \, dt + \frac{\Lambda^{\star}(x_i)}{2\pi} \right]$$

Putting together both the location and direction information, the final log-likelihood for ice sheet M is found to be

$$l(M | \{x_i, \theta_i\}_{i=1}^{n}) = \left[\sum_{i=1}^{n} \log \nu(\theta_i | x_i, M) \right] - \{(\Lambda(\mathcal{X}, \mathcal{T}) + \Lambda^{\star}(\mathcal{X}))\} \qquad (3.14)$$

where

$$\nu(\theta_i|x_i, M) = \int_0^T f_M(\theta_i|\mu(x_i, t^\star_{x_i}))\lambda(x_i, t^\star_{x_i}, M(x_i, t^\star_{x_i}))\, dt + \frac{\lambda^\star(x_i)}{2\pi}.$$

3.2.8 Parameter selection

The use of LALA requires several tool parameters to be determined. The tool allows users to select suitable values based on their expert knowledge, however, the following proposes some automated choices which are used in the rest of this chapter.

The rate of lineation formation at a location x_i and time t is defined to be $\lambda(x, t, M(x, t))$. The choice of $\lambda(x, t, M(x, t))$ is critical to LALA's final log-likelihood. In the absence of detailed expert information, the two-state approach described above is suggested, whereby lineation formation is assumed impossible (i.e., $\lambda(x, t, M(x, t)) = 0$) if the location x at time t does not meet the conditions given in Section 3.2.1. Otherwise, lineation formation is assumed to be possible and $\lambda(x, t, M(x, t))$ is taken to be some constant λ. The conditions for the impossibility of lineation formation are at the discretion of the user, however the conditions stated in Section 3.2.1 are used in this thesis.

Similarly, let $\lambda^\star(x)$ be the rate of lineation formation outside the study period. This parameter allows for the possibility of some observational evidence having formed separately from the ice sheet model set-up being scored by LALA. To find this value, first, create a grid matching the simulation domain area that indicates areas where conditions were conducive to lineation formation. For example, users may want to consider limiting to areas of the palaeo-ice sheet bed where there is adequate sediment available for lineation formation. Furthermore, regions of the simulation domain that cover the deep ocean cannot form lineations as an ice sheet may be unable to ground there. To rule out these areas where lineation formation is impossible, set $\lambda^\star(x) = 0$ where the formation is impossible and $\lambda^\star(x)$ to be some constant $\lambda^\star$ elsewhere. This rate also depends on the user-defined probability p, described below.

In such a two-state model, however, it is still required to select an appropriate value for λ during times of potential lineation formation and $\lambda^\star$ for times outside the simulation period. To assign these values, a suggested method is to first choose an initial ice sheet simulation, $M^\dagger$, that approximately accords with other palaeo information such as ice extent or volume. Then, the expected number of flowsets is $\mathbb{E}_{M^\dagger}[N]$, where N is the random variable described in Section 3.2.2. This expected number is exactly the rate parameter of the distribution of N, $\Lambda_{M_\dagger}$, (by standard properties of the Poisson distribution) and this can be separated into two components: a component accounting for flowsets formed during the study period, $\mathcal{T}$, and those formed outside of $\mathcal{T}$. The decomposed $\Lambda_{M_\dagger}$ can be written as

$$\Lambda_{M_\dagger} = \Lambda_{M_\dagger}(\mathcal{X},\mathcal{T}) + \Lambda^\star(\mathcal{X}). \tag{3.15}$$

Then, select the rate, $\Lambda_{M_\dagger}$, so that the expected number of flowsets formed in simulation $M^\dagger$, $\mathbb{E}_{M^\dagger}[N]$, is equal to the number of flowsets actually observed in the region of study, n, as below

$$\mathbb{E}_{M^\dagger}[N] = \Lambda_{M_\dagger} = n.$$

Each component in Equation 3.15 can be calculated using $\Lambda_{M_\dagger}(\mathcal{X},\mathcal{T}) = \lambda A_{M_\dagger}(\mathcal{X},\mathcal{T})$ and $\Lambda^\star(\mathcal{X}) = \lambda^\star A_{pre}(\mathcal{X})$ as outlined in Section 3.2.2. $A_{M_\dagger}(\mathcal{X},\mathcal{T})$ is defined as

$$A_{M_\dagger}(\mathcal{X},\mathcal{T}) = \int\int_{T_{M_\dagger}(x_i)} dt\,dx$$

and effectively integrates, both spatially and temporally, the region when the ice sheet simulation $M^\dagger$ can form flowsets. $A_{pre}(\mathcal{X})$ is then the area where formation could have been plausible outside of the simulated time period.

Using the value p described in Section 3.2.6 which is the probability of a flowset forming outside of the study period, the relation $\mathbb{E}_{M_\dagger}(N_{pre}) = p\mathbb{E}_{M_\dagger}(N) = np$ is assumed, i.e. the expected number of flowsets formed outside of the study period is calculated as the total number of expected flowsets, n, multiplied by the probability of forming outside the study period, p. From this, the following relation can be formed

$$\Lambda^\star(\mathcal{X}) = \lambda^\star A_{pre}(\mathcal{X}) = np$$

which can be rearranged to give the value of $\lambda^\star$

$$\lambda^\star = \frac{np}{A_{pre}(\mathcal{X})}. \tag{3.16}$$

The user is able to specify the value of p as they see fit, however, the default for LALA is to select $p = 0.01$ (i.e., out of 100 observed flowsets, one may be expected to have been formed outside of the study area). By substituting the above relations into Equation 3.15, the expected number of flowsets can be written as

$$n = \lambda A_{M_\dagger}(\mathcal{X},\mathcal{T}) + \lambda^\star A_{pre}(\mathcal{X}). \tag{3.17}$$

Finally, using the value of $\lambda^\star$ and rearranging Equation 3.17, λ can also be found

$$\lambda = \frac{n - \lambda^\star A_{pre}(\mathcal{X})}{A_{M_\dagger}(\mathcal{X},\mathcal{T})}. \tag{3.18}$$

This plausible value λ is then fixed and used for the scoring of all ice sheet simulations under consideration by the tool. An important note is that the value of $\Lambda^{\star}(\mathcal{X})$ will stay the same for every simulation as it only depends on the area possible for pre-study formation and $\lambda^{\star}$, but $\Lambda(\mathcal{X}, \mathcal{T})$ will change with each simulation as it depends on the value of $A_M(\mathcal{X}, \mathcal{T})$.

LALA also has the capability to demand a certain level of conformity in modelled and observed flow directions using the concentration parameter κ. As shown in Figure 3.1, the value of the concentration parameter, κ, changes the shape of the von Mises distribution, demanding a higher level of directional accordance if κ is large. The appropriate value of κ, a measure of the acceptable direction for an ice sheet simulation, is dependent upon two components. The first component relates to the variation in observer measurement of the true lineation direction - that any mapper introduces a level of individual measurement error. The second pertains to the uncertainty regarding the relationship between the true (mean) direction of a flowset and that of the numerically modelled ice flow of simulation M within the grid cell. This second component itself consists of two parts - that multiple lineations orientations are summarised into a single flowset at the scale of an ice sheet grid; and that the numerical ice sheet model output is somewhat coarse and may not represent localised variation in ice flow direction within a grid cell (within any grid cell, the direction of ice flow at a more localised scale may vary from the overall flow direction within the cell). These two components are considered, and a practical method for choosing a value of κ is explored in Section 3.4.4.

All of the parameters defined above are dimensionless. When using this tool, the values of κ and p can be changed according to how the user wants to use the tool. The values of $\lambda(x, t, M(x, t))$ and $\lambda^{\star}(x)$ can also be changed. For $\lambda(x, t, M(x, t))$ especially, the conditions under which the user believes lineations are able to form can be altered. If the assumptions include the same properties as investigated here, i.e. thickness, velocity and grounded ice, but different values are wanted, there is a pre-defined function that can be used to change the values. If extra conditions are to be included, the easiest method is to create a binary map with the area at each time step that meets the user's extended conditions and use this in place of the area calculated in the LALA tool.

In practice, the ice sheet model simulation will consist of individual time steps defined on a grid rather than over continuous time and space. Hence when testing an ice sheet model simulation, the integrals used so far will be replaced by discrete sums (over the grid cells, time steps, or both).

3.2.9 Worked example

To demonstrate the principles of LALA, a worked example is presented here. Consider a simulation, M, with a 5 by 5 grid cell domain, one flowset and three time steps. In Figure 3.2, the grid cells at each of the three time steps that could feasibly form a flowset are shown, following the conditions previously set out regarding grounded ice, minimum velocity and thickness. The location of the flowset is indicated in Figure 3.2 by a cross. Figure 3.3 indicates the difference in the simulated flow direction and the observed direction inferred from the geomorphological evidence. The observed direction for flow, assumed to be parallel to past flow direction is taken to be 45°. While the directions are shown in degrees for this illustrative example, calculations in LALA (and all of the equations presented in this paper) are actually conducted in radians (as mentioned in Section 3.2.3). LALA will perform this transformation from degrees to radians for the user if the input variable for radians is set to False. For this example, the value $\kappa = 5$ is arbitrarily chosen.

First, the values of λ and $\lambda^\star$, the rate of lineation formation during the study and in the pre-study respectively, need to be calculated using a simulation from within the ensemble. This simulation, say $M^\dagger$, can be identified through comparison to other metrics, such as ice extent (see Section 3.5). Assume that in the pre-study any grid cell could have formed a flowset, and so $A_{pre}(\mathcal{X}) = 25$, and a value for $A_{M^\dagger}(\mathcal{X}, \mathcal{T})$ of 42 for the time-integrated plausible area for lineation formation for the simulation $M^\dagger$ is chosen arbitrarily for this example. A more formal method for choosing $A_{M^\dagger}(\mathcal{X}, \mathcal{T})$ is discussed in Section 3.5. The values of λ and $\lambda^\star$ are the same for each model simulation in the ensemble, using the fixed model simulation $M^\dagger$. Under the Poisson process model, the number of flowsets expected from simulation $M^\dagger$ over the three time step study period, combined with the pre-study, is 1 as there is one flowset under consideration. In total therefore, according to simulation $M^\dagger$

$$\mathbb{E}_{M^\dagger}[N] = 42\lambda + 25\lambda^\star = 1. \tag{3.19}$$

Taking the default value $p = 0.01$, an assumption that there is a 1% probability that a flowset has formed outside the realm of the study is taken. This leads to the relationship

$$\mathbb{E}_{M^\dagger}[N_{pre}] = p\mathbb{E}_{M^\dagger}[N_{\mathcal{T}} + N_{pre}] = p\mathbb{E}_{M^\dagger}[N], \tag{3.20}$$

where N_{pre} is the number of flowsets formed in the pre-study, $N_{\mathcal{T}}$ is the number of flowsets formed in the study time frame and N is the random variable representing the observed total number of flowsets. The expected number of flowsets formed in the pre-study is $p\mathbb{E}_{M^\dagger}[N] = 25\lambda^\star$. Hence,

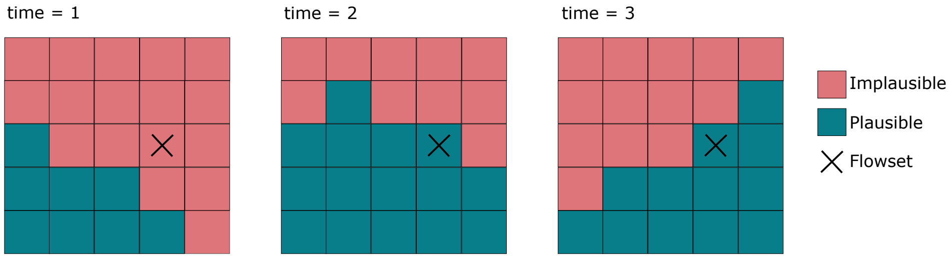

Figure 3.2: Three simulated time steps created to illustrate the use of plausible areas for lineation formation. The grid represents a 5×5 domain, and each box is coloured either blue or pink dependent on whether the location is deemed to be plausible or implausible, respectively, for the formation of lineations (i.e. grounded ice that exceeds minimum thresholds of ice velocity and thickness). By counting the total number of blue squares over the three time steps, the value $A_M(\mathcal{X}, \mathcal{T}) = 35$. The location of the flowset to be scored is marked with a black cross.

$$\lambda^{\star} = \frac{p\mathbb{E}_{M^{\dagger}}[N]}{A_{pre}(\mathcal{X})} = \frac{0.01 \times 1}{25} = 0.0004. \tag{3.21}$$

Using Equation 3.19 and substituting the value for $\lambda^{\star}$, λ can also be calculated

$$\lambda = \frac{\mathbb{E}_{M^{\dagger}}[N] - A_{pre}(\mathcal{X})\lambda^{\star}}{A_{M^{\dagger}}(\mathcal{X}, T)} = \frac{1 - (25 \times 0.0004)}{42} = 0.0236. \tag{3.22}$$

These values of λ and $\lambda^{\star}$ are fixed for the scoring of the other simulations from the same study. Now the log-likelihood for the location and number of lineations component can be calculated, using $A_M(\mathcal{X}, T) = 35$ counted from the example simulation, M, shown in Figure 3.2,

$$\Lambda(\mathcal{X}, \mathcal{T}) + \Lambda^{\star}(\mathcal{X}) = A_M(\mathcal{X}, \mathcal{T})\lambda + A_{pre}(\mathcal{X})\lambda^{\star} = 0.8359. \tag{3.23}$$

From Figure 3.2, it can be seen that flowset formation is only plausible at $t = 2$ and $t = 3$. Now, the likelihood that the simulation at these two time steps could have formed the flowset can be calculated, based on the direction of ice flow compared to the lineation direction. The true location of the observed flowset is indicated as x_1, the corresponding orientation of the flowset as θ_1 and the simulated flow direction at location x_1 and time step $t^{\star}$ as $\mu(x_1, t^{\star})$. At time step 2,

$$\begin{aligned} f_M(\theta_1 | \mu(x_1, 2)) &= \frac{1}{2}\left(f_{vonM}(\theta = 45^{\circ} | \mu = 135^{\circ}, \kappa = 5) + f_{vonM}(\theta = 45 + 180^{\circ} | \mu = 135^{\circ}, \kappa = 5)\right) \\ &= 0.0058 \end{aligned}$$

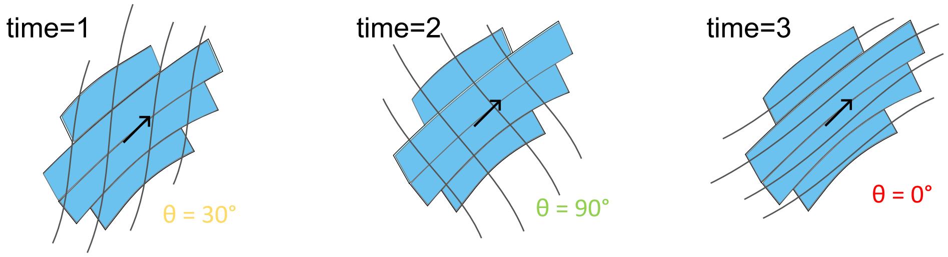

Figure 3.3: Three time steps showing the difference between the simulated ice flow direction and the inferred lineation direction created to illustrate how LALA scores an ice sheet simulation. The observed flowset is represented by the blue boxes with the black arrows showing the orientation given at the middle of the flowset. The simulated flow direction is indicated by the grey lines. The difference between the observed and modelled flow direction is indicated for each time step.

and at time step 3,

$$\begin{aligned} f_M(\theta_1|\mu(x_1,3)) &= \frac{1}{2}\left(f_{vonM}(\theta = 45^\circ|\mu = 45^\circ, \kappa = 5) + f_{vonM}(\theta = 45 + 180^\circ|\mu = 45^\circ, \kappa = 5)\right) \\ &= 0.4336. \end{aligned}$$

Intuitively, this highlights that the ice flow of simulation M at time $t = 3$ better aligns with the flowset than the ice flow at time $t = 2$. These values at the two time steps are then summed and multiplied by the rate of formation. The term $\frac{\lambda^\star}{2\pi}$ to account for unrelated flowsets is also added, to calculate the directional component for the likelihood (outlined in Section 3.2.6), giving

$$\nu(\theta_1|x_1, M) = \lambda\left(f_M(\theta_1|\mu(x_1,2)) + f_M(\theta_1|\mu(x_1,3))\right) + \frac{\lambda^\star}{2\pi} = 0.0104.$$

The component, $\nu(\theta_1|x_1, M)$, can be used in isolation to compare which flowsets contribute the most to the final score, and so can indicate which flowsets agree with the simulation the best.

The final log-likelihood for this model simulation is then the difference between the directional and locational components. Note, the logarithm of the directional component needs to be taken, but the location component is already in the correct form.

$$l(M|\{x_1, \theta_i\}_{i=1}^n) = \log(\nu(\theta_1|x_1, M)) - (\Lambda(\mathcal{X}, \mathcal{T}) + \Lambda^\star(\mathcal{X})) = -5.40. \tag{3.24}$$

Alone, a single value calculated from Equation 3.24 is of limited use. But, through multiple comparisons to simulations, the log-likelihood calculated by LALA can be used to compare ensemble members. Those simulations with greater log-likelihoods would be considered more likely to have generated the observed lineations; while those with lower log-likelihoods are less likely.

3.3 Practical application and considerations when using LALA

Here I briefly describe a workflow for using LALA. The initial intention and subsequent design of LALA was for comparing multiple ice sheet simulations, to identify fit to the geomorphological record. However, I anticipate that LALA could also be used to analyse which flowsets fit the best within a single model run, or the timing of best-fit between a simulation and the landform record. The code for LALA is available from `https://github.com/rosiearcher/LALA-Tool`. A synthetic example is included with the code.

Data preparation

Observed data of the flow direction of the former ice sheet in question must be collated. Lineation mapping across the study area should be grouped into flowsets (Clark, 1999): groups of lineations thought to form at similar times due to their proximity, similar morphology, and orientation (Greenwood and Clark, 2009; Hughes et al., 2014). Currently, a single pixel located at the centre of each flowset should be used within LALA. Expert interpretation is required for choosing this point for complicated flowsets and special attention should be given to the relative size of the flowsets compared to the model resolution. The flowset data should take the form of a netCDF grid, with the same resolution and extent as the model simulation output. Each flowset should be represented by one layer of the netCDF file, making the data a three-dimensional array with the flowset number as a dimension. This makes the individual flowsets more accessible and removes any overlapping lineation data (i.e., where lineations from two flowsets occupy the same grid cell, perhaps cross-cutting). A netCDF of the ice sheet simulation output is also required. This should contain the following variables over every simulated time step, with their standard names in PISM provided in brackets: basal velocity magnitudes in the u and v directions (uvel and vvel), ice thickness (thk), ice speed (velsurf_mag), and a mask of ice extent (mask). Finally, users can specify a third input netCDF file, which contains information pertaining to the regions where lineations are likely to have formed. In the absence of this file, the whole domain is presumed equally likely to have conditions conducive to lineation formation in the pre-study.

Code structure

LALA is written in Python (v3.0+), and requires the libraries numpy, pandas, netCDF4 and scipy. Users can call LALA from the command line, where all input parameters and paths to files can be specified. The user-defined parameters required as inputs are shown in Table 3.1. As a first step, LALA reads the relevant variables from the input netCDF files (Section 3.3) and converts them to numpy arrays. Iterating through each time step of the ice sheet simulation, LALA first calculates the simulated flow direction. The tool reads in the u and v velocity components from the model simulation, and then calculates the angle of the flow using standard trigonometry. To limit calculations to all regions where lineation formation is deemed possible, LALA identifies the locations which exceed the input thickness and velocity thresholds. These are defined by the user as minimum possible conditions for lineation formation (Table 3.1). The next step is to integrate the area where lineation formation is possible through time for the study area, as well as the area of possible lineation formation for the pre-study. The possible formation area for an ensemble member $M^\dagger$ thought to have a plausible size based upon other metrics is calculated and used to adaptively select values for λ and $\lambda^\star$ that will then be applied for the whole ensemble. Next, for each model run, LALA calculates the likelihood of the flowsets forming at each location. For each flowset, times where formation is possible are found and then scored across those time steps to form the directional likelihood (Equation 3.7). The directional likelihoods are summed over time for the n flowsets. The final likelihood sums the natural logarithms of each flowset score and sums to give the log-likelihood, and then the likelihood of locations is subtracted from this to give a score for the simulation (Equation 3.10). As output, LALA provides a Microsoft Excel (.xlsx) file with each model simulation number and its associated final log-likelihood score.

3.4 Defining the tolerance between modelled and observed flow directions

As demonstrated in the above sections, κ acts as a precision parameter for comparing simulated and observed flow directions. Higher values of κ will produce a lower tolerance for model-data misalignment, and vice versa. There are two aspects of the model-data comparison procedure that contribute to the value of κ that the user should define when using LALA: i) observational variability in the reported mean orientation of a flowset; and ii) uncertainty in the relationship between the mean flowset orientation and the (typically coarse) output of an ice sheet simulation (consisting of both the uncertainty introduced

Table 3.1: Inputs that need to be provided by the user to score ice sheet model simulations using LALA.

Parameter	Description
Lineation file	Path to a netCDF file containing information on observed flow directions
Simulation file	Path to a netCDF file of an ice sheet simulation to be tested (must contain variables listed in Section 3.3)
Lineation-conditions file	Path to a netCDF file containing information on whether an area is conducive to lineation formation
κ	Tolerance parameter when comparing observed and simulated model
p	Probability of lineations not relating to the study area or period (Section 3.2.6)
Thickness condition	Minimum simulated ice thickness under which lineations could form
Velocity condition	Minimum simulated ice speed under which lineations could form

when regridding lineation data to model resolution and the additional localised variability in the flow of an ice sheet within any grid cell around its overall, more coarsely modelled, mean cell flow direction). An experiment was conducted to provide insight into these two components and determine suitable values for κ.

3.4.1 Comparison experiment of lineation mapping between different mappers

Observations of palaeo-ice flow direction derived from glacial lineations are often mapped manually from digital elevation data (e.g. Finlayson et al., 2014; James et al., 2019; Leger et al., 2020). One form of observational uncertainty when considering palaeo-ice flow direction is that which arises from human error; interpretation of the landform record may vary from person to person. Here I discuss an experiment performed in collaboration with the geomorphological mapping community to quantify this source of uncertainty (Section 3.4.2). I then use the results from this experiment to examine the uncertainty from regridding lineation data to the scale of an ice sheet model (Section 3.4.3).

Across the deglaciated terrains of palaeo-ice sheets, Digital Elevation Models (DEMs) are available at different resolutions. This observational uncertainty experiment investigates whether the resolution affects the mapping variation. An important consideration here, and potentially for future users of LALA where different resolutions of data have been used for mapping, is whether areas mapped with different resolutions of data require different values of κ to account for the various uncertainties. To define inter-mapper uncertainty,

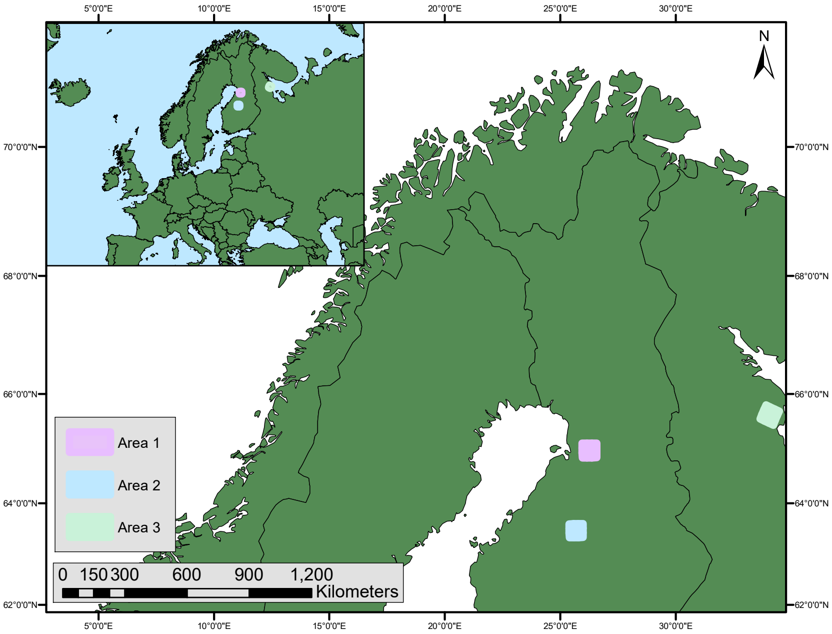

Figure 3.4: Overview of areas used in the lineation mapping experiment.

expert mappers were invited to map the same areas. For the purposes of this experiment, experts were defined as those who had conducted and published glacial geomorphological mapping in the past, or PhD students currently conducting mapping projects. I wished to investigate whether the resolution at which lineations are mapped affects the variation in orientation (and hence might also require different values of κ for model-data comparison). The experiment is designed for the common resolutions of DEMs (2 m and 30 m) available for the EISC to work with the simulations performed in this thesis. Data from two areas of Finland were used, both at a 2 m resolutions, and one area of Russia at the lower resolution of 30 m. The location of these areas are shown in Figure 3.4. The areas were each split into nine equally sized 5 × 5 km boxes. A selection of lineations were starred in each area to indicate to mappers the selected lineations to map (Figure 3.5). A summary of the data used, the resolutions and the number of lineations highlighted are given in Table 3.2. The participants were asked to draw one crestline for each lineation in the suspected orientation of flow and summary lines for each of the nine boxes that indicated their overall opinion of the ice flow in the specified region. An example of the summary lines of flow direction for one grid cell is shown in Figure 3.6. I received data from 24 participants.

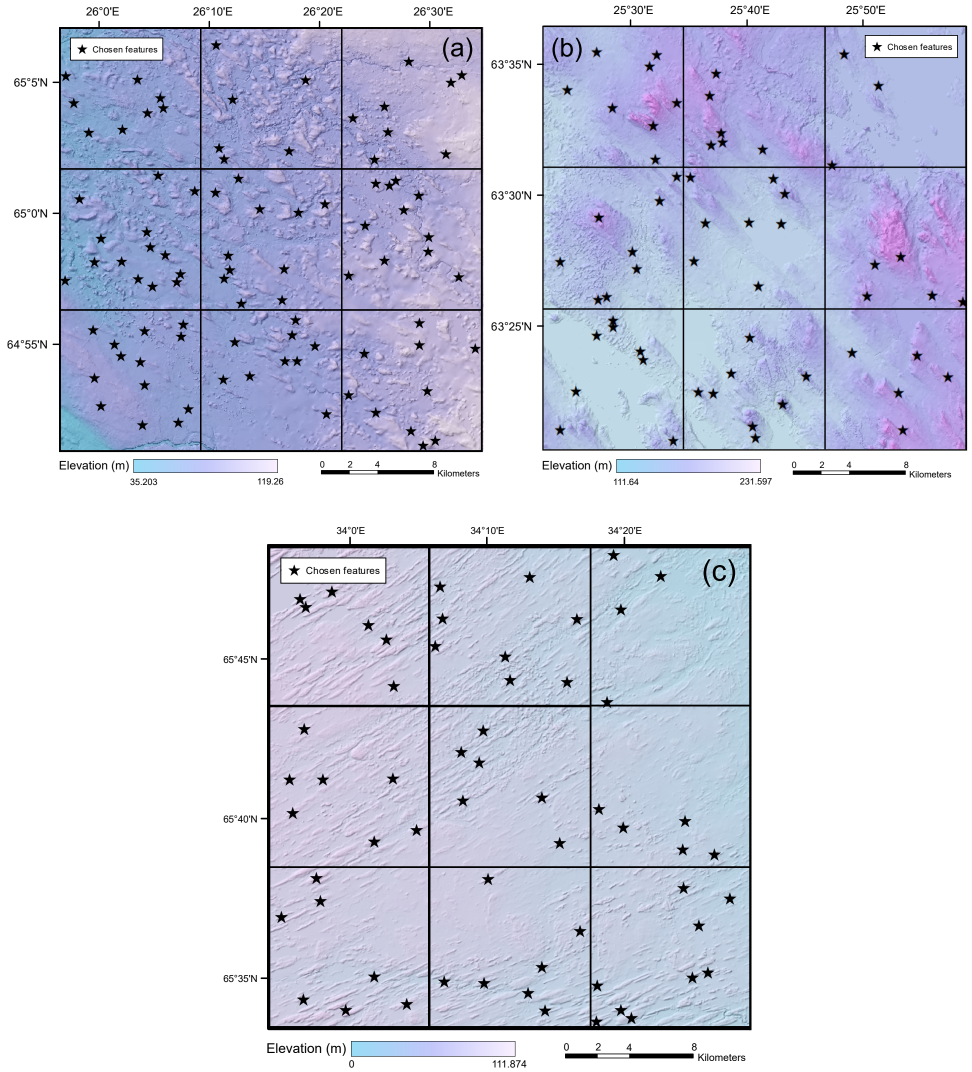

Figure 3.5: Maps of the three areas given to the observational error experiment participants. The black points show the location of the lineations participants were asked to map. The 3 × 3 grid shows the sections where summary lines were requested. *a)* Area 1 located in northern Finland. *b)* Area 2 located in central Finland. *c)* Area 3 in western Russia.

Table 3.2: Data used in the observational error experiment.

Area Number	Country	DEM Name	Horizontal Resolution (m)	Number of Lineations
1	Finland	National Land Survey of Finland DEM	2	90
2	Finland	National Land Survey of Finland DEM	2	59
3	Russia	Copernicus DEM GLO-30	30	59

3.4.2 Uncertainty from mapping interpretation

The variability in the reported ice flow direction between the different participants, and for each mapping resolution, were analysed across the boxes. I assumed that the summary directions reported by each user within a box followed a von Mises distribution, with each box having a potentially different mean direction μ_i but with the same concentration parameter κ_1 shared across all boxes of the same resolution. Using Markov Chain Monte Carlo I estimated both the mean directions μ_i and shared κ_1 to represent the intermapper variability in assessing flowset direction for a particular resolution. An example of this variability is shown in Figure 3.6.

Markov Chain Monte Carlo (MCMC) was used to estimate a set of von Mises parameters that adequately represents the flowset variation observed with the experimental mapping data in Section 3.5. These parameters are then used as the default choice for LALA. A Markov Chain, a path which moves through different states, was generated according to a Metropolis-Hastings (MH) algorithm (Hastings, 1970). The MH algorithm sampled a random point from a proposed density function. The point is then either accepted as the next state in the chain, or rejected, and a new sample point is tested. This is repeated until the distribution of acceptable points stabilises to form a posterior distribution. From this sampled posterior distribution, metrics such as the mean and variance can be calculated. Several thousands of iterations are performed until the Markov Chain reaches its stationary distribution. Examples of the Markov chains used for the analysis of area 2 are shown below in Figure 3.7.

I refer to this experiment as the Multiple Means experiment. For the Multiple Means experiment, first the two high resolution (2 m) mapping results were considered separately, later treating them as a single population which allowed a single value of κ_1 to be produced representing this resolution. Results are shown in Table 3.3. The concentration (denoting the level of mapping precision) for the lower-resolution data was significantly higher than for mapping conducted at a high resolution. This suggests that at a lower resolution, there was a very high level of directional agreement between participants. Several possibilities exist to explain this. This may be a consequence of the nature of the two different study areas (i.e., the 30 m resolution test area may have happened to be simpler than the 2 m resolution). Alternatively, the high resolution data may reveal more detail, representing a more complex landform record that is harder to interpret precisely. Overall however, the values of κ_1 are very high for both resolutions, suggesting that for the areas this experiment was conducted over, the reported summary directions were highly reproducible across mappers and that intermapper variability is not a significant source of uncertainty for model-data comparison.

Table 3.3: Values obtained from MCMC analysis of reported summary directions of lineations across boxes within the intermapper experiment. Results are presented separately for three different regions, two at a 2 m resolution and one at a 30 m resolution; as well as combining the two 2 m resolution areas. Each box was permitted to have a different overall mean direction.

Area	Resolution (m)	Multiple Means	Multiple Means Combined
1	2	85	209.2
2	2	270	
3	30	3000	N/A

3.4.3 Uncertainty between the direction of localised lineations and overall grid cell flow direction

The second source of uncertainty that must be considered for the LALA tool is that which results from the comparison of flow directions inferred at a lineation scale (generally 100s of m in scale) with those directions provided by an ice sheet simulation which typically has a much coarser output, representing mean ice flow direction at a several km scale. In the case of the model simulations from the BRITICE-CHRONO project (Clark et al., 2022) a 5 km horizontal resolution was used. These simulations are transient and run from 31 - 15 ka, outputting every 100 years, with the model domain covering both Britain and Ireland. To assess the uncertainty in model-data comparison this reduction introduces, the

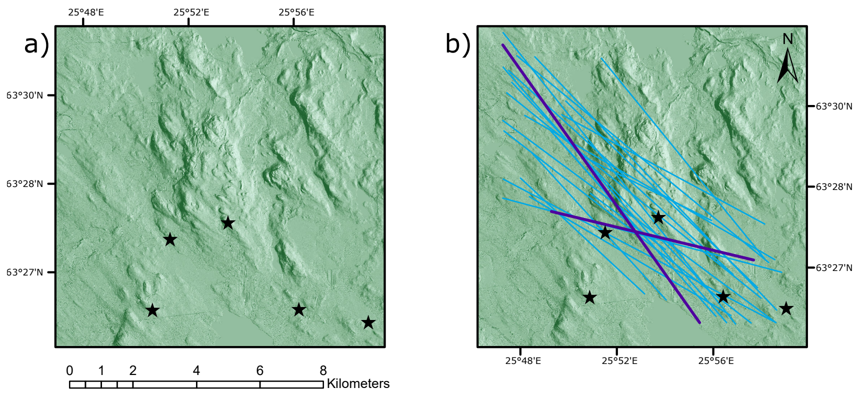

Figure 3.6: One of the nine boxes from area 2 where the mapping participants seemed to identify two overlapping directions. *a)* Hillshade of the area requested to be mapped, with the specific lineations to be mapped starred. *b)* The summary lines from the 24 participants are indicated in blue. The extreme angles are highlighted in purple to emphasise the difference between mappers. As the lines here indicate the inferred summary orientation for each box, and not the specific marked lineations, the lines are placed centrally within the box.

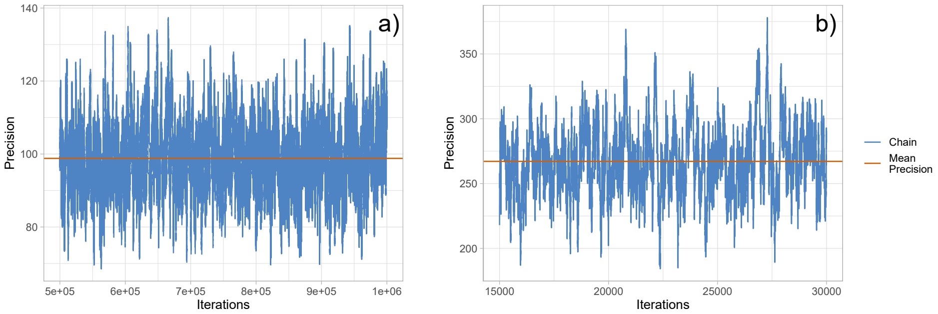

Figure 3.7: Sample chains from the MCMC for the 2 m resolution data in area 2. *a)* Considers there to be one mean across all the boxes. *b)* Considers a separate mean for each box, but the same precision. The red line shows the mean that the posterior distribution tends towards.

variability of the individual lineations within a 5 × 5 km box around their overall mean direction was considered. Boxes of this size were chosen to match the resolution of the BRITICE-CHRONO ensemble.

A single mapper's inferred directions for each of the 208 lineations were selected and then separated into 27 groups based on the 5 × 5 km box that contained them (see Figure 3.5). It was assumed that each group could have a different overall mean direction for the lineations, corresponding to the box's overall flow direction. The individual lineations within any box were then modelled by a von Mises distribution, with the appropriate box-dependent mean direction but the same concentration κ_2 for all boxes. MCMC was again performed estimating both the mean direction for each box and the value of κ_2. The posterior estimate for κ_2, across all 27 boxes and 208 lineations, was found to be approximately 92. This approach to estimating κ_2 accounts for variability in flow direction within a grid box. For large flowsets, perhaps recording highly variable flow directions, users may wish to either decrease the value of κ_2 to account for such complexity or subset a flowset into multiple grid boxes.

3.4.4 Combining the two components of directional variability

To use LALA for comparison of observed flowset direction with the output of numerical ice sheet models, the two components of uncertainty (κ_1 and κ_2) described above have to be combined into a single von Mises concentration parameter κ in Section 3.2.3. The experiment above indicates that intermapper (observer) variability in the reported flowset direction is very small (with extremely high values of κ_2). Consequently, the appropriate overall κ will be dominated by the variability introduced due to the need to compare flow directions at a highly-localised lineation scale with the coarser output of a numerical ice sheet model (which only has a resolution on a scale of several km). Therefore, an overall value of $\kappa = 90$ was selected for implemention of LALA. This value will be used to judge goodness-of-fit between an observed flowset and the flow direction of an ice sheet simulation. In a later version of LALA, I would however endeavour to vary κ spatially, accounting for areas of complex ice flow that likely require a lower concentration value.

3.4.5 Other potential sources of uncertainty in model-data comparison

The parameter κ captures the uncertainty in the directional component of the likelihood calculated by LALA. However, in any model-data comparison there are additional sources of uncertainty, related either to the numerical model utilised or the data itself (Ely et al., 2019). Often, these sources of uncertainty are potentially more difficult to quantify. From a data perspective, an uncertainty remains regarding the mechanics of lineation formation, which are still debated (Ely et al., 2023). Though this chapter suggests reasonable conditions under which lineations are formed and preserved, ultimately users of LALA may wish to alter these according to any further insights gained in this field. Furthermore, through the parameter p, LALA accounts for the misclassification of lineations from outside of the simulated time period. However, in an ideal situation, such instances of misclassified lineations should be removed from the dataset used to calculate the likelihood of ice sheet simulations. Model-data comparisons, perhaps facilitated by LALA, may prove a fruitful means for identifying any misfitting data, and act as a basis for reinterpreting the lineation record (see Section 3.5 for an example of this). From a modelling perspective, no ice-flow simulation is a perfect representation of reality. All numerical models abstract the physics of ice flow into approximations, and thus contain structural uncertainty related to the way this is implemented within the model. Thus, the angles of ice flow produced by the model are not perfect representations of the actual ice flow direction. Quantifying the impact of different approximations of ice flow upon the resulting modelled angle is a large task, and an important avenue for future research. A further uncertainty relates to the temporal resolution of the model output. Again, this is considered by LALA in the parameter p, which considers that lineation forming events could occur between modelled output time steps. However, precisely how modelled angle changes over temporal timescales is unknown, as are the precise timescales over which lineations form. As more insight is gained into these additional sources of uncertainty, future model-data comparison tools or adaptations of LALA may wish to take these into consideration.

3.5 Application to the British-Irish Ice Sheet

To demonstrate the utility of LALA using real model simulations, here, LALA is applied to an ensemble of simulations of the BIIS, from the BRITICE-CHRONO project (Clark et al., 2022). This 200-member ensemble was run at 5 km horizontal resolution using the Parallel Ice Sheet Model (PISM) (Winkelmann et al., 2011) – a hybrid shallow ice and shallow shelf approximation numerical ice sheet model. The simulations are transient and run from 31 - 15 ka with a model domain covering Britain and Ireland (Clark et al., 2022). The ensemble experiments varied ten parameters. The aim here is not to comment on the performance of a particular ice sheet simulation, and its resulting parameter combination, but rather to demonstrate the utility of LALA using a real example of ice flow simulations.

The BRITICE-CHRONO project (Clark et al., 2022) completed ice sheet-wide mapping of glacial landforms of the BIIS (Clark et al., 2018). From the lineation data, flowsets were constructed through grouping lineations thought to indicate similar past flow directions that occurred during the same period of time (Greenwood and Clark, 2009; Hughes et al., 2014). This flowset data was compiled in GIS, and converted into a netCDF to be used within the LALA tool. Only flowsets deemed to have formed in the same flow event, referred to as isochronous flowsets, were tested. A total of 94 flowsets were used here, 37 of which were located in England, Scotland and Wales (Hughes et al., 2014), and 57 from Northern Ireland and the Republic of Ireland (Greenwood and Clark, 2009). As the simulated ice sheets being tested cover the entire last glacial, the time period during which the mapped lineations are thought to have formed, the default value of $p = 0.01$ was used. Thus, in this application of LALA, any observed flowset has a 99% probability that it was formed during the simulated period.

To apply LALA, the appropriate values for the two parameters which define the rate of lineation formation must be calculated (Section 3.2.8). For this example, these are referred to as $\lambda^{\star}_{BC}(x)$, the rate of lineation formation across the BIIS outside of the simulated period, and $\lambda_{BC}(x, t, M(x, t))$, the rate of lineation formation across the BIIS during the study period. For $\lambda^{\star}_{BC}(x)$, LALA is supplied with a binary mask defining regions where lineation formation is possible (assigned a value of 1, which LALA later translates to $\lambda^{\star}_{BC}$ (Section 3.2.8)), and impossible (assigned a value of 0). The latter ruled-out regions were defined as those that were deemed to be insufficient sediment for lineation formation, offshore regions as these were not covered by Greenwood and Clark (2009) and Hughes et al. (2014), and regions beyond 50 km of the presumed limit of the BIIS (Clark et al., 2022). Hence, the total number of grid cells where lineations might occur was summed to be $A_{pre}(\mathcal{X}) = 7801$. Using this, and the number of observed flowsets ($n = 94$) the value of $\lambda^{\star}_{BC}$ can be calculated as

$$\lambda^{\star}_{BC} = p\frac{n}{A_{pre}(\mathcal{X})} = \frac{94}{100 \times 7801}. \tag{3.25}$$

To estimate the parameter λ_{BC}, the value $A(\mathcal{X}, \mathcal{T})$ must be calculated, the time-integrated area which meets the lineation formation criteria previously formulated. One could envisage estimating $A(\mathcal{X}, \mathcal{T})$ via a number of means, dependent upon the user's opinion regarding lineation formation and the availability of information regarding the overall extent and timing of glaciation across an area. For example, an empirical reconstruction could be used to inform about the time for which each cell was covered by ice. However, such reconstructions often lack information about the prevalence of other conditions thought to be important for lineation formation, such as basal thermal regime. The approach here is to utilise an initial simulation, $M^{\dagger}$, that scored well at matching the independent data of ice margin position (Li et al., 2008) and geochronological constraints (Ely et al., 2019). $M^{\dagger}$ is therefore of the approximate size and produced reasonable ice coverage for the BIIS. For simulation $M^{\dagger}$, the total number of grid cells (area) over time that meet the conditions for potential lineation formation (e.g. thickness, velocity, sediment availability) is $A_{M^{\dagger}}(\mathcal{X}, \mathcal{T}) = 6094155$. This is used to select λ_{BC} for the ensemble of simulations

$$\lambda_{BC} = (1-p)\frac{n}{A_{M^{\dagger}}(\mathcal{X}, \mathcal{T})} = \frac{99}{100} \times \frac{94}{6094155}. \tag{3.26}$$

These two rates, $\lambda^{\star}_{BC}(x)$ and $\lambda_{BC}(x, t, M(x,t))$, were then used in LALA to calculate the log-likelihood of each simulation from the ensemble. For the remaining input parameter, κ, the value 90 is taken, derived from the observational uncertainty experiment (Section 3.4.4).

To assess the utility of LALA, I visually inspected how a range of simulations compared to the reconstructed ice extents of Clark et al. (2022), at the 1 ka temporal resolution at which the reconstructed limits are provided. An example of this comparison, for the simulations which had the highest and lowest log-likelihoods, is shown in Figure 3.8. Note that for illustrative purposes in Figure 3.8 only a single time step, 21 ka BP, is demonstrated, whereas the visual assessment accounted for the time variance of the ice sheet geometry. Visual assessment of all 200 simulations within the ensemble, showed that the best-fitting simulation identified by LALA performed reasonably well in comparison to the ice extenets in Clark et al. (2022). Furthermore, the worst simulation exceeds the maximum reconstruction for almost the entire perimeter and is comparable in performance to other poorly performing models identified through qualitative means. The best-performing simulation (Figure 3.8a) has an extent that matches the reconstructed ice margin extent for the majority of its perimeter. In comparison, the extent of the worst performing model (Figure 3.8b) is consistently too large when compared to the empirical reconstruction. This conformity between reconstructed and simulated ice sheet geometry reflects how LALA produces a higher log-likelihood for simulations that produce lineation forming conditions (velocity, ice thickness and grounded extent) over the model domain, and penalises simulations that spread over an extent which is too large. The best fitting simulation (Figure 3.8a) also showed the overall best directional score, and vice versa for the worst fitting simulation. As LALA considers more than just flow direction alone, a quantitative comparison between LALA and AFDA is not currently possible. However, note that higher-ranked simulations by LALA were also those assessed to fit more flowsets by AFDA.

A further utility of LALA is to consider which flowsets are more readily matched and those which are less often matched. To do so required isolation of only the component of the log-likelihood that relates to the flow direction (Equation 3.7). When scoring a whole model simulation, LALA sums the values obtained by Equation 3.7 to calculate the final log-likelihood. To give an indication of the best-matched flowsets across the ensemble, instead keep the Equation 3.7 values separate. Then, each flowset will have a value for each model simulation. In this application, these values were summed from each of the simulations on a per-flowset basis. The nature of this comparison may provoke iterative conversations between those who collect and collate data, and the numerical modeller: is the match, or lack of, a consequence of the model, the nature of the of data, or some other factor? In Figure 3.9 the flowsets are ranked from best to worst fit over time. Although the evidence for these flowsets here is not revisited, there are some notable features of this map. First, a number of the poorly-fitted flowsets are narrow and small features (e.g. FS58 in the Republic of Ireland, FS24 on the border between Northern Ireland and the Republic of Ireland, and FS47 in Northern Ireland). These flowsets were perhaps poorly chosen for model-data comparison, as their narrow size may be below what is feasibly resolved by the model. In western Scotland, FS24 is composed of two distinct patches of lineations, which cross the fjord topography. Perhaps these lineations have been incorrectly grouped together, or the model is unable to recreate flow counter to the valley topography. The reasons for the well matched flowsets may be highly variable, as their character and distribution seem to lack geographic, topographic or geometric similarity (Figure 3.9). Another possibility to consider is that these flowsets are looser constraints on ice sheet models, or the ensemble simulation is particularly good at replicating these flow directions. Such possibilities should be considered in future work.

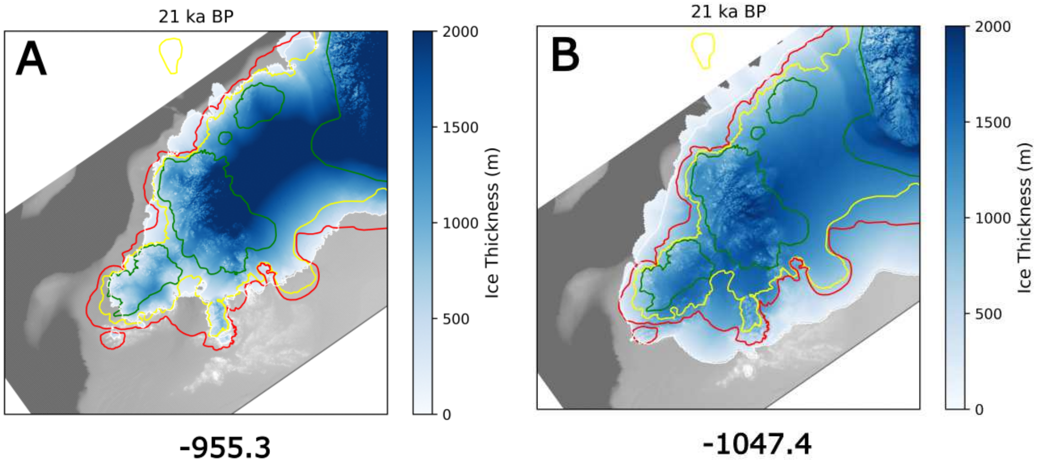

Figure 3.8: Modelled extents of the BIIS at 21 ka BP in two different simulations. The final log-likelihood score for each simulation is indicated below. Note that this figure shows just one time step, but the final scores are cumulative over all time steps. The lines denote the maximum (red), optimum (yellow) and minimum (green) reconstructed extent of the BIIS from Clark et al. (2022). The faint white-line is the grounding line or ice margin. A) The best-fit simulation. Note how much of the perimeter of the ice sheet is close to the 'optimum' reconstruction. B) The worst-fitting simulation. Note how the ice sheet extent is too large compared to the empirical reconstruction. The time-integrated score for each simulation given by LALA is below. The better scoring model simulation for flow was also better at getting the timing and extent correct.

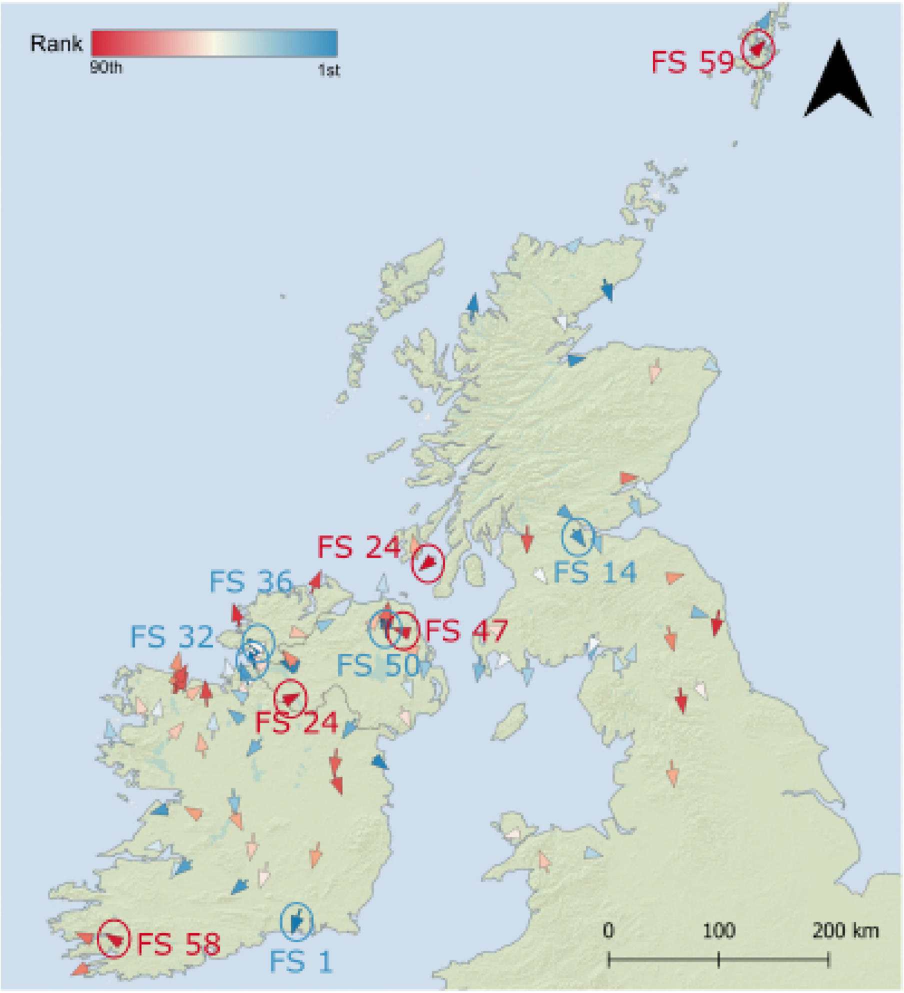

Figure 3.9: Ranked fit of all flowsets over all 200 model simulations, as picked out by LALA, with the arrows indicating the direction of the past ice flow being compared to the model output, and the colour of the arrow representing the rank such that the blue matches the best and the red matches the worst.

3.6 Summary

Rigorous tools for comparing numerical simulations of palaeo ice sheet behaviour and available data constraints can greatly aid in model improvement. Here a new method for determining the log-likelihood of an ice sheet simulation matching flow geometry given a set of mapped subglacial lineations was presented. This tool, named the Likelihood of Accordant Lineations Analysis (LALA) tool, considers both the orientation and spatial distribution of lineations across a palaeo-ice sheet area. To achieve this, the statistical underpinning of considering lineation formation to be a marked, inhomogeneous, Poisson point process was used. Unlike previous tools, LALA provides a continuous numerical output (rather than a binary yes or no), suited for emulating ensembles of simulations. The main purpose of LALA is to provide a means for comparing ice sheet simulations within an ensemble, assigning each simulation with a log-likelihood, such that the best-fitting simulations can be identified. To demonstrate the underpinning of LALA, a toy example of its application was provided.

Several parameters are required as a user input to run LALA. As LALA is designed to be adaptable, these can be changed by the user depending upon assumptions of lineation formation and to adapt to different experimental circumstances. Here, a number of reasonable starting points for assigning these parameters are provided. This includes an analysis of an experiment which quantified the observational error that arises from multiple expert mappers interpreting former ice flow directions from the landform record. This uncertainty was found to be small, especially compared to the uncertainty that arises from the differing resolutions of subglacial lineations (100s of m) to the scale of an ice sheet model grid (several km), which was found to be much larger. Finally, to demonstrate the utility of LALA, the tool was applied to an ensemble of simulations of the British-Irish Ice Sheet and observations of lineations from the literature. This application highlights how LALA can be used to distinguish between simulations within an ensemble and, in the future, find more plausible parameter spaces for ice sheet simulations.

Notation for Chapter 3

Symbol	Description
A	Plausible area for flowset formation
θ_i	Observed direction of flowset i
$I_0(\kappa)$	A scaling constant in the probability density function of the von Mises distribution. It is the modified Bessel function of order 0.
κ	Concentration parameter for the von Mises distribution, that accounts for variability in regridding and observational error
Λ	Mean of Poisson distribution describing the number of flowsets formed
λ	The rate of the Poisson point process across the studied time period
$\lambda^\star$	The rate of the Poisson point process outside of the studied time period
M	An ice sheet simulation
$M_\dagger$	An ice sheet simulation with a reasonable extent
$\mu(x, t)$	Direction of the simulated ice flow from ice sheet model output at a given location x and time t
N	Random variable representing the number of flowsets observed
n	Number of flowsets observed in the study region
p	Probability that a flowset formed outside of the simulated time period
$\mathcal{S}$	Set of conditions defined for possible lineation formation
T_M	Number of time steps where lineation formation is deemed possible
$\mathcal{T}$	Time period of the ice sheet simulation
t	Specified time step
$t^\star_{x_i}$	True time when flowset formed at location x_i
ϕ	True value of flowset direction
$\mathcal{X}$	Study region
x_i	Location of flowset i

Chapter 4

Simulation sensitivity of model parameters: evaluating parameter contribution to influencing ice flow direction

4.1 Introduction

The parameter space defined in Chapter 2 has 20 dimensions, meaning it would take an unfeasible amount of computational expense and time to explore fully. The parameters that have been perturbed are required to run PISM, but may only have a small impact on the output when the values are varied across the prescribed ranges. If a parameter does not cause significant changes in the output, then there is little benefit to including the parameter in further perturbed parameter ensembles. Therefore, testing which parameters are important to vary and which ones insignificantly alter the model simulation output is of great interest. Here, I use the word 'important' when referring to parameters that greatly impact how much the model output varies.

A sensitivity analysis calculates how much the different input parameters affect a chosen predictor variable. Historically, in glaciology, the 'one-at-a-time' (OAT) sampling method is used (e.g. Goelzer et al., 2013; Hubbard, 2006; Zweck and Huybrechts, 2005), but there are issues with using sensitivity analysis on these samples. The OAT sampling technique explores a very small portion of the parameter space and thus has the potential of missing the full effects of the parameters. Also, using this sampling method means the ability to calculate the effects of parameter interactions, how much parameters may affect the output in combination, is lost (Saltelli et al., 2019). Sensitivity analyses using an OAT design are a type of local sensitivity analysis that has the limitations described above, but there are global methods available that can overcome some of these problems. Global sensitivity analyses are not new and have been used in many disciplines, for example in medicine (e.g. Hickson et al., 2011; Wu et al., 2013), engineering (e.g. Hall et al., 2005; Liu et al., 2006) and biochemistry (e.g. van Riel, 2006; White et al., 2000) and even in the wider field of geoscience (e.g. Butler et al., 2014; Harper et al., 2011; Kelleher et al., 2013; Nossent et al., 2011) but are rarely used in glaciology. There has historically been a general problem with interpreting the results of sensitivity analyses: the findings are very specific to the model and model set-up and do not say anything about the physical process underlying the model in question (Pilkey and Pilkey-Jarvis, 2007; Saltelli et al., 2019). Therefore, it is important to emphasise that, for example, any inferences made using the results in this chapter only apply to the EISC modelled over 40 to 5 ka with the set-up outlined in Chapter 2.

Several sensitivity analysis methods are available, some with larger simplifications and faster run times, others with more complexity or additional metrics. The decision on the method required for a certain study can be made by considering the assumptions that can be made using the specific model. For example, if it is likely that the model will respond linearly to the predictor variables, then a linear regression-based approach could be appropriate, but this is not often the case with more complex models. There is also a decision to be made between local and global sensitivity analyses. A local method assesses the sensitivity of small changes in the underlying function, whereas a global method calculates sensitivity over the entire input parameter space. For this Chapter, the focus is on using Generalised Additive Models (GAMs, explored later) to underpin the analysis as the method can generate the sensitivity efficiently and works well on high-dimensional inputs (Strong et al., 2014).

The aim of this Chapter is to showcase the benefits of using a Latin hypercube sampling method compared to a OAT approach and apply a sensitivity analysis to the large perturbed parameter ensemble given in Chapter 2. Section 4.2 explains the method of variance-based sensitivity analyses and how GAMs can be used to complete this analysis. Outputs with which to test the sensitivity of the model are also outlined. Section 4.3 presents the sensitivity analysis results for four different aspects of the simulated ice sheet. The results of the sensitivity analysis are used in Chapter 6 when refining the parameter input space for the calibrated to flow geometry ensemble, which is rarely done to reduce the dimensionality of models generally (Sun and Hahn, 2006; van Werkhoven et al., 2009) and to my knowledge yet to be done in glaciology.

4.2 Method

4.2.1 Experimental design

When performing perturbed parameter ensembles, as discussed in Chapter 2, the design of the samples should be carefully considered. As the model can only be run a finite number of times, the largest amount of the unknown parameter space must be explored in the smallest number of simulations. The large ensemble that was completed with the set-up outlined in Chapter 2 utilised input parameters sampled using a maximin Latin hypercube (see Section 2.5.2). Commonly in glaciology, (e.g. Goelzer et al., 2013; Hubbard, 2006) a simpler sampling procedure is used and is known as OAT sampling. The OAT method keeps the parameters at a fixed value, other than the one parameter of interest which is set to either the maximum or minimum value. As such, the OAT method naturally creates an ensemble of simulations with double the number of members compared to the dimension of the parameter space.

The OAT method, however, has many flaws. The first one is that compared to a Latin hypercube sampling method, described in Section 2.5.2, the OAT design explores a tiny fraction of the parameter space. It is also not possible to evaluate interactions, which can be shown by considering the design matrix. Let there be two parameters with ranges $[p, q]$ and $[r, s]$ and default values a and b respectively. To visualise this, this can be written in matrix form, such that for some model outputs $\boldsymbol{y}$,

$$Var(\boldsymbol{y}) = \boldsymbol{\beta} X + \boldsymbol{\varepsilon} \tag{4.1}$$

where $\boldsymbol{\beta} = (\beta_0, \beta_1, \beta_2, \beta_3)^T$ represents the vector of sensitivity effects and $\boldsymbol{\varepsilon}$ is a vector containing error terms. The matrix X is a design matrix describing the parameter values for each experiment. In an OAT design, a pairwise interaction design matrix could look like

$$X = \begin{pmatrix} 1 & p & b & pb \\ 1 & q & b & qb \\ 1 & a & r & ar \\ 1 & a & s & as \end{pmatrix}. \tag{4.2}$$

with 4 simulations represented by each row of the matrix.

To find a value for the interaction effect, β_3, an estimate of the coefficients, $\tilde{\boldsymbol{\beta}}$, must be found. Standard results state that the formula to find the estimates is

$$\tilde{\boldsymbol{\beta}} = (XX^T)^{-1} X^T \boldsymbol{y}. \tag{4.3}$$

Solutions for the above equation cannot be found if the matrix XX^T cannot be inverted. It can, therefore, be shown that there are no solutions to find the interaction terms, thus limiting the utility of this design. Using several matrix properties, it can be proven that $\det(XX^T) = 0$, where det represents the determinant of a matrix: a scalar calculated from the values in the matrix that if zero, implies the matrix is not invertible. The relevant properties state that for a matrix, A, of size $n \times m$:

1. The rank of the matrix must be $\operatorname{rank}(A) \leq \min\{n, m\}$.
2. If $\operatorname{rank}(A) < \min\{n, m\}$, then $\det(A) = 0$.
3. If $\operatorname{rank}(A) = a$, then $\operatorname{rank}(A^T) = a$.
4. The determinant of the product of two matrices is the same as multiplying the determinants of the two matrices before multiplication $\det(A^T A) = \det(A^T)\det(A)$.

To find the rank of a matrix, the matrix needs to be reduced to row echelon form. This can be done as follows

$$X = \begin{pmatrix} 1 & p & b & pb \\ 1 & q & b & qb \\ 1 & a & r & ar \\ 1 & a & s & as \end{pmatrix} \xrightarrow[r_4 \to r_1 - r_4]{\substack{r_2 \to r_1 - r_2 \\ r_3 \to r_1 - r_3}} \begin{pmatrix} 1 & p & b & pb \\ 0 & p-q & 0 & b(p-q) \\ 0 & p-a & b-r & pb-ar \\ 0 & p-a & b-s & pb-as \end{pmatrix}$$

$$\xrightarrow[r_4 \to (p-a)r_2 - r_4]{\substack{r_2 \to r_2/(p-q) \\ r_3 \to (p-a)r_2 - r_3}} \begin{pmatrix} 1 & p & b & pb \\ 0 & 1 & 0 & b \\ 0 & 0 & r-b & a(b-r) \\ 0 & 0 & s-b & a(b-s) \end{pmatrix}$$

$$\xrightarrow[r_4 \to (s-b)r_3 - r_4]{r_3 \to r_3/(r-b)} \begin{pmatrix} 1 & p & b & pb \\ 0 & 1 & 0 & b \\ 0 & 0 & 1 & -a \\ 0 & 0 & 0 & 0 \end{pmatrix}$$

From this, the rank of the matrix can be seen to be $3 < 4$ and hence, by property 2, $\det(X) = 0$. By property 3 and 4, the transverse also has a rank of 3 and so $\det(X^T) = 0$, hence $\det(XX^T) = \det(X)\det(X^T) = 0$, as required. This idea extends to larger matrices as adding more parameters does not affect that two rows will be linearly dependent on each other so the matrix can never have full rank. Conversely, in the Latin hypercube design, the design matrix will always have full rank as all the rows are linearly independent, meaning a solution to the interaction terms can be found.

The subject of a minimum number of simulations required for performing a sensitivity analysis is widely discussed and whilst there is no consensus on the number of simulations that should be completed, Loeppky et al. (2009) argues that using ten times the number of parameters ($10p$) is sufficient. This informal rule has been used effectively in many studies when using Gaussian process emulation (discussed in Chapter 5) (e.g. Chapman et al., 1994; Johnson et al., 2015; Jones et al., 1998), and so I have followed this idea here and complete 200 simulations as there are 20 parameters to perturb.

4.2.2 Variance-based sensitivity analysis using regression

Variance-based sensitivity analyses are based on the decomposition of variance of a function,

$$Var(Y) = E(Var(Y|X_i)) + Var(E(Y|X_i)), \tag{4.4}$$

where X_i represents each parameter in the perturbation experiment and Y represents an output of interest. The term $Var(E(Y|X_i))$ is often referred to as the explained term, as it calculates how much of the total variance can be explained by a parameter X_i. The term $E(Var(Y|X_i))$ represents the remaining variance that is not explained by the specifically chosen parameter.

Sobol' (1993) proposed an index to represent the effect that a certain input parameter has on the function output using ideas from variance decomposition. This index is known as the main effect index, mE, and can be calculated for each parameter by

$$mE_{X_i} = \frac{Var_{X_i}(E(Y|X_i))}{Var(Y)}, \tag{4.5}$$

given in Strong et al. (2014). This formulation follows naturally from Equation 4.4, looking solely at the term calculating the variance explained by the parameter, standardised by dividing by the total variance in the output. Explicitly, the numerator calculates how much the expected value of a chosen parameter given the output varies. This is divided by the total variance in the output. The numerator can be calculated by approximating the conditional expectation to the regression line. Then, the estimated values are fitted to the regression line. The regression problem can be solved using GAMs.

The interaction effects may be important to the variance of the model output as two or more inputs may work together to change the output. The amount of variation of the conditional expectation of the output given the inputs in question is considered to calculate these values and the main effect index of the chosen inputs subtracted from this value. The pairwise interaction effect, interactions between two parameters, can be calculated with the method described in the next section. The formula for the pairwise interactions, iE is

$$iE_{X_i,X_j} = \frac{Var(E(Y|X_i,X_j))}{Var(Y)} - (mE_{X_i} + mE_{X_j}), \tag{4.6}$$

for two parameters X_i and X_j.

4.2.3 Generalised additive models

GAMs are an extension of Generalised Linear Models (GLMs) first described by Nelder and Wedderburn (1972), and GLMs are an extension of linear models, first attributed to Carl Friedrich Gauss. To show how these techniques relate to each other, I will first start by explaining the theory behind linear models and then build on that to reach GAMs.

Linear models can be written in the form $\boldsymbol{y} = X\boldsymbol{\beta} + \boldsymbol{e}$, where $\boldsymbol{y}$ are the observations, X is a design matrix describing the independent variables, $\boldsymbol{\beta}$ are the coefficients of the outlined model, and $\boldsymbol{e}$ are the normally distributed errors, with constant variance and mean 0. In other words, linear models assume that the predictions, y_i, are normally distributed conditional on a fixed input point, x_i, with a constant variance. The normality condition is restrictive, and extensions are needed to account for other relationships.

Seemingly counter-intuitively, the term linear in this context does not necessarily dictate the regression line being a straight line. The linearity property refers to the coefficients of the predictor variables and not the predictor variables themselves. For example,

$$y_i = \beta_0 + \beta_1 x_i^3 + \beta_2 w_i^2 + e_i \tag{4.7}$$

may have squared and cubed terms, but these terms are the predictor variables. The coefficients, β_i, are linear and so the regression line is classed as a linear model. However,

$$y_i = e^{\beta_0} x_i + \beta_1^2 w_i + e_i \tag{4.8}$$

is a nonlinear model, as the coefficients (e^{β_0} and β_1^2) are nonlinear.

Nelder and Wedderburn (1972) extended this idea by allowing the errors on the predictions to follow any distribution within the exponential family, including normal, exponential and Poisson distributions. Instead of the mean directly relating to a linear combination of the predictor variables as in linear models ($\mu_i = x_i^T \boldsymbol{\beta}$), now a function of the mean relates to the linear predictor

$$g(\mu_i) = x_i^T \boldsymbol{\beta}. \tag{4.9}$$

The function $g(\cdot)$ is called the link function and links the parameter of a probability distribution in the exponential family to the linear predictor. The extension of linear models to GLMs allows for many more distributions to be modelled. However, GLMs still work on the assumption that the distribution parameter relies on a linear predictor.

Generalised linear models were then extended by Hastie and Tibshirani (1987) into generalised additive models. GAMs are used to represent a function of the expected values using the sum of smooth functions, not necessarily linear, relating to each predictor variable. In the case of my simulations, the predictor values are the input parameters, of which there are 20,

$$g(E(Y)) = s_0 + s_1(x_1) + s_2(x_2) + \cdots + s_{20}(x_{20}), \tag{4.10}$$

where the s_i are smooth functions.

The formulation of GAMs is more flexible than their GLM predecessor as the distribution between the predictor variables and predictions is not required to be linear.

4.2.4 Metrics

One rationale for undertaking a sensitivity analysis is because the model is so computationally expensive to run, and so reducing the number of simulations needed is a high reward. One of the reasons for the computational expense is the huge output each simulation produces. Typically in GAM sensitivity analyses, a single metric is used to calculate the main effects. In this Chapter, I will complete sensitivity analyses to investigate four different aspects of the modelled ice sheet: ice volume, ice velocity, ice shelf extents and the model-data flow match. One-dimensional metrics need to be derived from the spatial and temporal outputs.

To investigate the parameters that affect the simulated ice volume, a Principal Component Analysis (PCA) to reduce the temporal dimensionality of the output data is created. A PCA (method described fully in Section 2.3.1) still contains a large amount of output information but in a reduced number of dimensions. For a PCA of the simulated ice volume, I reduce the number of temporal dimensions, and rather than individually analyse the 355 time steps recorded by the model, I only take the first principal component, which contains 87% of the total variance.

For the ice velocity of the simulated ice sheet, a second metric was derived. To do this, the time step with highest ice mass was isolated and the median velocity of all the grounded ice at this time step is found. Also, at this time step, the percentage of ice shelf pixels compared to the grounded ice pixels is calculated to see how the parameter inputs affect the size of the ice shelves. The number of ice shelf pixels, p_{IS}, and grounded ice pixels, p_{GI} are counted, and then the percentage of ice shelf pixels of the total amount of ice is calculated as

$$p = \frac{p_{IS}}{p_{IS} + p_{GI}}.$$

This metric is used as it compares the amount of ice shelf pixels to the amount of grounded pixels. Using this metric instead of the number of ice shelf pixels alone, means the relative amount of ice shelf pixels is encapsulated rather than just a larger ice mass also having larger ice shelves.

Finally, the score from LALA (Chapter 3) that quantifies the model-data match of the observed and modelled flow directions will be calculated. The details of how LALA is applied to the EISC are expanded on in the section below (Section 4.2.5). As the focus of my thesis is to find an optimal model simulation that matches the observed past flow directions as accurately as possible, the sensitivity analysis using the LALA scores will be used to decide on the parameters to keep and use in further modelling experiments (Chapter 6).

4.2.5 Application of LALA to simulations of the ice sheet complex

Before using LALA, two values are required to be computed (Chapter 3). The first one is the time-integrated total area of an ideal model run (equivalent to $A_{\dagger}(\mathcal{X}, \mathcal{T})$ in Section 3.2.9). To do this, the DATED-1 reconstructions (Hughes et al., 2016) of ice extent and timing were used and compared to the model grid. The number of grid cells occupied by the reconstruction is calculated and extrapolated to match the time steps used in the model simulations every 100 years.The reconstructions in DATED-1 do not quite cover the whole time period I have modelled, but the database does contain reconstructions for the four time periods 38-34 ka, 32-30 ka, 29-28 ka, 27 ka as well as a reconstruction for every 1000 years from 25 to 10 ka. The missing two missing time steps 33 ka and 26 ka are taken to be the same as the closest previous reconstructed time step available, so 34 ka and 27 ka respectively. As the DATED-1 reconstructions end at 10 ka, for the time period after this, I looked to Patton et al. (2017), whose previously modelled EISC showed the last ice was present at 8.7 ka BP. For the time before the DATED-1 reconstructions (starting at 38 ka), a nominal value is used to represent the ice caps on the Scandinavian mountains that the model was forced with. The final value for $A_{\dagger}(\mathcal{X}, \mathcal{T})$ is therefore calculated to be 3,009,320 grid cells over simulated time.

The second value that needs to be calculated is the area in which lineations could have formed (equivalent to $A_{pre}(\mathcal{X})$ in Section 3.2.9). In this application, the criteria followed are areas where lineations have been mapped and terrestrial areas where the substrate is sediment rather than bedrock. This value was calculated using the yield stress map and an outline of the areas looked for lineations over Fennoscandia and Russia (explained below). The value for this is 5164.

Across my study region, many researchers have studied and mapped glacial features (e.g. Clark et al., 2018; Glückert, 1973; Hättestrand et al., 2004). However, recent releases of higher-resolution data have not been widely used, and previous studies are not mapped systematically, making use of the previous data in LALA difficult. The PALGLAC project, which has also funded this PhD investigation, has created a consistent product of inferred flow direction across the Fennoscandian region using high-resolution (2 m) DEMs combined with data across the Kola Peninsula (Boyes, 2022; Boyes et al., 2023). An optimised sampling technique has been developed, see Butcher et al. (in prep), splitting the domain into hexagons and using representative sampling, as shown in Figure 4.1. The first lineations are mapped according to 25 km^2 hexagons, and a subset of the represented flow directions are recorded. In a second round of mapping, larger 100 km^2 hexagons are considered, with flow directions added in areas not searched in the first round, and cross-cuts being accounted for. Then, flow summary lines are drawn based on a visual analysis. The flow summary lines have been termed linkages and are the flow direction data that will be compared to the model simulations using LALA. This process was followed over Norway, Sweden and Finland. The linkages in northwest Russia are drawn directly rather than following the exact process described above. As this product is only currently available over Scandinavia and Russia (Boyes et al., 2023; Butcher et al., in prep), see Figure 1.2, all other areas of the model domain are not checked for a model-data match.

The product created (Butcher et al., in prep) is then manually assigned to the model grid, separating the directions into each grid cell, making it possible to compare the simulations to the data. Cross-cutting relations are preserved in multiple layers and are each scored over each time step. The ability to incorporate the chronology of the cross-cuts is not currently within the scope of LALA.

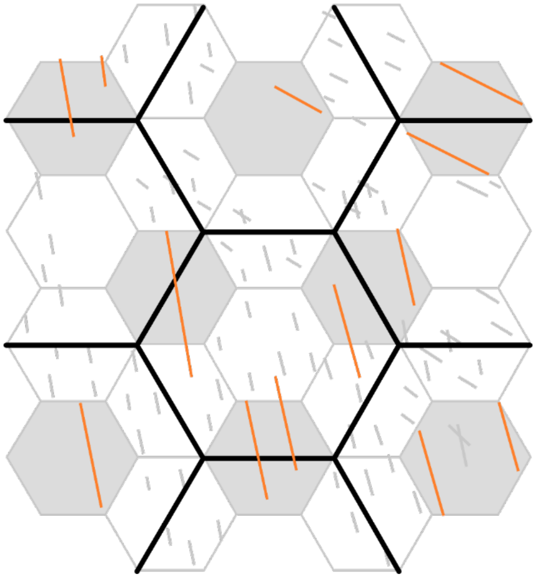

Figure 4.1: The multi-scale grid of hexagons used for sampling the domain. Ice flow directions inferred from landforms are first mapped in the smaller hexagons (25 km^2) with the aim to capture a sample of lineations (represented by the grey lines) that are representative of the population of local flow directions as well as including any cross-cutting relationships. Only the white, smaller hexagons are initially mapped, and the grey hexagons are omitted. At a later pass, further flow directions are added in areas omitted in the first pass (represented by the orange lines) using the larger hexagons (100 km^2) ensuring missed cross-cutting relationships are captured. Taken from Butcher et al. (in prep).

4.3 Results

4.3.1 Model results

Of the 200 model simulations designed for the initial ensemble described in Chapter 2, 182 completed successfully. The remaining 18 failed as the stress balances could not be resolved. Ideally, the full ensemble would have been obtained so as to observe the parameter space as effectively as possible. Unfortunately, that has not been possible here, but, as over 90% of the simulations were completed the majority of the parameter space has been covered and so the analysis can continue. The input parameter sets and the LALA scores are presented from highest to lowest LALA score in Appendix A.

Using the LALA tool, as set out in Section 4.2.5, the most and least successful simulations according to the flow geometry over Scandinavia can be isolated. The best simulation had a LALA value of −101,608 and the worst simulation scored −134,050. The simulated ice thickness at five time steps (31 ka, 26 ka, 21 ka, 16 ka and 11 ka) for these two simulations are presented in Figure 4.2, with the most credible ice extents, as inferred by Hughes et al. (2016). Considering each time step in turn for the best simulation:

- ***31 ka***. The BIIS and the SIS are already joined in the model simulation, which is not inferred at this time step in the data. The modelled BIIS is generally too large, as is the modelled SIS in the east and west margins, but simulated ice is missing on the southernmost part compared to what the data suggests. The modelled ice is also grounded off the Scottish coast and northern coast of Norway.

- ***26 ka***. The modelled BIIS has ice slightly too far south compared to the empirical evidence. The modelled SIS is quite well represented but, again, compared to the data informed reconstructions (Hughes et al., 2016), slightly too large. The modelled SBKIS has some ice missing over the western block extending from Svalbard, and an unexpected ice sheet has grown in the north.

- ***21 ka***. In this time step, the simulated ice has grown very thick, and a large amount of ice has grounded off the northern European coast. The modelled SIS has a good fit to the extent data, as does the western coast of the SBKIS.

- ***16 ka***. Once again, the simulated BIIS is too large in all directions and data suggests that it should have separated from the SIS but is yet to do so. The modelled SIS has a reasonable southern extent. The modelled SBKIS has grown too far east, and there is a small portion of missing ice in the northern part of the expected extent.

- ***11 ka***. The modelled BIIS has almost completely disappeared, with just some small ice caps remaining in Scotland. The simulated SBKIS is now grounded in the Barents Sea, which was predicted but expected earlier. There are large simulated ice shelves off the north coast of Norway, and a remaining section of grounded ice in the Norwegian Sea.

The worst simulation grows far too early, having already reached LGM size at 31 ka. The ice remains at around the same extent for the next 15,000 years. At 11 ka, the BIIS has shrunk, but the SIS and the SBKIS are both still large and connected.

By separating out the LALA scores, such that each grid cell in the lineation product (Butcher et al., in prep) effectively has its own score before being summed for the final score, the pattern of model-data match can be seen. The scores across all perturbed ensemble members are combined. As some grid cells have multiple layers and would unfairly weight certain areas, the mean of the layers is taken. Figure 4.3 shows these results. The best matches occur in a strip from central Norway east across central Sweden and Finland all the way to south of the Kola Peninsula. The northern parts of Norway and Finland also have areas of good matches. The worst matches overwhelmingly occur in the southernmost areas of Norway, Sweden and Finland.

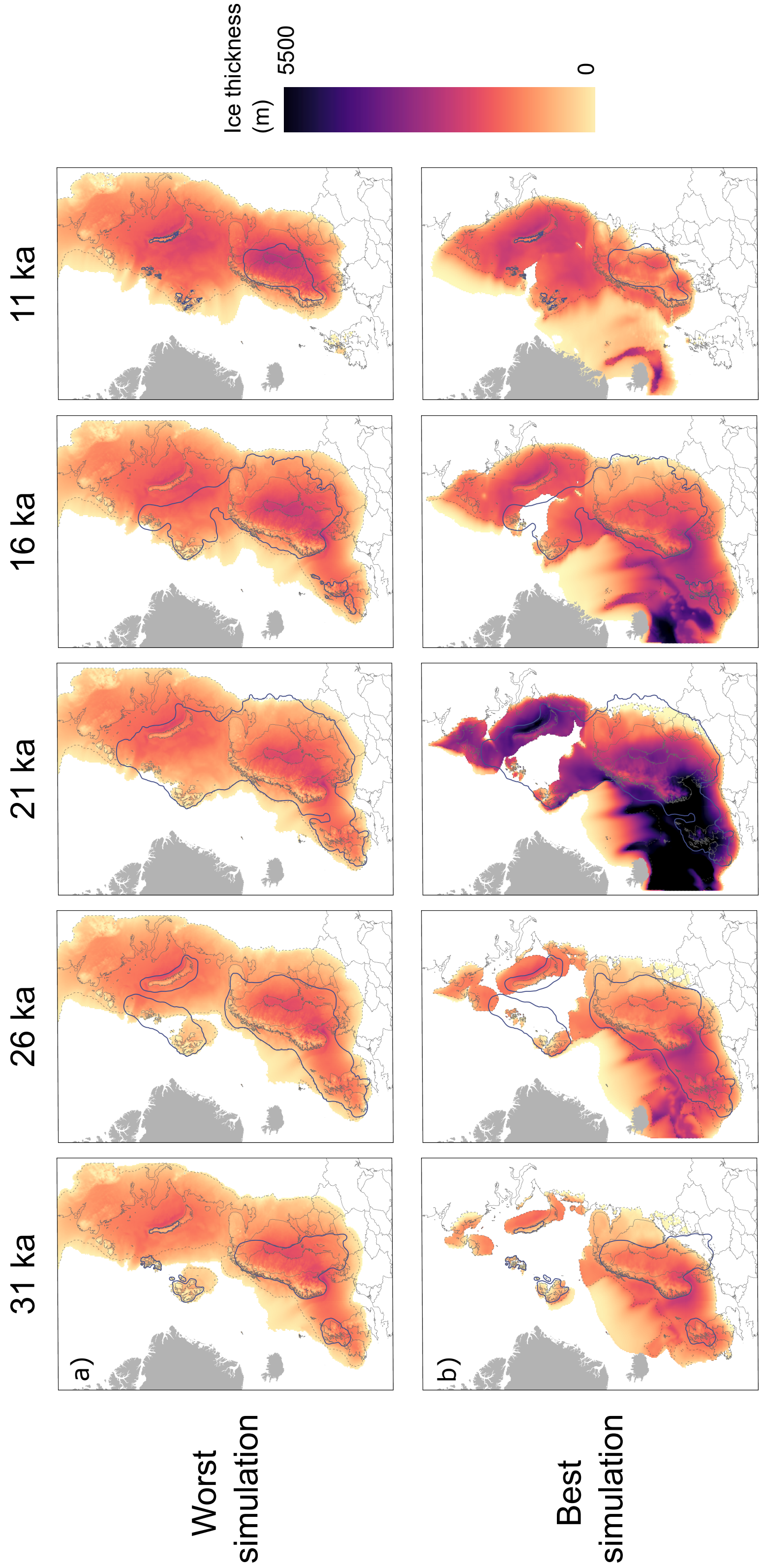

Figure 4.2: The modelled ice thickness for the simulations that scored the lowest a) and the highest b) using LALA at five time steps. Data-driven reconstructions taken from Hughes et al. (2016) are shown in blue.

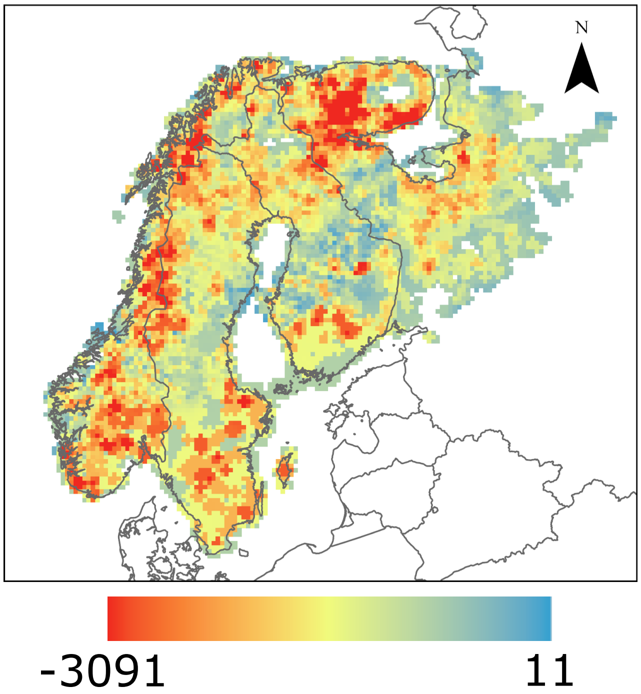

Figure 4.3: Total LALA scores across all the ensemble members based on grid cell. The grid cells with the lowest scores are in red and the best scores are in blue. Note that as the LALA score is calculated using continuous distributions, the likelihood can exceed one and thus the log-likelihood can be greater than zero.

Table 4.1: Parameters and assigned categories.

Category	Parameter Name	Parameter Symbol
Flow	Flow exponent	n
	Flow enhancement	E
Calving	Calving thickness threshold	H_{cr}
Sliding	Thin till yield stress	τ_c^{thin}
	Thick till yield stress	τ_c^{thick}
	Offshore sediment yield stress	$\tau_c^{offshore}$
	Bedrock yield stress	$\tau_c^{bedrock}$
	Ice stream yield stress	$\tau_c^{streams}$
	Sliding law exponent	q
Precipitation	Precipitation decay gradient for Britain	$m_{britain}$
	Precipitation decay gradient for Fennoscandia	m_{scandi}
	Precipitation decay gradient for the Barents Sea	$m_{barents}$
	Precipitation decay rate	β
	PDD snow	F_s
	PDD ice	F_i
Temperature	One principal component weighting for temperature at PI	α_1^{PI}
	Two principal component weightings for temperature at LGM	$\alpha_1^{LGM}/\alpha_2^{LGM}$
	Melt factor	F_{melt}
	Temperature lapse rate	γ_T
Dummy	Dummy variable randomly sampled from a uniform distribution in $[-1, 1]$	

4.3.2 Individual parameter contributions to the model output

In Figure 4.4, the main effects indices are calculated for the large ensemble using the four metrics described in Section 4.2.4. I have grouped the parameters and colour-coded them accordingly on the bar charts to more easily spot patterns of parameters that are important for different outputs, described in Table 4.1. A dummy variable that randomly samples a point across a uniform distribution in the range $[-1, 1]$ is added to the parameter design during the sensitivity analysis. The dummy variable acts as an efficacy test as, if the model estimated a large main effect for a variable known not to affect the simulation output, there may be a problem with the method.

Figure 4.4a shows the main effects for the PCA of ice volume. From this analysis, the flow exponent is found to be the most important, explaining over 75% of the variance of the output. The precipitation decay gradient over Fennoscandia can explain around 10% of the variance and the remaining parameters are relatively small. The analysis regarding the median ice velocity at the largest ice mass time step, shown in Figure 4.4b, has a more even spread of the variance across the parameters. Whilst the flow exponent is still relatively important in this analysis, it is the only one where the flow exponent parameter does not have the highest main effect value. Instead, the exponent in the basal shear stress power law takes the highest main effect value. Also important for affecting the ice velocity is the Fennoscandian precipitation adaptation. Overall, the main sensitivity of the ice velocity is built up of more parameters than the rest of the analyses.

Figure 4.4c uses a metric to explore the amount of ice shelf pixels created in the same time step as for the ice velocity metric. Then, this value p is used as a metric to test the sensitivity of the model to forming ice shelves. The main effect of the flow exponent for this output is similar to the main effect for the ice volume PCA, in that the value is much higher than the rest of the main effects. The heat flux tuning parameter is the second most important main effect, which does not have a large effect in any other analyses. Unexpectedly, the calving parameter does not have a large impact on the amount of ice shelves, as shown by the small main effect value. Presumably, as the analysis here focuses on the terrestrial lineations, parameters concerning marine environments are deemed less important. This highlights the importance of interpreting the results within the realms of the study, e.g. concrete conclusions about marine locations cannot be made without considering any of the marine evidence.

The final panel, Figure 4.4d, shows the main effects indices for each input parameter when using the score calculated using LALA. Once again, the flow exponent main effect is the largest, but not as significantly different as previous analyses. In this analysis, the temperature parameters from the PCA have a heightened importance, where they have not mattered as much before. Overall, the flow exponent seems to be important for many of the aspects of the simulated ice sheet, and the parameters for the temperature lapse rate and calving threshold are the least important.

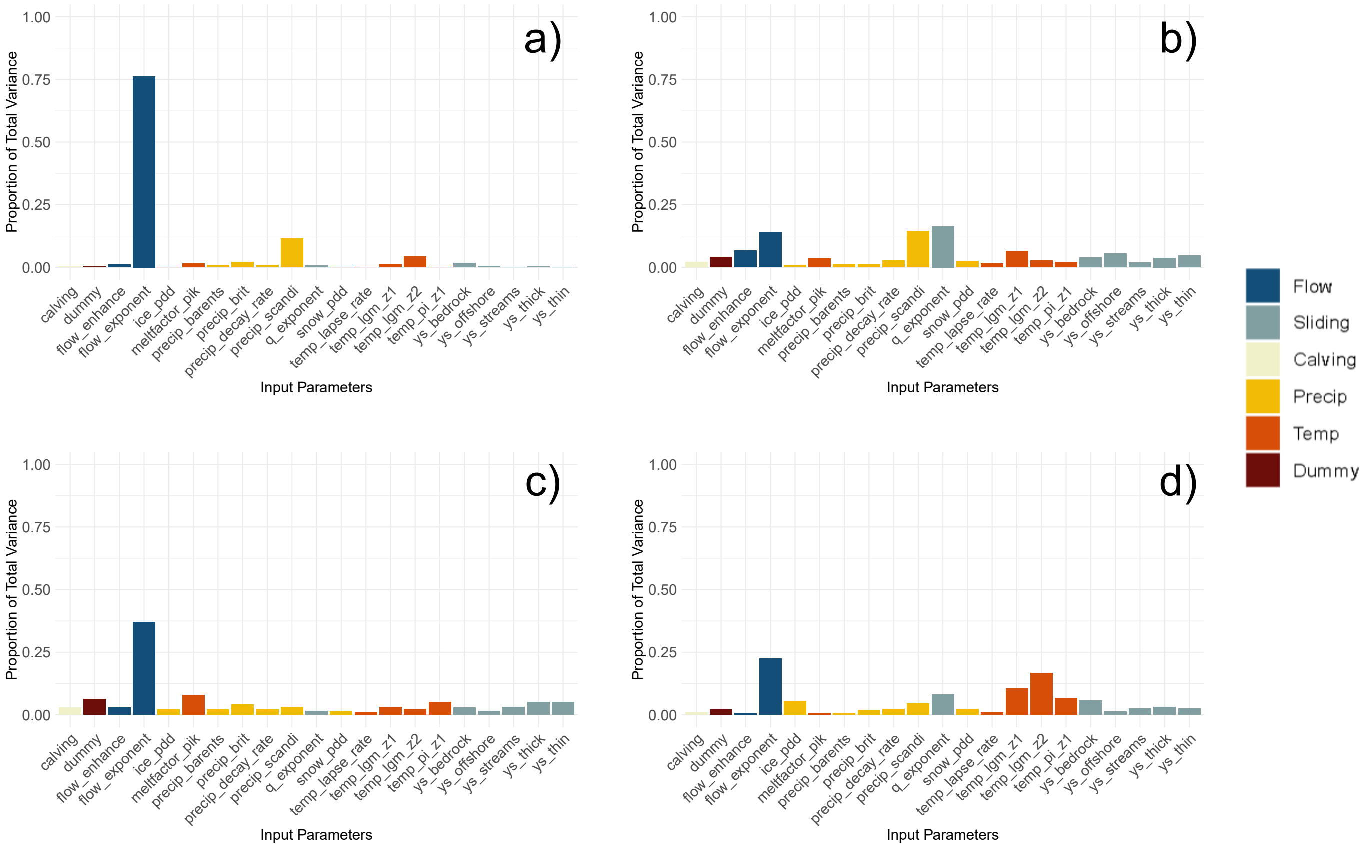

Figure 4.4: The main effect index bar charts for four different metrics of the sensitivity analysis. The metrics used are a) PCA of ice volume; b) the median ice velocity at the time step with the largest ice mass; c) the percentage of ice shelves compared to total ice at the time step with the largest ice mass; and d) the scores obtained by using LALA.

4.3.3 Pairwise parameter contributions to the model output

As described in Section 4.2.2, the pairwise interaction effects can be calculated. The values of the pairwise interaction effects are shown in Figure 4.5.

For the PCA, the highest number of interaction effects are found (Figure 4.5a). The flow law exponent, whilst having the largest main effect index, has the fewest number of interactions. The precipitation gradient over Britain, however, has the highest number of interactions and interacts with all parameters except for the flow law exponent. The dummy variable has a relatively large interaction effect value of around 7% with the offshore sediment yield stress. As such, the interaction effects focussed on here will exceed this value. The PDD melt rate for ice interacts with the flow law enhancement factor, and the precipitation gradient over Britain interacts with both the offshore sediment yield stress and the first principal component for the LGM temperature. All three of these interaction effects have values over 8%.

A contrast to the ice volume metric interactions is the number of interaction effects for the median ice velocity (Figure 4.5b) and the percentage of ice shelves (Figure 4.5c) as these are both much less influential. The median velocity measure has only three interaction effects, between yield stress for thick sediments and the dummy variable as well as the principal component for the PI temperature interacting with both the yield stress for bedrock and the precipitation decay gradient over Britain. The values of the first two interaction effects described are approximately the same, and as one of these includes the dummy variable, they could both be reasonably assumed to be within error. The interaction between the PI temperature and the precipitation decay gradient over Britain is larger at about 5%. For the percentage of ice shelves metric, three parameters interact with the enhancement factor for the flow law: two of the principal components, one for the PI temperature and the first one for the LGM temperature, and the heat flux tuning parameter. The yield stress for offshore sediment and thin sediment, as well as the precipitation decay gradient over Britain and the second principal component for LGM temperature, are also calculated to interact, and all five of these interactions are calculated to have approximately the same magnitude of effect (around 3%). A slightly larger interaction is found between the same principal component and the bedrock yield stress.

There is an array of interaction effects when using the GAM sensitivity analysis method with the LALA scores, as shown in Figure 4.5d. There is one supposed interaction with the dummy variable and the precipitation decay gradient over Britain, calculated to be about 5%, and so I will only describe the interactions with values above this. The exponent in the flow law interacts with the precipitation decay gradient over Britain and Scandinavia. Interaction effects with the flow law exponent only seem to occur with the LALA scores,

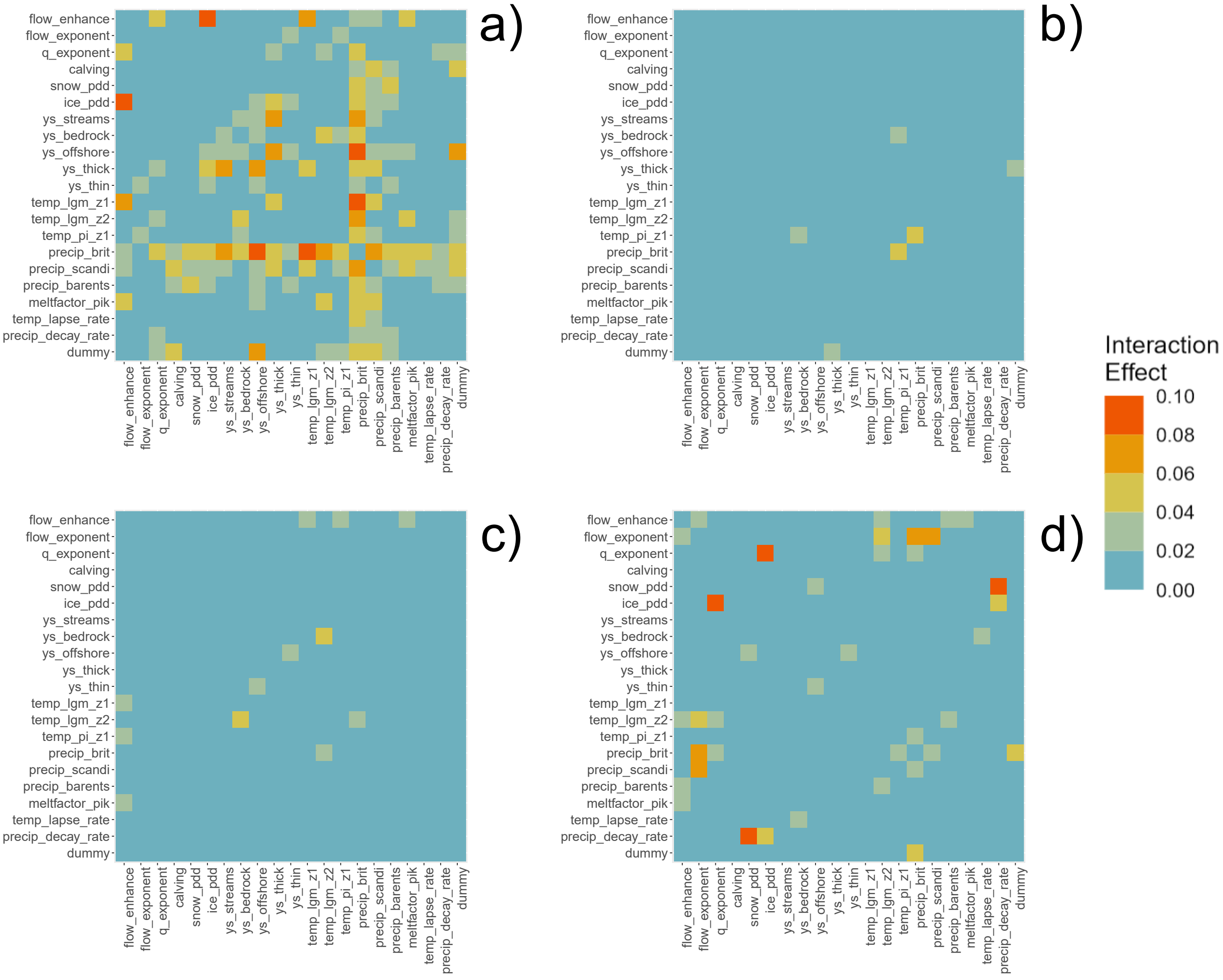

Figure 4.5: The pairwise interaction effects using the four metrics. The metrics used are a) PCA of ice volume; b) the median ice velocity at the time step with the largest ice mass; c) the percentage of ice shelves compared to total ice at the time step with the largest ice mass; and d) the scores obtained by using LALA.

other than some small effects with the ice volume metric. There are two larger interactions, both over 8%, between the PDD melt rate for ice and the exponent in the basal shear stress power law, and the PDD melt rate for snow and the precipitation decay rate.

4.4 Discussion

4.4.1 Initial model simulations

The best simulation according to LALA, shown in Figure 4.2, had a relatively successful extent match for the SIS even though the ensemble was only optimised and scored using the flow directions. Areas of mismatch for the SIS seem to largely be due to the BIIS having grown too thick too quickly, leading to unusual areas of grounded ice in the deep Norwegian Sea. The SBKIS eventually, at 11 ka, reached an extent that more closely matches the predicted extent at 21 ka. The simulation that scored the poorest, grew to be very large quickly and stayed approximately the same size for the duration of the simulation. The extent is reasonably accurate at the 21 ka time step. This suggested that LALA is penalising simulations for growing too large for too long, which was one of the aims of the tool because the score includes a term for the area of possible lineation formation and does not just score matching flow directions.

Figure 4.3 identified the southern areas of the linkage area as having the worst model-data fit. Working out the reasons for this could be of great use for improving numerical models to capture these pieces of data. But what could have caused this pattern of model-data fit? One idea is that, at the edges of the ice extent, the ice sheet's movement is more complicated (ice is thinner and extra sub-marginal processes may occur) and unlikely to be accurately modelled, especially at a relatively low resolution, as was used in this ensemble. Alternatively, it may be that this southern region was actually very complex dynamically because the ice flow and margins were, in the real world, interacting with marine and lake water bodies for long periods of time. By contrast, the west-east band of good fit to the north is more topographically simple (flat) and was often covered with grounded ice. Further north, where the ice divide may have migrated, the matches are less strong, suggesting difficulties for the model in capturing the flow variations. In short, it seems that the degree of matching varies spatially, potentially guided by where the ice sheet had stability for long amounts of time compared to areas that were often dynamically changing.

Having identified the simulation that best matches the flow direction data from the initial ensemble, comparisons can be made to other modelling studies of the EISC. Figure 4.6 illustrates the closest matching time steps from Patton et al. (2016) and Patton et al.

(2017) model simulation to the ones used in Figure 4.2. The extents obtained in Figure 4.2 are very different to those in Figure 4.6, but the aims of the two studies are quite different up to this point. Patton et al. (2016) presents an optimal simulation having manually tuned the input parameters and validated the results against several types of evidence. My study has sampled the parameter space using a Latin hypercube design and tested the outputs solely against the flow direction data. At this point, the best fitting simulation that I have presented (Figure 4.2) is not the final step or the best possible simulation, just the best so far. A further ensemble will be performed in Chapter 6, implementing the results found in this chapter and Chapter 5 to improve the model-data fit. The main aim is to fit the orientation data and investigate if, by matching this data well, other data such as ice extent will fit as well.

4.4.2 Sensitivity analysis indices

When considering the various precipitation gradients and their effect on simulated ice volume, changing the gradient for the Fennoscandian region was found to have had the largest effect on the variance of the ice volume out of the three different gradients. The three parts of the EISC all contribute to the overall ice volume. The BIIS is the smallest ice sheet within the complex, so ice volume changes in this section will only make a small difference to the overall value. The SIS is the largest part of the ice sheet complex and so the main effect of the precipitation gradient over this area makes sense to be important to the variance of the ice volume.

The ice sheet covering the Barents Sea is now known to have been extensive, covering a large area (Montelli et al., 2023). In my model set-up however, only around 26% of the total simulations had grounded ice in the Barents Sea at 21 ka. Exploring this further, by extracting the parameter inputs of the simulations that produced grounded ice in the Barents Sea, the parameters seemed to have no obvious relation: there are no specific parameter values that seem to drive the formation of this ice. None of the parameters in the sliding group, including the basal yield stress values, contribute greatly to the total of the main effects.

Whilst the main effect indices seem to identify only a few important parameters, the pairwise interactions suggest that more of the parameters may contribute considerably to the variance of the ice volume principal component. The precipitation gradient over Britain seems particularly important to include in potential future simulations even when it may have been discarded if considering the main effect index alone. Similarly, the PDD melt rate for ice and the enhancement factor for the flow law could have been ignored for subsequent

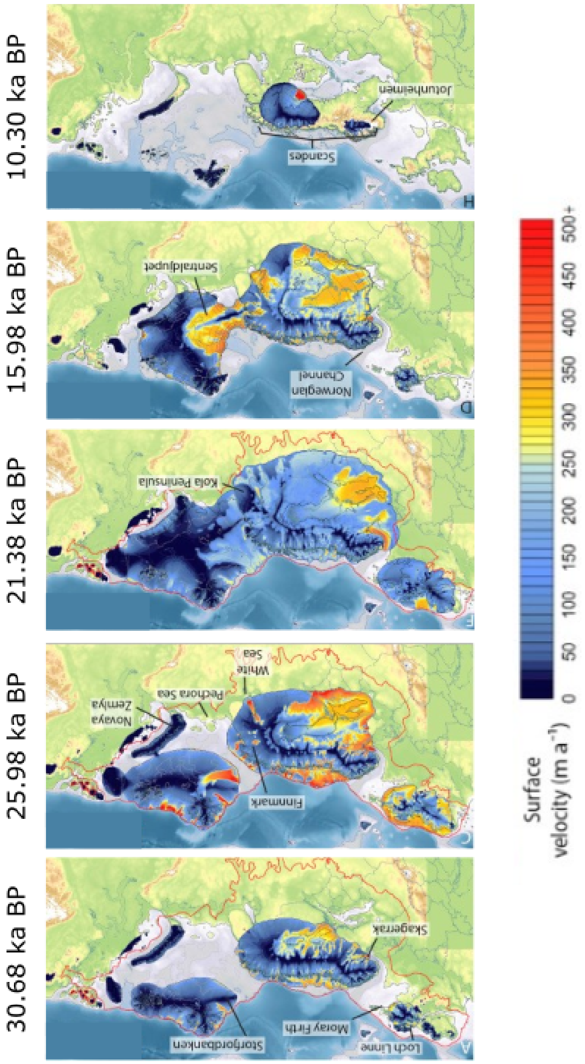

Figure 4.6: A simulation of EISC from Patton et al. (2016) and Patton et al. (2017), edited to extract time steps closest to the ones studied in this chapter.

simulations, but the interaction effects suggest they may be important when considering the ice volume. These findings highlight the importance of investigating both the main and interaction effects indices.

The calving parameter has minimal impact on the total variance for all four metrics investigated in this chapter, shown in Figure 4.4. There are also no interaction effects of note including the calving parameter. From this, either the calving process may not be a big driver in this setup or the calving parameterisation used in these simulations may not be best suited for this application. This is surprising, as the SBKIS was predominantly marine-based and thus suggests calving processes would have a large role to play in the evolution of the ice sheet. Petrini et al. (2020) simulated the deglaciation of the SBKIS and found that the ocean warming had the largest effect on the retreat of this ice sheet. The study described in Petrini et al. (2020) does differ from my study in the sense that Petrini et al. (2020) does not attempt to grow the SBKIS, and instead starts with an ice sheet already in place at the LGM matching the empirical reconstruction from (Hughes et al., 2016).

As expected, the parameters controlling the ice flow, the exponent and the enhancement factor of the flow law, impact the variance of the ice velocity, with approximately 20% combined main effects. The six sliding parameters also have an increased variance contribution, but the exponent for the basal shear stress is especially important. Both of these results are unsurprising, as more sliding should lead to faster ice velocities and vice versa. Interestingly, the precipitation main effects contribute to the total variance more than the combined temperature parameters.

There are very few interaction effects for the median velocity, and all relate to precipitation, PI temperature and different yield stresses. The interactions, when considering the percentage of ice shelves, involve temperature, precipitation, yield stresses and the flow law enhancement factor. The value of these effects is quite small, but considering the small number of main effects that seem significant, the interactions may be more informative.

4.4.3 Simulated flow direction and reducing the parameter space

Reconstructing ice flow direction was the main focus of this thesis, and thus, the sensitivity analysis using the LALA scores will inform parameter selection in later chapters. Whilst the flow law exponent is the most significant contributor to the overall score variance, as it is for almost all of the other results, other parameters provide quite large portions of the variance as well. The main effect indices for the temperature principal components are all larger than the previous results. Of these, the component for the PI temperature has the smallest

Table 4.2: Parameters to be kept constant in the second wave of simulations and the percentage each parameter contributes to the variance of the LALA scores.

Parameter	Main Effect Value
Flow enhancement	0.8%
Calving thickness threshold	1.3%
Offshore sediment yield stress	1.5%
Precipitation decay gradient, Britain	2.2%
Precipitation decay gradient, Barents	0.7%
Melt factor	0.7%
Temperature lapse rate	1.2%

main effect index at around 7%, the first component for the LGM contains 10.8% and the second component 17%. In total, the three temperature principal components contribute to around 35% of the variance.

In Hill et al. (2021), ice sheet modelling experiments are conducted to predict the contribution to sea level from the Filchner-Ronne basin on the Antarctic Ice Sheet under different climate scenarios. In contrast to the work presented here, when performing sensitivity tests, they found that the precipitation input contributed more to the change in global mean sea level than temperature input consistently over different representative concentration pathways considered. The precipitation input in Hill et al. (2021) was the largest variance contributor of all the parameters, and the parameters for the sliding law exponent and the flow law exponent hardly contribute at all. These differences highlight the importance of performing individual analyses for different model set-ups and applications.

The surface mass balance of the simulated ice sheet in this study is controlled by a PDD model, as explained in Chapter 2. The sensitivity analysis has indicated that the rate at which ice melts has a larger impact on the model-data flow match than the rate of snow melt. Presumably, this is because the layer of ice is thicker than that of snow, and so the ice melting has a bigger impact over the entire modelled ice sheet than the snow melt.

By ordering the main effect indices from largest to smallest, approximately 97% of the variance of the LALA scores can be explained by 13 of the parameters. Using this information, the 7 remaining parameters are discarded from the next perturbed parameter ensemble and kept constant at their default values, given in Table 2.2. The main effect values for the less important parameters (Table 4.2) are also all below the value calculated for the dummy variable (described in Section 4.3.2), which is a good indication that the values could be explained by randomness.

4.4.4 Reflections for future applications

Currently, the results of sensitivity analyses are used to identify areas of uncertainty in a model (e.g. Hill et al., 2021; Zweck and Huybrechts, 2005) but not completed before running subsequent ensembles. Here, I have used the results to reduce the parameter space by 35%, thus saving computational resources for future ensembles. Limited examples where results from sensitivity analyses are used to reduce the initial parameter space can be found across scientific fields, e.g. chemical engineering (Sun and Hahn, 2006) and hydrological modelling (van Werkhoven et al., 2009). Sensitivity analysis in glaciology (and further afield) is, at this time, underutilised as a method to reduce the dimensionality of the parameter space before running refined ensembles.

4.5 Summary

The sensitivity analysis used here has been demonstrated to constrain an ice sheet model parameter space, reducing the dimensions from 20 to 13. The reduction in dimensionality reduces the number of simulations required to fill the parameter space adequately, and thus, future ensembles can be completed in a shorter amount of time with fewer computer resources.

The four sensitivity analyses representing four different aspects of the simulated ice sheet all identified the flow law exponent as being an important parameter to include in the ensemble. In contrast and somewhat surprisingly, the calving parameter is consistently identified as a parameter that hardly contributes to the variance. Apart from the flow law exponent and the calving parameter, the importance of the other parameters varies widely between metrics.

Notation for Chapter 4

Symbol	Description
$A(T^*)$	Ice softness for ice at pressure adjusted temperature
$A_{pre}(\mathcal{X})$	Area where lineations could form within the overall study region $\mathcal{X}$ outside of the studied time period $\mathcal{T}$
$A_{\dagger}(\mathcal{X}, \mathcal{T})$	Integrated area over time of an ideal ice extent for the EISC
iE	Pairwise interaction effect between two parameters
mE	Main effect index for an input parameter
p	Percentage of modelled ice shelf pixels compared to the total number of ice pixels
p_{GI}	Number of modelled grounded ice pixels
p_{IS}	Number of modelled ice shelf pixels
X	Random variable representing the input parameters
Y	Random variable representing the model output given certain input parameter sets
$\boldsymbol{y}$	Values of model output for certain input parameter sets

Chapter 5

Emulating the flow of the last Eurasian Ice Sheet Complex

5.1 Introduction

Whilst numerical models are a powerful tool for ice sheet modelling, they are limited by high computational expense and long run times. For models with large input parameter spaces, this means there are gaps in the output simulations, as sampling sufficient parameter space is unfeasible due to computational limitations. An emulator is a statistical tool that acts as a surrogate of the original model and, in essence, can fill in the output for gaps in the unsampled input parameter space. A selection of numerical model runs are taken to train or build the emulator, comparing the parameter inputs that produce a certain output. Then, the emulator can estimate or predict the outputs for untested input parameters. It runs separately from the model and can produce results in a fraction of the time. Emulators have been used for a variety of different applications, from an HIV study in Uganda (Andrianakis et al., 2015) to wind engineering (Moonen and Allegrini, 2015). An emulator can then be combined with a history matching process (Andrianakis et al., 2015) to narrow down the non-implausible input parameter space. History matching uses expectations and variances, both simple and efficient calculations, to iteratively remove areas of the parameter space based on whether they fit the model output and observations well enough (Craig et al., 1997).

To model large palaeo-ice sheets over glacial timescales requires large computer resources. Compromises are usually either made by using approximations to the physics implemented in a model (e.g. Clason et al., 2014) or by performing a narrow range of simulations with

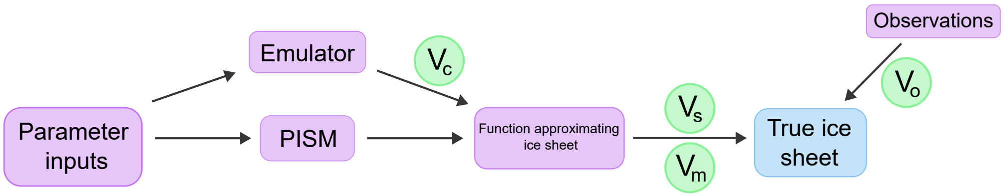

Figure 5.1: A flowchart adapted from Andrianakis et al. (2015) demonstrating how the emulator bypasses the main model. There are four areas of uncertainty, emulator uncertainty (V_c), ensemble variability (V_s), model discrepancy (V_m) and observation uncertainty (V_o).

a more sophisticated model (e.g. Åkesson et al., 2018; Patton et al., 2017). The hybrid model used in this thesis, as described in Chapter 2, is computationally expensive. Ideally, thousands of model simulations would be completed to fully understand how each parameter and parameter combinations affect the output. However, a single simulation in PISM across the EISC and over 35,000 years took anywhere from a couple of days to a few weeks to complete on approximately 20 computer cores. The time and computer power required make it unfeasible to complete thousands of simulations; hence, smaller ensembles are performed instead. This restriction requires a reduction in the parameter space that can be explored, and techniques to compensate for this are therefore required.

Emulation allows for the exploration of the range of parameters without the need for an increase in computational resources. An emulator is a statistical representation of a model, working with a small number of training simulations and then filling in the gaps separately from the model, increasing efficiency. A statistical emulator takes the model output and finds a function that can reproduce the required output (Grow and Hilton, 2014). There are different types of statistical surrogates, but this thesis focuses on emulation with a Gaussian process foundation. A Gaussian process is a continuous and infinite extension of a multivariate normal distribution. When sampling from a multivariate normal distribution, the output is a vector of finite dimensions. A sample from a Gaussian process gives a continuous function. This property allows for confidence intervals to be formed. This study will look to create a Gaussian process emulator for use on the EISC. As the emulator bypasses solving the differential equations in the model, it runs much faster and so can be run many more times than would be reasonable to run the whole model, demonstrated in Figure 5.1. The emulator can be used in combination with a history matching process (Andrianakis et al., 2015), which is a method that aims to find the set of inputs which match a particular observation (or set of observations). The resulting parameter set can then be used in the ice sheet model to give better, closer to the data, model outputs in a shorter amount of time.

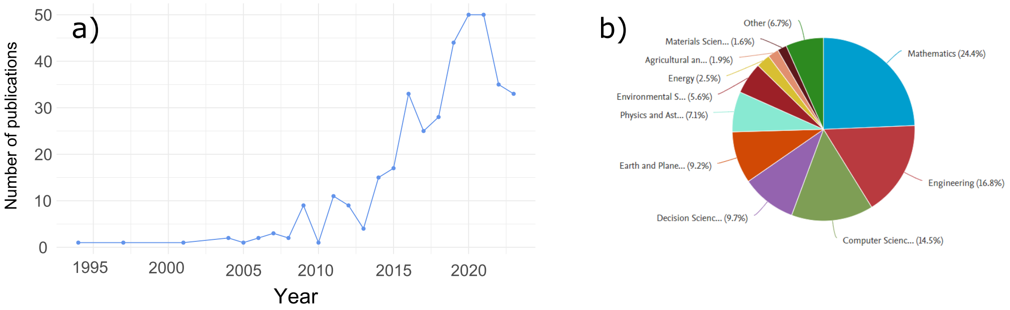

Figure 5.2: *a)* The number of publications per year from 1994 to 2023 according to a Scopus search with the key search term 'Gaussian process emulation'. *b)* The breakdown of disciplines of the publications.

A Scopus search in February 2024 shows a recent uptake in paper publications using Gaussian process emulators in various fields (Figure 5.2a). However, the use of emulation within glaciology has been limited (Figure 5.2b). Some studies in glaciology touch on this, having used statistical techniques to compare palaeo-data and ice sheet model output (e.g. Pollard et al., 2016; Tarasov et al., 2012). Emulation is increasingly being used for defining the uncertainty of predictions into the future of ice sheet behaviour (e.g. Edwards et al., 2021; Hill et al., 2021; Ritz et al., 2015; Wernecke et al., 2020), but the use of Gaussian process emulators to compare palaeo-ice sheet models and data, is thus far underutilised.

In contemporary glaciology, Ritz et al. (2015) explored the potential effects of the Marine Ice Sheet Instability (MISI) on the sea level contribution from the Antarctic Ice Sheet. Ice mass change over time was used to weight the best model outputs compared to the present day, and then statistical models were used to measure the probability of MISI occurring. Edwards et al. (2019) used a Gaussian process emulator to estimate future contributions to sea level rise by the Antarctic Ice Sheet under different Representative Concentration Pathways (RCP). Wernecke et al. (2020) looks at the rise in sea level contribution from the Antarctic Ice Sheet using the BISICLES ice sheet model and by using ice sheet thickness observations to calibrate an emulator and a history matching process, a higher proportion of the input space was sampled in a relatively short time than by running the ice sheet model alone. Processes such as MISI, which causes grounding line retreat, can be tested thoroughly using statistical methods. Hill et al. (2021) used polynomial chaos expansion to create a surrogate model for their ice flow model. The focus of the study was to investigate the levels of contribution to global mean sea level associated with a specific area in Antarctica under different RCP climate scenarios. The study also tracked the propagation of uncertainties through the model's input parameters. Hence, emulation is proving to be a useful tool in contemporary glaciology.

The emulator approach in the palaeo-glaciology field has only limited examples. Tarasov et al. (2012) uses an artificial neural network emulator to study the contribution to meltwater pulse 1a from the North American ice complex using training metrics such as relative sea level, marine limits and geodetic data. Pollard et al. (2016) takes an ensemble of a hybrid ice sheet model outputs focussing on the deglaciation of the West Antarctic Ice Sheet and compares a simple averaging method to more advanced techniques such as emulators and MCMC to find the best parameter fits for four separate parameters. This simple technique was found to work comparably to the more advanced version, but this is mainly due to the fact that only four parameters were considered with a large ensemble containing 625 members. Most recently, Pollard et al. (2023) used Gaussian process emulation to refine an input parameter space of simulations of the penultimate glaciation of the EISC. Thus, the use of emulation in palaeo-glaciology is somewhat limited and underutilised.

The aim of this Chapter is to produce an emulator and find parameter sets that would be conducive to creating simulations that score well using LALA. The Chapter starts in Section 5.2 by outlining the model simulations and scoring each using the LALA tool to assess the model-data compatibility of the observed and modelled flow directions. I then describe the two main methods of Gaussian process emulation and history matching, acting as a surrogate to the PISM model. Section 5.3 reveals the best prior model for the emulator and new parameter sampling distributions, optimised to find the best model-data match according to the ice flow data. The results from the statistical surrogate model are presented, as well as what this means for PISM re-runs that are employed later in the thesis. Section 5.4 discusses the implications and insights gained from the emulator.

5.2 Method

5.2.1 Model simulations

A 200-member perturbed parameter ensemble, described in Chapter 2, was simulated using a Latin hypercube design. The simulations were performed over a large domain containing Britain, Ireland, Fennoscandia, Russia, Northern Europe and the Barents Sea. Once completed, each simulation outputs two files: one with spatial metrics every 100 years and one with summary metrics every 10 years. The spatial outputs include the ice thickness and velocity in each grid cell, whilst the summary outputs include the ice volume and mass of the whole simulated ice mass. Both of these outputs will be useful for visualising and comparing the simulations. However, the LALA score (Chapter 3) will be used within the emulator as the project aims to find a parameter set that best captures the past flow directions.

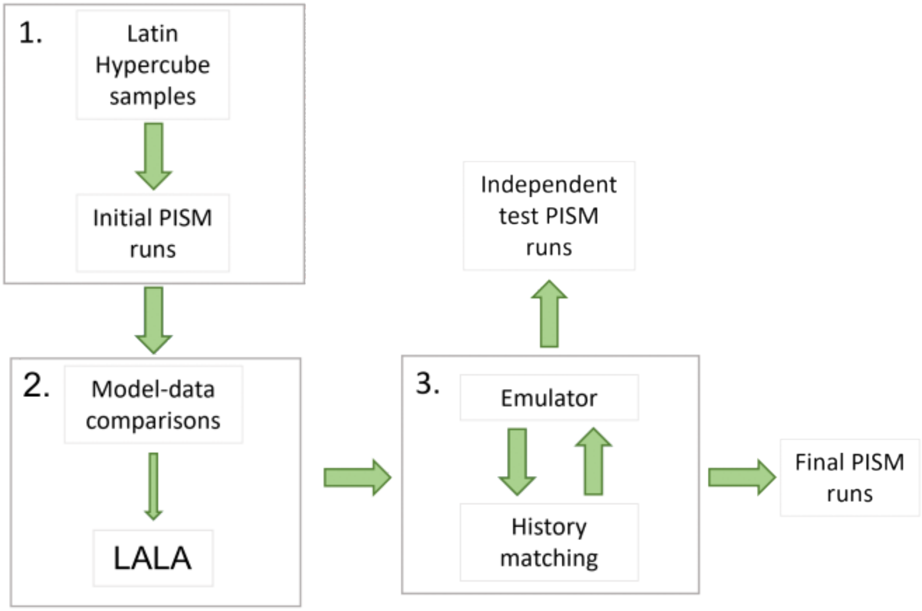

Figure 5.3: A flowchart showing how the emulator framework operates for this specific project.

5.2.2 Emulation

After the simulations have been completed and scores from LALA have been obtained (Chapter 3), an emulator can now be used (Figure 5.3). In this thesis, I focus on Gaussian process emulation, which I describe below. This relies on Bayesian inference, the principals of which are discussed more fully in Section 1.5. The basic principle starts with some test points, X, used to form a prior distribution that represents any information known about the underlying distribution before any data is observed. The prior distribution can be uninformative if little is known about the distribution before observing any data. Then training data, $\boldsymbol{y}$, at input points X', are observed. The joint distribution between the test and training distributions is calculated. Using conditioning, the posterior distribution is derived and represents the distribution of the test points whilst knowing the location of the training points. When using Gaussian processes within Bayesian inference, Gaussian (also commonly known as normal) distributions are used. Gaussian distributions have the useful property of being closed, meaning that conditioning on, or marginalising, the new distribution will also be Gaussian, making calculations simpler.

To illustrate the method of emulation using Gaussian processes, a toy example is presented with one dimension to make visualisations easier. In practice, the emulator will be predicting across 20 dimensions - one for each parameter included in the perturbed ensemble.

According to Bayesian methodology, a prior distribution must first be defined. As Gaussian processes are being used, the prior distribution will be distributed with a multivariate normal distribution with mean vector, $\boldsymbol{\mu}$, and covariance matrix, Σ. The standard choice for the mean vector is $\mathbf{0}$ and will be used for the prior here, as seen in Rasmussen et al. (2006). To form a covariance matrix, a function known as a kernel is used to generate values according to the assumed shape of the distribution. For example, the relationship may be deemed linear and so a linear kernel can be used or if it is assumed the distribution has sharp peaks and troughs, a periodic kernel can be chosen. In this example, a squared exponential kernel has been chosen to generate the covariance matrix for the prior distribution. The squared exponential kernel function takes two points, say x_i and x_j, and outputs

$$k(x_i, x_j) = \sigma_f^2 \exp\left(-\frac{(x_i - x_j)^2}{2l^2}\right), \tag{5.1}$$

where σ_f and l are hyperparameters controlling the height and length of the wavelengths of the samples. Both of the hyperparameters will be tuned to find optimised values to best account for the data when using the model, but for the prior, the values $l = 2$ and $\sigma_f^2 = 0.5$ are taken. For the set of test points, X, and hyperparameter values, this kernel generates a covariance matrix shown in Figure 5.4. The prior distribution is now fully defined and can be written as $p_X \sim \mathcal{GP}(\mathbf{0}, K(X, X))$. Notice that in this case the prior distribution indicates the possible functions that could represent the data, rather than the more typical scenario where the prior represents possible values for a certain parameter. Figure 5.5 plots several samples taken from the prior distribution. The samples are centred around the mean and around 95% of the curves are contained in $[-2\sigma_f, 2\sigma_f]$, as expected from the two-σ rule.

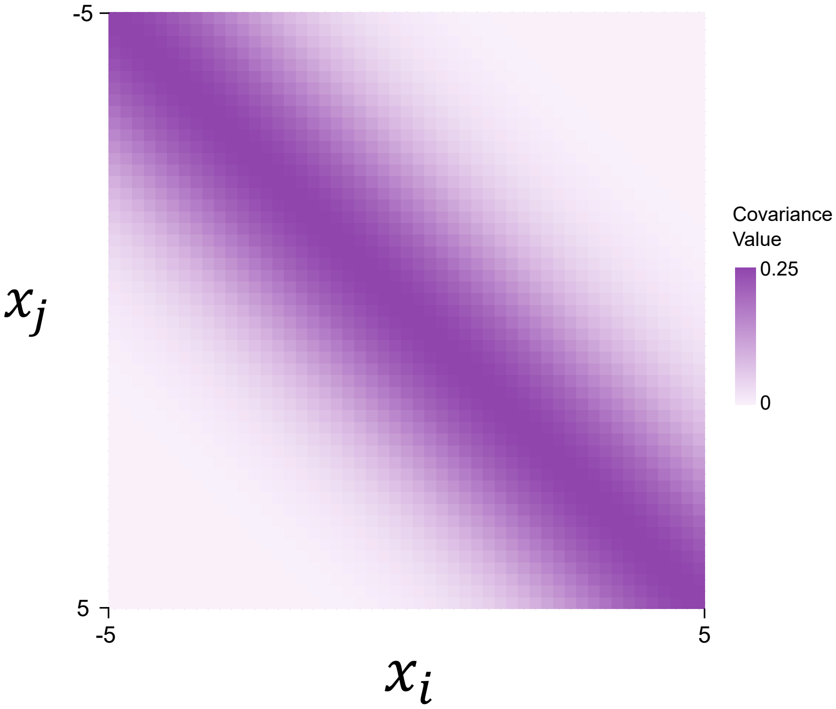

Figure 5.4: A covariance matrix generated by a squared exponential kernel (see Equation 5.1) with parameters $l = 2$ and $\sigma_f^2 = 0.5$, between two points x_i and x_j both with values between $[-5, 5]$.

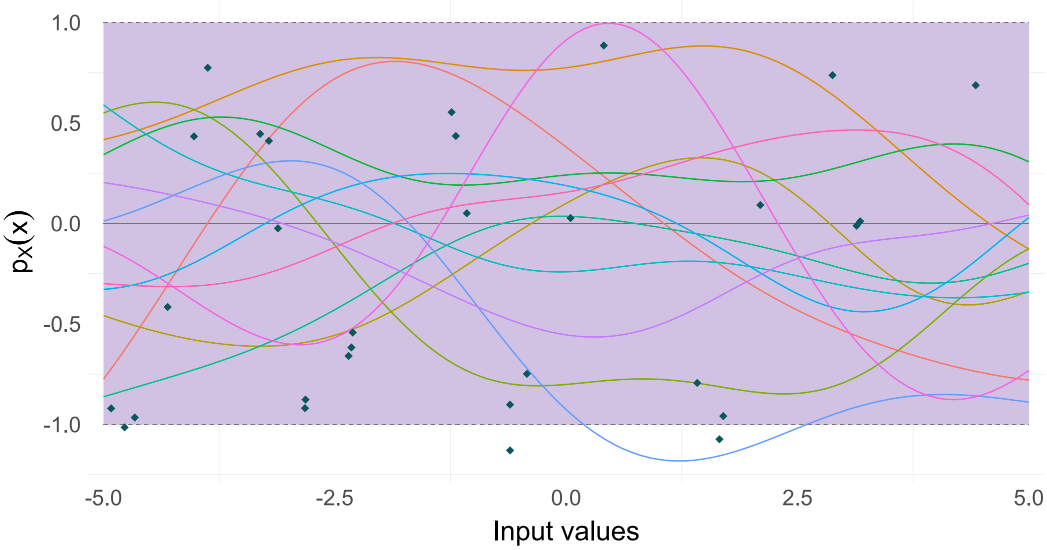

Figure 5.5: A selection of 12 samples taken from the prior distribution, $p_X(x)$, using a squared exponential kernel. The samples are centred around the specified mean, 0, and mostly fall between $[\mu - 2\sigma_f, \mu + 2\sigma_f]$. These bounds are plotted as dotted lines.

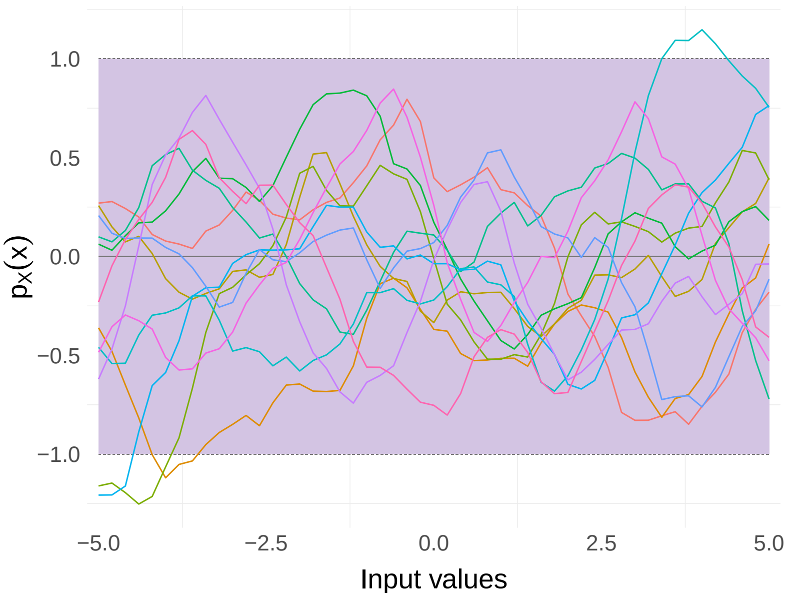

Figure 5.6: A selection of 12 samples taken from the prior distribution, $p_X(x)$, using a Matérn 5/2 kernel. The samples are centred around the specified mean, 0, and mostly fall between $[\mu - 2\sigma_f, \mu + 2\sigma_f]$. These bounds are plotted as dotted lines.

Another kernel often used when emulating high-dimensional spaces is called the Matérn kernel. The Matérn kernel has the form

$$k(x_i, x_j) = \sigma^2 \frac{2^{1-\nu}}{\Gamma(\nu)} \left(\sqrt{2\nu} \frac{|x_i - x_j|}{\rho} \right)^{\nu} K_\nu \left(\sqrt{2\nu} \frac{|x_i - x_j|}{\rho} \right) \tag{5.2}$$

where σ^2, ρ and ν are parameters to be chosen, $\Gamma(\cdot)$ is the gamma function defined as $\Gamma(n) = (n-1)!$ and K_ν is the second kind modified Bessel function defined as

$$K_\nu(x) = \sum_{m=0}^{\infty} \frac{1}{m!\,\Gamma(m+\nu+1)} \left(\frac{x}{2}\right)^{2m+\alpha}. \tag{5.3}$$

Certain values of ν simplify the Matérn kernel and values of 1/2, 3/2 and 5/2 are commonly used in an emulator context. For this study, a value of $\nu = 5/2$ which simplifies the kernel calculation to

$$k(x_i, x_j) = \sigma^2 \left(1 + \frac{\sqrt{5}d}{\rho} + \frac{5d^2}{3\rho^2} \right) \exp\left(-\frac{\sqrt{5}d}{\rho} \right) \tag{5.4}$$

with the hyperparameters to be optimised in the same way as before. Samples from the Matérn 5/2 kernel are more jagged than the squared exponential kernel, as shown in Figure 5.6. Both the squared exponential and the Matérn kernel will be tested in Section 5.3, and the predictive capabilities of each will be evaluated.

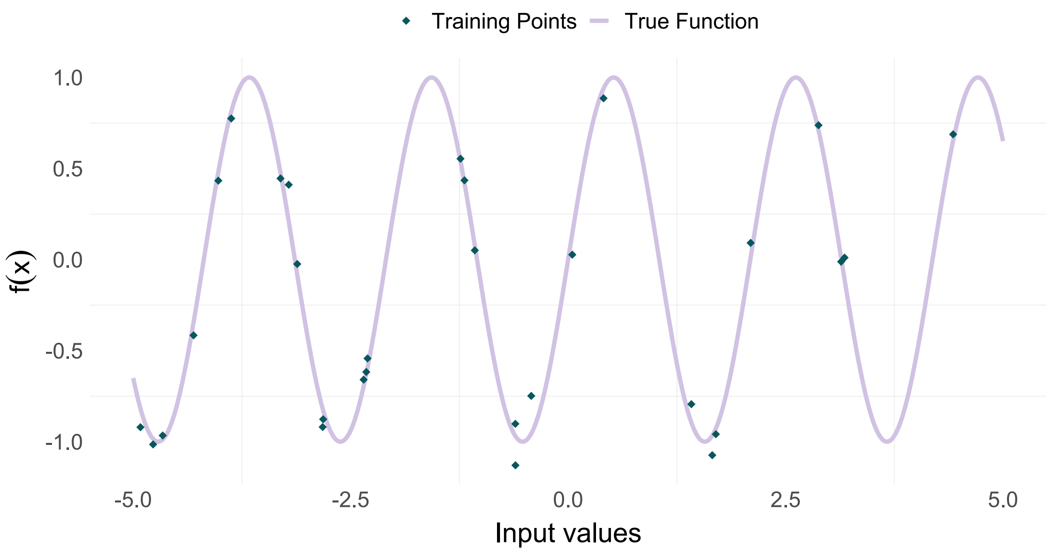

Figure 5.7: The 30 "noisy" observations, or training data $y_i = f(x_i) + \varepsilon_i$, plotted alongside the true function, $f(x_i)$, aiming to be predicted.

For this worked example, training data will be sampled from the function $y_i = f(x_i) + \varepsilon_i$ where $f(x_i) = \sin(3x_i)$ is the underlying, true function and has a small, normally distributed error $\boldsymbol{\varepsilon} \sim \mathcal{N}(0, \sigma_n^2)$ which are independent and identically distributed with mean 0 and variance σ_n^2 [1], added. The squared exponential kernel is used and the domain is restricted to $[-5, 5]$. A small amount of noise is added as this more closely represents a real situation. Rarely do observed measurements exactly match the underlying true value and so this noise needs to be accounted for. Thirty observations at the points x_i' are observed to have the values y_i, where $i \in \{1, \ldots, 30\}$, are sampled, displayed in Figure 5.7. The distribution of the training points according to the prior is $p_{X'} \sim \mathcal{GP}(\mathbf{0}, K(X', X') + \sigma_n^2 I)$.

The joint distribution between the test, X, and training values, X', based on the defined prior distribution is as follows.

$$p_{X,X'} = \begin{pmatrix} p_X \\ p_{X'} \end{pmatrix} \sim \mathcal{GP}\left(\begin{bmatrix} \boldsymbol{\mu}_X \\ \boldsymbol{\mu}_{X'} \end{bmatrix}, \begin{bmatrix} K(X,X) & K(X,X') \\ K(X',X) & K(X',X') + \sigma_n^2 I \end{bmatrix} \right). \tag{5.5}$$

By standard results of conditioning multivariate Normal distributions, proven in (for example) Eaton (2007),

---

[1] There are two variances in this Chapter with different subscripts to make them distinct. The two variances represent the vertical spread of functions about the mean in the Gaussian process and the variance of the error around the data points denoted σ_f^2 and σ_n^2, respectively.

$$p(\boldsymbol{y} \mid X, X', \boldsymbol{y}) = \mathcal{GP}\big(\boldsymbol{\mu}_X + K(X,X')[K(X',X') + \sigma_n^2 I]^{-1}(\boldsymbol{y} - \boldsymbol{\mu}_{X'}),$$
$$K(X,X) - K(X,X')[K(X',X') + \sigma_n^2 I]^{-1} K(X',X)\big) \quad (5.6)$$

is calculated to be the posterior distribution.

As the mean vectors, $\boldsymbol{\mu}_X$ and $\boldsymbol{\mu}_{X'}$, have been taken to be zero, and using the symmetry property of $K(X,X') = K(X',X)^T$ the mean and covariance of the posterior distribution can be written as

$$\tilde{\boldsymbol{\mu}} = K(X,X')\,[K(X',X') + \sigma_n^2 I]^{-1}\,\boldsymbol{y}, \quad (5.7)$$

$$\tilde{\Sigma} = K(X,X) - K(X,X')\,[K(X',X') + \sigma_n^2 I]^{-1}\,K(X,X')^T. \quad (5.8)$$

From the posterior distribution, which is a Gaussian process with mean $\tilde{\boldsymbol{\mu}}$ and covariance $\tilde{\Sigma}$ defined above by Equations 5.7 and 5.8, samples can be taken in the same way as for the prior distribution. A selection of these samples is shown in Figure 5.8. The updated samples from the posterior distribution show an improvement on the prior samples as the data has now been considered. To improve the predictive capabilities of this model, the hyperparameters can be altered. These parameters can be optimised using maximum likelihood estimation of the marginal distribution, $p_{X'}$, to give the best model fit. The log-likelihood of the marginal distribution can be calculated as

$$\log(p(\boldsymbol{y}|X', l, \sigma_f^2)) = \log(\mathcal{GP}(\mathbf{0}, K(X',X') + \sigma_n^2 I). \quad (5.9)$$

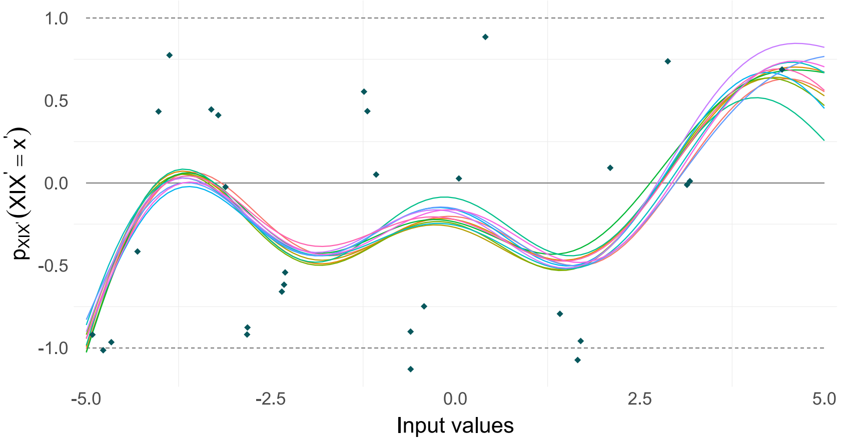

Figure 5.8: 12 samples from the posterior distribution, $p(\boldsymbol{y} \mid X, X', \boldsymbol{y})$ represented by the coloured lines. The dotted lines represent the bounds calculated using the two-σ rule, and the points are the training data shown in Figure 5.7.

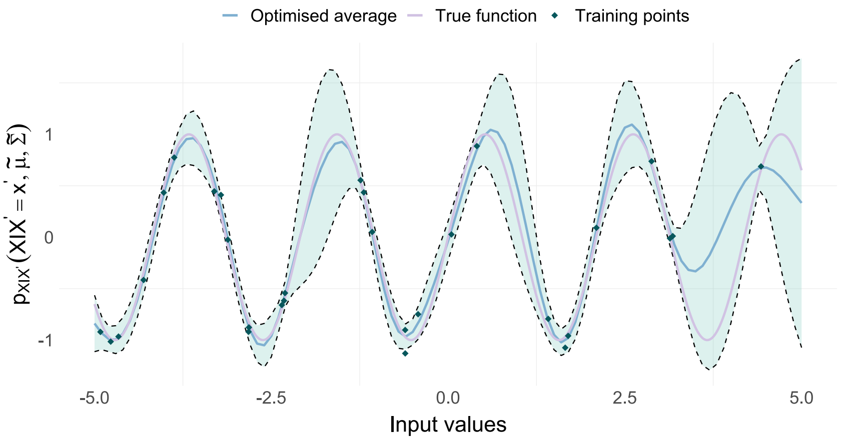

Figure 5.9: The mean from the optimised posterior distribution in blue, using the hyperparameter values $l = 0.470$ and $\sigma_f^2 = 0.662$. and the 95% confidence interval. The true function is highlighted in purple.

Partial differential with respect to each hyperparameter of the marginal likelihood are then maximised to find the optimum values for the two hyperparameters. In the case of the example in Figures 5.5 and 5.7, the optimal hyperparameters are found to be $l = 0.470$ and $\sigma_f^2 = 0.662$.

Figure 5.9, shows the optimised posterior distribution using these values. It is clear how much of an impact this process has on improving the fit of the model closer to the data. Optimising the hyperparameters is thus found to be incredibly important when estimating the parameters of the ice sheet model.

For the emulator created for the ice sheet model, an important step is to scale the input values to all be in the same range. As the kernels rely on the difference between the parameter values, if some are orders of magnitude larger than others, these parameters will be deemed overly important within the emulator. For this study, I have scaled all parameters to be within $[-1, 1]$ to account for this.

5.2.3 History Matching

Once the emulator has found a surface that fits and is optimised to the data, new parameter sets can be found for a certain specified output using history matching. History matching is a method to quantify how plausible certain inputs are to produce a given output (Andrianakis et al., 2015) (Figure 5.3). This will help determine the optimum parameter inputs to score the highest in LALA. In this section, the history matching method in Andrianakis et al. (2015) is used and will be showcased following on from the worked example above. First, the posterior distribution with optimised hyperparameters is evaluated at the vector of test points, $\boldsymbol{x}$, and stored in the vector $h(\boldsymbol{x})$. Using these results, an implausibility measure $I(\boldsymbol{x})$ can be calculated for the desired output to match, say z, using the following formula:

$$I(\boldsymbol{x}) = \frac{|z - \mathbb{E}[h(\boldsymbol{x})]|}{[V_o + V_c(\boldsymbol{x}) + V_s + V_m]^{1/2}}, \tag{5.10}$$

where V_o, V_s and V_m are the observation uncertainty, ensemble variability and model discrepancy respectively and are set to zero for simplicity in the toy example. $V_c(\boldsymbol{x})$ is the emulator uncertainty at the specified test points and so is equivalent to $\mathbb{V}[h(\boldsymbol{x})]$. Figure 5.1 shows where the uncertainties come from in the numerical model and emulation workflow. Breaking down this formula, the numerator finds the difference between the output being investigated and the expected value of the posterior distribution at the test points. The denominator sums the different sources of uncertainty and adjusts the implausibility measure proportionally. With this measure, any test points where $I(\boldsymbol{x}) > c$ for some determined value c would be considered implausible.

Say that in this example, the point of interest is $z = 0.2$. Figure 5.10 shows the averaged optimised posterior distribution and highlights the output of 0.2 and visually shows the inputs that could produce this value. For simplicity, take V_o, V_s and V_m to be zero. The values for $V_c(\boldsymbol{x})$ are in the leading diagonal in the covariance matrix for the optimised posterior distribution. After finding $h(\boldsymbol{x})$, the implausibility measure can be calculated, and the implausible inputs can be identified. The threshold value c must be decided upon. A common choice for the cut-off is $c = 3$ (e.g. Andrianakis et al., 2015; Vernon et al., 2010), based on a theorem from Pukelsheim (1994) that states that for any continuous and unimodal distribution, within 3σ of the mean will always contain at least 95% of the probability mass. This rule can be used as the quantity $|z - \mathbb{E}[h(\boldsymbol{x})]|$ follows these criteria. Hence,

$$|z - \mathbb{E}[h(\boldsymbol{x})]| < 3\sigma \tag{5.11}$$

where, $\sigma = [V_o + V_c(\boldsymbol{x}) + V_s + V_m]^{1/2}$. Rearranging this gives the inequality $I(\boldsymbol{x}) < 3$ for inputs considered non-implausible to achieve the output z.

The emulator will then be used to create a surface linking the input parameters to the chosen LALA output, and then history matching will be used to evaluate new parameter sets. This process will be repeated as new PISM simulations are performed to validate the results. The workflow for this Chapter is shown in Figure 5.3.

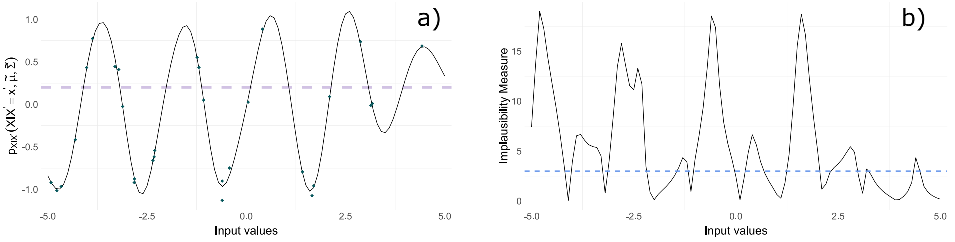

Figure 5.10: *a)* The optimised posterior mean is calculated using the test points. The purple line indicates the observed value of interest. *b)* The implausibility measure is evaluated at each test point. The dotted blue line is drawn at $I(\boldsymbol{x}) = 3$, which in the toy example is the limit as to the values deemed implausible or not. The values that fall below the blue line are possible to give the desired output when used within the original model as an input.

5.3 Results

5.3.1 Emulator results

After running the emulator, it becomes important to validate whether the estimations are accurate. One method to assess if the estimations are precise enough is to use leave-one-out validation. Leave-one-out validation is where the emulator is trained using all but one of the inputs and then the removed input is used as a test. This is repeated for each of the training inputs, and then the true and estimated LALA scores can be plotted against each other. The aim is for the plotted points to be as close to the line $y = x$ as possible (i.e. the estimated output is as close to the true values as possible).

The first attempt to fit the emulator (using the prior mean and kernel from the worked example) was not very successful and the leave-one-out validation showed that the emulator was not producing accurate predictions, as shown in Figure 5.11a. Ideally, all the points in the scatterplot in Figure 5.11a would cross the line $y = x$, which would represent that the estimated LALA scores are the same as the true LALA scores. The first kernel choice only correctly predicts 101 of the training points within error. Looking at the histogram, Figure 5.11b, the emulator is missing the extreme lower values and over-estimating the higher scores, giving a slight positive skew on the estimated value distribution compared to a relatively symmetrical distribution for the true training values. To improve the predictive capabilities of the emulator, the kernel was updated such that instead of having just one length hyperparameter; each parameter had its own length hyperparameter that would be optimised. Hence, the kernel now has 21 hyperparameters to optimise. The updated kernel has the form

$$k(\boldsymbol{x}, \boldsymbol{x}') = \sigma_f^2 \exp\left(-\sum_{i=1}^{20} \frac{(x_i - x_i')^2}{2l_i^2}\right). \tag{5.12}$$

Using this altered kernel, the leave-one-out validation is now shown in Figure 5.12. The kernel with individual hyperparameters for each input slightly improves the simpler kernel and predicts 110 of the training points correctly. The histogram comparing true and estimated values is more accurate in the tails of the distribution but is now under predicting the scores around the mean of the training points.

Another extension to the kernel to enhance the emulator's predictions is to experiment with a different prior mean. Up until this point, the prior mean was taken to be $\mathbf{0}$. The extreme values are not being well predicted because where there is less data, the emulator relies more heavily on the prior mean and so the predicted values are skewed higher than they are. Instead of using the constant prior of $\mathbf{0}$, the value of $\mathbb{E}(\boldsymbol{y})$, the mean of the training data, will be used, with results shown in Figure 5.13. The change of the prior mean has once again improved the fit, although only slightly, now correctly predicting 118 points. However, there is still a relatively large proportion, roughly 35%, of training points that are not being accurately predicted using the emulator.

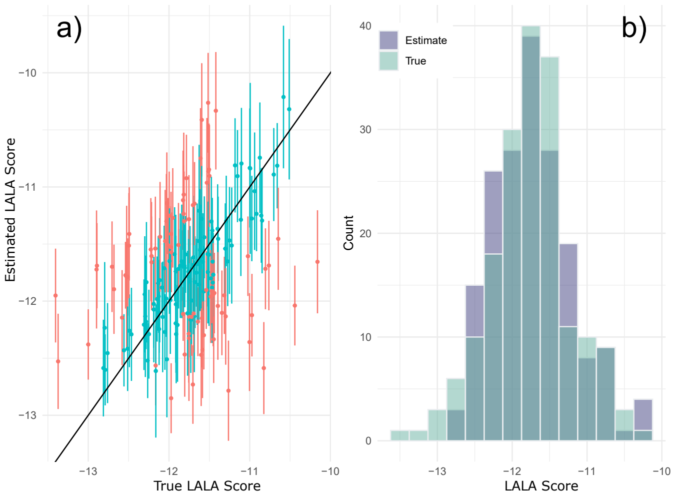

Figure 5.11: Leave-one-out validation for the emulator using standard squared exponential kernel with 2 hyperparameters. A total of 101 points were predicted correctly, within error. *a)* Points in blue are deemed to have been accurately predicted as a point within error crosses the line $y = x$. Points in red, however, are deemed to have not been predicted correctly as no point within error crosses the line $y = x$. *b)* Green bars represent the true LALA scores obtained by the initial ensemble, and purple bars represent the estimated scores using leave-one-out validation.

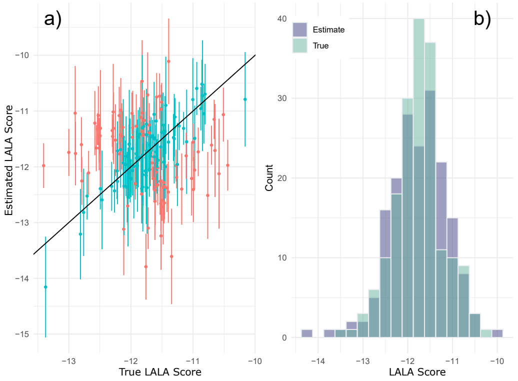

Figure 5.12: Leave-one-out validation for the emulator using adapted squared exponential kernel with 21 hyperparameters. A total of 110 points were predicted correctly, within error. *a)* Points in blue are deemed to have been accurately predicted as a point within error crosses the line $y = x$. Points in red, however, are deemed to have not been predicted correctly as no point within error crosses the line $y = x$. *b)* Green bars represent the true LALA scores obtained by the initial ensemble, and purple bars represent the estimated scores using leave-one-out validation.

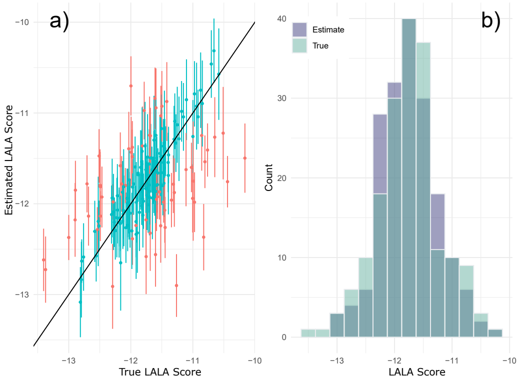

Figure 5.13: Leave-one-out validation for the emulator using adapted squared exponential kernel with 21 hyperparameters and using a prior mean of $\mathbb{E}(\boldsymbol{y})$. A total of 118 points were predicted correctly, within error. *a)* Points in blue are deemed to have been accurately predicted as a point within error crosses the line $y = x$. Points in red, however, are deemed to have not been predicted correctly as no point within error crosses the line $y = x$. *b)* Green bars represent the true LALA scores obtained by the initial ensemble, and purple bars represent the estimated scores using leave-one-out validation.

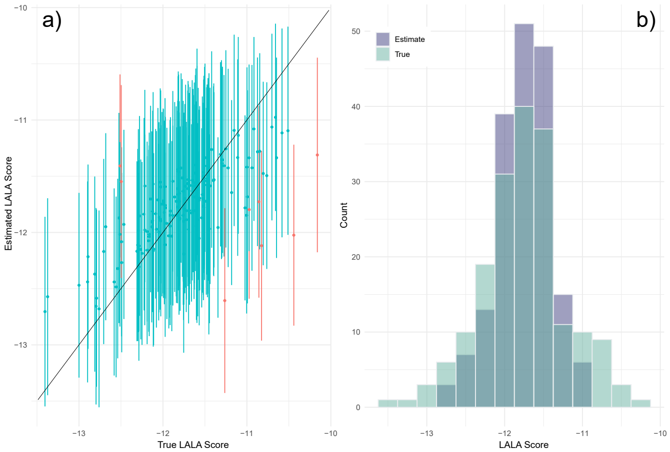

Figure 5.14: Leave-one-out validation for the emulator using Matérn 5/2 with 21 hyperparameters and using a prior mean of $\mathbb{E}(\boldsymbol{y})$. A total of 174 points were predicted correctly, within error. *a)* Points in blue are deemed to have been accurately predicted as a point within error crosses the line $y = x$. Points in red, however, are deemed to have not been predicted correctly as no point within error crosses the line $y = x$. *b)* Green bars represent the true LALA scores obtained by the initial ensemble, and purple bars represent the estimated scores using leave-one-out validation.

So far, I have focussed on the squared exponential kernel, but without a good fit by the emulator, so now the Matérn kernel is tested to see if the predictive power of the emulator improves. With a constant prior distribution of $\mathbb{E}(\boldsymbol{y})$ and the Matérn kernel, a much larger number of points are correctly predicted, 174 points, shown in Figure 5.14. Finally, a linear prior distribution combining all of the parameters was used within the Matérn kernel, giving a slight increase in predictive capabilities, correctly predicting 175 points, once more, shown in Figure 5.15. Hence, a Matérn 5/2 kernel with a linear prior distribution has given the best predictions and thus is used as the basis of the emulator moving forwards.

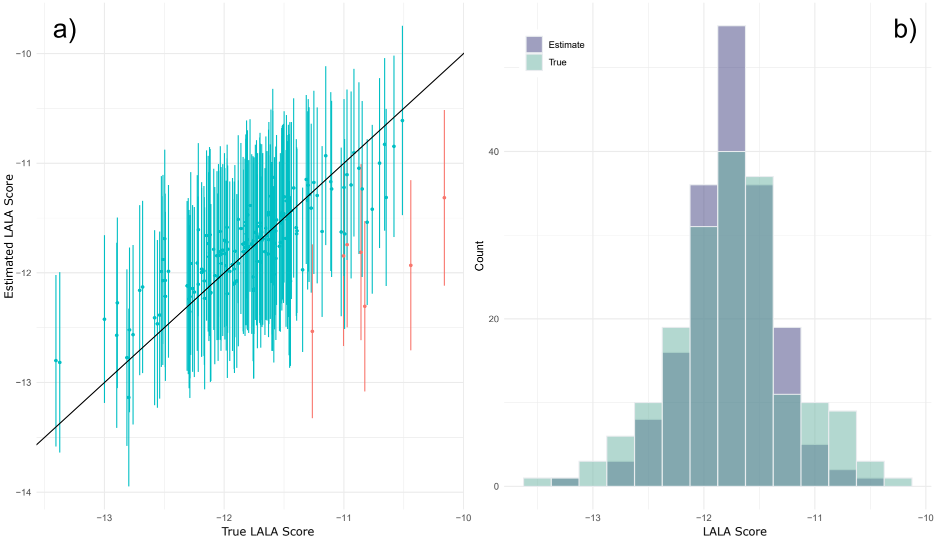

Figure 5.15: Leave-one-out validation for the emulator using Matérn 5/2 with 21 hyperparameters and using a linear prior distribution. A total of 175 points were predicted correctly, within error. *a)* Points in blue are deemed to have been accurately predicted as a point within error crosses the line $y = x$. Points in red, however, are deemed to have not been predicted correctly as no point within error crosses the line $y = x$. *b)* Green bars represent the true LALA scores obtained by the initial ensemble, and purple bars represent the estimated scores using leave-one-out validation.

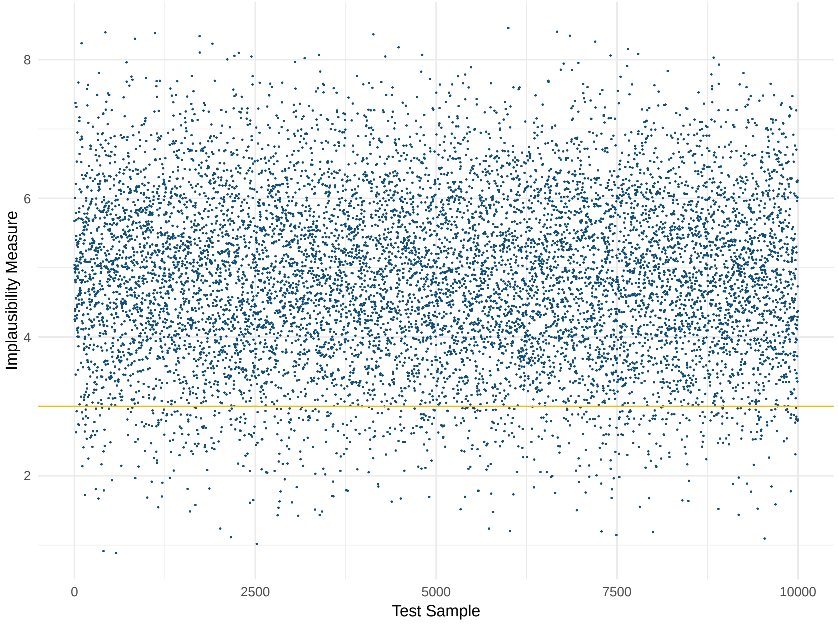

Figure 5.16: Implausibility values calculated for each test sample, for the output value -10. The horizontal yellow line marks the cut-off of $I(\boldsymbol{x}) = 3$.

When calculating the implausibility measure, 10,000 new input parameter sets were generated using a Latin hypercube design. Then, an output value of -10000 in LALA is chosen to measure the implausibility of the new inputs in replicating this value. The 10,000 points and the corresponding implausibility values are plotted in Figure 5.16, with a cut-off of 3 highlighted in yellow. In total, there are 633 test inputs that fall below the threshold.

Now that the test inputs that will score highly using LALA have been identified, inferences about the parameters can be made. Plotting the 633 non-implausible inputs for each parameter individually, the distribution of parameter values that score well using LALA are mostly non-uniform, shown in Figure 5.17. The uniform sampling that was first performed to sample parameter inputs for the initial ensemble (see Section 2.5.3) no longer seems appropriate, so for future ensembles (Chapter 6), parameter inputs will be sampled using these distributions.

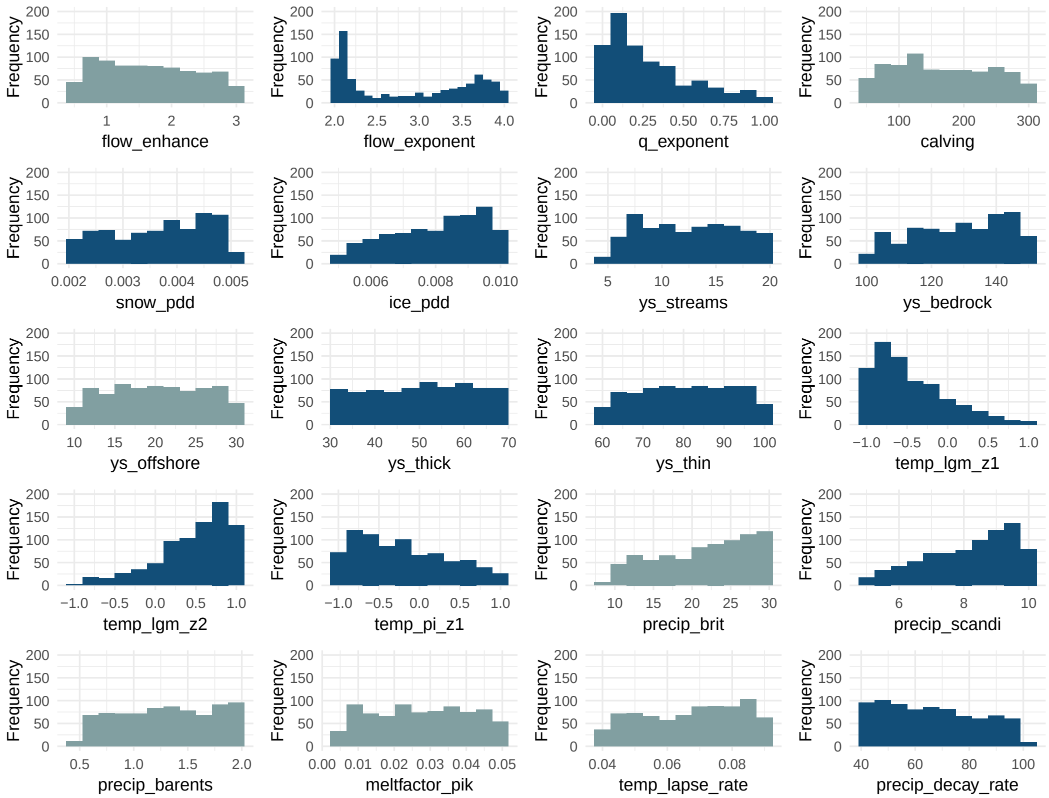

Figure 5.17: Distribution of each parameter in the non-implausible space determined by the history matching process. Parameters with greyed-out histograms have been excluded from the parameter space based on results in Chapter 4 due to their lack of importance in affecting modelled outputs.

5.4 Discussion

5.4.1 High dimensional prediction with an emulator

The best fitting emulator tested in this chapter used a Matérn 5/2 kernel with separate hyperparameters for each parameter and a linear prior distribution. The emulator correctly predicted 175 out of 182 LALA scores from the training simulations within error. Several studies concur with the finding that the Matérn kernel is successful in high-dimensional scenarios, as they better predict rougher surfaces (e.g. Johnson et al., 2015; Rasmussen et al., 2006). It is likely a better assumption that a rougher surface is required to represent the LALA scores in the 20 dimensional parameter space, as it is a complex model and hard to tell if the output will be smooth in each dimension (some small changes may result in drastic effects in the output). Whilst the errors are relatively large, as seen in Figure 5.15a, the true and estimated LALA scores are comparable (Figure 5.15b). Almost all of the wrong predictions fall below the line $y = x$ and are therefore being underestimated. Although the ideal situation would be that all points are correctly predicted, this seems unlikely with such complicated physics controlling the underlying model. As the aim of the study is to create model simulations with the highest score for LALA as possible and thus fitting the lineations closely, underestimates are the better option for incorrect predictions. The use of leave-one-out-validation is critical to ensure a successful emulator is created. Visualising the predicted surface with high-dimensional surfaces is nearly impossible, so validation methods that allow a visual check are vital.

Whilst emulation provides a powerful tool to act as a surrogate to the main numerical simulator, choices for emulator set-up are important. The choice of the kernel and the prior mean can all have large impacts on the predictive success of the surrogate, as seen in the previous section. Ensuring the emulator accurately predicts the training data is imperative to check the set-up is appropriate for the application. Comparing the results using the squared exponential kernel and the Matérn kernel both using a prior mean of $\mathbb{E}(\boldsymbol{y})$, in Figure 5.13 and Figure 5.14 respectively, shows the biggest improvement of 118 correctly predicted points to 174. This suggests that when constructing an emulator, the choice of kernel has the most weight when looking to improve predictability. The prior mean seems to improve the emulator in smaller increments, so, whilst still important, the larger focus should be on the choice of kernel.

5.4.2 Calibrating parameter distributions

For the initial ensemble, a maximin Latin hypercube design was used to sample from the parameter ranges. As little information was known about the parameters at the start of the study, all values within a parameter range were considered to be equally plausible and thus sampled uniformly. Now that the history matching procedure has been performed, the non-implausible parameter sets have been identified, and the individual parameter ranges can be plotted, shown in Figure 5.17. From this, it can be inferred that the parameters should be sampled in the same way deemed plausible in Figure 5.17. This is a type of Bayesian calibration (Kennedy and O'Hagan, 2001), but, to my knowledge, this is the first time it has been used in this way.

In other studies (e.g. Eckert et al., 2010; Turner et al., 2023), a method called expert elicitation (Oakley and O'Hagan, 2007) is used to determine the prior distribution of parameter ranges to sample. Expert elicitation can be a pragmatically difficult and lengthy process; there are relatively few people who have the required expertise and the time to partake in elicitation surveys. Here, I used a simple uniform distribution for all parameters, with ranges found to work well in other settings (Ely et al., 2024). Using history matching, distributions to sample from for future ensembles have been extracted automatically (Figure 5.17) without having to spend time choosing more complex distributions initially. This method is much faster and can utilise simulations that already needed to be run, so no extra computational power or researcher time are required.

Certain distributions of non-implausible values for different parameters (Figure 5.17) appear significantly different to the uniform distributions originally sampled in Chapter 2. For example, the principal components used for the temperature inputs denoted as `temp_lgm_z1`, `temp_lgm_z2` and `temp_pi_z1` for the first and second components for the LGM temperature input and the first component of the PI temperature input respectively. The climate models that impact these values can be investigated using a biplot, shown in Figure 5.18. A biplot visually represents the projected points onto the principal component axes combined with vectors of each variable, which show the variables that have the most impact on each principal component. For the LGM components, shown in Figure 5.18a, the MPI model affects the first component in the positive direction and the MIROC model in the negative direction. Similarly, the ISPL model affects the second component in the positive direction and the COSMOS model in the negative direction. Figure 5.17 shows that the first component is more likely to have a low value than a high value, so the MIROC model contribution is more important to improving the LALA score than the MPI model. Following the same logic, the ISPL contribution is the most important for the second component. The PI temperature input is slightly right-skewed, meaning the MPI model holds slightly more importance, but the skew is not as obvious as it is for the LGM components. Hence, the contributions from the MIROC and ISPL models seem to be more important in increasing LALA scores for the principal components of the LGM temperature input, and the MPI

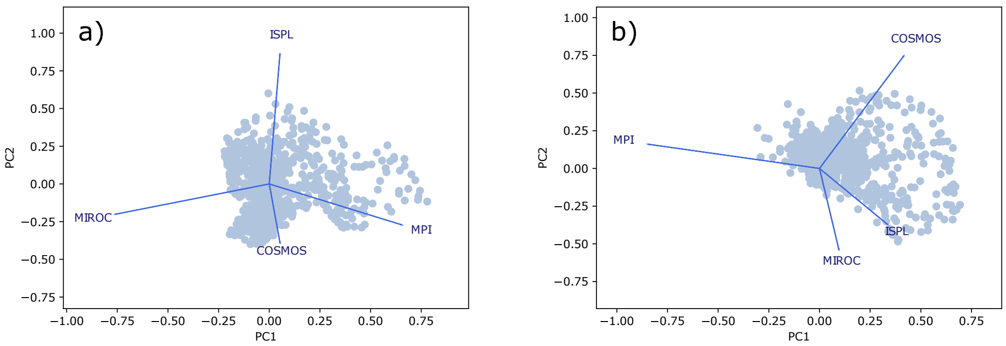

Figure 5.18: *a)* Biplot for the principal components for the LGM temperature input. *b)* Biplot for the principal components for the PI temperature input. Sample of points projected onto the principal component axes, shown as light blue circles. The vectors are shown as blue lines, each representing one of the climate models. The length and direction of the vector describe how much each model informs the principal components.

model contribution is more important in increasing LALA scores for the principal component of the PI temperature input.

The exponent for the flow law, denoted `flow_exponent`, also has an interesting distribution (Figure 5.17). There is a peak on the far left of the range and a smaller peak in the upper half of the range. The most common value used in ice sheet modelling studies is 3 (e.g. Gillet-Chaulet et al., 2012; Larour et al., 2012*b*; Pollard and DeConto, 2012), but from the distribution I obtained for the flow law exponent parameter, it seems that this is an unlikely value to obtain the model simulation I am aiming for. It is important to note that whilst these results are interesting and the method new, the results are only valid for my model set-up over the region and time periods I have modelled. Another study that follows this workflow may find different parameters or parameter sampling distributions are needed to achieve a good model-data match. For example, if another study were to model the EISC over the last 40 ka using an alternative model to PISM or different boundary conditions to mine then the exact sampling distributions found in this chapter are not guaranteed to improve the flow geometry fit to the new model simulations. The workflow outlined in this thesis would need to be performed with new initial simulations and analysis to find a flow calibrated parameter space unique to the model set-up.

5.4.3 Wider use

In palaeo-glaciology, flow geometry is sometimes compared after an ensemble is produced as a way to assess the success of the experiment (e.g. Ely et al., 2024; Gandy et al., 2021;

Patton et al., 2016). As yet, this is the first time data explaining past flow patterns, or, to my knowledge, any data at all, has been used to adjust the input parameter space. This approach could be easily adapted to explore parameter spaces for data sources such as geochronological timings or ice extents. Currently, the tools available to quantify the model-data matches for these data (Ely et al., 2019; Li et al., 2008) cannot be used within an emulator (Archer et al., 2023), and more work needs to be done to create compatible metrics.

The ultimate aim should be to have model-data comparison tools that create metrics that can be combined into one to represent the overall success of model simulations to all available data. With an overall metric, an emulator can be built to predict parameter sets to produce output simulations with good model-data matches over multiple types of evidence, such as flow, timing and extent. Not only would this identify important parameter areas but it could also help identify pieces of evidence poorly represented in the numerical models that may need to be re-evaluated or areas within the domain that would benefit from further investigation, e.g. collecting geochronological timings.

Overall, using data to refine the parameter space can improve ice sheet modelling twofold. First, parameter ranges can be isolated and focussed on so that further simulations can most effectively explore the relevant parameter space. Secondly, if past ice sheets can be modelled effectively, uncertainty in future projections can be reduced.

5.5 Summary

In this Chapter, I have created an emulator that predicts 175 out of 182 LALA scores correctly within error for the initial ensemble. Then, using a history matching process, untested parameter input sets were identified and predicted to score highly with LALA. The parameter sets that are thought to score well against the flow direction are then plotted to see the likelihood of the parameter values within the range to update the sampling procedure. This feeds into Chapter 6, where the new parameter distributions will be sampled, and a flow calibrated ensemble will be run, looking to improve the LALA scores obtained.

Notation for Chapter 5

Symbol	Description
$\boldsymbol{\varepsilon}$	Vector of errors on the training data
$f(\cdot)$	True underlying function
$h(\cdot)$	Output of optimised posterior distribution
$I(\cdot)$	Implausibility measure
$k(\cdot,\cdot)$	Kernel function
l	Kernel hyperparameter determining the wavelength of samples
$\boldsymbol{\mu}$	Mean vector
Σ	Covariance matrix
σ_f^2	Kernel hyperparameter determining the amplitude of the samples
σ_n^2	Variance of the observational error
V_c	Uncertainty associated with the emulator
V_m	Uncertainty associated with model discrepancy
V_o	Uncertainty associated with observations
V_s	Uncertainty associated with ensemble variability
X'	Input points associated with the training data
X	Test points
$\boldsymbol{y}$	Training data

Chapter 6

Flow calibrated model simulations and discussion

6.1 Introduction

So far, I have created a model-data comparison tool to calculate how likely a model simulation is to explain the observed flow directions in Chapter 3, assessed the sensitivity of the model input parameters to the flow directions in Chapter 4, and coded an emulator to estimate a surface to fill in output gaps in the parameter space and then used history matching to find input parameter sets that predict a high flow direction match in Chapter 5.

In this discussion chapter, I will describe and analyse the results of this new, flow calibrated ensemble. Next, I analyse the difference between the calibrated and the original ensemble; what is different? I then compare the flow calibrated ensemble to ice extent and timings using geomorphological and geochronological evidence and ask if the flow calibrated ensemble has also improved the model-data fit to reconstructed ice extent and timing. Finally, I describe the wider implications of this work and potential future avenues to explore following this thesis.

6.2 Set-up of the flow calibrated simulations

The model set-up for the refined simulations is based on the set-up defined in Chapter 2 with adaptations based on the results from Chapter 4 and Chapter 5. These new flow calibrated simulations have three main changes: changing the range of the flow exponent parameter, reducing the number of parameters, and no longer sampling the remaining parameters uniformly.

The exponent in Glen's flow law has proven to be an important parameter in this model set-up and consistently plays a big role in the fluctuations of the outputs. Unfortunately, higher values of this parameter also cause the simulations to take exponentially longer to complete. Due to time constraints for this study, I reduce the range of this parameter from $[2, 4]$ to $[2, 3]$. From the implausibility measure, the number of simulations estimated to score highly with LALA with a flow exponent between the updated range is over 50%, including a large spike at the lowest end of the range, so there are still many parameter inputs predicted to achieve the score being aimed for even with the space reduction.

Based on the sensitivity analysis performed in Chapter 4, there were 13 parameters deemed to be most important and 7 that would be discarded for the second ensemble (Table 4.2). Compared to the uniform sampling done initially, an improved sampling method using the history matching approach was described in Chapter 5. For the flow calibrated ensemble, the new parameters will be sampled using a maximin Latin hypercube design with the distributions found in Figure 5.17. As there are 13 remaining parameters, 130 simulations were run, using the same ten times the number of parameters rule used previously for the initial ensemble.

6.3 Flow calibrated simulation results

6.3.1 Successful simulations

Of the 130 simulations performed, 68 completed successfully. The remaining 62 simulations failed, either due to isolated pixels growing to be unfeasibly thick and causing the simulation to crash or for the stress balance equations being unable to resolve. A similar but smaller subset of the initial ensemble simulations also failed with the same issues, as discussed in Section 4.3.1. Most of the frequency distributions for each parameter look similar (Figure 6.1) when comparing the successful simulation's parameter inputs to the distributions sampled from in Figure 5.17. The one that looks the most different is the exponent for the sliding law, denoted `q_exponent`, shown in Figure 6.1. Looking at the low end of this parameter range, there seem to be simulations missing with these values. When the value of the `q_exponent` is around zero, the fastest velocities will be calculated from Equation 2.22 and the ice sheet model can crash. If this study were completed again, I would reduce the range of this parameter to have a minimum value larger than zero, as the simulations with the value of the sliding law exponent at the low end either fail or take a very long time to complete.

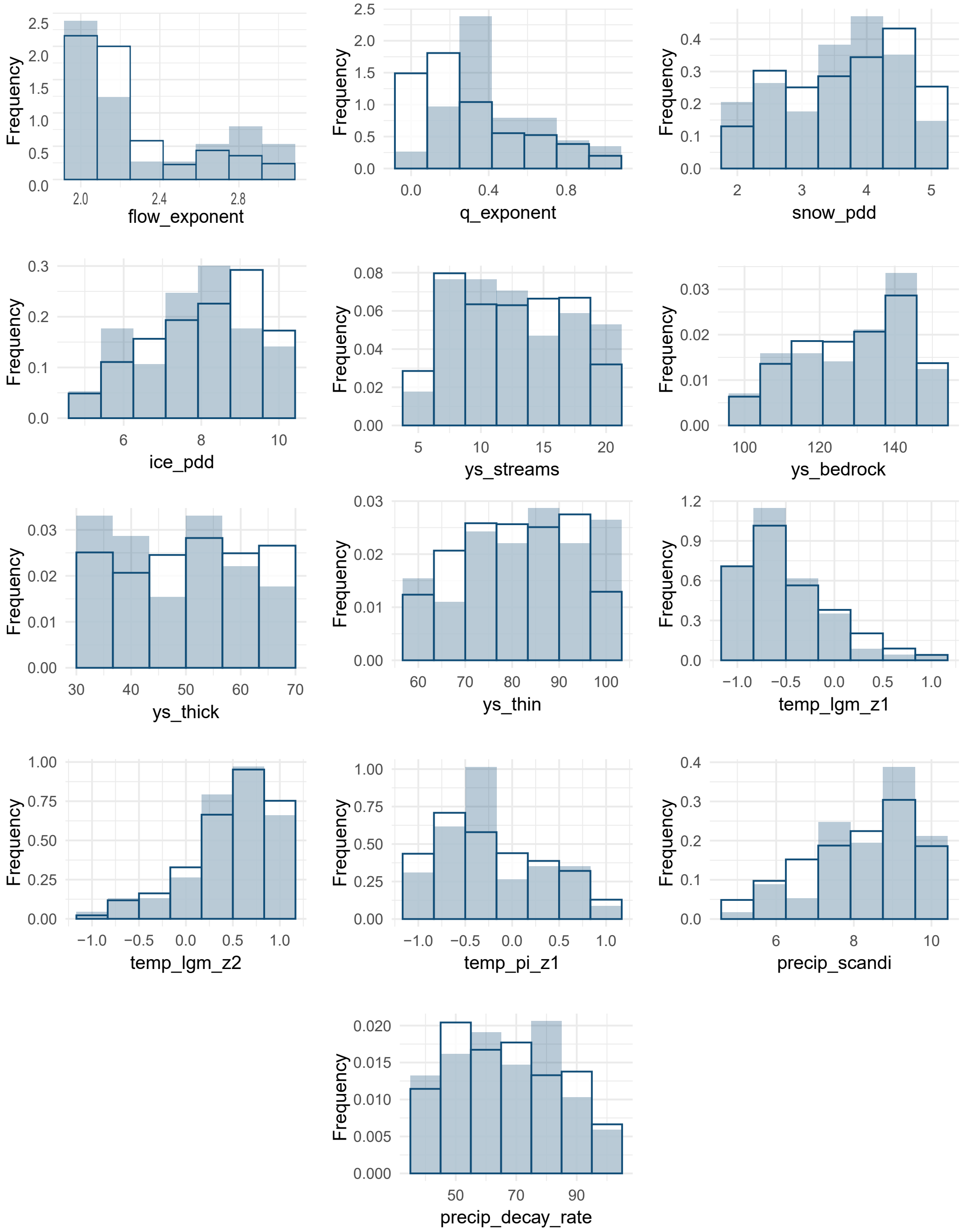

Figure 6.1: Distributions sampled for the flow calibrated ensemble represented by the outlined bars and the successful parameter values from the flow calibrated ensemble shown as blue bars.

6.3.2 Flow calibrated ensemble results

From the 68 successful simulations in the flow calibrated ensemble, summary metrics can be derived to explore overall patterns of the ensemble at different time steps. Figure 6.2 contains five metrics at the five time steps considered in previous chapters. The summary metrics for every simulated one thousand years are given in Appendix B. The input parameter sets for the flow calibrated ensemble are presented in order of their LALA scores from best to worst in Appendix C. The calculated metrics in Figure 6.2 are the percentage of grounded ice, the mean ice thickness, the standard deviation of thickness, the mean velocity and the coefficient of variation for velocity all per grid cell (16×16 km). The coefficient of variance is the ratio between the mean and the standard deviation, and the higher the value, the higher the dispersal from the mean.

- *Grounded ice percentage:* All of the simulations have already joined the BIIS and the SIS by 31 ka and this saddle remains until 11 ka where almost all the simulations have separated into the two ice sheets. The timing of the ice grounding in the SBKIS is more variable, but persists until the end of the majority of simulations. Most of the simulations produce two separate ice masses in the SBKIS region, one in the east and one in the west. The joining of these two ice masses happens in some simulations. In those simulations where joining does happen, this occurs at different time steps. The Baltic Sea, in the flow calibrated simulations, has grounded ice much less often than in the original ensemble. Grounded ice percentages exceeding 50% are found in between the British Isles and Iceland. This is surprising given that the present-day water depths here may point to ice accumulation over the Faroe Islands and/or problems with this aspect of the simulations.

- *Ice thickness:* The area surrounding the southern coast of Norway had consistently thick ice, but with little variance across the simulations. Most of the ice thickness variation occurs off the northern coast of Britain and Norway, where either thick ice forms or no ice forms at all.

- *Ice velocity:* The fastest flowing ice tends to be north of the North Sea but migrates to the SBKIS towards the end of the simulations. As only terrestrial data was used to assess the model-data match, marine areas are likely under-represented and could affect the simulations identified to be the best flow data fit.

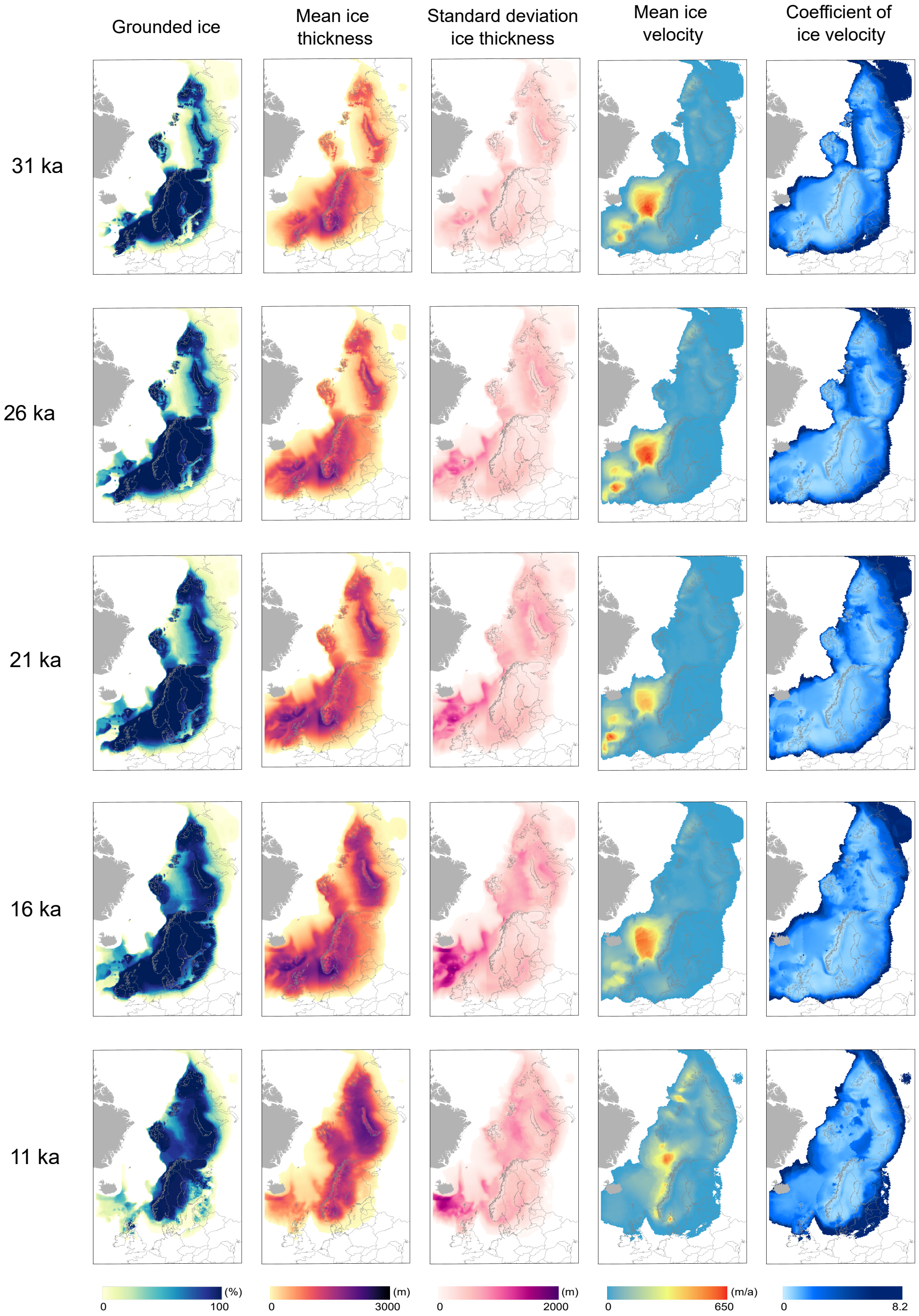

Figure 6.2: Summary variables for all successful simulations in the flow calibrated ensemble at five time steps, 31, 26, 21, 16 and 11 ka. The variables considered are the percentage of grounded ice (%), average ice thickness (m), standard deviation of ice thickness (m), average ice velocity (m/a) and the coefficient of variation of velocity. The horizontal resolution is 16×16 km.

Ice volume variation over time, for all the simulations of the flow calibrated ensemble is shown in Figure 6.3, generally reaching a maximum at around 13 ka. This is later than often cited (e.g. Patton et al., 2016), due to the timing of the modelled maximum SBKIS coming much later than evidence suggests (Hughes et al., 2016). The ice volume for the best-performing simulation according to LALA is shown in green in Figure 6.3 and is approximately in the middle of the minimum and maximum simulation between 40 and 20 ka. Between 20 and 13 ka the best-performing simulation is closer to the top of the ice volume range but for the remainder of the time returns to the middle of the simulations. The overall maximum ice volume across the whole ensemble occurs at approximately 13 ka where all three ice sheets are present. The dip that occurs after this is when the BIIS deglaciates. A second ensemble wide ice volume peak is reached at around 10 ka, where the SIS readvances and the SBKIS fully ground across the Barents Sea. The remaining peaks shown at the end of the time period are individual ensemble members that grow the SBKIS late in the simulation.

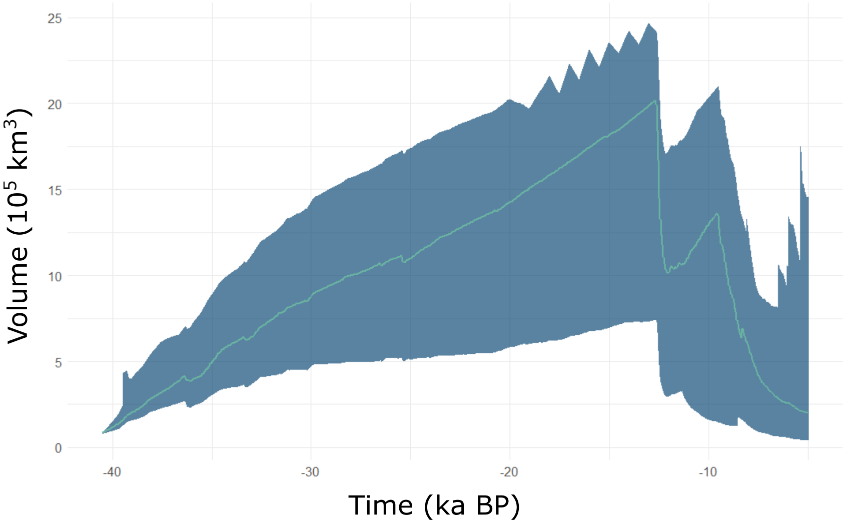

Figure 6.3: Ice volume variation over time for the whole grounded Eurasian Ice Sheet Complex from the flow calibrated simulations. The green line represents the best scoring LALA simulation, and the solid blue represents variation due to different simulations.

6.4 Discussion

6.4.1 Did the flow optimisation routine improve LALA scores?

Plotting the LALA scores from the initial ensemble and comparing them to the scores obtained from the second wave (Figure 6.4), the scores from the second wave seem to have been improved from the original results. To formally confirm that the scores from the second wave have been statistically significantly improved by the processes implemented in the previous chapters, I perform a Student's *t*-test. The Student's *t*-test is a hypothesis test used to determine if two samples have statistically significantly different means.

The null hypothesis, H_0, and the alternative hypothesis, H_1, are stated below

$$H_0 : \bar{x}_1 = \bar{x}_2 \tag{6.1}$$

$$H_1 : \bar{x}_1 \neq \bar{x}_2 \tag{6.2}$$

where $\bar{x}_1 = -11.75$ is the mean of the scores from the initial ensemble and $\bar{x}_2 = -10.90$ is the mean of the scores from the second ensemble. The assumption when using this hypothesis test is that both samples follow a Gaussian distribution. Scores from the initial ensemble, shown in purple in Figure 6.4, visually look to be normally distributed. To check the second ensemble also conforms to this assumption and confirm that the initial ensemble does as well, a Shapiro-Wilk normality test is performed. The Shapiro-Wilk normality test evaluates the null hypothesis that a sample comes from a Gaussian distribution. When performing this test on the initial ensemble and second ensemble, the p-values are both greater than 0.05, so there is no evidence to suggest the samples are not from a normal distribution. Hence, the Student's *t*-test is valid and can be continued. The test statistic needed to test the hypotheses is

$$t = \frac{\bar{x}_1 - \bar{x}_2}{\sqrt{\frac{s_1^2}{n_1} + \frac{s_2^2}{n_2}}} \tag{6.3}$$

where $s_1 = 0.55$ and $s_2 = 0.46$ are the standard errors and $n_1 = 182$ and $n_2 = 62$ are the number of simulations both for the initial and second ensembles, respectively. The degrees of freedom, denoted *df*, needed to determine the distribution the test statistic is to be compared to is

$$df = \frac{(s_1^2 + s_2^2)^2}{\frac{s_1^4}{n_1 - 1} + \frac{s_2^4}{n_2 - 1}}. \tag{6.4}$$

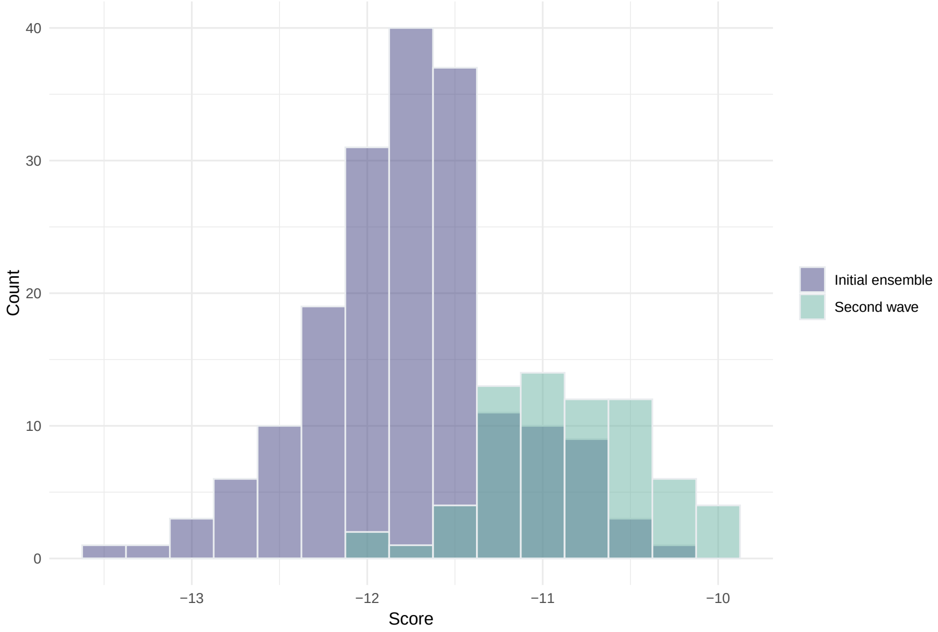

Figure 6.4: Comparison of the scores from LALA for the initial ensemble, in purple, and the second ensemble, in green.

Substituting the derived values into Equation 6.3, the test statistic is calculated to be $t = -12.77$. Comparing this value to a Student's t-distribution with 142.08 degrees-of-freedom (calculated using Equation 6.4), the p-value can be obtained and is 1.67×10^{-22}. Hence, the null hypothesis can be rejected, and there is strong evidence to show the second ensemble has a statistically significantly greater mean than the initial ensemble. Therefore, the flow optimisation has significantly improved the LALA scores.

Visually comparing the model-data fit per grid cell, as shown in Figure 6.5, the flow optimised simulations have improved some areas of fit, but had the opposite effect in others. Areas 1 and 2 are less well matched in the flow calibrated ensemble, but not significantly. Area 1 is a small area and had a bad fit in the initial simulations already, this poor match has extended further to the north in the calibrated ensemble. The same has occurred in area 2, where in the initial ensemble the poor model-data match fills only the centre of the circled area (Figure 6.4a), but model-data match in area 2 of the calibrated ensemble fills more of the circle (Figure 6.4b). These two areas in the north of the domain are presumably, due to spatial proximity, affected by the SBKIS and the SIS, and as the simulations are only calibrated to the SIS, a worse estimation of the SBKIS could be affecting these matches. The change in the SBKIS between the two ensembles is discussed further in the sections below (Section 6.4.2 and Section 6.4.4). Areas 3 and 4 have an improved fit in the flow calibrated ensemble. The spatial patterns of good and bad model-data match are approximately the

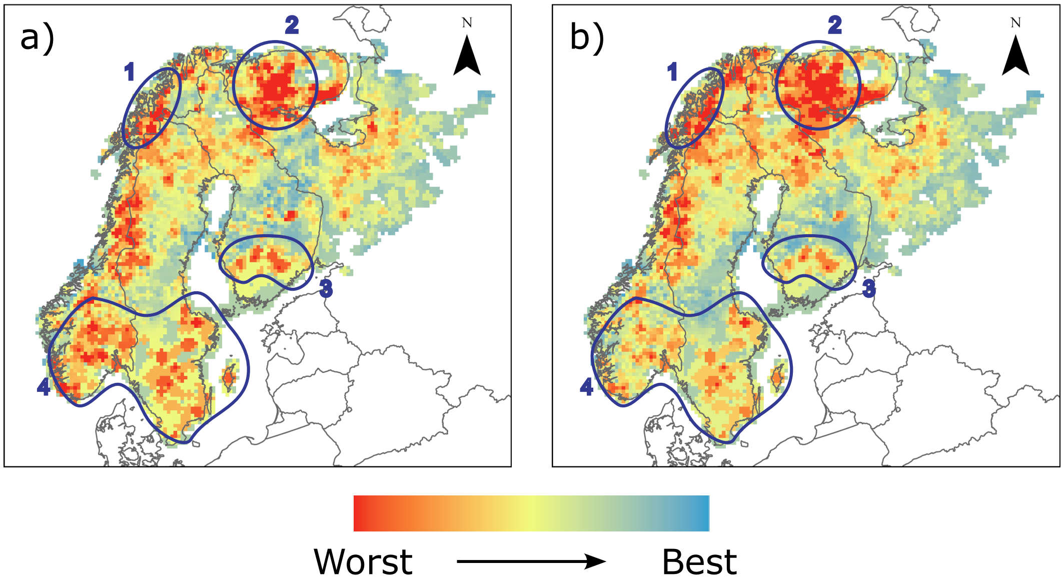

Figure 6.5: Comparison of LALA scores per grid cell from a) the initial ensemble and b) the flow calibrated ensemble. The circled areas are areas where a considerable difference between the ensemble scores are identified. Areas 1 and 2 have a worse fit in the flow calibrated ensemble compared to the initial ensemble and areas 3 and 4 have an improved fit.

same in the two ensembles (in areas 3 and 4), but in the flow calibrated ensemble, the match has improved. The area in the south of Norway and Sweden, area 4, is the largest area and has improved the most between the ensembles. The scores across the remainder of the domain are approximately the same. As the areas of improvement are larger than the areas of decreased model-data match, visually there seems to be an overall improved match.

6.4.2 How well does the flow calibrated ensemble explain the extent and timing?

Figure 6.6 shows the percentage of grounded ice at 21 ka across all ensemble members of the two sets of simulations: the initial ensemble and the flow calibrated ensemble. Comparing the two results, the eastern area of the SBKIS has ice cover less often in the flow calibrated ensemble, which more closely matches the hypothesised extent, than in the initial ensemble. The middle of the Barents Sea is also less often fully grounded at this time. Four islands/archipelagos, Svalbard, Novaya Zemlya, Zemyla and Severnaya Zemyla, (locations shown in Figure 2.7) are consistently covered in grounded ice in both ensembles. The latter, Severnaya Zemyla, is not contained in the reconstructed extent of the EISC in Hughes et al. (2016) but Patton et al. (2016) does simulate small ice caps over the islands. The amount

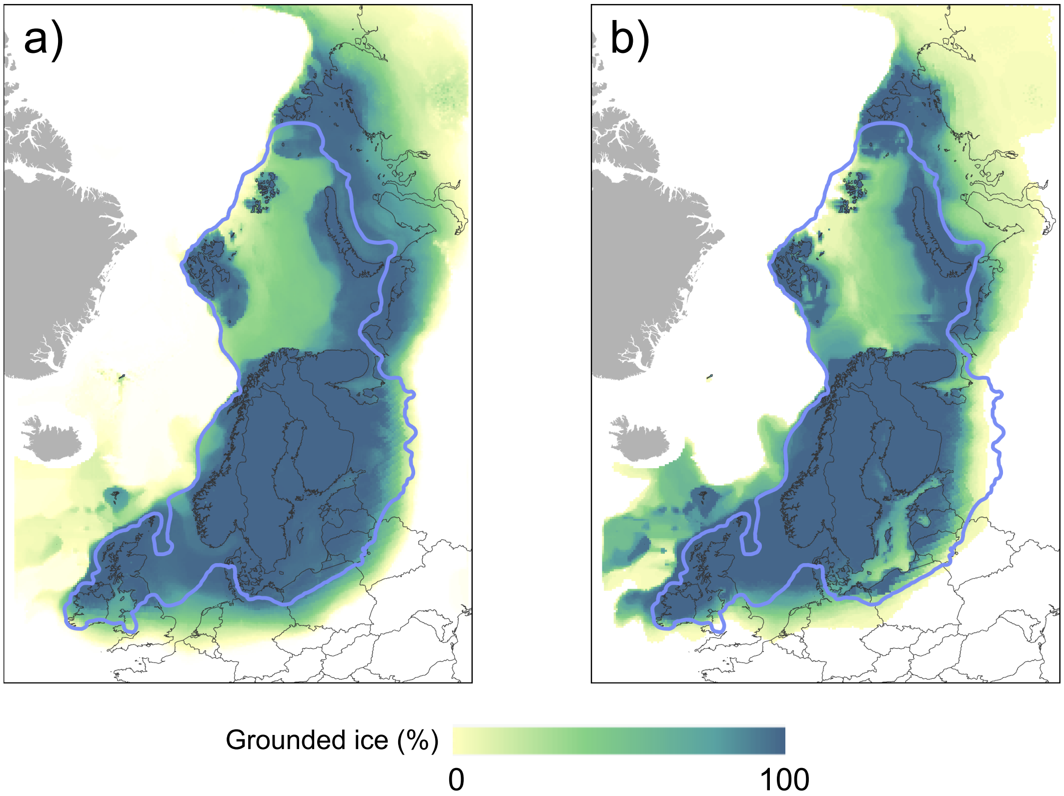

Figure 6.6: The percentage of grounded ice over all the ensemble members for a) the initial ensemble and b) the second wave of flow calibrated simulations at 21 ka. The most credible ice extent at 21 ka inferred from the observational record in Hughes et al. (2016) is shown in purple.

of data available to constrain the SBKIS is limited, so the predicted timings and extent have low confidence (Hughes et al., 2016) and hence, no significant weight should be put on aiming to match the extent at this time.

The flow calibrated ensemble, Figure 6.6b, better fits the southern margin of Fennoscandia and Britain, but the join between the BIIS and the SIS continues to grow further south than the data would suggest. The northern part where the two ice sheets join regularly matches the derived extent. There is a cut-out in the ice sheet join that never fits with either of the ensembles, but once again, there is limited evidence for this.

In the flow calibrated ensemble, (Figure 6.6b) ice is consistently growing out past the reconstructed ice margin off the west coast of Ireland. A recent study (Clark et al., 2022) has found evidence that this area, Porcupine Bank (location shown in Figure 2.7), had grounded ice, differing from the reconstruction in Hughes et al. (2016). It is interesting that the flow optimised ensemble has consistently grown ice over this area, as the initial ensemble did not (Figure 6.6a). Ice is also more likely to ground off the northern coast of

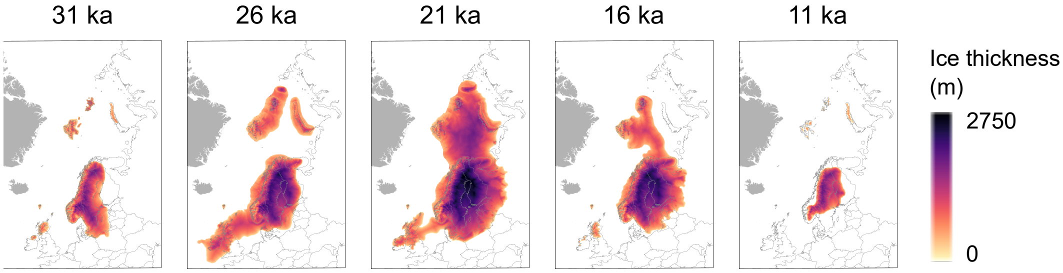

Figure 6.7: Ice thickness at five time steps from models produced in Bradley et al. (2023).

Scotland and Norway. Potentially, the prevalence of extra ice grounding in these areas may be related. It seems that the flow calibrated ensemble has shifted the ice covering the BIIS and SIS further north. This is highlighted most prominently in the southern BIIS margin which now more closely matches the predicted extent, as well as the northern extent in Norway consistently fills the predicted extent but struggles in the south eastern portion of the SIS. This change could be a result of the new sampled distribution of the precipitation gradient over Scandinavia, see Figure 6.1. The updated parameter distribution favours a larger precipitation reduction (Figure 2.11). Unexpectedly, after optimising the parameter space, the Baltic Sea has gone from almost always having grounded ice at 21 ka to filling it much less often. The flow calibrated ensemble also occasionally misses parts of the Gulf of Bothnia. This could also be due to the same reason as hypothesised above, but seems unlikely due to not being very deep compared to the surrounding grounded areas (only around 150 m). It is surprising though, given the initial ensemble always grounded ice in these regions.

6.4.3 Does the best performing LALA simulation conform to empirical reconstruction and to other modelling studies?

Reconstructing ice thickness based on empirical evidence is limited (e.g. Whitehouse, Bentley and Le Brocq, 2012), and there are minimal examples for the EISC. Bradley et al. (2023) used the ICESHEET model (Gowan et al., 2016), which is a perfectly plastic numerical model, to simulate the EISC. The aim of this study was to simulate plausible ice thickness, judged against sea level constraints and using the Hughes et al. (2016) reconstructed ice extents and basal shear strength data from Clark et al. (2022). The modelled outputs are in Figure 6.7. Comparing my simulations to the extent of this model is not useful, as the extents of the Bradley et al. (2023) models are, by design, exactly the same as the Hughes et al. (2016) extents. However, comparing the thicknesses has some merit. The Bradley et al. (2023) model has a maximum thickness of approximately 2750 m (Figure 6.7) reached

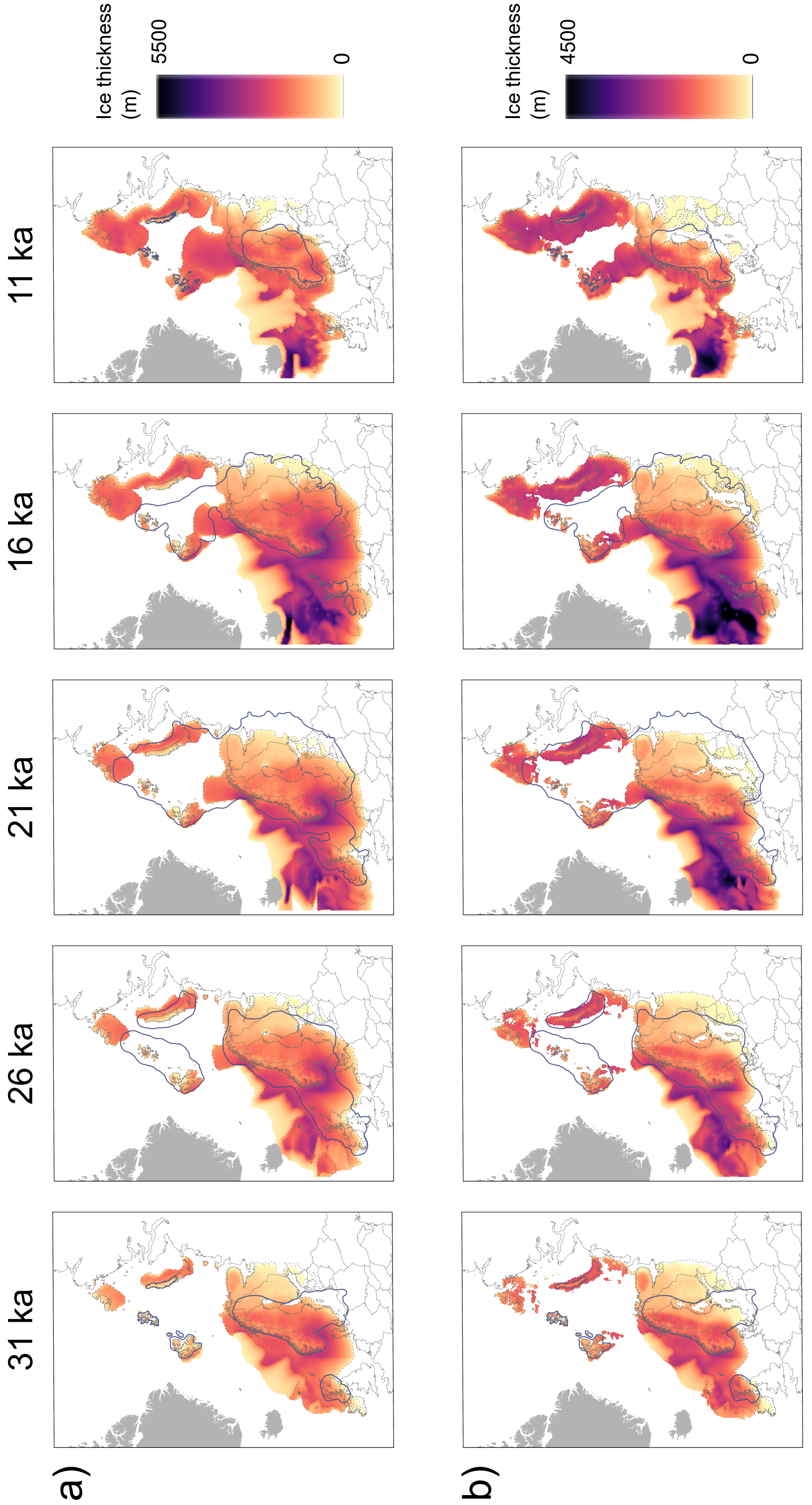

Figure 6.8: The best-performing simulations according to LALA when scored using a) linkages over Fennoscandia and b) linkages over Fennoscandia combined with flowsets over Britain and Ireland. Estimated ice extents according to Hughes et al. (2016) are shown in blue for each time step.

over Norway and Sweden. My best simulation according to LALA (Figure 6.8a) has a much larger maximum thickness at around 5500 m but achieves this off the north coast of Britain and Ireland. This is a very thick estimation and higher even than the known thickness estimated from the ICE-5G glacial isostatic adjustments model (Peltier, 2004), which predicts a maximum thickness of 2500 m over the SIS. As noted earlier, my modelled maximum ice thickness is in deep water beyond the empirically defined limits and so is either suspect or the empirical estimates are wrong. The thickness in my simulation at the same point and time (21 ka) has a maximum of only 1600 m, much lower than the estimated 2750 m from Bradley et al. (2023). It is not unexpected that my flow optimised modelling, with no sea level constraints, differs from the most recent and arguably the best estimate of ice thickness from Bradley et al. (2023) because, of course, this latter model was specifically optimised for ice thickness to match sea level records. It raises the serious question of whether my simulations grow too much ice and why this would be the case. Potentially, the temperature input, found to have a large impact on the variance of the LALA scores in Chapter 4 could have contributed to this. Clason et al. (2014) found success when using the NGRIP core for the glacial index approach for the climate forcing, whereas in this study I used the GRIP core (see Section 2.3.1). This may be something to explore if the simulations are tuned to better fit other sources of empirical evidence.

The aim of the complementary studies Patton et al. (2016) and Patton et al. (2017) was to find an optimal reconstruction compared to multiple forms of evidence by tuning the parameter space. Again, this contrasts with my study, which focused on improving the flow direction model-data match. However, the modelled ice extent from Patton et al. (2017, 2016) is useful to compare to my flow optimised model as their model is not forced to conform to observations, unlike Bradley et al. (2023). Interestingly, in my best scoring simulation, the modelled ice sheet is too extensive and thick, but the modelling performed by Patton et al. (2017, 2016) is not extensive enough. In these studies, the modelling is tuned to attempt to conform to ice extents, but it is specifically noted that there was a major problem over the North Sea where the model failed to sufficiently glaciate. When they tuned the model to try and make it fit over the North Sea, the resulting ice extent and thickness were too great. It thus seems, when considering both my simulation and that of Patton et al. (2017, 2016), that there exists a problem in modelling the marine sectors of the EISC, notably over the North Sea and adjacent shelves in deeper waters.

6.4.4 Does improving simulations of the flow of the Scandinavian Ice Sheet lead to simulations of neighbouring ice sheets that better recreate their empirical ice extents?

The evidence used to score against past flow directions covers Fennoscandia, but the domain of the model simulations covers the whole of the EISC. If there is a consistent set of flow parameters for ice sheet modelling, perhaps improving flow of the SIS might also improve simulations of the BIIS and SKBIS. Figure 6.8a contains the simulated ice thickness across five time steps for the best-performing simulation according to LALA scoring with the Fennoscandian linkages. This simulation has grounded ice exceeding the northern margin of the ice sheet complex throughout, which has been discussed in Section 6.4.3. At 31 ka, the ice sheet over Britain generally matches the reconstructed ice extent, with some ice extending past the reconstructed extent and into Northern Ireland. The match to the reconstructed SBKIS extent (at 31 ka) is a good fit over Svalbard and Zemyla with ice extending too far East over Novaya Zemyla and ice covering Severnaya Zemyla which is not reconstructed at all (see Figure 2.7 for location of named areas). The three ice sheets making up the EISC are empirically reconstructed to be completely independent at this time step, but as found in the majority of simulations (Figure 6.2) the BIIS and SIS join early in this best fit simulation (Figure 6.8a). This joining occuring too early in the simulations suggests that the climate input is not being represented in the model quite correctly. The precipitation input change, discussed in Section 2.4.2, greatly improved the southern margin of the EISC over land but may not have worked effectively in marine-based areas such as the North Sea. areas. In future, the joins between the boxes indicating the precipitation gradient used could be smoothed out (Figure 2.10), to investigate whether this had a role in the early join between the SIS and BIIS.

Five thousand years later, at 26 ka, the modelled ice over the BIIS is smaller than the reconstruction (Figure 6.8a). The western simulated ice extent does not quite stretch far enough, and the ice predicted over Wales is completely missing (Clark et al., 2022). The eastern sector of the SBKIS is almost completely missing and the western sector appears to have approximately the correct area of ice, but is shifted too far west. The time step at 21 ka is similar, as in there is still missing ice over Wales and a lot of ice missing over the Barents Sea (Jakobsson et al., 2014; Newton and Huuse, 2017; Winsborrow et al., 2010). These areas of missing ice contrast significantly to the results of the initial ensemble, where the ice was often far too south and west (Figure 4.2).

LALA penalises model simulations for growing too large, and these results seem to show this aspect being relatively successful. Unfortunately, the flow calibrated model fails to reproduce the full reconstructed extent of the SBKIS (Jakobsson et al., 2014; Newton and

Huuse, 2017; Winsborrow et al., 2010), as was achieved, albeit too large, in the initial ensemble (Figure 6.6). Perhaps this work suffers from the lack of evidence over SBKIS, as in the sensitivity analysis, parameters that control this ice sheet may have been removed. There is little chance for new evidence over the SBKIS as a large area of this is in Russian controlled waters. One potential workaround for this is to use estimated flow directions from reconstructions to reduce the weighting of the flow over SIS.

So far, the linkages over Fennoscandia have been considered when scoring model simulations with LALA. To see if the inclusion of the flow data currently available over Britain and Ireland improves the simulated ice extent, the flowsets, as described in Section 3.5, are compared to the flow calibrated ensemble. As both outputs from LALA are log-likelihoods, they can be combined by summing them. The scores from the Fennoscandian flow linkages range approximately between $[-120{,}000, -100{,}000]$ whilst the scores over Britain and Ireland, from flowsets are much smaller, approximately between $[-1000, -900]$, due to less data points being scored. If the scores were summed in their current state, the SIS score would be weighted more greatly than the score for the BIIS. Hence, before the log-likelihoods are summed, the scores are scaled to be in the same range. Figure 6.8b shows the simulated ice thickness across the same time steps for the best-performing simulation when combining the two LALA scores, the score for the Fennoscandian linkages and flowsets over the BIIS.

When scoring the flow directions with the flowsets over the BIIS, the southern margin of the join between the BIIS and SIS conforms more to the empirical reconstruction. The addition of the flowsets seems to have improved the fit of the SIS southern margin, which is suspected to be due to the ice sheet coalescence between the BIIS and SIS having reduced compared to the best fitting simulation when just using the Fennoscandian linkages. The ice volume reduction in this area may make it less likely for the ice to sprawl as far south as it previously had. Also potentially due to the ice volume reduction, the maximum ice thickness in the best-performing simulation using both BIIS and SIS data is around 1000 m less that just with the SIS flow data. This reduction in ice thickness brings my simulation (Figure 6.8b) closer to the models in Bradley et al. (2023).

Figure 6.8a shows a slightly more successfully simulated SBKIS compared to the empirical reconstruction, in the sense that grounded ice covers more of the Barents Sea compared to Figure 6.8b, but as seen across all the simulations (Figure 6.2) the timing of this growth does not match the empirical data. Another area that seems to have been captured with the Fennoscandian linkages but not when including the BIIS flowsets is both the Gulf of Bothnia and the Baltic Sea. With just the linkages, the best-performing simulation has grounded ice across both of these regions, which is suggested by the observational data, but when including the flowsets, ice never grows over the Baltic Sea and is patchy over the Gulf of Bothnia. Thus, improving the spatial distribution of data to include the BIIS has reduced fidelity to the data over the SIS.

So, does including the British-Irish flowsets with the Fennoscandian linkages improve the overall fit of the Eurasian Ice Sheet Complex? The answer is probably somewhat. However, this is an imperfect experiment because I combined data that was not entirely consistent across the domain; it varied according to the type and resolution of the data as well as the protocol for summarising the glacial lineations. The flow data over the SIS are linkages and cover almost the whole of Fennoscandia (Figure 1.2) whereas the data over Britain consists of single points taken from the centre of flowsets (Figure 3.9). However, there are some improvements when including the BIIS flowsets. Areas are improved when including the flowsets, such as the margin south of Norway and Sweden, but other areas are missed, such as the Gulf of Bothnia and the Baltic Sea. The timing and extent of the SBKIS does not improve but are not radically different. It would be interesting to include flow evidence from the Barents Sea area; however evidence in this area is sparse (e.g. Jakobsson et al., 2014; Newton and Huuse, 2017; Winsborrow et al., 2010). I suspect that the simulated southern ice margin for the best-performing simulation with both types of data (Figure 6.8b) better conforms to the reconstruction because the data over the BIIS is included. The worse fit in the Barents Sea seems to potentially have a more random element: the tool found the best simulation for the BIIS and SIS areas, but as the model rarely fits the SBKIS extent in any simulation it is hard to determine if the change in the choice of simulation has any regard to this ice sheet.

6.5 Implications for reconstructing and simulating past ice sheets

In this thesis, I have shown that the workflow of performing a sensitivity analysis to reduce the dimensionality of the parameter space, emulating and history matching with evidence of ice flow to update the parameter distributions to sample from, and performing another ensemble is an effective method to find simulations with improved model-data matches. Aside from the methodological developments, the most important aspect for any study applying this or a similar workflow is the question to be answered by the modelling study. I have improved the ensemble scores when comparing to flow direction over the SIS, and some other model-data matches have been improved surrounding ice extents and timing, but some areas have been made worse. The manual tuning of parameters becomes less important when following this methodology compared to previous studies (e.g. Patton et al., 2017, 2016), but comparing to other forms of evidence is still imperative as considering flow direction alone does not resolve all pieces of evidence.

Whilst this workflow can optimise the parameter inputs, the initial model setup is still vital. If the model setup is not correct, there is only so far this workflow can succeed. Initial testing can help inform if an aspect of the model design is producing completely unrealistic simulations, and also the extent to which changing the parameters are causing variation in the output of the simulations. In Chapter 2, I demonstrated this with a smaller ensemble that was not varying the extent of the southern margin (Figure 2.9). If I had continued the workflow with this setup, the results would not have been as clear as the precipitation input was overriding all other variance in the output.

Findings could suggest where new evidence is most needed to reduce uncertainty in the model to improve reconstructions of palaeo-ice sheets. Domain areas where evidence is hard to find, either in regions where evidence is less likely to form (in oceanic areas) or for geopolitical reasons are difficult to obtain (like Russia), can benefit from using model results to inform the reconstruction. For example, the ice shelves and grounded ice off the northern coast of Britain and Norway (Figure 6.6b) are not usually hypothesised. This could be investigated further to ascertain if such grounded ice could have actually existed here or whether the model is at fault. At this point in the study, concrete conclusions about ice shelves cannot be made due to the lack of comparison to marine landforms, but is an interesting line of enquiry for future studies. Also, if a model is optimised by the flow, more confidence can be given to the flow directions modelled in areas lacking evidence for use in reconstructions.

Palaeo-proxies for the extent of ice shelves are limited (Dowdeswell, Canals, Jakobsson, Todd, Dowdeswell and Hogan, 2016; Smith et al., 2019). Numerical modelling is one avenue to explore the potential past ice shelf configurations. The ice shelves estimated by this modelling study are extensive and regularly grounded with thick ice. Evidence and numerical modelling studies demonstrate that during the penultimate glaciation ice shelves could ground in ocean depths up to around 1280 m (Gasson et al., 2018). For the last glacial cycle, few ice shelves have been hypothesised (although see Ely et al. (2024)). My modelling predicts ice shelves could have been extensive, radiating out from the continental shelf break and grounding on high points of the sea floor (Figure 6.8a). This may be due to model deficiencies in ice-ocean interactions or may serve as an interesting hypothesis for future data-based investigations.

6.6 Potential avenues for future work

In this thesis, I have developed a procedure for scoring model simulations against flow direction. Now that a model which recreates flow direction can be made with this procedure, the outputs from the model could be useful for other applications. If the flow geometry is correct, model simulations can be used to explore the movement of erratics and minerals in Eurasia. Using the direction of ice flow and the geological makeup of the bed, the transportation and final location of erratics and minerals could be located (Hooke et al., 2013), which could be useful for future mineral prospecting work.

I have focussed on using a wealth of directional data available over the EISC. However, there is a range of other constraints that could be used to validate and improve model simulations, e.g. moraines, sea level data and geochronological evidence. In order to use this data effectively in the same system, better model-data comparison tools are required. Creating a model-data comparison tool for geochronological data needs careful consideration. A large amount of expert judgement is required, both when deciding the context a date gives (ice free, ice marginal etc) but also how reliable each piece of data is (Small et al., 2017). There are also lots of different methods for determining the age of the geochronological evidence, such as radiocarbon, optical stimulated luminescence or cosmogenic nuclides. Combining all of these different contexts and methods is not trivial. If Bayesian model-data comparison tools could be formed for all, or some, of the other pieces of evidence, they could be easily combined by multiplying the likelihoods together to achieve one overall score which could then be emulated. However, the variety of settings and geochronological techniques from which ages are derived makes assigning a likelihood to a geochronological constraint a non-trivial task.

The same system as performed in this thesis could be performed on modelling other ice sheets. The Laurentide Ice Sheet is another palaeo-ice sheet with a large amount of flow data (Dulfer et al., 2023; Stoker et al., 2024). The workflow described in this thesis could be replicated with the Laurentide Ice Sheet or other palaeo-ice sheets with extensive flow data. The Antarctic Ice Sheet also has observations of past ice flow (e.g. Anderson et al., 2014). The ability to correctly simulate the past dynamics of ice sheets is important when aiming to project the simulations into the future. Running an ice sheet from the past before projecting into the future is called creating a spin-up (e.g. Fyke et al., 2014; Saito et al., 2016). The spin-up state of a contemporary ice sheet model has implications for projections of sea level rise (Aschwanden et al., 2013). The approach described in this thesis could be an effective way to create spin-ups before performing projections. For example, LALA could be used directly using velocity data over the Antarctic (Rignot et al., 2017) and Greenland (Joughin et al., 2015) ice sheets, using the directions of the speeds over the ice sheet as a proxy to the landforms used in the applications of LALA over the SIS and the BIIS. This seems to be an important area of study: quantifying how correctly replicating the history of an ice sheet can reduce the uncertainty of future projections.

6.7 Summary

In this chapter, I discussed the main findings of my work, compared my results to investigations in the literature, and explored wider implications and future extensions following this thesis. I have shown that the workflow used throughout my thesis has improved the model-data match to flow directions. I have compared my best-performing simulations to other modelling studies as well as to other forms of observational data, i.e. extent and timing. I have discussed the implications of my work regarding the reconstruction and simulation of palaeo-ice sheets, and future uses for the methods in this thesis.

Chapter 7

Summary and conclusions

The aim of my thesis, stated in Chapter 1, was to 'combine ice sheet modelling with Bayesian inference to simulate the flow of the last Scandinavian Ice Sheet'. I had several objectives to complete in order to achieve this.

Objective 1: Create a statistically rigorous model-data comparison tool to compare model-simulated and inferred past ice flow direction

I conceptualised and created the Likelihood of Accordant Lineations Analysis (LALA) tool to compare observed flow geometry from glacial landforms with simulated flow directions in a statistically rigorous way (Chapter 3). The tool expands on a previous attempt at model-data comparison tools for flow direction, the Automated Flow and Directional Analysis tool (AFDA) by Li et al. (2007), and has two main advantages. First, it tackles the comparison of flow directions in a more statistically robust manner, and second, it produces a continuous output score rather than the binary yes or no fit produced by AFDA. This latter point was essential because such a continuous quantification of fit permits the application of Bayesian inference methods, such as emulation, to ice sheet modelling. LALA was tested and applied to the British-Irish Ice Sheet (BIIS) (Section 3.5) using published flowsets to demonstrate proof of concept and has now been published in Archer et al. (2023). The tool picked out the best and the worst simulations from a previously run ice sheet model ensemble of the British-Irish Ice Sheet (Clark et al., 2022). When compared to a reconstruction of the ice extent at 21 ka (Hughes et al., 2016), the best-performing simulation, according to LALA, was found to better match the reconstruction compared to the worst-performing simulation. In this case, flow optimising significantly improved the overall ice sheet simulation. Whilst LALA provides a step forward in statistically comparing observed and modelled flow directions, there are still limitations and avenues for future work, such as not accounting for cross-cutting relationships. Cross-cuts provide relative timings of past ice flow directions and would be useful extra information to include in future versions of LALA.

Objective 2: Run a perturbed ensemble of simulations of the ice sheet complex using the Parallel Ice Sheet Model

I tested and re-designed a model setup over 40 to 5 ka across a large domain over Eurasia, using the Parallel Ice Sheet Model. Twenty parameters were identified as important for varying within an ensemble across categories such as flow, calving, temperature, precipitation, and sliding. Using this setup, I ran a 200 member perturbed parameter ensemble, following the $10p$ rule, and using a maximin Latin hypercube design to ensure the largest exploration of the parameter space possible in a small number of simulations. Of the 200 model simulations, 18 of these failed due to stress balances being unresolved numerically. This seems to occur when the basal shear stress power law exponent had a value of around 0, so future work should adjust the initial constraints of this parameter to ensure the whole ensemble is completed.

Objective 3: Complete a sensitivity analysis to determine which model input parameters are the most important for influencing ice flow directions judged against empirical observations of flow. Explore and determine which parameters can be discarded to reduce the dimensionality of the parameter space

Using the output from the initial ensemble in Objective 2, each simulation was scored against observations using the LALA tool. I then performed a sensitivity analysis using generalised additive models, which is a variance-based sensitivity analysis that can calculate main effect indices (the contribution to the output variance by each input parameter) as well as the pairwise interaction effects (the contribution to the output variance by two parameters working in combination). The results obtained from the analysis were used to reduce the parameter input space from 20 dimensions down to just 13 (Chapter 4) by determining the least important parameters in explaining ice flow directions and other metrics on ice volume, ice shelves and velocity. The exponent for the flow law was consistently picked out as being the most important parameter affecting four different model outputs, concerning ice volume, ice shelves, ice velocity and LALA scores. Conversely, the calving parameter was found to have almost no effect on any of the four metrics considered. Presumably, this is an artefact of optimising only to terrestrial landforms and omitting marine data. Including marine data could be an interesting line of research for future work.

Objective 4: Use a Gaussian process emulator to optimise the parameter sampling design and identify model simulations that will better explain the documented flow geometries

In Chapter 5, I built a Gaussian process emulator and tested different kernels and prior means to find a prior distribution that would best predict the calculated LALA scores (obtained in Chapter 4 and shown in full in Appendix A). To test the efficacy of the emulator, I used leave-one-out-validation, where I systematically removed one input parameter set from the dataset and used the emulator to predict the remaining results. The best prior distribution I found predicted 175 out of 182 scores correctly within error (Figure 5.15) and used a Matérn kernel with a linear prior mean. Then, using history matching, I identified untested parameter inputs that should produce high LALA scores. By using these non-implausible parameter sets, I updated the sampling distributions from the uniform sampling utilised in the initial ensemble (Section 2.5.3) to match the distributions shown in Figure 5.17. By using this emulation method, subsequent ensembles were found to have an improved chance of simulating higher scores of LALA than the initial ensemble. This both demonstrates the novelty of this approach using observed flow directions in ice sheet modelling and that this method increases the chance of building improved simulations regarding flow geometry. Further work could be done to investigate reducing the prediction errors in the leave-one-out validation to improve the accuracy of the emulation and history matching process.

Objective 5: Run new simulations to find an optimal model to fit the collated data on ice flow

Combining the results from Chapter 4, that reduced the input parameter space, and those in Chapter 5, that flow calibrated the distributions for parameters to be sampled, all using the new model-data comparison tool from Chapter 3, a new ensemble was designed. This ensemble used 13 parameters and so 130 simulations were attempted. Of those, 68 simulations were completed. I demonstrated statistically that the flow optimised ensemble was a significant improvement in the model-data match scoring compared to the initial ensemble that did not consider flow directions. Thus, I achieved my aim of using ice sheet modelling and Bayesian inference in tandem to find simulations that best simulate the past flow geometry of the last Eurasian Ice Sheet Complex. Whilst the flow direction model-data match has been improved, the extent and timing do not match the available data. More work is needed to include these data into the calibration process, aiming for a numerical model set-up optimised to fit all available strands of evidence.

7.1 Wider context and further work

For many decades, simulations of palaeo-ice sheets by ice sheet models have been entirely separate investigations from those that reconstruct such palaeo-ice sheets by piecing together the empirical observational record of their activity. More recently, specific tools have been developed to quantitatively compare and score aspects of model simulations to the empirically reconstructed behaviour. This has mostly been achieved for ice extent and variations over time (Li et al., 2008), for comparisons of ice thickness against sea level observations (Bradley et al., 2023; Peltier, 2004) and with initial forays into comparing model simulations against observations of palaeo-ice flow (Ely et al., 2021; Gandy et al., 2019). Furthermore, some ice sheet modelling investigations have taken a data calibrated approach whereby empirical datasets are used to guide or nudge an ice sheet model simulation to hopefully more correct solutions. Notable examples of these are Tarasov et al. (2012) for the Laurentide Ice Sheet, Whitehouse, Bentley, Milne, King and Thomas (2012) for the Antarctic Ice Sheet, and Clark et al. (2022) and Ely et al. (2024) for the British-Irish Ice Sheet. None of these recent advances have used ice flow in the data calibration modelling workflow. The main achievement of this thesis is in further advancing data modelling interactions, specifically in relation to ice flow geometry.

More specifically, LALA, a statistically rigorous tool for scoring modelled flow directions against the observational landform record has been devised, built, tested and applied. Approaches using Bayesian inference, while widely applied in other fields such as medicine, engineering and computer science (e.g. Borko and Bernick, 1964; Florentin, 1962; Talbot and Harrison Jr, 1966), have now, in this thesis, been applied to ice sheet modelling. This has been achieved via sensitivity analyses to reduce the parameter space, and emulation that seeks to find the model parameter combinations that best explain the observed flow geometry. Creating and simulating a new, flow calibrated ensemble using the optimised parameter sampling scheme found that improved ice sheet simulations could be realised. For the first time, Bayesian inference has been used to calibrate the flow geometry in an ice sheet model workflow. It has been demonstrated and analysed for the specific case of the Scandinavian Ice Sheet within the wider Eurasian Ice Sheet Complex.

Ultimately, I hope these advances and their discussion prompt further work integrating other types of observational evidence into ice sheet modelling, such as ice extents and timings. Using the methodology presented here, improving model simulations based on their model-data fit is possible. Other palaeo-ice sheets, including the Laurentide, Antarctic and

Greenland ice sheets, could also be modelled and optimised in the same way presented in this thesis. For the Scandinavian Ice Sheet specifically, the immediate plans of the PALGLAC project (led by CD Clark at the University of Sheffield), is to re-run the highest scoring, flow optimised model simulation produced in this thesis, subjected to climate and mass balance nudges to better match the reconstructed ice extent. The aim is to yield a preferred simulation that satisfies the empirically reconstructed ice extent and timing constraints while remaining faithful to the flow geometry observations. If achieved, this could provide an improved reconstruction of this ice sheet and be used in sea level, glacial isostatic and glaciological investigations, as well as for a better understanding of erratic and mineral dispersal by ice flow and possible use in mineral exploration.

Bibliography

Åkesson, H., Morlighem, M., Nisancioglu, K. H., Svendsen, J. I. and Mangerud, J. (2018), 'Atmosphere-driven ice sheet mass loss paced by topography: Insights from modelling the south-western Scandinavian Ice Sheet', *Quaternary Science Reviews* **195**, 32–47.

Albrecht, T., Martin, M., Haseloff, M., Winkelmann, R. and Levermann, A. (2011), 'Parameterization for subgrid-scale motion of ice-shelf calving fronts', *The Cryosphere* **5**(1), 35–44.

Anderson, J. B., Conway, H., Bart, P. J., Witus, A. E., Greenwood, S. L., McKay, R. M., Hall, B. L., Ackert, R. P., Licht, K., Jakobsson, M. et al. (2014), 'Ross Sea paleo-ice sheet drainage and deglacial history during and since the LGM', *Quaternary Science Reviews* **100**, 31–54.

Anderson, N. J. and Leng, M. J. (2004), 'Increased aridity during the early Holocene in West Greenland inferred from stable isotopes in laminated-lake sediments', *Quaternary Science Reviews* **23**(7-8), 841–849.

Andrews, J. T. (1982), 'On the reconstruction of pleistocene ice sheets: A review', *Quaternary Science Reviews* **1**(1), 1–30.
URL: *https://www.sciencedirect.com/science/article/pii/0277379182900178*

Andrianakis, I., Vernon, I. R., McCreesh, N., McKinley, T. J., Oakley, J. E., Nsubuga, R. N., Goldstein, M. and White, R. G. (2015), 'Bayesian History Matching of Complex Infectious Disease Models Using Emulation: A Tutorial and a Case Study on HIV in Uganda', *PLoS Comput. Biol.* **11**(1), e1003968.

Archer, R., Ely, J., Heaton, T., Butcher, F., Hughes, A. and Clark, C. (2023), 'Assessing ice sheet models against the landform record: The Likelihood of Accordant Lineations Analysis (LALA) tool', *Earth Surface Processes and Landforms* **48**(14), 2754–2771.

Arnold, N. and Sharp, M. (2002), 'Flow variability in the Scandinavian ice sheet: modelling the coupling between ice sheet flow and hydrology', *Quaternary Science Reviews* **21**(4-6), 485–502.

Aschwanden, A., Aðalgeirsdóttir, G. and Khroulev, C. (2013), 'Hindcasting to measure ice sheet model sensitivity to initial states', *The Cryosphere* **7**(4), 1083–1093.

Bamber, J. L., Oppenheimer, M., Kopp, R. E., Aspinall, W. P. and Cooke, R. M. (2019), 'Ice sheet contributions to future sea-level rise from structured expert judgment', *Proceedings of the National Academy of Sciences* **116**(23), 11195–11200.

Barr, I. D. and Lovell, H. (2014), 'A review of topographic controls on moraine distribution', *Geomorphology* **226**, 44–64.

Batchelor, C. L., Margold, M., Krapp, M., Murton, D. K., Dalton, A. S., Gibbard, P. L., Stokes, C. R., Murton, J. B. and Manica, A. (2019), 'The configuration of Northern Hemisphere ice sheets through the quaternary', *Nature Communications* **10**(1).

Benn, D. and Evans, D. J. (2014*a*), *Glaciers and glaciation*, Routledge, pp. 14–15.

Benn, D. and Evans, D. J. (2014*b*), *Glaciers and glaciation*, Routledge, chapter 11, pp. 442–579.

Benn, D. I., Warren, C. R. and Mottram, R. H. (2007), 'Calving processes and the dynamics of calving glaciers', *Earth-Science Reviews* **82**(3), 143–179.

Bennett, M. M. and Glasser, N. F. (2011), *Glacial geology: ice sheets and landforms*, John Wiley & Sons.

Blatter, H. (1995), 'Velocity and stress fields in grounded glaciers: a simple algorithm for including deviatoric stress gradients', *Journal of Glaciology* **41**(138), 333–344.

Bochow, N., Poltronieri, A., Robinson, A., Montoya, M., Rypdal, M. and Boers, N. (2023), 'Overshooting the critical threshold for the Greenland ice sheet', *Nature* **622**(7983), 528–536.

Borko, H. and Bernick, M. (1964), 'Automatic document classification part II. Additional experiments', *Journal of the ACM (JACM)* **11**(2), 138–151.

Boulton, G. and Hagdorn, M. (2006), 'Glaciology of the British Isles Ice Sheet during the last glacial cycle: form, flow, streams and lobes', *Quaternary Science Reviews* **25**(23-24), 3359–3390.

Boulton, G. S. (1987), A theory of drumlin formation by subglacial sediment deformation., *in* 'Drumlin symposium.', AA Balkema Publishers, pp. 25–86.

Boulton, G. S., Dongelmans, P., Punkari, M. and Broadgate, M. (2001), 'Palaeoglaciology of an ice sheet through a glacial cycle: the European ice sheet through the Weichselian', *Quaternary Science Reviews* **20**(4), 591–625.

Boulton, G. S., Hagdorn, M. and Hulton, N. R. (2003), 'Streaming flow in an ice sheet through a glacial cycle', *Annals of Glaciology* **36**, 117–128.

Bowen, D., Phillips, F., McCabe, A., Knutz, P. and Sykes, G. (2002), 'New data for the last glacial maximum in Great Britain and Ireland', *Quaternary Science Reviews* **21**(1-3), 89–101.

Boyes, B. M. (2022), The last Fennoscandian Ice Sheet: a palaeo-glaciological reconstruction on the Kola Peninsula and Russian Lapland, PhD thesis, University of Brighton.

Boyes, B. M., Linch, L. D., Pearce, D. M. and Nash, D. J. (2023), 'The last Fennoscandian Ice Sheet glaciation on the Kola Peninsula and Russian Lapland (Part 1): Ice flow configuration', *Quaternary Science Reviews* **300**, 107871.

Braconnot, P., Harrison, S. P., Kageyama, M., Bartlein, P. J., Masson-Delmotte, V., Abe-Ouchi, A., Otto-Bliesner, B. and Zhao, Y. (2012), 'Evaluation of climate models using palaeoclimatic data', *Nature climate change* **2**(6), 417–424.

Bradley, S. L., Ely, J. C., Clark, C. D., Edwards, R. J. and Shennan, I. (2023), 'Reconstruction of the palaeo-sea level of Britain and Ireland arising from empirical constraints of ice extent: Implications for regional sea level forecasts and Laurentide ice volume.', *Journal of Quaternary Science* .

Budd, W. and Jenssen, D. (1975), 'Numerical modelling of glacier systems', *IAHS publ* **104**, 257–291.

Budd, W. and Jenssen, D. (1989), 'The Dynamics of the Antarctic Ice Sheet', *Annals of Glaciology* **12**, 16–22.

Budich, R. G., Giorgetta, M. A., Jungclaus, J. H., Redler, R. and Reick, C. H. (2010), 'The MPI-M Millennium Earth System Model: an assembling guide for the COSMOS configuration'.

Bueler, E. and Brown, J. (2009), 'Shallow shelf approximation as a "sliding law" in a thermomechanically coupled ice sheet model', *Journal of Geophysical Research: Earth Surface* **114**(F3).

Bueler, E., Brown, J. and Lingle, C. (2007), 'Exact solutions to the thermomechanically coupled shallow ice approximation: effective tools for verification', *J. Glaciol.* **53**(182), 499–516.

Bueler, E., Lingle, C. S. and Brown, J. (2007), 'Fast computation of a viscoelastic deformable Earth model for ice-sheet simulations', *Annals of Glaciology* **46**, 97–105.

Butcher, F., Hughes, A. L. C., Dulfer, H. E., Clark, C. D., Ely, J., Lewington, E. L. M., Boyes, B. M., Scoffield, A. C., Howcutt, S. and Diemont, C. R. (in prep), 'Flow Pattern Evolution of the Scandinavian Ice Sheet over Finland, Sweden, and Norway, Reconstructed from Subglacial Bedforms'.

Butler, M. P., Reed, P. M., Fisher-Vanden, K., Keller, K. and Wagener, T. (2014), 'Identifying parametric controls and dependencies in integrated assessment models using global sensitivity analysis', *Environmental modelling & software* **59**, 10–29.

Calov, R. and Greve, R. (2005), 'A semi-analytical solution for the positive degree-day model with stochastic temperature variations', *Journal of Glaciology* **51**(172), 173–175.

Calov, R., Greve, R., Abe-Ouchi, A., Bueler, E., Huybrechts, P., Johnson, J. V., Pattyn, F., Pollard, D., Ritz, C., Saito, F. and Tarasov, L. (2010), 'Results from the ice sheet model intercomparison project - Heinrich event intercomparison (ISMIP HEINO)', *J Glaciol* **56**(197), 371–383.

Campbell, W. J. and Rasmussen, L. A. (1969), 'Three-dimensional surges and recoveries in a numerical glacier model', *Canadian Journal of Earth Sciences* **6**(4), 979–986.

Chandler, B. M., Lovell, H., Boston, C. M., Lukas, S., Barr, I. D., Ívar Örn Benediktsson, Benn, D. I., Clark, C. D., Darvill, C. M., Evans, D. J., Ewertowski, M. W., Loibl, D., Margold, M., Otto, J.-C., Roberts, D. H., Stokes, C. R., Storrar, R. D. and Stroeven, A. P. (2018), 'Glacial geomorphological mapping: A review of approaches and frameworks for best practice', *Earth-Science Reviews* **185**, 806–846.
URL: *https://www.sciencedirect.com/science/article/pii/S0012825217305986*

Chapman, W. L., Welch, W. J., Bowman, K. P., Sacks, J. and Walsh, J. E. (1994), 'Arctic sea ice variability: Model sensitivities and a multidecadal simulation', *Journal of Geophysical Research: Oceans* **99**(C1), 919–935.

Choi, Y., Morlighem, M., Wood, M. and Bondzio, J. H. (2018), 'Comparison of four calving laws to model Greenland outlet glaciers', *The Cryosphere* **12**(12), 3735–3746.
URL: *https://tc.copernicus.org/articles/12/3735/2018/*

Chorlton, J. C. and Lister, H. (1968), Snow accumulation over Antarctica, *in* A. J. Gow and et al., eds, 'International Symposium on Antarctic Glaciological Exploration (ISAGE)', Vol. 86, Int. Ass. scient. Hydrol. Pub., pp. 254–263.

Chorlton, J. C. and Lister, H. (1971), 'Geographical Control of Glacier Budget Gradients in Norway', *Norsk Geografisk Tidsskrift - Norwegian Journal of Geography* **25**(3-4), 159–164.

Clark, C. D. (1993), 'Mega-scale glacial lineations and cross-cutting ice-flow landforms', *Earth surface processes and landforms* **18**(1), 1–29.

Clark, C. D. (1997), 'Reconstructing the evolutionary dynamics of former ice sheets using multi-temporal evidence, remote sensing and GIS', *Quaternary Science Reviews* **16**(9), 1067–1092.

Clark, C. D. (1999), 'Glaciodynamic context of subglacial bedform generation and preservation', *Annals of Glaciology* **28**, 23–32.

Clark, C. D. (2010), 'Emergent drumlins and their clones: from till dilatancy to flow instabilities', *Journal of Glaciology* **56**(200), 1011–1025.

Clark, C. D., Ely, J. C., Hindmarsh, R. C. A., Bradley, S., Ignéczi, A., Fabel, D., Ó Cofaigh, C., Chiverrell, R. C., Scourse, J., Benetti, S., Bradwell, T., Evans, D. J. A., Roberts, D. H., Burke, M., Callard, S. L., Medialdea, A., Saher, M., Small, D., Smedley, R. K., Gasson, E., Gregoire, L., Gandy, N., Hughes, A. L. C., Ballantyne, C., Bateman, M. D., Bigg, G. R., Doole, J., Dove, D., Duller, G. A. T., Jenkins, G. T. H., Livingstone, S. L., McCarron, S., Moreton, S., Pollard, D., Praeg, D., Sejrup, H. P., Van Landeghem, K. J. J. and Wilson, P. (2022), 'Growth and retreat of the last British–Irish Ice Sheet, 31000 to 15000 years ago:the BRITICE-CHRONO reconstruction', *Boreas* **51**(4), 699–758.

Clark, C. D., Ely, J. C., Spagnolo, M., Hahn, U., Hughes, A. L. and Stokes, C. R. (2018), 'Spatial organization of drumlins', *Earth Surface Processes and Landforms* **43**(2), 499–513.

Clark, C. D., Hughes, A. L., Greenwood, S. L., Jordan, C. and Sejrup, H. P. (2012), 'Pattern and timing of retreat of the last British-Irish Ice Sheet', *Quaternary Science Reviews* **44**, 112–146.

Clark, C. D., Hughes, A. L., Greenwood, S. L., Spagnolo, M. and Ng, F. S. (2009), 'Size and shape characteristics of drumlins, derived from a large sample, and associated scaling laws', *Quaternary Science Reviews* **28**(7), 677–692.

Clark, P. U., Dyke, A. S., Shakun, J. D., Carlson, A. E., Clark, J., Wohlfarth, B., Mitrovica, J. X., Hostetler, S. W. and McCabe, A. M. (2009), 'The last glacial maximum', *science* **325**(5941), 710–714.

Clason, C. C., Applegate, P. and Holmlund, P. (2014), 'Modelling Late Weichselian evolution of the Eurasian ice sheets forced by surface meltwater-enhanced basal sliding', *Journal of Glaciology* **60**(219), 29–40.

Clason, C. C., Greenwood, S. L., Selmes, N., Lea, J. M., Jamieson, S. S., Nick, F. M. and Holmlund, P. (2016), 'Controls on the early Holocene collapse of the Bothnian Sea Ice Stream', *Journal of Geophysical Research: Earth Surface* **121**(12), 2494–2513.

Colinge, J. and Blatter, H. (1998), 'Stress and velocity fields in glaciers: Part I. Finite-difference schemes for higher-order glacier models', *Journal of Glaciology* **44**(148), 448–456.

Cornford, S. L., Martin, D. F., Graves, D. T., Ranken, D. F., Le Brocq, A. M., Gladstone, R. M., Payne, A. J., Ng, E. G. and Lipscomb, W. H. (2013), 'Adaptive mesh, finite volume modeling of marine ice sheets', *Journal of Computational Physics* **232**(1), 529–549.

Craig, P. S., Goldstein, M., Seheult, A. H. and Smith, J. A. (1997), Pressure matching for hydrocarbon reservoirs: a case study in the use of Bayes linear strategies for large computer experiments, *in* 'Case studies in Bayesian statistics', Springer, pp. 37–93.

Davies, B. (2020), 'A hierarchy of ice-sheet models'.

URL: *https://www.antarcticglaciers.org/glaciers-and-climate/numerical-ice-sheet-models/hierarchy-ice-sheet-models-introduction/*

Davies, B. J., Golledge, N. R., Glasser, N. F., Carrivick, J. L., Ligtenberg, S. R., Barrand, N. E., Van Den Broeke, M. R., Hambrey, M. J. and Smellie, J. L. (2014), 'Modelled glacier response to centennial temperature and precipitation trends on the Antarctic Peninsula', *Nature Climate Change* **4**(11), 993–998.

DeConto, R. M. and Pollard, D. (2016), 'Contribution of Antarctica to past and future sea-level rise', *Nature* **531**(7596), 591–597.

Dongelmans, P. (1996), 'Glacial dynamics of the Fennoscandian ice sheet: a remote-sensing study', *KB thesis scanning project 2015* .

Dowdeswell, E., Todd, B. and Dowdeswell, J. (2016), 'Crag-and-tail features: convergent ice flow through Eclipse Sound, Baffin Island, Arctic Canada', *Geological Society, London, Memoirs* **46**(1), 55–56.

Dowdeswell, J., Canals, M., Jakobsson, M., Todd, B., Dowdeswell, E. and Hogan, K. (2016), 'The variety and distribution of submarine glacial landforms and implications for ice-sheet reconstruction', *Geological Society, London, Memoirs* **46**(1), 519–552.

Dulfer, H. E., Stoker, B. J., Margold, M. and Stokes, C. R. (2023), 'Glacial geomorphology of the northwest Laurentide Ice Sheet on the northern Interior Plains and western Canadian Shield, Canada', *Journal of Maps* **19**(1), 2181714.

Duller, G. (2008), *Luminescence Dating: guidelines on using luminescence dating in archaeology*, English Heritage Publishing.

Dyke, A. S. (2008), 'The Steensby Inlet Ice Stream in the context of the deglaciation of northern Baffin Island, eastern Arctic Canada', *Earth Surface Processes and Landforms: The Journal of the British Geomorphological Research Group* **33**(4), 573–592.

Eaton, M. L. (2007), 'Multivariate Statistics: A Vector Space Approach', *Lecture Notes-Monograph Series* **53**, i–512.
URL: *http://www.jstor.org/stable/20461449*

Eckert, N., Naaim, M. and Parent, E. (2010), 'Long-term avalanche hazard assessment with a Bayesian depth-averaged propagation model', *Journal of Glaciology* **56**(198), 563–586.

Edwards, T. L., Brandon, M. A., Durand, G., Edwards, N. R., Golledge, N. R., Holden, P. B., Nias, I. J., Payne, A. J., Ritz, C. and Wernecke, A. (2019), 'Revisiting Antarctic ice loss due to marine ice-cliff instability', *Nature* **566**(7742), 58–64.

Edwards, T. L., Nowicki, S., Marzeion, B., Hock, R., Goelzer, H., Seroussi, H., Jourdain, N. C., Slater, D. A., Turner, F. E., Smith, C. J. et al. (2021), 'Projected land ice contributions to twenty-first-century sea level rise', *Nature* **593**(7857), 74–82.

Ely, J. C., Clark, C. D., Bradley, S. L., Gregoire, L., Gandy, N., Gasson, E., Veness, R. L. and Archer, R. (2024), 'Behavioural tendencies of the last British–Irish Ice Sheet revealed by data–model comparison', *Journal of Quaternary Science* .

Ely, J. C., Clark, C. D., Hindmarsh, R. C., Hughes, A. L., Greenwood, S. L., Bradley, S. L., Gasson, E., Gregoire, L., Gandy, N., Stokes, C. R. et al. (2021), 'Recent progress on combining geomorphological and geochronological data with ice sheet modelling, demonstrated using the last British–Irish Ice Sheet', *Journal of Quaternary Science* **36**(5), 946–960.

Ely, J. C., Clark, C. D., Small, D. and Hindmarsh, R. C. A. (2019), 'Atat 1.1, the automated timing accordance tool for comparing ice-sheet model output with geochronological data', *Geoscientific Model Development* **12**(3), 933–953.

Ely, J. C., Clark, C. D., Spagnolo, M., Hughes, A. L. and Stokes, C. R. (2018), 'Using the size and position of drumlins to understand how they grow, interact and evolve', *Earth Surface Processes and Landforms* **43**(5), 1073–1087.

Ely, J. C., Stevens, D., Clark, C. D. and Butcher, F. E. (2023), 'Numerical modelling of subglacial ribs, drumlins, herringbones, and mega-scale glacial lineations reveals their developmental trajectories and transitions', *Earth Surface Processes and Landforms* **48**(5), 956–978.

Ely, J., Stevens, D., Clark, C. and Butcher, F. (2022), 'Numerical modelling of subglacial ribs, drumlins, herringbones, and mega-scale glacial lineations reveals their developmental trajectories and transitions', *Earth Surface Processes and Landforms* .

Evans, D. J., Roberts, D. H. and Cofaigh, C. O. (2015), 'Drumlin sedimentology in a hard-bed, lowland setting, Connemara, western Ireland: implications for subglacial bedform generation in areas of sparse till cover', *Journal of Quaternary Science* **30**(6), 537–557.

Fastook, J. L. and Chapman, J. E. (1989), 'A map-plane finite-element model: three modeling experiments', *Journal of Glaciology* **35**(119), 48–52.

Fastook, J. L. and Holmlund, P. (1994), 'A glaciological model of the younger dryas event in scandinavia', *Journal of Glaciology* **40**(134), 125–131.

Feldmann, J., Albrecht, T., Khroulev, C., Pattyn, F. and Levermann, A. (2014), 'Resolution-dependent performance of grounding line motion in a shallow model compared with a full-Stokes model according to the MISMIP3d intercomparison', *Journal of Glaciology* **60**(220), 353–360.

Finlayson, A., Fabel, D., Bradwell, T. and Sugden, D. (2014), 'Growth and decay of a marine terminating sector of the last British–Irish Ice Sheet: a geomorphological reconstruction', *Quaternary Science Reviews* **83**, 28–45.

Florentin, J. (1962), 'Optimal, probing, adaptive control of a simple Bayesian system', *International Journal of Electronics* **13**(2), 165–177.

Fornacon-Wood, I., Mistry, H., Johnson-Hart, C., Faivre-Finn, C., O'Connor, J. P. and Price, G. J. (2022), 'Understanding the differences between Bayesian and frequentist statistics', *International journal of radiation oncology, biology, physics* **112**(5), 1076–1082.

Forsström, P.-L. and Greve, R. (2004), 'Simulation of the Eurasian ice sheet dynamics during the last glaciation', *Global and Planetary Change* **42**(1), 59–81. Ice sheets and neotectonics.

URL: *https://www.sciencedirect.com/science/article/pii/S0921818104000359*

Fowler, A. (2000), 'An instability mechanism for drumlin formation', *Geological Society, London, Special Publications* **176**(1), 307–319.

Fuchs, M. and Owen, L. A. (2008), 'Luminescence dating of glacial and associated sediments: review, recommendations and future directions', *Boreas* **37**(4), 636–659.

Fyke, J., Sacks, W. and Lipscomb, W. (2014), 'A technique for generating consistent ice sheet initial conditions for coupled ice sheet/climate models', *Geoscientific Model Development* **7**(3), 1183–1195.

Gagliardini, O. (2022), 'Elmer/Ice'.
URL: *http://elmerice.elmerfem.org/*

Gandy, N., Gregoire, L. J., Ely, J. C., Cornford, S. L., Clark, C. D. and Hodgson, D. M. (2019), 'Exploring the ingredients required to successfully model the placement, generation, and evolution of ice streams in the British-Irish Ice Sheet', *Quaternary Science Reviews* **223**, 105915.

Gandy, N., Gregoire, L. J., Ely, J. C., Cornford, S. L., Clark, C. D. and Hodgson, D. M. (2021), 'Collapse of the last Eurasian Ice Sheet in the North Sea modulated by combined processes of ice flow, surface melt, and marine ice sheet instabilities', *Journal of Geophysical Research: Earth Surface* **126**(4), e2020JF005755.

Gasson, E. G., DeConto, R. M., Pollard, D. and Clark, C. D. (2018), 'Numerical simulations of a kilometre-thick Arctic ice shelf consistent with ice grounding observations', *Nature communications* **9**(1), 1510.

Gillet-Chaulet, F., Gagliardini, O., Seddik, H., Nodet, M., Durand, G., Ritz, C., Zwinger, T., Greve, R. and Vaughan, D. G. (2012), 'Greenland ice sheet contribution to sea-level rise from a new-generation ice-sheet model', *The Cryosphere* **6**(6), 1561–1576.

Giorgetta, M. A., Jungclaus, J., Reick, C. H., Legutke, S., Bader, J., Böttinger, M., Brovkin, V., Crueger, T., Esch, M., Fieg, K. et al. (2013), 'Climate and carbon cycle changes from 1850 to 2100 in MPI-ESM simulations for the Coupled Model Intercomparison Project phase 5', *Journal of Advances in Modeling Earth Systems* **5**(3), 572–597.

Glen, J. W. (1955), 'The creep of polycrystalline ice', *Proceedings of the Royal Society of London. Series A. Mathematical and Physical Sciences* **228**(1175), 519–538.

Glückert, G. (1973), 'Two large drumlin fields in central Finland', *Fennia-International Journal of Geography* **120**(1).

Glückert, G. (1974), 'Map of glacial striation of the Scandinavian ice sheet during the last (Weichsel) glaciation in northern Europe', *Bulletin of the Geological Society of Finland* **46**, 1–8.

Goelzer, H., Huybrechts, P., Fürst, J. J., Nick, F. M., Andersen, M. L., Edwards, T. L., Fettweis, X., Payne, A. J. and Shannon, S. (2013), 'Sensitivity of Greenland ice sheet projections to model formulations', *Journal of Glaciology* **59**(216), 733–749.

Goelzer, H., Nowicki, S., Payne, A., Larour, E., Seroussi, H., Lipscomb, W. H., Gregory, J., Abe-Ouchi, A., Shepherd, A., Simon, E. et al. (2020), 'The future sea-level contribution of the Greenland ice sheet: a multi-model ensemble study of ISMIP6', *The Cryosphere Discussions* **2020**, 1–43.

Gowan, E., Tregoning, P., Purcell, A., Lea, J., Fransner, O., Noormets, R. and Dowdeswell, J. (2016), 'ICESHEET 1.0: a program to produce paleo-ice sheet reconstructions with minimal assumptions', *Geoscientific Model Development* **9**(5), 1673–1682.

Greenwood, S., Clason, C. and Jakobsson, M. (2016), 'Ice-flow and meltwater landform assemblages in the Gulf of Bothnia', *Geological Society, London, Memoirs* **46**(1), 321–324.

Greenwood, S. L. and Clark, C. D. (2009), 'Reconstructing the last Irish Ice Sheet 1: changing flow geometries and ice flow dynamics deciphered from the glacial landform record', *Quaternary Science Reviews* **28**(27-28), 3085–3100.

Greve, R. (1997), 'Application of a polythermal three-dimensional ice sheet model to the Greenland ice sheet: response to steady-state and transient climate scenarios', *Journal of Climate* **10**(5), 901–918.

Grow, A. and Hilton, J. (2014), 'Statistical emulation', *Wiley StatsRef: Statistics Reference Online* pp. 1–8.

Gudlaugsson, E., Humbert, A., Andreassen, K., Clason, C. C., Kleiner, T. and Beyer, S. (2017), 'Eurasian ice-sheet dynamics and sensitivity to subglacial hydrology', *Journal of Glaciology* **63**(239), 556–564.

Hall, J., Tarantola, S., Bates, P. and Horritt, M. (2005), 'Distributed sensitivity analysis of flood inundation model calibration', *Journal of hydraulic engineering* **131**(2), 117–126.

Harper, E. B., Stella, J. C. and Fremier, A. K. (2011), 'Global sensitivity analysis for complex ecological models: a case study of riparian cottonwood population dynamics', *Ecological Applications* **21**(4), 1225–1240.

Hastie, T. and Tibshirani, R. (1987), 'Generalized Additive Models: Some Applications', *Journal of the American Statistical Association* **82**(398), 371–386.

Hastings, W. K. (1970), 'Monte Carlo sampling methods using Markov chains and their applications'.

Hättestrand, C., Götz, S., Näslund, J.-O., Fabel, D. and Stroeven, A. P. (2004), 'Drumlin formation time: evidence from northern and central Sweden', *Geografiska Annaler: Series A, Physical Geography* **86**(2), 155–167.

Hickson, R., Mercer, G., Lokuge, K. et al. (2011), 'Sensitivity analysis of a model for tuberculosis'.

Hill, E. A., Rosier, S. H., Gudmundsson, G. H. and Collins, M. (2021), 'Quantifying the potential future contribution to global mean sea level from the Filchner–Ronne basin, Antarctica', *The Cryosphere* **15**(10), 4675–4702.

Hill, E. A., Urruty, B., Reese, R., Garbe, J., Gagliardini, O., Durand, G., Gillet-Chaulet, F., Gudmundsson, G. H., Winkelmann, R., Chekki, M. et al. (2022), 'The stability of present-day Antarctic grounding lines–Part A: No indication of marine ice sheet instability in the current geometry', *The Cryosphere Discussions* **2022**, 1–34.

Hinck, S., Gowan, E. J., Zhang, X. and Lohmann, G. (2022), 'PISM-LakeCC: Implementing an adaptive proglacial lake boundary in an ice sheet model', *The Cryosphere* **16**(3), 941–965.

Hindmarsh, R. C. (1998), 'Drumlinization and drumlin-forming instabilities: viscous till mechanisms', *Journal of Glaciology* **44**(147), 293–314.

Hindmarsh, R. C. A., Boulton, G. S. and Hutter, K. (1989), 'Modes of Operation of Thermo-Mechanically Coupled Ice Sheets', *Annals of Glaciology* **12**, 57–69.

Hooke, R. L., Cummings, D. I., Lesemann, J.-E. and Sharpe, D. R. (2013), 'Genesis of dispersal plumes in till', *Canadian Journal of Earth Sciences* **50**(8), 847–855.

Hubbard, A. (2006), 'The validation and sensitivity of a model of the Icelandic ice sheet', *Quaternary Science Reviews* **25**(17-18), 2297–2313.

Hughes, A. L. C., Gyllencreutz, R., Lohne, Ø. S., Mangerud, J. and Svendsen, J. I. (2016), 'The last Eurasian ice sheets – a chronological database and time-slice reconstruction, DATED-1', *Boreas* **45**(1), 1–45.

Hughes, A. L., Clark, C. D. and Jordan, C. J. (2014), 'Flow-pattern evolution of the last British Ice Sheet', *Quaternary Science Reviews* **89**, 148–168.

Hutter, K. (1982), 'Dynamics of glaciers and large ice masses', *Annual Review of Fluid Mechanics* **14**(1), 87–130.

Huybrechts, P. (1990), 'A 3-D model for the Antarctic ice sheet: a sensitivity study on the glacial-interglacial contrast', *Climate Dynamics* **5**, 79–92.

Huybrechts, P. and Oerlemans, J. (1988), 'Evolution of the East Antarctic Ice Sheet: A Numerical Study of Thermo-Mechanical Response Patterns With Changing Climate', *Annals of glaciology* **11**, 52–59.

Huybrechts, P. and Payne, T. (1996), 'The EISMINT benchmarks for testing ice-sheet models', *Annals of Glaciology* **23**, 1–12.

Jakobsson, M., Andreassen, K., Bjarnadóttir, L. R., Dove, D., Dowdeswell, J. A., England, J. H., Funder, S., Hogan, K., Ingólfsson, Ó., Jennings, A. et al. (2014), 'Arctic Ocean glacial history', *Quaternary Science Reviews* **92**, 40–67.

James, W. H., Carrivick, J. L., Quincey, D. J. and Glasser, N. F. (2019), 'A geomorphology based reconstruction of ice volume distribution at the Last Glacial Maximum across the Southern Alps of New Zealand', *Quaternary Science Reviews* **219**, 20–35.

Johnson, J. S., Cui, Z., Lee, L. A., Gosling, J. P., Blyth, A. M. and Carslaw, K. S. (2015), 'Evaluating uncertainty in convective cloud microphysics using statistical emulation', *Journal of Advances in Modeling Earth Systems* **7**(1), 162–187.

Jones, B. and Johnson, R. T. (2009), 'Design and analysis for the Gaussian process model', *Quality and Reliability Engineering International* **25**(5), 515–524.
URL: *https://onlinelibrary.wiley.com/doi/abs/10.1002/qre.1044*

Jones, D. R., Schonlau, M. and Welch, W. J. (1998), 'Efficient global optimization of expensive black-box functions', *Journal of Global optimization* **13**, 455–492.

Joughin, I., Smith, B., Howat, I. and Scambos, T. (2015), 'MEaSUREs Greenland Ice Sheet Velocity Map from InSAR Data, Version 2'. https://doi.org/10.5067/OC7B04ZM9G6Q. Accessed on 05/09/2024.

Jungclaus, J. H., Fischer, N., Haak, H., Lohmann, K., Marotzke, J., Matei, D., Mikolajewicz, U., Notz, D. and Von Storch, J. (2013), 'Characteristics of the ocean simulations in the Max Planck Institute Ocean Model (MPIOM) the ocean component of the MPI-Earth system model', *Journal of Advances in Modeling Earth Systems* **5**(2), 422–446.

Kageyama, M., Braconnot, P., Bopp, L., Caubel, A., Foujols, M.-A., Guilyardi, E., Khodri, M., Lloyd, J., Lombard, F., Mariotti, V. et al. (2013a), 'Mid-Holocene and Last Glacial

Maximum climate simulations with the IPSL model—part I: comparing IPSL_CM5A to IPSL_CM4', *Climate dynamics* **40**, 2447–2468.

Kageyama, M., Braconnot, P., Bopp, L., Mariotti, V., Roy, T., Woillez, M.-N., Caubel, A., Foujols, M.-A., Guilyardi, E., Khodri, M. et al. (2013b), 'Mid-Holocene and last glacial maximum climate simulations with the IPSL model: part II: model-data comparisons', *Climate dynamics* **40**, 2469–2495.

Kelleher, C., Wagener, T., McGlynn, B., Ward, A., Gooseff, M. and Payn, R. (2013), 'Identifiability of transient storage model parameters along a mountain stream', *Water Resources Research* **49**(9), 5290–5306.

Kennedy, M. C. and O'Hagan, A. (2001), 'Bayesian calibration of computer models', *Journal of the Royal Statistical Society: Series B (Statistical Methodology)* **63**(3), 425–464.

Kingman, J. F. C. (1993), *Poisson Processes*, Vol. 3 of *Oxford Studies in Probability*, The Clarendon Press Oxford University Press, New York. Oxford Science Publications.

Kopp, R. E., DeConto, R. M., Bader, D. A., Hay, C. C., Horton, R. M., Kulp, S., Oppenheimer, M., Pollard, D. and Strauss, B. H. (2017), 'Evolving Understanding of Antarctic Ice-Sheet Physics and Ambiguity in Probabilistic Sea-Level Projections', *Earth's Future* **5**(12), 1217–1233.

Krbetschek, M., Rieser, U. and Stolz, W. (1996), 'Optical dating: some luminescence properties of natural feldspars', *Radiation Protection Dosimetry* **66**(1-4), 407–412.

Lambeck, K., Purcell, A., Zhao, J. and Svensson, N.-O. (2010), 'The Scandinavian Ice Sheet: from MIS 4 to the end of the Last Glacial Maximum', *Boreas* **39**(2), 410–435.

Larour, E., Seroussi, H., Morlighem, M. and Rignot, E. (2012*a*), 'Continental scale, high order, high spatial resolution, ice sheet modeling using the Ice Sheet System Model', *J. Geophys. Res.* **117**.

Larour, E., Seroussi, H., Morlighem, M. and Rignot, E. (2012*b*), 'Continental scale, high order, high spatial resolution, ice sheet modeling using the Ice Sheet System Model (ISSM)', *Journal of Geophysical Research: Earth Surface* **117**(F1).

Lazeroms, W. M., Jenkins, A., Gudmundsson, G. H. and Van De Wal, R. S. (2018), 'Modelling present-day basal melt rates for Antarctic ice shelves using a parametrization of buoyant meltwater plumes', *The Cryosphere* **12**(1), 49–70.

Leger, T. P., Hein, A. S., Bingham, R. G., Martini, M. A., Soteres, R. L., Sagredo, E. A. and Martínez, O. A. (2020), 'The glacial geomorphology of the Río Corcovado, Río Huemul and Lago Palena/General Vintter valleys, northeastern Patagonia (43 S, 71 W)', *Journal of Maps* **16**(2), 651–668.

Li, Y., Napieralski, J. and Harbor, J. (2008), 'A Revised Automated Proximity and Conformity Analysis Method to Compare Predicted and Observed Spatial Boundaries of Geologic Phenomena', *Comput. Geosci.* **34**(12), 1806–1814.

Li, Y., Napieralski, J., Harbor, J. and Hubbard, A. (2007), 'Identifying Patterns of Correspondence between Modeled Flow Directions and Field Evidence: An Automated Flow Direction Analysis', *Comput. Geosci.* **33**(2), 141–150.

Libby, W. F. (1954), 'Radiocarbon dating', *Endeavour* **13**(49), 5–16.

Lingle, C. S. and Clark, J. A. (1985), 'A numerical model of interactions between a marine ice sheet and the solid earth: Application to a West Antarctic ice stream', *Journal of Geophysical Research: Oceans* **90**(C1), 1100–1114.

Lipscomb, W. H., Leguy, G. R., Jourdain, N. C., Asay-Davis, X., Seroussi, H. and Nowicki, S. (2021), 'ISMIP6-based projections of ocean-forced Antarctic Ice Sheet evolution using the Community Ice Sheet Model', *The Cryosphere* **15**(2), 633–661.

Lisiecki, L. E. and Raymo, M. E. (2007), 'Plio–Pleistocene climate evolution: trends and transitions in glacial cycle dynamics', *Quaternary Science Reviews* **26**(1-2), 56–69.

Liu, H., Chen, W. and Sudjianto, A. (2006), 'Relative entropy based method for probabilistic sensitivity analysis in engineering design', *Journal of Mechanical Design* **128**(2), 326–336.

Lliboutry, L. (1968), 'General Theory of Subglacial Cavitation and Sliding of Temperate Glaciers', *Journal of glaciology* **7**(49), 21–58.

Loeppky, J. L., Sacks, J. and Welch, W. J. (2009), 'Choosing the Sample Size of a Computer Experiment: A Practical Guide', *Technometrics* **51**(4), 366–376.

Luethgens, C., Boese, M. and Preusser, F. (2011), 'Age of the Pomeranian ice-marginal position in northeastern Germany determined by Optically Stimulated Luminescence (OSL) dating of glaciofluvial sediments', *Boreas* **40**(4), 598–615.

MacAyeal, D. R., Rommelaere, V., Huybrechts, P., Hulbe, C. L., Determann, J. and Ritz, C. (1996), 'An ice-shelf model test based on the Ross Ice Shelf, Antarctica', *Annals of Glaciology* **23**, 46–51.

Mahaffy, M. W. (1976), 'A three-dimensional numerical model of ice sheets: Tests on the Barnes Ice Cap, Northwest Territories', *Journal of Geophysical Research (1896-1977)* **81**(6), 1059–1066.

Man, W., Zhou, T. and Jungclaus, J. H. (2014), ‘Effects of large volcanic eruptions on global summer climate and East Asian monsoon changes during the last millennium: Analysis of MPI-ESM simulations’, *Journal of Climate* **27**(19), 7394–7409.

Martin, M. A., Winkelmann, R., Haseloff, M., Albrecht, T., Bueler, E., Khroulev, C. and Levermann, A. (2011), ‘The Potsdam parallel ice sheet model (PISM-PIK)–Part 2: dynamic equilibrium simulation of the Antarctic ice sheet’, *The Cryosphere* **5**(3), 727–740.

McKay, M. D., Beckman, R. J. and Conover, W. J. (1979), ‘A comparison of three methods for selecting values of input variables in the analysis of output from a computer code’, *Technometrics* **42**, 239–245.

Menzies, J. (1984), *Drumlins: A Bibliography*, Geobooks, Norwich.

Montelli, A., Solovyeva, M., Akhmanov, G., Mazzini, A., Piatilova, A., Bakay, E. and Dowdeswell, J. A. (2023), ‘The geomorphic record of marine-based ice dome decay: Final collapse of the Barents Sea ice sheet’, *Quaternary Science Reviews* **303**, 107973.

Moonen, P. and Allegrini, J. (2015), ‘Employing statistical model emulation as a surrogate for CFD’, *Environmental Modelling I& Software* **72**, 77–91.

Morlighem, M., Rignot, E., Binder, T., Blankenship, D., Drews, R., Eagles, G., Eisen, O., Ferraccioli, F., Forsberg, R., Fretwell, P. et al. (2020), ‘Deep glacial troughs and stabilizing ridges unveiled beneath the margins of the Antarctic ice sheet’, *Nature geoscience* **13**(2), 132–137.

Morlighem, M., Williams, C. N., Rignot, E., An, L., Arndt, J. E., Bamber, J. L., Catania, G., Chauché, N., Dowdeswell, J. A., Dorschel, B., Fenty, I., Hogan, K., Howat, I., Hubbard, A., Jakobsson, M., Jordan, T. M., Kjeldsen, K. K., Millan, R., Mayer, L., Mouginot, J., Noël, B. P. Y., O’Cofaigh, C., Palmer, S., Rysgaard, S., Seroussi, H., Siegert, M. J., Slabon, P., Straneo, F., van den Broeke, M. R., Weinrebe, W., Wood, M. and Zinglersen, K. B. (2017), ‘BedMachine v3: Complete Bed Topography and Ocean Bathymetry Mapping of Greenland From Multibeam Echo Sounding Combined With Mass Conservation’, *Geophysical Research Letters* **44**(21), 11,051–11,061.
URL: *https://agupubs.onlinelibrary.wiley.com/doi/abs/10.1002/2017GL074954*

Näslund, J., Rodhe, L., Fastook, J. and Holmlund, P. (2003), ‘New ways of studying ice sheet flow directions and glacial erosion by computer modelling—examples from Fennoscandia’, *Quaternary science reviews* **22**(2), 245–258.

Nelder, J. A. and Wedderburn, R. W. M. (1972), ‘Generalized Linear Models’, *Journal of the Royal Statistical Society. Series A. General* **135**(3), 370–384.

Newton, A. M. and Huuse, M. (2017), 'Glacial geomorphology of the central Barents Sea: implications for the dynamic deglaciation of the Barents Sea Ice Sheet', *Marine Geology* **387**, 114–131.

Niu, L., Lohmann, G., Hinck, S., Gowan, E. J. and Krebs-Kanzow, U. (2019), 'The sensitivity of Northern Hemisphere ice sheets to atmospheric forcing during the last glacial cycle using PMIP3 models', *Journal of Glaciology* **65**(252), 645–661.

Nossent, J., Elsen, P. and Bauwens, W. (2011), 'Sobol' sensitivity analysis of a complex environmental model', *Environmental Modelling & Software* **26**(12), 1515–1525.

Nowicki, S., Goelzer, H., Seroussi, H., Payne, A. J., Lipscomb, W. H., Abe-Ouchi, A., Agosta, C., Alexander, P., Asay-Davis, X. S., Barthel, A. et al. (2020), 'Experimental protocol for sea level projections from ISMIP6 stand-alone ice sheet models', *The Cryosphere* **14**(7), 2331–2368.

Nye, J. F. (1952), 'The Mechanics of Glacier Flow', *Journal of Glaciology* **2**(12), 82–93.

Oakley, J. E. and O'Hagan, A. (2007), 'Uncertainty in prior elicitations: a nonparametric approach', *Biometrika* **94**(2), 427–441.
URL: *https://doi.org/10.1093/biomet/asm031*

O'Hagan, A. (2008), The Bayesian Approach to Statistics, *in* T. Rudas, ed., 'Handbook of probability: theory and applications', Sage Publications, pp. 85–100.

Ohgaito, R., Sueyoshi, T., Abe-Ouchi, A., Hajima, T., Watanabe, S., Kim, H.-J., Yamamoto, A. and Kawamiya, M. (2013), 'Can an Earth System Model simulate better climate change at mid-Holocene than an AOGCM? A comparison study of MIROC-ESM and MIROC3', *Climate of the Past* **9**(4), 1519–1542.

on Climate Change (IPCC), I. P. (2022), *Annex I: Glossary*, Cambridge University Press, p. 541–562.

Patton, H., Hubbard, A., Andreassen, K., Auriac, A., Whitehouse, P. L., Stroeven, A. P., Shackleton, C., Winsborrow, M., Heyman, J. and Hall, A. M. (2017), 'Deglaciation of the Eurasian ice sheet complex', *Quat. Sci. Rev.* **169**, 148–172.

Patton, H., Hubbard, A., Andreassen, K., Winsborrow, M. and Stroeven, A. P. (2016), 'The build-up, configuration, and dynamical sensitivity of the Eurasian ice-sheet complex to Late Weichselian climatic and oceanic forcing', *Quat. Sci. Rev.* **153**, 97–121.

Pattyn, F. (2003), 'A new three-dimensional higher-order thermomechanical ice sheet model: Basic sensitivity, ice stream development, and ice flow across subglacial lakes', *Journal of*

Geophysical Research: Solid Earth **108**(B8).
URL: *https://agupubs.onlinelibrary.wiley.com/doi/abs/10.1029/2002JB002329*

Pattyn, F., Perichon, L., Aschwanden, A., Breuer, B., de Smedt, B., Gagliardini, O., Gudmundsson, G. H., Hindmarsh, R. C. A., Hubbard, A., Johnson, J. V., Kleiner, T., Konovalov, Y., Martin, C., Payne, A. J., Pollard, D., Price, S., Rückamp, M., Saito, F., Souček, O., Sugiyama, S. and Zwinger, T. (2008), 'Benchmark experiments for higher-order and full-Stokes ice sheet models (ISMIP–HOM)', *The Cryosphere* **2**(2), 95–108.

Pattyn, F., Schoof, C., Perichon, L., Hindmarsh, R. C. A., Bueler, E., de Fleurian, B., Durand, G., Gagliardini, O., Gladstone, R., Goldberg, D., Gudmundsson, G. H., Huybrechts, P., Lee, V., Nick, F. M., Payne, A. J., Pollard, D., Rybak, O., Saito, F. and Vieli, A. (2012), 'Results of the Marine Ice Sheet Model Intercomparison Project, MISMIP', *The Cryosphere* **6**(3), 573–588.

Payne, A. and Baldwin, D. (1999), 'Thermomechanical modelling of the Scandinavian ice sheet: implications for ice-stream formation', *Annals of Glaciology* **28**, 83–89.

Payne, A. J., Huybrechts, P., Abe-Ouchi, A., Calov, R., Fastook, J. L., Greve, R., Marshall, S. J., Marsiat, I., Ritz, C., Tarasov, L. and Thomassen, M. P. A. (2000), 'Results from the EISMINT model intercomparison: the effects of thermomechanical coupling', *Journal of Glaciology* **46**(153), 227–238.

Payne, A. J., Vieli, A., Shepherd, A. P., Wingham, D. J. and Rignot, E. (2004), 'Recent dramatic thinning of largest West Antarctic ice stream triggered by oceans', *Geophysical research letters* **31**(23).

Peltier, W. R. (2004), 'Global glacial isostasy and the surface of the ice-age Earth: the ICE-5G (VM2) model and GRACE', *Annu. Rev. Earth Planet. Sci.* **32**, 111–149.

Petrini, M., Colleoni, F., Kirchner, N., Hughes, A. L., Camerlenghi, A., Rebesco, M., Lucchi, R. G., Forte, E., Colucci, R. R., Noormets, R. et al. (2020), 'Simulated last deglaciation of the Barents Sea Ice Sheet primarily driven by oceanic conditions', *Quaternary Science Reviews* **238**, 106314.

Pilkey, O. H. and Pilkey-Jarvis, L. (2007), *Useless arithmetic: why environmental scientists can't predict the future*, Columbia University Press.

Pollack, H. N., Hurter, S. J. and Johnson, J. R. (1993), 'Heat flow from the Earth's interior: analysis of the global data set', *Reviews of Geophysics* **31**(3), 267–280.

Pollard, D., Chang, W., Haran, M., Applegate, P. and DeConto, R. (2016), 'Large ensemble modeling of the last deglacial retreat of the West Antarctic Ice Sheet: comparison of simple and advanced statistical techniques', *Geoscientific Model Development* **9**(5), 1697–1723.

Pollard, D. and DeConto, R. (2012), 'Description of a hybrid ice sheet-shelf model, and application to Antarctica', *Geoscientific Model Development* **5**(5), 1273–1295.

Pollard, D., DeConto, R. M. and Alley, R. B. (2015), 'Potential Antarctic Ice Sheet retreat driven by hydrofracturing and ice cliff failure', *Earth and Planetary Science Letters* **412**, 112–121.

Pollard, O. G., Barlow, N. L., Gregoire, L., Gomez, N., Cartelle, V., Ely, J. C. and Astfalck, L. C. (2023), 'Quantifying the Uncertainty in the Eurasian Ice-Sheet Geometry at the Penultimate Glacial Maximum (Marine Isotope Stage 6)', *The Cryosphere Discussions* pp. 1–31.

Pörtner, H., Roberts, D., Tignor, M., Poloczanska, E., Mintenbeck, K., Alegrìa, A., Craig, M., Langsdorf, S., Löschke, S., Möller, V., Okem, A., Rama, B., Belling, D., Dieck, W., Götze, S., Kersher, T., Mangele, P., Maus, B., Mühle, A. and Weyer, N. (2022), *Climate Change 2022: Impacts, Adaptation and Vulnerability Working Group II Contribution to the Sixth Assessment Report of the Intergovernmental Panel on Climate Change.*

Preusser, F., Chithambo, M. L., Götte, T., Martini, M., Ramseyer, K., Sendezera, E. J., Susino, G. J. and Wintle, A. G. (2009), 'Quartz as a natural luminescence dosimeter', *Earth-Science Reviews* **97**(1-4), 184–214.

Preusser, F., Degering, D., Fuchs, M., Hilgers, A., Kadereit, A., Klasen, N., Krbetschek, M., Richter, D. and Spencer, J. Q. (2008), 'Luminescence dating: basics, methods and applications', *E&G Quaternary Science Journal* **57**(1/2), 95–149.

Pukelsheim, F. (1994), 'The Three Sigma Rule', *The American Statistician* **48**(2), 88–91.

Punkari, M. (1997), 'Subglacial processes of the Scandinavian Ice Sheet in Fennoscandia inferred from flow-parallel features and lithostratigraphy', *Sedimentary Geology* **111**(1-4), 263–283.

Raddatz, T., Reick, C., Knorr, W., Kattge, J., Roeckner, E., Schnur, R., Schnitzler, K.-G., Wetzel, P. and Jungclaus, J. (2007), 'Will the tropical land biosphere dominate the climate–carbon cycle feedback during the twenty-first century?', *Climate dynamics* **29**, 565–574.

Rasmussen, C. E., Williams, C. K. et al. (2006), *Gaussian processes for machine learning*, Vol. 1, Springer.

Rasmussen, L. and Campbell, W. (1973), 'Comparison of three contemporary flow laws in a three-dimensional, time-dependent glacier model', *Journal of Glaciology* **12**(66), 361–373.

Raymo, M. E., Kozdon, R., Evans, D., Lisiecki, L. and Ford, H. L. (2018), 'The accuracy of mid-Pliocene δ18O-based ice volume and sea level reconstructions', *Earth-Science Reviews* **177**, 291–302.

Reeh, N. (1984), 'Reconstruction of the glacial ice covers of Greenland and the Canadian Arctic islands by three-dimensional, perfectly plastic ice-sheet modelling', *Annals of Glaciology* **5**, 115–121.

Reeh, N. (1991), 'Parameterization of melt rate and surface temperature in the Greenland ice sheet', *Polarforschung* **59**(3), 113–128.

Reese, R., Garbe, J., Hill, E., Urruty, B., Naughten, K., Gagliardini, O., Durand, G., Gillet-Chaulet, F., Gudmundsson, G. H., Chandler, D. et al. (2023), 'The stability of present-day Antarctic grounding lines–Part 2: Onset of irreversible retreat of Amundsen Sea glaciers under current climate on centennial timescales cannot be excluded', *The Cryosphere* **17**(9), 3761–3783.

Reimer, P. J., Austin, W. E. N., Bard, E., Bayliss, A., Blackwell, P. G., Bronk Ramsey, C., Butzin, M., Cheng, H., Edwards, R. L., Friedrich, M. and et al. (2020), 'The IntCal20 Northern Hemisphere Radiocarbon Age Calibration Curve (0–55 cal kBP)', *Radiocarbon* **62**(4), 725–757.

Rignot, E., Mouginot, J. and Scheuchl, B. (2017), 'MEaSUREs InSAR-Based Antarctica Ice Velocity Map, Version 2'. https://doi.org/10.5067/D7GK8F5J8M8R. Accessed on 05/09/2024.

Ritz, C. (1997), 'EISMINT Intercomparison Experiment: Comparison of existing Greenland models'. [Online; accessed 14-August-2024].
URL: *https://web.archive.org/web/20220120054655/http://homepages.vub.ac.be/ phuybrec/eismint/greenland.html*

Ritz, C., Edwards, T. L., Durand, G., Payne, A. J., Peyaud, V. and Hindmarsh, R. C. (2015), 'Potential sea-level rise from Antarctic ice-sheet instability constrained by observations', *Nature* **528**(7580), 115–118.

Ritz, C., Fabre, A. and Letréguilly, A. (1996), 'Sensitivity of a Greenland ice sheet model to ice flow and ablation parameters: consequences for the evolution through the last climatic cycle', *Climate Dynamics* **13**, 11–23.

Roeckner, E., Bäuml, G., Bonaventura, L., Brokopf, R., Esch, M., Giorgetta, M., Hagemann, S., Kirchner, I., Kornblueh, L., Manzini, E. et al. (2003), 'The atmospheric general circulation model ECHAM 5. PART I: Model description'.

Roeckner, E., Brokopf, R., Esch, M., Giorgetta, M., Hagemann, S., Kornblueh, L., Manzini, E., Schlese, U. and Schulzweida, U. (2004), 'The atmospheric general circulation model ECHAM5 Part II: Sensitivity of simulated climate to horizontal and vertical resolution'.

Rutt, I. C., Hagdorn, M., Hulton, N. and Payne, A. (2009), 'The Glimmer community ice sheet model', *Journal of Geophysical Research: Earth Surface* **114**(F2).

Saito, F., Abe-Ouchi, A., Takahashi, K. and Blatter, H. (2016), 'SeaRISE experiments revisited: potential sources of spread in multi-model projections of the Greenland ice sheet', *The Cryosphere* **10**(1), 43–63.

Saltelli, A., Aleksankina, K., Becker, W., Fennell, P., Ferretti, F., Holst, N., Li, S. and Wu, Q. (2019), 'Why so many published sensitivity analyses are false: A systematic review of sensitivity analysis practices', *Environmental modelling & software* **114**, 29–39.

Seroussi, H., Nowicki, S., Payne, A. J., Goelzer, H., Lipscomb, W. H., Abe Ouchi, A., Agosta, C., Albrecht, T., Asay-Davis, X., Barthel, A. et al. (2020), 'ISMIP6 Antarctica: a multi-model ensemble of the Antarctic ice sheet evolution over the 21 st century', *The Cryosphere Discussions* **2020**, 1–54.

Shackleton, N. J. (1973), 'Oxygen isotope analysis as a means of determining season of occupation of prehistoric midden sites', *Archaeometry* **15**(1), 133–141.

Shaw, J. (1983), 'Drumlin formation related to inverted melt-water erosional marks', *Journal of Glaciology* **29**(103), 461–479.

Siegert, M. J. and Dowdeswell, J. A. (2004), 'Numerical reconstructions of the Eurasian Ice Sheet and climate during the Late Weichselian', *Quaternary Science Reviews* **23**(11-13), 1273–1283.

Small, D., Clark, C. D., Chiverrell, R. C., Smedley, R. K., Bateman, M. D., Duller, G. A., Ely, J. C., Fabel, D., Medialdea, A. and Moreton, S. G. (2017), 'Devising quality assurance procedures for assessment of legacy geochronological data relating to deglaciation of the last British-Irish Ice Sheet', *Earth-Science Reviews* **164**, 232–250.

Smalley, I. J. (1981), 'Conjectures, hypotheses, and theories of drumlin formation (In memory of Stanislaw Baranowski)', *Journal of Glaciology* **27**(97), 503–505.

Smalley, I. J. and Unwin, D. J. (1968), 'The formation and shape of drumlins and their distribution and orientation in drumlin fields', *Journal of Glaciology* **7**(51), 377–390.

Smith, J. A., Graham, A. G., Post, A. L., Hillenbrand, C.-D., Bart, P. J. and Powell, R. D. (2019), 'The marine geological imprint of Antarctic ice shelves', *Nature Communications* **10**(1), 5635.

Sobol', I. (1993), 'Sensitivity analysis for non-linear mathematical models', *Mathematical Modeling & Computational Experiment* **1**, 407–414.

Spagnolo, M., Clark, C. D., Ely, J. C., Stokes, C. R., Anderson, J. B., Andreassen, K., Graham, A. G. and King, E. C. (2014), 'Size, shape and spatial arrangement of mega-scale glacial lineations from a large and diverse dataset', *Earth Surface Processes and Landforms* **39**(11), 1432–1448.

Spagnolo, M., Clark, C. D., Hughes, A. L. and Dunlop, P. (2011), 'The topography of drumlins; assessing their long profile shape', *Earth Surface Processes and Landforms* **36**(6), 790–804.

Spagnolo, M., Clark, C. D., Hughes, A. L., Dunlop, P. and Stokes, C. R. (2010), 'The planar shape of drumlins', *Sedimentary Geology* **232**(3-4), 119–129.

Stoker, B. J., Dulfer, H. E., Stokes, C. R., Brown, V. H., Clark, C. D., Ó Cofaigh, C., Evans, D. J., Froese, D., Norris, S. L. and Margold, M. (2024), 'Ice flow dynamics of the northwestern Laurentide Ice Sheet during the last deglaciation', *EGUsphere* **2024**, 1–60.

Stokes, C. R., Clark, C. D. and Storrar, R. (2009), 'Major changes in ice stream dynamics during deglaciation of the north-western margin of the Laurentide Ice Sheet', *Quaternary Science Reviews* **28**(7-8), 721–738.

Stokes, C. R., Tarasov, L., Blomdin, R., Cronin, T. M., Fisher, T. G., Gyllencreutz, R., Hättestrand, C., Heyman, J., Hindmarsh, R. C., Hughes, A. L. et al. (2015), 'On the reconstruction of palaeo-ice sheets: recent advances and future challenges', *Quaternary Science Reviews* **125**, 15–49.

Stokes, G. G. (1843), 'On some cases of fluid motion', *Mathematical and Physical Papers vol.1* **8**, 105–137.

Strong, M., Oakley, J. E. and Brennan, A. (2014), 'Estimating Multiparameter Partial Expected Value of Perfect Information from a Probabilistic Sensitivity Analysis Sample: A Nonparametric Regression Approach', *Medical Decision Making* **34**(3), 311–326.

Sueyoshi, T., Ohgaito, R., Yamamoto, A., Chikamoto, M., Hajima, T., Okajima, H., Yoshimori, M., Abe, M., O'ishi, R., Saito, F. et al. (2013), 'Set-up of the PMIP3 paleoclimate experiments conducted using an Earth system model, MIROC-ESM', *Geoscientific Model Development* **6**(3), 819–836.

Sun, C. and Hahn, J. (2006), 'Parameter reduction for stable dynamical systems based on Hankel singular values and sensitivity analysis', *Chemical engineering science* **61**(16), 5393–5403.

Talbot, S. and Harrison Jr, W. (1966), 'Computer evaluation of graphical physiologic data for diagnosis of coronary heart disease', *Methods of Information in Medicine* **5**(02), 81–85.

Tarasov, L., Dyke, A., Neal, R. and Peltier, W. (2012), 'A data-calibrated distribution of deglacial chronologies for the North American ice complex from glaciological modeling', *Earth and Planetary Science Letters* **315**, 30–40.

the PISM authors (n.d.), 'Publications'. `https://www.pism.io/publications/`.

Tulaczyk, S., Kamb, W. B. and Engelhardt, H. F. (2000), 'Basal mechanics of ice stream B, West Antarctica: 1. Till mechanics', *Journal of Geophysical Research: Solid Earth* **105**(B1), 463–481.

Turner, F. (2020), Ice Cores and Emulation: Learning More About Past Ice Sheet Shapes, PhD thesis, University of Sheffield.

Turner, F. E., Buck, C. E., Jones, J. M., Sime, L. C., Vallet, I. M. and Wilkinson, R. D. (2023), 'Reconstructing the Antarctic ice-sheet shape at the Last Glacial Maximum using ice-core data', *Journal of the Royal Statistical Society Series C: Applied Statistics* **72**(5), 1493–1511.
URL: *https://doi.org/10.1093/jrsssc/qlad078*

Valcke, S., Guilyardi, E. and Larsson, C. (2006), 'Prism and enes: a European approach to earth system modelling.', **18**(2), 231–245.

van der Veen, C. J. (1989), 'A numerical scheme for calculating stresses and strain rates in glaciers', *Mathematical geology* **21**, 363–377.

van Der Veen, C. J. and Whillans, I. (1989), 'Force budget: I. Theory and numerical methods', *Journal of Glaciology* **35**(119), 53–60.

van Riel, N. A. (2006), 'Dynamic modelling and analysis of biochemical networks: mechanism-based models and model-based experiments', *Briefings in bioinformatics* **7**(4), 364–374.

van Werkhoven, K., Wagener, T., Reed, P. and Tang, Y. (2009), 'Sensitivity-guided reduction of parametric dimensionality for multi-objective calibration of watershed models', *Advances in Water Resources* **32**(8), 1154–1169.

Vernon, I., Goldstein, M. and Bowerz, R. G. (2010), 'Galaxy formation: A Bayesian uncertainty analysis', *Bayesian analysis* **5**(4), 619–670.

von Mises, R. (1981), 'Uber die "Ganzzahligkeit" der Atomgewicht und verwandte Fragen', *Physikal. Z.* **19**, 490–500.
URL: *https://cir.nii.ac.jp/crid/1571135650500724992*

Weertman, J. (1957), 'On the Sliding of Glaciers', *Journal of glaciology* **3**(21), 33–38.

Weis, M., Greve, R. and Hutter, K. (1999), 'Theory of shallow ice shelves', *Continuum Mechanics and Thermodynamics* **11**, 15–50.

Wernecke, A., Edwards, T. L., Nias, I. J., Holden, P. B. and Edwards, N. R. (2020), 'Spatial probabilistic calibration of a high-resolution Amundsen Sea Embayment ice sheet model with satellite altimeter data', *The Cryosphere* **14**(5), 1459–1474.

Wetzel, P., Haak, H., Jungclaus, J. and Maier-Reimer, E. (2004), 'The Max-Planck-institute global ocean/sea ice model'.

White, M. A., Thornton, P. E., Running, S. W. and Nemani, R. R. (2000), 'Parameterization and sensitivity analysis of the BIOME–BGC terrestrial ecosystem model: Net primary production controls', *Earth interactions* **4**(3), 1–85.

Whitehouse, P. L., Bentley, M. J. and Le Brocq, A. M. (2012), 'A deglacial model for Antarctica: geological constraints and glaciological modelling as a basis for a new model of Antarctic glacial isostatic adjustment', *Quaternary Science Reviews* **32**, 1–24.

Whitehouse, P. L., Bentley, M. J., Milne, G. A., King, M. A. and Thomas, I. D. (2012), 'A new glacial isostatic adjustment model for Antarctica: calibrated and tested using observations of relative sea-level change and present-day uplift rates', *Geophysical Journal International* **190**(3), 1464–1482.

Winkelmann, R., Martin, M. A., Haseloff, M., Albrecht, T., Bueler, E., Khroulev, C. and Levermann, A. (2011), 'The Potsdam parallel ice sheet model (PISM-PIK)–Part 1: Model description', *The Cryosphere* **5**(3), 715–726.

Winsborrow, M. C., Andreassen, K., Corner, G. D. and Laberg, J. S. (2010), 'Deglaciation of a marine-based ice sheet: Late Weichselian palaeo-ice dynamics and retreat in the southern Barents Sea reconstructed from onshore and offshore glacial geomorphology', *Quaternary Science Reviews* **29**(3-4), 424–442.

Wu, J., Dhingra, R., Gambhir, M. and Remais, J. V. (2013), 'Sensitivity analysis of infectious disease models: methods, advances and their application', *Journal of The Royal Society Interface* **10**(86), 20121018.

Zweck, C. and Huybrechts, P. (2005), 'Modeling of the northern hemisphere ice sheets during the last glacial cycle and glaciological sensitivity', *Journal of Geophysical Research: Atmospheres* **110**(D7).

Appendix A Initial ensemble parameter inputs and LALA scores

Model Number	E	n	q	H_{cr}	F_s	F_i	τ_c^s	τ_c^b	τ_c^o	τ_c^{tk}	τ_c^{tn}	α_1^{LGM}	α_2^{LGM}	α_1^{PI}	m_{br}	m_s	m_{ba}	F_{melt}	γ_T	β	LALA Score
128	1.273	2.068	0.942	68.325	2.761	9.978	11.791	148.770	22.345	51.903	82.492	-0.187	0.156	-0.442	10.193	9.180	0.757	0.020	0.076	94.954	-101608
121	0.740	2.001	0.428	287.469	2.822	7.950	17.543	120.666	11.975	39.579	71.884	0.010	0.253	-0.480	10.287	6.211	1.354	0.022	0.062	44.095	-104411
130	1.623	3.964	0.382	60.278	2.287	9.726	12.088	127.797	29.781	35.022	87.402	-0.905	0.942	-0.414	25.240	9.845	1.418	0.017	0.053	88.935	-105111
119	1.784	3.910	0.038	256.569	4.987	5.086	17.950	109.904	17.685	55.063	95.900	-0.889	0.571	-0.657	17.171	9.851	1.965	0.022	0.060	56.388	-105817
67	2.147	2.033	0.749	88.418	4.290	5.451	14.584	137.927	16.248	33.143	66.049	-0.954	-0.494	-0.679	16.277	6.545	1.292	0.024	0.087	80.669	-106468
9	1.364	2.089	0.228	196.829	4.182	8.071	16.350	142.465	20.919	52.918	64.426	-0.220	0.426	-0.476	28.852	8.200	1.739	0.033	0.056	99.320	-106595
189	1.751	3.865	0.349	270.094	3.106	6.254	15.920	139.190	28.510	56.679	74.878	-0.335	0.785	0.215	28.498	9.778	1.604	0.027	0.044	82.507	-107021
43	1.962	3.500	0.009	166.570	4.328	8.414	10.464	147.829	22.803	45.974	89.399	0.788	-0.534	-0.341	12.058	9.119	0.946	0.022	0.072	41.803	-107630
30	1.649	3.449	0.010	255.592	2.769	8.386	10.950	144.951	16.388	44.426	85.318	0.052	-0.528	0.959	11.469	8.763	1.067	0.010	0.072	42.796	-108053
3	2.002	2.551	0.122	105.385	3.621	8.267	13.813	127.455	19.609	53.566	65.184	-0.327	0.989	-0.226	22.630	7.440	1.796	0.014	0.072	49.463	-108253
136	2.285	2.016	0.086	123.982	3.116	9.170	19.424	103.986	13.858	54.156	64.990	-0.342	-0.562	-0.598	16.065	6.012	1.167	0.040	0.070	65.897	-108472
70	0.965	3.660	0.551	263.267	2.053	8.451	9.316	129.901	25.211	42.756	92.137	-0.779	0.922	-0.290	25.051	8.045	1.801	0.041	0.043	69.202	-108572
101	0.980	3.715	0.225	265.356	3.406	9.595	12.250	117.995	11.455	33.747	71.364	-0.633	0.244	-0.111	25.371	7.483	0.825	0.044	0.088	42.415	-108743
153	2.370	3.726	0.308	221.296	4.891	9.797	9.789	144.605	14.666	47.963	64.708	-0.388	0.887	0.169	23.349	7.644	1.254	0.028	0.058	67.974	-109160
171	0.853	2.079	0.805	140.361	4.791	7.495	15.805	149.933	13.007	44.683	97.729	-0.278	-0.965	-0.331	29.578	8.283	0.916	0.029	0.078	49.739	-109397
140	0.752	2.571	0.740	178.065	4.429	7.038	19.070	142.022	23.673	33.823	83.490	-0.071	0.900	-0.186	16.445	6.511	1.940	0.029	0.087	90.911	-109726
179	0.815	2.331	0.292	253.666	3.450	7.987	13.962	147.444	14.731	43.124	89.831	-0.565	0.873	-0.123	20.923	6.870	1.704	0.049	0.071	62.568	-109739
68	2.757	2.376	0.052	100.855	2.032	5.382	17.382	134.940	29.417	30.075	60.875	0.703	0.939	-0.770	11.214	6.973	0.899	0.047	0.089	54.408	-109941
21	1.104	2.183	0.078	145.471	2.485	7.380	12.165	142.695	25.966	66.168	62.504	0.838	-0.111	-0.866	26.294	9.449	0.931	0.036	0.054	40.883	-109988
10	0.878	2.023	0.482	278.651	2.794	8.687	10.674	104.220	20.007	61.139	85.967	0.968	-0.345	0.872	29.798	7.757	1.146	0.026	0.061	79.857	-110030
66	1.038	3.193	0.102	154.137	4.926	8.138	16.991	122.461	19.989	48.552	76.537	0.727	0.314	-0.577	17.207	8.488	1.687	0.046	0.084	55.668	-110224
28	0.690	3.936	0.726	201.487	2.907	6.493	10.193	107.490	16.792	59.766	64.123	-0.876	0.524	-0.682	23.707	8.569	1.784	0.008	0.056	93.593	-111026
93	1.738	2.841	0.959	160.551	4.774	9.188	18.295	146.826	24.252	40.076	62.126	-0.372	0.856	-0.038	20.230	8.310	1.871	0.013	0.059	60.636	-111095
51	1.688	2.159	0.656	167.768	3.437	9.521	7.776	149.231	15.290	57.746	66.240	-0.052	0.955	-0.422	14.262	9.750	0.754	0.024	0.069	53.690	-111515
166	2.648	2.867	0.059	102.616	3.565	7.972	8.293	148.670	12.993	41.027	79.149	-0.047	-0.243	0.631	24.191	9.207	0.535	0.032	0.087	57.915	-111819
173	1.017	2.201	0.005	77.172	3.495	5.010	9.249	125.168	21.097	60.881	63.483	-0.704	-0.352	-0.158	18.205	7.167	1.990	0.038	0.047	46.450	-112229
73	2.708	3.985	0.234	285.557	4.526	8.122	9.862	126.883	16.914	54.666	97.265	-0.070	0.808	-0.822	16.566	6.332	0.577	0.031	0.063	46.949	-112508
96	0.521	2.461	0.100	75.866	3.899	8.234	16.241	117.607	28.158	67.115	83.836	0.951	-0.224	-0.876	22.763	8.451	0.796	0.045	0.062	79.001	-112634
42	0.719	3.783	0.477	262.056	2.747	7.740	12.547	129.573	13.523	55.216	72.590	-0.547	0.224	0.195	20.410	9.511	0.733	0.042	0.059	98.637	-112728
46	2.549	3.457	0.368	138.321	3.272	7.132	6.147	112.070	15.982	43.224	76.769	0.243	0.849	-0.959	21.233	9.345	1.758	0.039	0.081	43.296	-112907
167	2.510	2.057	0.159	109.178	4.379	5.784	12.416	108.609	29.038	53.969	90.994	-0.836	-0.205	-0.841	22.351	5.442	1.383	0.027	0.049	91.310	-112978
125	2.988	3.949	0.929	111.184	4.106	8.086	12.834	108.973	13.431	51.096	75.782	-0.597	0.120	-0.646	14.510	9.283	1.107	0.042	0.064	46.615	-113027

26	1.841	2.111	0.606	249.730	3.031	7.201	18.474	110.157	19.214	30.223	90.783	-0.620	0.199	-0.370	12.973	8.380	0.545	0.019	0.071	52.996	-113143
33	0.797	2.642	0.032	195.531	2.269	7.783	9.086	133.039	15.676	53.266	96.082	-0.028	-0.277	0.823	28.812	8.631	0.942	0.021	0.081	60.000	-113446
39	2.568	3.656	0.541	275.267	3.202	7.654	16.479	106.243	18.576	63.937	78.884	-0.152	0.520	-0.440	26.830	7.059	0.629	0.041	0.069	81.347	-113914
172	1.224	2.142	0.784	282.418	3.276	5.889	13.167	101.284	27.478	51.201	80.145	-0.141	0.167	-0.795	11.139	9.012	1.566	0.008	0.041	61.335	-113945
157	0.575	2.952	0.799	73.432	2.936	7.579	7.085	128.583	14.508	39.759	81.066	-0.123	0.994	-0.251	22.155	5.994	1.590	0.045	0.048	70.421	-113974
107	2.360	2.274	0.717	220.574	2.236	9.037	18.688	112.530	24.085	35.440	60.232	-0.963	0.497	0.681	21.355	8.864	1.544	0.011	0.086	71.214	-114196
54	1.317	3.844	0.216	155.795	4.946	5.316	13.719	130.758	19.405	44.238	78.215	-0.933	-0.992	0.329	22.330	6.975	0.563	0.023	0.061	61.081	-114384
123	1.889	2.281	0.073	189.509	4.312	6.583	19.198	101.758	18.486	49.383	75.448	0.569	-0.592	0.662	27.974	8.066	1.216	0.010	0.068	55.466	-114463
150	2.978	2.104	0.181	162.132	3.798	7.111	11.564	144.493	26.012	53.666	80.576	0.233	-0.128	0.442	25.808	5.888	0.585	0.038	0.057	87.895	-114516
192	2.158	3.116	0.344	149.020	4.148	9.069	12.681	127.544	21.438	34.106	99.277	0.045	0.262	0.095	22.721	9.807	0.891	0.008	0.090	40.285	-114532
124	1.920	2.295	0.972	127.320	2.883	7.518	10.725	119.544	27.163	55.796	84.681	-0.744	0.608	0.898	12.387	6.390	0.648	0.005	0.046	77.376	-114581
146	2.079	2.503	0.259	294.657	3.066	7.720	18.106	131.483	17.708	43.525	63.020	-0.850	0.174	0.238	26.007	8.697	1.398	0.014	0.045	89.701	-114596
152	1.472	2.840	0.310	98.540	3.318	8.732	11.204	149.341	18.144	69.813	69.104	-0.485	0.416	0.462	21.467	7.463	1.273	0.032	0.061	76.498	-114636
86	0.924	3.108	0.931	180.902	2.306	7.676	14.966	149.599	10.685	64.101	84.142	-0.502	0.206	0.983	29.051	9.313	1.778	0.039	0.079	71.699	-114666
154	2.462	2.960	0.147	64.803	4.392	6.040	14.994	128.247	24.599	57.154	73.385	0.574	0.460	-0.303	23.968	7.547	0.636	0.021	0.069	62.376	-114703
95	2.865	2.800	0.889	231.590	3.717	8.152	5.873	132.722	16.147	67.389	85.571	-0.807	0.394	0.736	20.786	9.724	1.263	0.033	0.079	86.037	-114750
74	1.976	3.677	0.280	95.777	2.209	7.816	15.977	136.689	11.532	48.619	80.371	-0.451	-0.471	-0.102	27.347	7.797	1.950	0.025	0.043	79.364	-114799
186	2.230	2.979	0.562	295.611	4.354	6.927	13.390	103.443	15.899	58.735	69.919	0.095	0.862	0.402	18.975	9.367	1.464	0.016	0.082	92.325	-114834
195	1.003	3.748	0.841	85.621	2.392	6.571	10.786	136.189	10.087	38.838	70.716	-0.671	0.076	0.028	29.334	7.196	1.042	0.011	0.062	50.704	-114992
117	2.887	2.223	0.517	289.044	4.445	5.844	19.601	140.645	13.633	67.874	73.894	0.080	0.552	-0.556	16.175	6.317	1.982	0.047	0.082	46.267	-115042
59	2.128	3.739	0.920	192.970	4.508	9.500	8.943	138.487	23.780	42.151	96.735	0.186	0.736	-0.905	13.443	8.355	0.809	0.021	0.060	86.563	-115044
56	2.924	3.922	0.912	228.554	3.681	7.905	15.623	135.411	22.984	66.955	97.888	-0.170	0.547	0.589	26.586	7.501	1.749	0.044	0.081	88.415	-115120
40	2.689	2.473	0.406	78.990	4.857	5.698	11.120	113.595	17.094	35.701	73.004	-0.787	0.904	-0.463	10.780	7.286	0.655	0.030	0.066	80.983	-115153
60	1.326	2.752	0.722	62.280	4.865	9.903	5.130	130.669	13.941	45.647	99.002	0.226	0.723	0.301	19.454	6.837	1.269	0.047	0.079	45.920	-115182
113	0.599	3.592	0.900	131.870	3.869	6.135	16.804	137.575	28.930	60.787	99.642	-0.668	-0.087	0.281	24.875	8.442	1.022	0.013	0.080	48.916	-115199
185	0.836	2.819	0.916	273.539	4.572	6.207	14.733	142.843	16.002	31.361	75.208	-0.826	-0.079	-0.580	28.063	5.524	1.678	0.030	0.046	42.161	-115306
135	2.331	2.778	0.764	162.708	4.069	6.643	5.511	134.450	20.611	32.240	94.761	-0.119	0.439	0.150	17.978	9.990	1.160	0.011	0.053	88.253	-115381
99	2.964	3.289	0.769	119.362	2.828	8.571	14.358	128.804	19.572	43.675	90.153	-0.698	-0.334	-0.900	25.643	8.228	1.310	0.044	0.055	47.893	-115626
144	2.103	3.006	0.862	182.340	3.698	9.354	8.135	134.506	25.573	46.166	72.680	0.451	0.304	-0.852	26.408	6.753	1.926	0.034	0.055	74.998	-115680
65	2.320	3.244	0.681	192.468	4.965	6.024	13.234	100.432	23.802	40.885	74.452	-0.427	0.042	-0.619	26.117	7.904	0.861	0.012	0.083	45.486	-115694
180	2.896	2.219	0.788	54.460	2.546	7.251	9.420	123.588	20.434	52.622	81.630	0.507	0.634	-0.931	19.587	6.236	1.229	0.049	0.075	76.710	-115795
198	1.764	3.852	0.334	144.077	2.243	5.038	8.425	119.885	14.200	50.051	77.781	0.886	-0.176	-0.963	9.118	7.245	1.722	0.037	0.078	59.554	-115853
176	2.670	2.124	0.168	239.404	3.597	7.752	7.420	129.319	24.977	30.919	66.403	-0.262	0.698	0.100	12.700	5.968	1.196	0.020	0.083	96.077	-115929
111	1.161	2.317	0.389	93.506	2.728	9.600	14.020	140.919	14.325	48.825	88.446	-0.420	0.916	-0.995	9.844	7.100	0.909	0.006	0.054	91.078	-115940
127	1.056	2.654	0.829	159.725	4.466	7.838	8.743	118.172	13.302	63.127	71.142	-0.819	-0.543	-0.737	23.223	9.396	1.726	0.050	0.054	84.984	-115951
196	2.654	3.477	0.804	247.898	2.338	8.515	19.359	115.165	27.281	40.681	81.951	-0.586	0.327	0.400	17.758	5.852	1.615	0.045	0.065	40.933	-116009
14	0.512	3.328	0.503	94.732	2.153	6.519	6.741	102.061	12.350	58.535	67.354	-0.473	-0.015	-0.533	16.493	6.743	1.491	0.009	0.067	49.267	-116015
69	2.062	2.258	0.050	206.230	4.972	6.809	17.811	120.306	18.919	61.497	92.559	-0.870	0.473	0.576	22.984	5.421	0.838	0.024	0.058	84.618	-116092
116	2.248	3.767	0.965	299.667	4.706	6.998	12.039	145.548	15.091	68.467	65.413	-0.217	0.488	0.601	12.285	9.097	0.625	0.012	0.054	81.424	-116142
88	1.491	3.633	0.022	66.158	4.194	5.207	14.762	115.838	13.779	35.880	83.648	0.000	-0.936	0.336	18.735	6.916	0.521	0.030	0.077	70.668	-116259
159	2.857	2.048	0.253	228.863	3.186	9.893	7.265	100.859	27.563	36.876	96.460	-0.757	-0.773	-0.504	18.366	5.386	0.524	0.034	0.048	91.679	-116266
44	2.790	2.568	0.142	194.004	4.483	8.890	12.965	125.676	26.950	60.520	76.156	0.349	0.293	-0.015	25.438	9.232	1.319	0.016	0.066	41.539	-116293
149	2.741	2.995	0.128	223.261	3.961	9.571	6.065	125.849	12.613	65.347	80.609	0.105	-0.296	-0.296	18.575	8.810	1.426	0.037	0.061	86.453	-116294
63	2.529	3.512	0.948	187.200	3.456	8.764	15.084	118.414	22.125	62.684	94.146	-0.551	0.684	0.763	22.896	5.594	1.183	0.019	0.065	58.969	-116416

170	0.926	3.700	0.372	243.460	3.381	6.159	18.213	110.683	15.404	37.886	74.134	0.735	0.963	-0.833	9.285	9.886	0.816	0.043	0.053	50.902	-116515
36	2.784	3.435	0.451	114.092	3.335	8.962	18.861	114.750	25.405	42.317	65.901	0.528	0.815	-0.549	18.067	7.854	0.806	0.029	0.044	93.807	-116594
37	1.377	2.164	0.997	185.175	3.756	7.562	11.969	121.891	26.598	31.948	95.513	0.875	0.599	-0.710	14.192	8.520	1.051	0.040	0.080	67.357	-116774
112	1.127	3.022	0.173	266.725	4.649	8.433	15.469	125.372	28.677	54.549	91.128	-0.606	-0.921	-0.071	21.910	7.686	1.540	0.015	0.084	63.793	-116835
108	2.398	3.308	0.028	142.016	2.888	9.314	15.174	134.195	10.157	33.563	62.856	0.170	0.758	0.370	20.091	5.646	0.505	0.026	0.042	94.259	-116863
109	1.348	3.565	0.687	157.922	2.410	8.491	8.622	147.213	20.164	52.450	67.869	0.332	0.679	0.904	27.862	8.844	1.760	0.034	0.048	78.763	-116943
190	0.683	3.872	0.263	81.097	3.358	6.969	11.608	133.998	23.546	58.896	81.315	-0.097	0.536	0.865	11.656	5.216	1.898	0.036	0.071	57.351	-116973
169	1.444	2.200	0.361	72.099	2.510	9.635	16.868	105.832	12.245	32.852	86.933	-0.947	-0.405	0.933	10.860	6.684	1.825	0.043	0.060	72.430	-117005
182	1.522	3.361	0.326	115.302	3.811	9.420	14.644	113.149	18.623	49.108	85.197	-0.795	-0.705	0.802	9.513	9.260	0.514	0.050	0.084	47.600	-117032
8	1.680	2.099	0.324	62.635	4.544	7.226	10.398	112.268	18.898	38.549	86.761	0.637	0.275	0.531	13.737	6.706	0.988	0.041	0.053	72.904	-117038
129	1.851	3.032	0.630	116.640	3.998	8.808	6.958	121.177	28.446	34.757	92.784	-0.361	-0.259	0.341	25.514	8.950	1.618	0.048	0.073	69.567	-117207
134	1.831	2.593	0.674	179.519	2.081	5.184	14.864	111.893	17.471	49.923	80.800	-0.193	0.769	-0.499	15.244	7.926	0.726	0.008	0.084	68.319	-117223
49	2.624	2.242	0.198	127.659	4.460	9.379	9.958	113.943	23.252	54.849	68.258	-0.317	-0.398	-0.058	13.359	7.824	1.439	0.010	0.057	77.601	-117299
100	0.726	3.058	0.540	251.869	4.668	6.399	6.439	114.243	29.513	57.895	89.760	-0.302	0.349	-0.945	10.400	8.607	1.915	0.016	0.090	82.724	-117394
6	2.771	3.817	0.597	91.450	4.593	6.704	16.123	117.152	27.659	61.922	63.860	-0.134	-0.468	-0.394	19.236	9.544	0.967	0.033	0.047	95.457	-117498
75	1.533	2.727	0.834	202.648	2.603	8.837	15.569	132.837	24.486	65.504	77.095	-0.974	-0.635	0.435	15.321	5.085	1.993	0.006	0.085	63.366	-117527
118	2.722	2.749	0.162	280.597	2.364	8.578	6.838	141.655	12.881	62.032	87.165	-0.202	-0.137	0.674	27.546	8.669	1.519	0.034	0.063	93.252	-117529
178	1.437	2.134	0.936	243.946	2.451	7.328	5.968	108.460	28.351	47.275	98.485	-0.241	-0.947	0.049	18.290	6.422	0.606	0.038	0.068	68.865	-117546
197	0.894	2.611	0.692	112.053	4.848	6.442	13.573	105.372	17.191	41.925	89.002	-0.236	0.189	-0.145	18.503	9.055	1.559	0.049	0.050	80.231	-117584
47	0.626	3.333	0.459	207.701	2.631	5.343	9.426	138.684	16.595	45.511	90.445	-0.431	0.335	-0.765	17.668	7.609	1.484	0.019	0.083	97.007	-117585
191	1.735	3.831	0.041	206.957	2.274	8.359	14.254	111.744	14.945	35.222	93.639	0.415	-0.303	0.562	9.364	9.966	1.414	0.006	0.044	87.376	-117698
85	1.579	3.552	0.392	274.671	3.223	6.892	11.711	145.027	19.361	69.205	76.369	-0.925	-0.446	0.245	10.657	7.382	0.699	0.012	0.051	43.801	-117839
183	1.901	3.127	0.866	259.348	2.696	9.293	8.310	120.888	17.287	56.077	98.243	0.422	0.660	0.740	23.140	8.335	1.448	0.018	0.048	50.202	-117953
35	1.233	2.489	0.240	242.071	4.220	8.312	6.011	148.475	16.805	38.023	67.573	-0.167	0.137	0.416	19.363	7.312	1.956	0.023	0.068	92.018	-118049
132	1.551	2.178	0.604	250.446	2.523	8.786	9.025	144.169	10.859	61.768	88.877	0.535	0.110	0.560	21.622	8.929	0.883	0.018	0.042	61.799	-118052
164	2.449	2.683	0.440	269.459	4.747	8.222	11.831	119.256	18.719	34.492	82.257	0.492	0.713	-0.193	28.697	5.019	0.974	0.032	0.052	53.876	-118082
7	1.717	3.887	0.437	137.178	3.535	8.706	6.275	107.854	29.103	58.274	98.609	-0.520	-0.411	0.134	27.787	5.135	1.457	0.048	0.075	65.477	-118127
52	1.403	3.343	0.116	52.699	2.061	9.441	16.713	139.872	20.240	32.426	68.524	0.168	-0.588	0.615	21.968	9.404	1.665	0.049	0.088	62.951	-118173
34	2.590	3.548	0.568	212.747	4.499	9.767	17.283	133.356	11.801	31.703	60.465	0.777	0.971	0.503	26.660	7.404	0.961	0.040	0.046	62.174	-118194
145	1.673	3.586	0.353	277.186	4.686	5.851	5.602	111.499	21.242	37.678	73.413	-0.518	-0.217	0.859	23.693	6.198	1.283	0.043	0.086	52.705	-118198
16	1.999	3.213	0.192	200.318	3.548	8.291	16.257	100.707	20.745	49.491	87.338	0.068	0.741	-0.004	13.214	6.131	1.364	0.027	0.060	73.391	-118246
1	1.651	2.712	0.298	291.575	3.616	7.001	15.304	131.814	13.136	63.659	79.462	0.641	0.797	0.591	13.601	9.697	1.846	0.033	0.045	58.421	-118258
31	2.033	3.290	0.758	129.802	4.369	5.402	13.449	101.609	24.781	56.458	75.855	0.557	0.617	-0.975	26.852	7.891	1.649	0.036	0.075	57.401	-118394
38	1.081	2.321	0.062	150.816	4.679	8.991	6.223	106.988	21.764	31.195	68.917	0.308	0.582	0.620	10.100	5.349	1.371	0.028	0.087	71.079	-118419
138	1.000	2.761	0.214	297.098	4.026	5.622	14.493	143.080	22.788	51.686	61.326	-0.895	-0.390	0.074	29.896	6.671	1.141	0.041	0.089	67.150	-118602
156	1.545	3.180	0.988	156.306	4.016	7.445	12.889	116.068	25.169	47.625	72.349	0.600	0.657	-0.813	27.240	6.605	0.774	0.046	0.040	64.299	-118815
194	1.072	3.358	0.424	236.663	2.681	7.420	10.312	146.250	11.195	32.776	81.473	0.193	0.373	-0.757	16.731	6.947	1.862	0.036	0.089	51.926	-118824
55	2.934	2.384	0.618	290.220	4.174	8.193	9.188	114.366	27.780	64.640	61.429	-0.683	-0.573	0.425	16.913	6.883	1.839	0.041	0.070	54.843	-118945
77	2.098	2.347	0.791	271.966	3.966	9.234	17.689	132.052	12.740	37.201	66.754	0.468	0.360	0.179	14.606	8.541	0.780	0.049	0.081	50.036	-119106
105	1.609	2.680	0.731	184.512	3.051	6.092	5.023	104.866	22.254	64.250	77.577	0.208	0.626	-0.093	9.789	5.849	1.529	0.007	0.057	84.003	-119140
199	0.644	2.369	0.238	297.623	2.656	6.532	10.895	124.338	11.661	64.801	91.670	0.037	0.507	0.995	15.139	5.167	1.851	0.025	0.076	60.394	-119157
147	1.876	3.521	0.592	204.106	2.594	5.944	7.488	128.266	25.662	52.172	82.155	0.756	0.564	-0.041	10.531	9.596	0.872	0.035	0.070	87.098	-119165
87	1.295	2.782	0.584	279.021	2.860	7.063	18.030	104.547	18.295	41.510	76.985	-0.017	-0.154	-0.383	29.144	9.487	1.011	0.046	0.050	44.669	-119302
181	1.420	3.095	0.203	164.618	3.886	9.121	9.718	141.849	23.363	50.426	85.714	0.859	-0.973	-0.744	21.067	9.744	1.112	0.040	0.043	99.679	-119531

98	2.264	3.172	0.083	148.289	2.807	7.323	18.789	108.116	21.183	68.609	77.924	0.366	0.401	-0.702	21.529	5.819	1.174	0.011	0.045	78.316	-119707
165	1.928	3.403	0.707	233.687	2.577	7.188	7.604	126.371	20.807	68.051	93.009	0.518	-0.762	0.777	20.721	8.126	1.509	0.048	0.067	56.961	-119733
158	2.837	3.606	0.648	138.972	4.077	7.453	18.919	141.343	26.399	42.811	77.369	0.214	0.649	-0.728	24.043	5.540	0.546	0.027	0.056	78.470	-119750
72	1.147	2.358	0.573	216.362	2.991	9.948	8.009	127.081	29.908	51.434	64.277	0.482	0.148	0.186	21.171	9.912	1.498	0.023	0.052	76.287	-119762
177	2.216	2.589	0.737	213.863	3.424	5.232	5.685	143.386	10.336	36.306	90.394	-0.647	0.058	0.483	19.778	9.140	1.131	0.045	0.041	77.137	-119829
160	1.970	3.825	0.107	50.264	3.256	6.843	12.478	119.169	11.310	48.213	62.253	0.917	-0.196	0.528	21.810	5.111	1.431	0.009	0.064	56.102	-119942
91	0.616	2.538	0.396	212.431	3.301	5.583	6.709	117.426	24.179	52.333	69.489	0.396	0.824	0.693	20.635	9.471	1.316	0.021	0.077	55.035	-119974
120	0.603	3.468	0.269	87.112	4.093	6.247	17.126	107.561	11.278	39.172	93.837	0.110	-0.281	-0.180	15.542	7.589	1.833	0.047	0.086	64.554	-120119
61	0.953	3.207	0.825	55.919	4.721	9.664	15.705	126.652	17.599	57.323	62.618	0.973	0.774	-0.663	24.288	5.483	1.200	0.018	0.041	80.035	-120259
161	2.514	3.389	0.114	187.636	4.918	6.868	15.366	105.037	10.251	54.290	71.507	0.842	-0.751	-0.205	18.866	8.900	0.571	0.014	0.059	60.913	-120266
139	2.477	3.894	0.068	121.487	2.617	9.813	7.962	116.868	14.863	45.266	92.349	0.405	-0.009	0.277	22.100	5.044	1.330	0.043	0.043	64.662	-120322
48	2.209	3.397	0.968	70.276	2.952	7.613	7.884	130.456	18.022	58.052	98.159	0.377	0.013	-0.403	24.841	9.620	1.773	0.032	0.057	63.673	-120334
137	0.704	3.414	0.247	68.897	3.994	8.658	5.761	118.534	17.926	39.324	70.924	0.814	-0.651	-0.165	26.015	5.711	1.632	0.038	0.078	96.681	-120475
114	1.287	2.915	0.499	173.424	4.600	5.809	6.560	135.150	12.435	46.571	94.253	-0.445	0.038	0.458	11.571	8.078	0.659	0.011	0.052	84.348	-120506
5	0.945	3.683	0.873	173.936	3.852	6.068	17.602	104.346	26.194	59.357	88.067	0.073	0.452	-0.804	28.630	5.612	1.356	0.043	0.067	77.930	-120599
18	1.095	2.517	0.840	166.240	2.218	6.762	14.117	146.638	16.633	32.105	69.701	-0.081	0.836	0.255	11.409	9.641	0.596	0.026	0.051	83.659	-120783
22	2.465	3.166	0.532	168.839	3.925	6.794	8.485	143.570	23.470	62.497	86.269	0.317	0.130	-0.325	24.357	7.090	1.677	0.041	0.058	85.633	-120870
151	0.908	2.696	0.376	134.256	2.138	9.467	18.139	141.204	25.857	69.154	87.635	0.472	0.082	0.966	25.152	5.284	0.685	0.007	0.047	74.755	-121108
84	0.870	2.401	0.611	59.196	4.630	9.693	10.127	140.465	23.044	56.238	88.790	0.616	-0.147	0.844	11.871	8.411	1.942	0.007	0.071	90.546	-121150
92	2.603	3.620	0.576	133.648	4.264	9.219	5.392	135.955	12.594	30.517	93.247	0.672	0.098	0.721	19.166	8.275	1.892	0.028	0.072	70.011	-121168
79	1.480	3.378	0.853	217.947	3.749	5.136	11.027	136.903	14.004	65.075	65.723	-0.911	-0.861	-0.212	23.871	9.040	1.884	0.022	0.089	43.482	-121223
62	1.798	3.279	0.651	136.112	2.475	8.945	19.679	139.378	14.435	64.511	79.958	-0.033	-0.059	0.716	11.821	8.001	0.747	0.039	0.077	51.317	-121224
23	1.238	3.152	0.644	216.076	3.502	7.097	19.866	135.638	19.069	47.061	91.844	-0.291	-0.265	0.266	19.007	8.784	0.614	0.006	0.044	73.013	-121276
45	0.668	2.935	0.556	240.391	3.578	5.637	9.631	147.679	21.904	67.593	95.161	-0.991	-0.823	-0.369	24.562	6.160	1.079	0.031	0.085	45.119	-121335
175	2.631	3.698	0.135	152.999	2.988	8.030	12.614	116.672	21.511	36.703	94.521	0.947	0.233	-0.693	29.385	5.368	1.337	0.023	0.059	64.951	-121471
89	0.803	2.448	0.179	177.432	2.002	5.964	18.554	111.203	29.281	60.256	60.647	-0.534	-0.064	-0.278	14.813	7.993	0.675	0.019	0.049	94.817	-121631
20	2.576	3.315	0.282	101.804	4.623	6.652	13.048	124.031	24.645	67.754	74.637	-0.103	-0.799	0.117	12.500	8.589	1.092	0.018	0.074	98.410	-121653
15	0.529	2.660	0.637	89.590	3.920	9.259	7.139	136.321	25.003	66.406	82.930	0.280	0.065	0.784	17.015	8.155	0.768	0.034	0.088	40.521	-121689
94	0.568	2.633	0.715	258.188	4.811	6.900	16.551	146.129	15.362	66.771	97.180	0.356	-0.047	-0.250	20.499	9.655	0.999	0.005	0.075	65.550	-121881
25	0.558	3.020	0.678	199.259	4.221	7.525	7.364	103.065	25.747	36.454	71.790	-0.355	-0.318	-0.069	28.212	6.104	1.227	0.016	0.051	74.072	-121883
102	1.176	2.945	0.753	267.800	2.711	7.159	16.064	121.350	24.307	44.843	98.868	-0.498	-0.693	-0.517	10.971	7.717	1.478	0.038	0.046	75.637	-122159
57	0.841	3.043	0.907	77.507	3.665	8.347	18.972	123.500	12.149	59.972	84.332	0.389	0.706	0.971	23.575	5.236	1.074	0.015	0.058	98.819	-122165
174	2.912	2.426	0.414	84.371	4.902	5.757	13.857	118.842	28.884	65.904	60.028	-0.629	-0.601	0.050	28.412	7.972	1.473	0.017	0.045	93.083	-122247
104	2.843	2.703	0.660	57.721	3.375	5.514	7.641	130.121	23.164	34.979	70.338	-0.729	-0.432	0.701	22.519	7.559	1.573	0.039	0.076	87.614	-122491
58	1.708	2.896	0.271	284.505	4.409	6.285	10.065	116.440	10.756	55.800	78.680	-0.465	-0.510	-0.267	12.788	6.637	1.388	0.006	0.055	52.153	-122638
76	2.344	2.395	0.493	56.317	2.095	9.711	14.386	139.681	14.125	63.527	91.443	-0.768	-0.818	0.834	15.048	5.185	0.711	0.046	0.074	48.390	-122791
64	1.454	2.459	0.530	254.500	3.050	5.428	17.001	106.659	21.328	37.593	86.067	-0.652	-0.165	0.149	17.459	6.578	1.212	0.024	0.073	66.421	-122842
80	2.423	3.223	0.899	99.796	4.822	6.328	11.463	102.266	10.965	40.327	79.771	0.323	-0.490	0.039	15.821	5.696	0.704	0.020	0.082	58.604	-122865
162	0.658	3.061	0.817	113.200	3.652	8.605	13.696	131.124	18.395	66.279	70.074	-0.284	-0.677	0.062	14.906	5.929	1.343	0.035	0.065	95.680	-122929
2	1.871	2.267	0.700	234.125	3.143	8.530	7.194	102.683	19.765	31.546	67.181	0.712	-0.366	-0.637	17.388	8.743	0.670	0.013	0.085	92.544	-123000
27	1.505	2.903	0.317	219.976	3.474	9.331	8.769	145.771	29.692	68.396	79.205	0.587	-0.789	-0.987	19.613	7.750	1.820	0.022	0.052	97.902	-123097
12	1.197	2.234	0.511	107.288	2.177	5.560	16.445	138.062	19.819	45.053	83.058	0.936	-0.623	0.004	29.628	7.031	0.921	0.014	0.062	66.357	-124650
78	2.262	3.073	0.463	104.308	2.845	8.004	19.964	131.644	27.862	38.671	72.177	0.450	-0.183	0.354	9.538	7.201	0.854	0.042	0.066	85.478	-124908
13	2.677	2.418	0.189	170.131	4.131	6.688	5.223	132.391	15.194	43.985	96.829	0.288	-0.739	0.495	29.787	7.349	1.709	0.015	0.070	58.077	-124922

81	1.356	2.872	0.848	96.345	3.837	5.982	9.554	115.331	26.421	53.044	61.017	-0.406	-0.687	0.083	15.955	6.060	1.903	0.047	0.073	52.587	-124963
148	2.021	3.750	0.667	146.905	2.193	6.317	11.429	124.530	12.065	44.060	96.226	0.125	-0.914	0.389	13.690	5.321	1.026	0.030	0.079	90.028	-125111
187	2.199	3.485	0.857	264.186	2.446	7.895	18.637	124.845	28.233	41.316	87.841	0.806	0.285	0.756	19.839	8.706	1.583	0.031	0.078	74.369	-125125
24	2.382	2.308	0.405	292.846	3.125	5.158	8.885	105.611	29.370	34.282	84.866	-0.990	-0.953	-0.522	9.660	9.930	1.557	0.010	0.068	97.664	-125244
155	2.500	2.492	0.208	260.803	4.045	8.641	11.268	103.697	22.494	30.772	89.486	0.260	-0.103	0.311	11.060	6.266	0.881	0.017	0.064	72.377	-125387
32	1.031	2.734	0.471	74.348	3.950	5.053	15.780	109.532	22.649	40.416	63.299	0.153	-0.460	-0.624	25.758	6.462	0.834	0.026	0.066	75.702	-125575
131	1.635	2.521	0.585	209.373	2.558	7.366	5.231	138.994	27.990	50.716	69.277	0.133	-0.511	-0.918	9.062	7.262	0.787	0.025	0.063	53.269	-125809
41	2.943	3.427	0.877	126.023	3.524	5.291	13.324	122.055	26.881	68.813	82.611	-0.257	-0.612	0.520	24.444	5.762	0.849	0.031	0.047	88.703	-126811
188	1.302	2.792	0.301	245.158	2.323	8.912	11.363	126.211	15.761	63.363	74.384	0.904	-0.025	-0.355	27.658	5.789	1.240	0.009	0.080	59.331	-127055
115	2.819	2.627	0.773	143.443	3.008	9.536	19.305	120.046	26.642	42.506	73.681	0.798	-0.841	-0.131	26.487	6.091	1.599	0.015	0.074	73.735	-127609
0	1.209	2.888	0.419	190.734	3.640	7.291	6.417	114.836	25.340	61.235	95.234	0.742	-0.376	-0.920	16.861	7.143	1.639	0.017	0.080	89.283	-127905
168	1.946	2.859	0.892	287.944	4.731	5.654	10.608	109.230	21.885	62.232	68.753	0.658	-0.557	0.223	12.032	5.567	1.972	0.020	0.050	94.368	-127965
126	2.065	2.549	0.954	171.332	3.732	5.106	13.500	115.501	10.424	57.426	99.478	-0.575	-0.800	0.546	12.234	5.907	0.554	0.025	0.086	68.692	-128123
17	2.404	2.926	0.775	90.243	4.559	6.468	15.261	123.170	27.066	56.893	61.742	0.684	0.001	-0.883	12.592	6.047	1.527	0.035	0.083	51.450	-128921
184	2.040	2.985	0.984	51.631	2.118	6.180	6.615	100.081	19.191	60.145	94.906	0.023	-0.853	0.811	27.024	8.905	1.097	0.012	0.056	71.830	-128973
133	1.174	2.823	0.979	224.124	3.324	9.078	16.688	137.315	13.239	55.477	93.509	0.865	-0.032	0.295	13.925	8.189	1.008	0.025	0.069	44.486	-129997
29	1.810	2.432	0.813	210.083	2.025	6.610	12.336	110.905	17.815	59.563	92.815	0.667	-0.909	0.641	14.747	9.162	1.657	0.043	0.051	47.451	-133732
11	1.595	2.606	0.507	198.384	2.357	5.707	8.191	121.521	16.473	36.001	99.967	0.828	-0.325	0.917	13.110	8.978	0.695	0.037	0.082	85.051	-134050
4	2.176	3.792	0.880	120.542	2.922	5.546	6.926	122.740	11.748	33.334	95.660	0.696	-0.725	0.477	27.144	6.281	1.245	0.019	0.073	83.325	FAILED
19	2.960	3.535	0.355	81.421	2.122	9.145	19.781	101.243	24.876	47.402	78.467	0.925	-0.740	-0.789	14.133	6.783	1.300	0.048	0.067	69.986	FAILED
50	0.779	3.977	0.431	176.219	4.279	7.631	17.332	106.411	26.762	46.227	75.053	0.543	-0.895	-0.607	28.258	6.489	1.924	0.014	0.088	75.252	FAILED
53	1.125	3.997	0.138	183.247	4.122	5.274	9.881	102.785	22.585	48.055	68.058	0.439	0.351	0.885	19.965	7.849	0.605	0.007	0.049	48.402	FAILED
71	2.166	3.959	0.153	230.094	2.532	6.746	14.153	113.294	23.937	59.056	84.435	0.267	-0.711	0.658	24.732	6.813	1.699	0.017	0.042	41.226	FAILED
82	2.118	3.641	0.525	226.030	3.781	5.481	19.717	107.028	20.530	46.950	78.172	0.598	-0.982	-0.453	15.417	5.457	1.877	0.031	0.065	44.827	FAILED
83	0.766	3.771	0.285	235.659	2.970	6.104	19.532	129.024	21.622	50.233	61.965	0.298	-0.831	0.928	27.410	9.561	1.117	0.035	0.064	82.963	FAILED
90	0.549	3.808	0.548	152.457	2.429	9.843	19.102	110.394	26.287	62.974	63.709	0.996	-0.094	0.797	17.829	6.434	0.723	0.008	0.055	97.402	FAILED
97	1.392	3.149	0.625	247.000	3.173	6.367	18.378	143.828	28.712	65.744	86.472	0.623	-0.429	0.122	15.643	5.275	1.055	0.037	0.042	67.767	FAILED
103	1.824	3.235	0.018	108.735	4.310	5.359	5.319	133.713	10.512	50.811	72.866	-0.714	-0.650	-0.563	12.998	7.673	1.737	0.014	0.050	66.796	FAILED
106	1.254	3.132	0.094	283.425	2.390	9.863	5.580	123.991	29.810	38.233	66.995	0.763	-0.667	-0.234	17.569	5.673	1.810	0.029	0.040	96.157	FAILED
110	2.553	3.901	0.633	118.513	3.232	8.864	17.482	112.878	15.554	46.623	91.320	0.983	0.210	0.365	23.469	8.109	1.647	0.028	0.076	96.827	FAILED
122	2.289	3.571	0.469	227.208	4.235	9.007	8.551	122.798	11.049	41.605	88.238	0.143	-0.876	0.016	20.314	5.069	0.980	0.029	0.077	81.893	FAILED
141	1.564	3.257	0.338	122.558	3.161	7.861	12.725	140.228	17.375	69.765	83.358	-0.393	0.024	-0.021	10.002	7.017	1.127	0.045	0.063	99.712	FAILED
142	2.429	3.081	0.445	238.093	2.661	9.972	17.884	145.447	27.322	49.743	70.559	-0.734	0.383	0.205	15.855	5.737	1.035	0.013	0.041	56.517	FAILED
143	2.307	3.624	0.695	82.555	3.089	5.924	17.161	137.089	22.019	69.571	65.207	0.003	0.447	-0.087	29.178	6.571	1.179	0.026	0.049	54.254	FAILED
163	2.811	3.505	0.990	130.425	3.825	6.406	10.532	148.159	28.040	37.185	67.788	0.899	-0.889	-0.310	13.941	7.366	0.950	0.036	0.085	90.104	FAILED
193	2.736	3.267	0.486	66.405	4.783	5.747	7.718	109.357	20.330	39.916	97.407	-0.848	-0.238	0.941	14.391	6.351	1.407	0.009	0.074	82.250	FAILED

Appendix B Flow calibrated ensemble

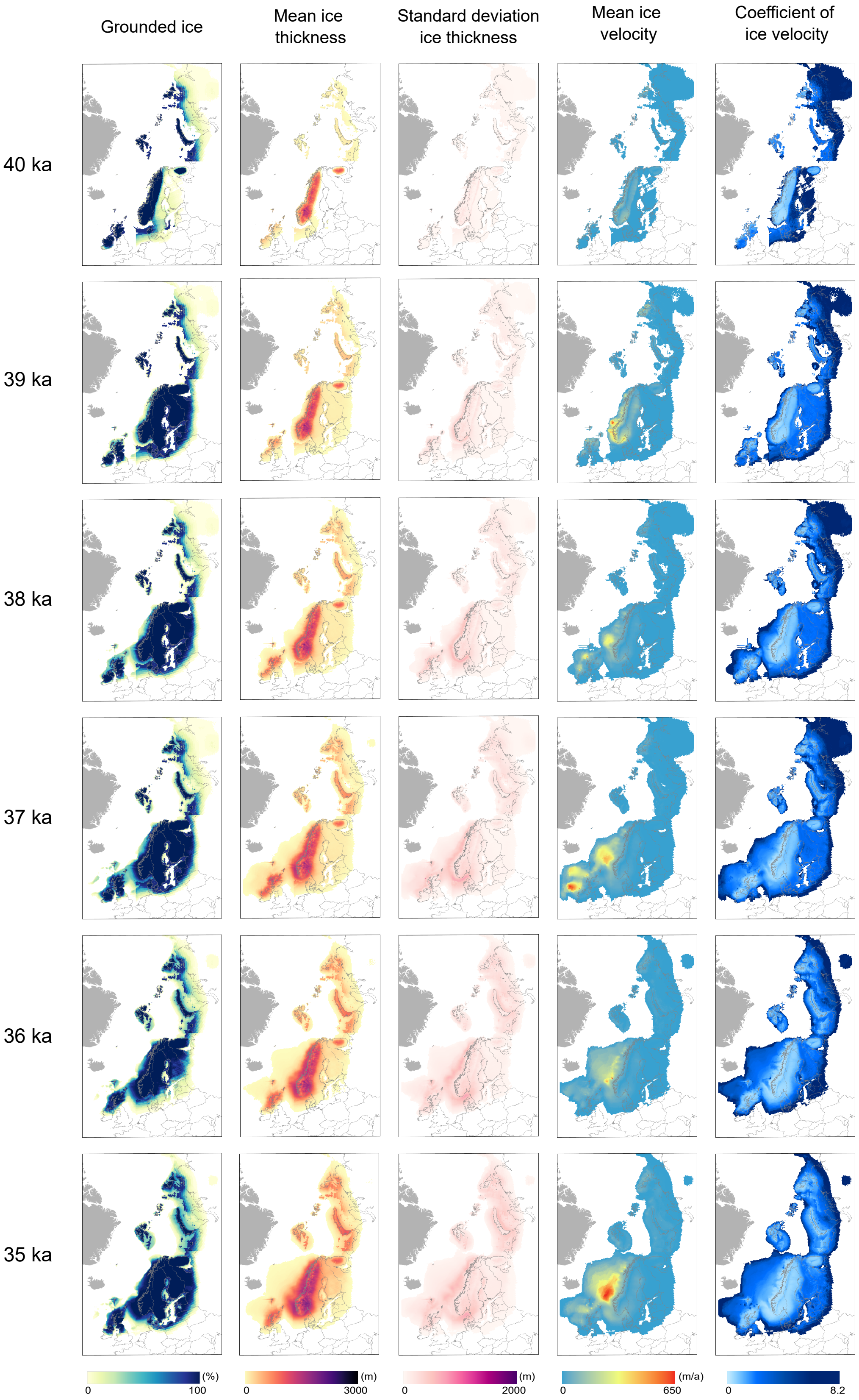

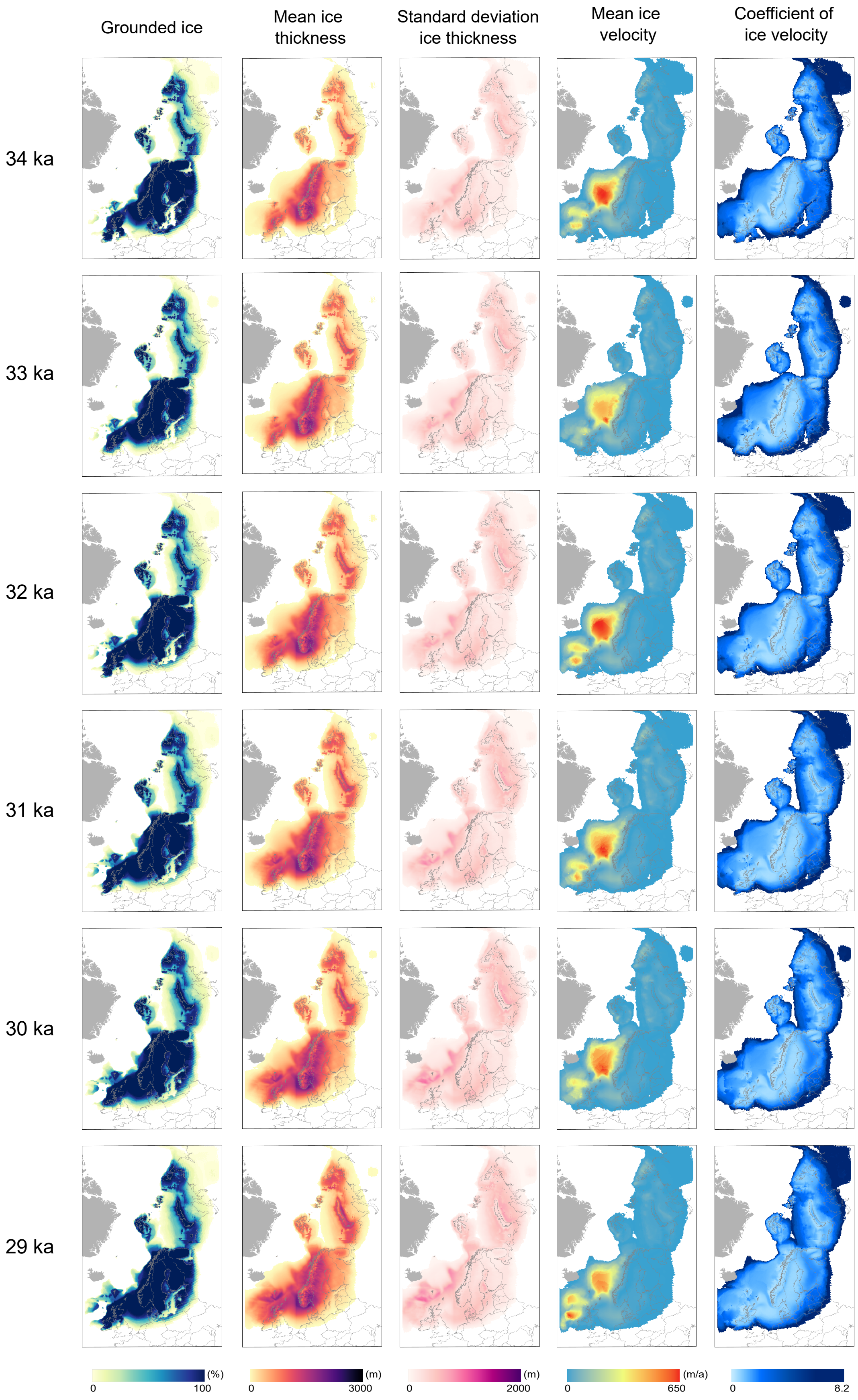
Grounded ice
Mean ice thickness
Standard deviation ice thickness
Mean ice velocity
Coefficient of ice velocity
34 ka
33 ka
32 ka
31 ka
30 ka
29 ka
(%)
0
100
(m)
0
3000
(m)
0
2000
(m/a)
0
650
0
8.2

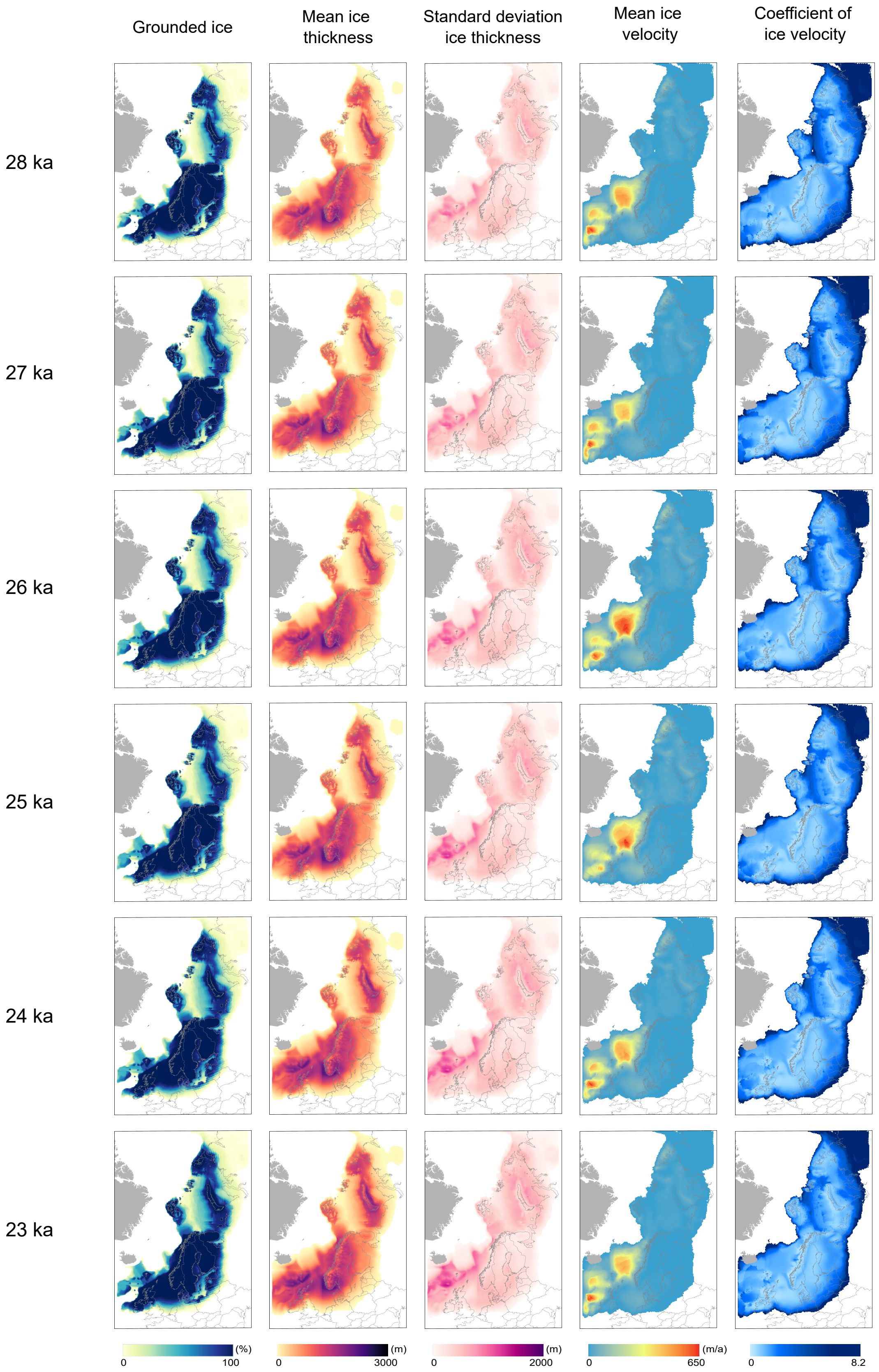
Grounded ice
Mean ice thickness
Standard deviation ice thickness
Mean ice velocity
Coefficient of ice velocity
28 ka
27 ka
26 ka
25 ka
24 ka
23 ka
(%)
0
100
(m)
0
3000
(m)
0
2000
(m/a)
0
650
0
8.2

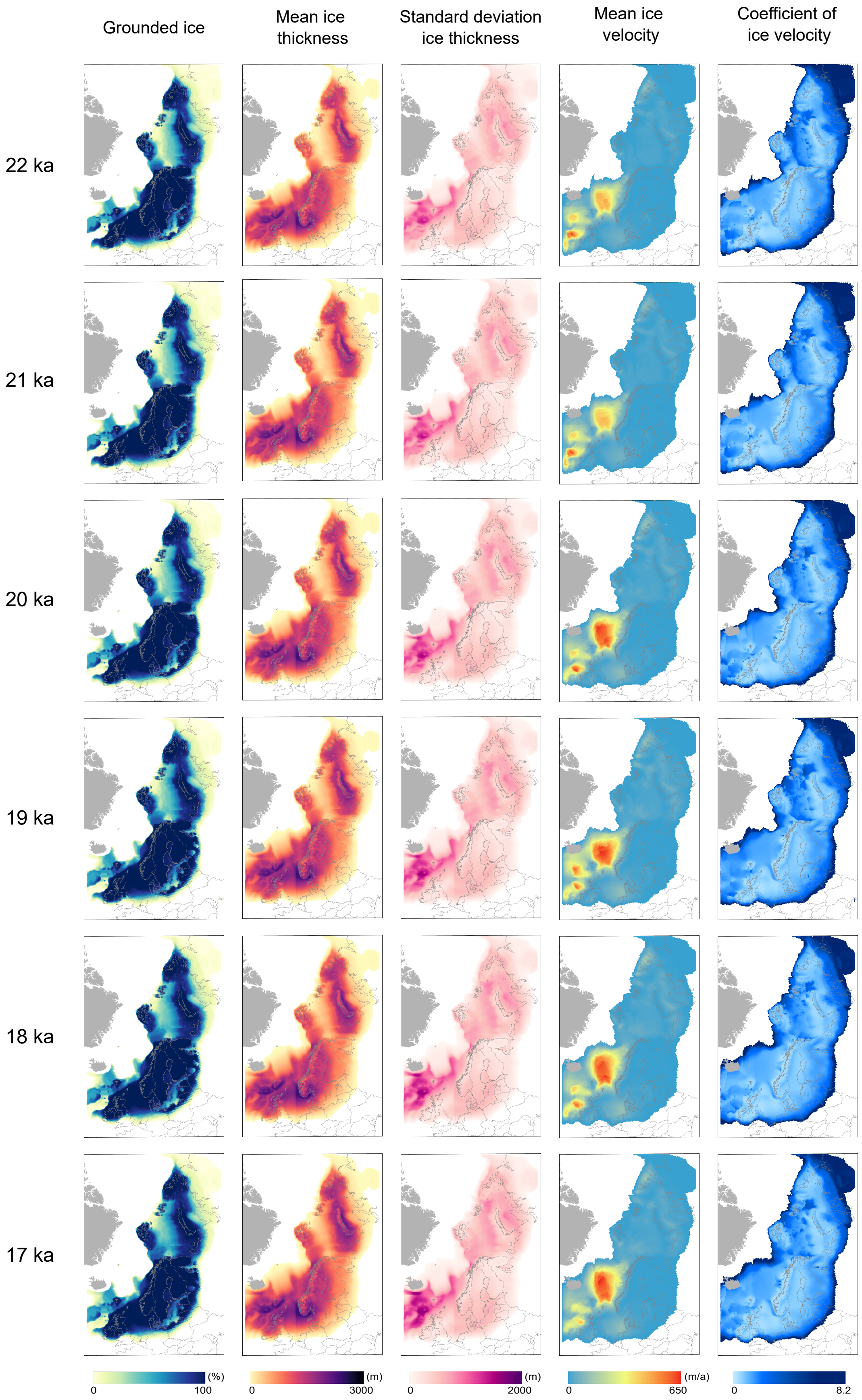
Grounded ice
Mean ice thickness
Standard deviation ice thickness
Mean ice velocity
Coefficient of ice velocity
22 ka
21 ka
20 ka
19 ka
18 ka
17 ka
(%)
0
100
(m)
0
3000
(m)
0
2000
(m/a)
0
650
0
8.2

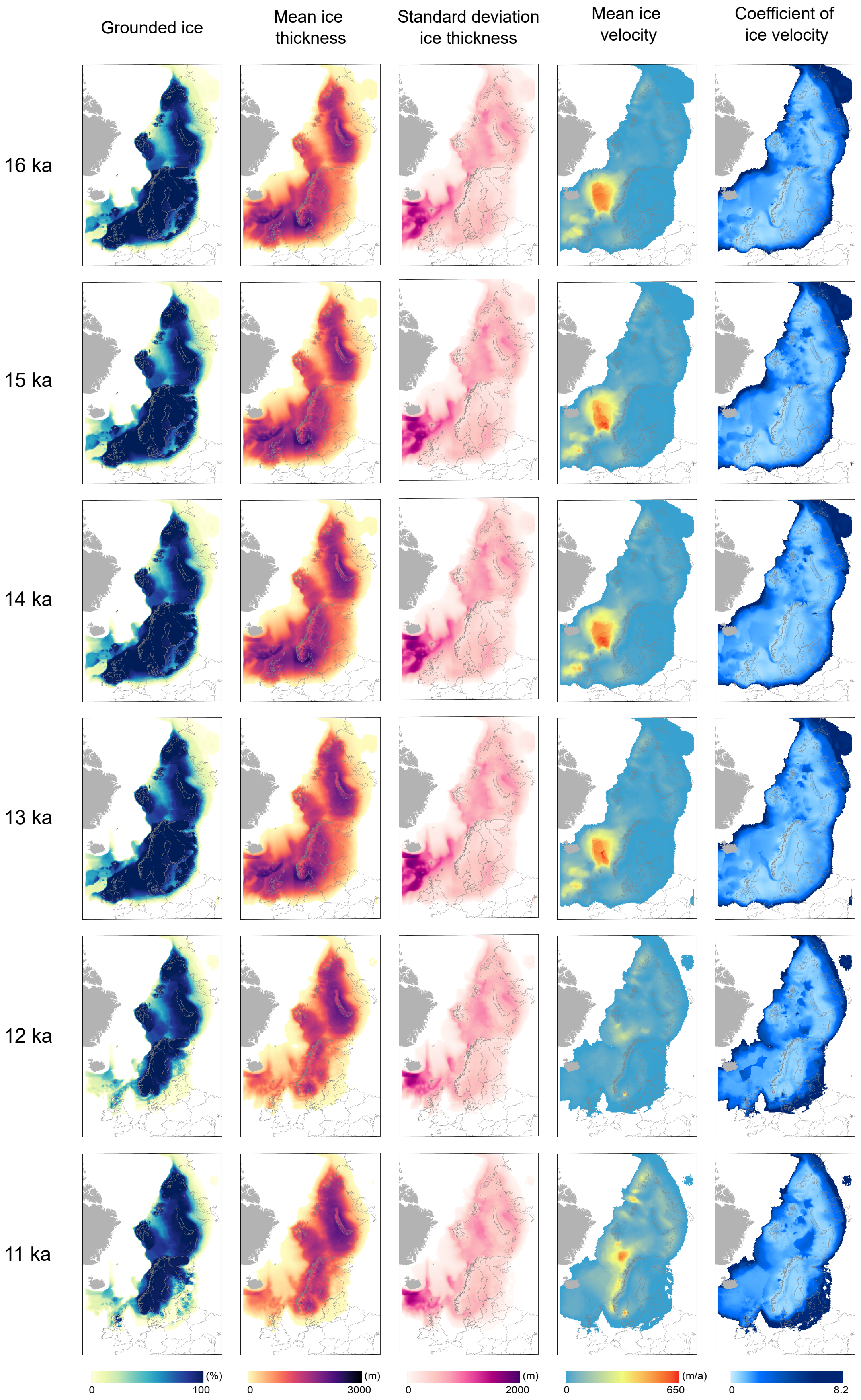
Grounded ice
Mean ice thickness
Standard deviation ice thickness
Mean ice velocity
Coefficient of ice velocity
16 ka
15 ka
14 ka
13 ka
12 ka
11 ka
(%)
0
100
(m)
0
3000
(m)
0
2000
(m/a)
0
650
0
8.2

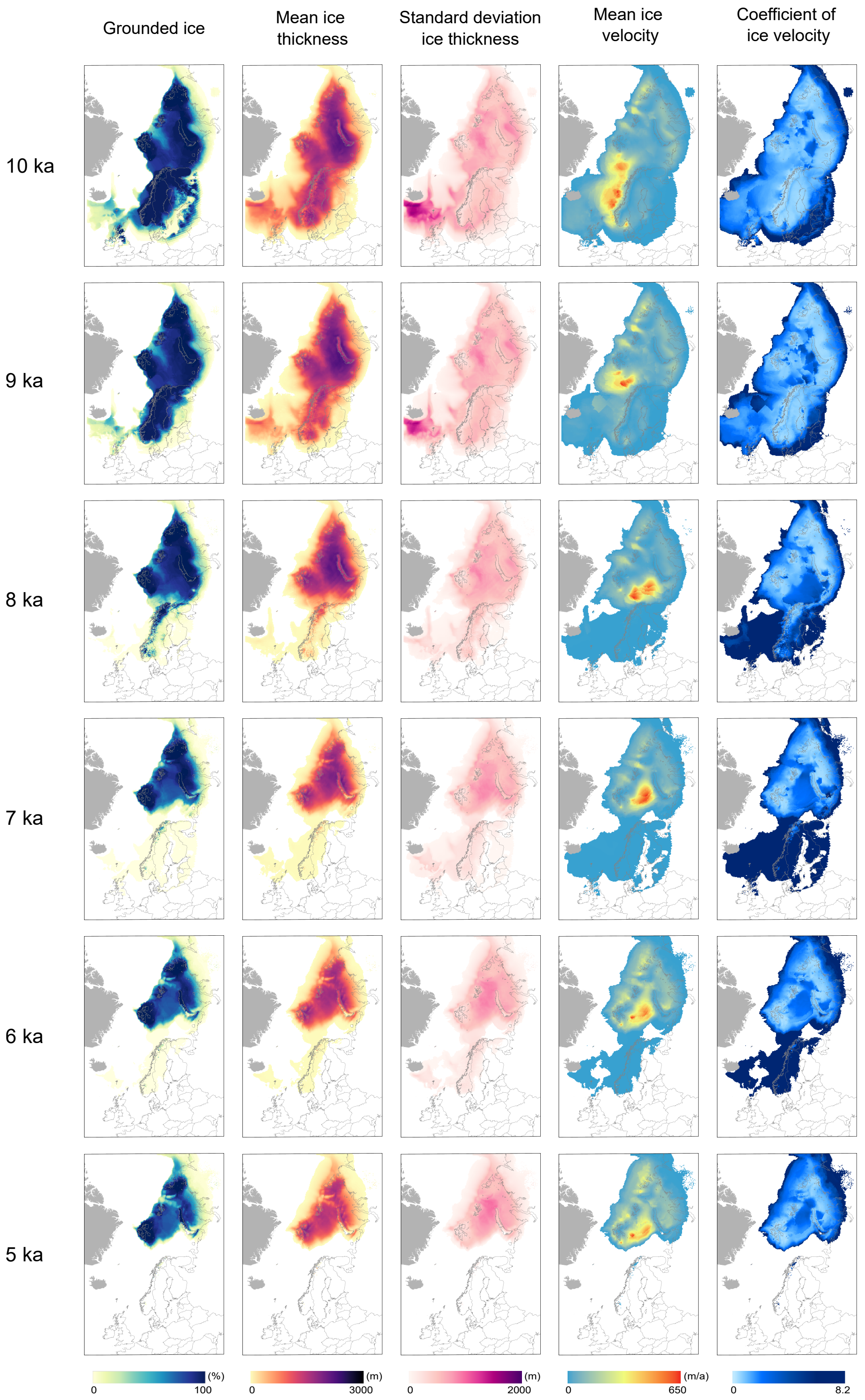

Figure B.1: Summary metrics for the flow calibrated ensemble every one thousand simulated years. The variables considered are the percentage of grounded ice (%), average ice thickness (m), standard deviation of ice thickness (m), average ice velocity (m/a) and the coefficient of variation of velocity.

Appendix C Flow calibrated ensemble parameter inputs and LALA scores

Model Number	n	q	F_s	F_i	τ_c^s	τ_c^b	τ_c^{tk}	τ_c^{tn}	α_1^{LGM}	α_2^{LGM}	α_1^{PI}	m_s	β	LALA Score
24	2.007863	0.860196	0.004889	0.006445	18.50879	131.881	52.73085	94.01515	-0.80255	0.909833	-0.86197	6.132171	41.54881	-99938
27	2.047126	0.004889	0.002532	0.008239	6.305647	146.2656	35.4611	72.22064	-0.67519	0.312053	-0.91965	9.527009	65.92187	-100474
35	2.004108	0.453337	0.004082	0.009354	8.609901	141.5007	52.99522	98.87187	-0.83438	0.981969	-0.22258	9.289256	40.27689	-100867
54	2.014215	0.343315	0.003847	0.007208	11.01503	144.1656	42.03689	97.91012	-0.74891	0.915153	-0.77722	8.44711	77.89626	-101102
22	2.033683	0.343057	0.003006	0.005424	8.204957	118.5336	41.34034	75.8934	-0.29546	0.884719	-0.92209	9.606295	84.35379	-101883
120	2.037418	0.357052	0.004062	0.008371	7.014879	102.5009	50.18169	60.09906	-0.85053	0.205129	-0.29813	9.533521	69.37533	-102094
41	2.007358	0.248453	0.002127	0.007842	19.40598	148.6386	69.32074	62.6381	-0.74408	0.76325	0.213936	9.299953	43.27975	-102433
17	2.038562	0.385082	0.00384	0.007681	11.18707	109.7135	39.89804	86.06154	0.095381	0.78999	0.012519	9.397	57.27747	-102823
10	2.038122	0.357563	0.004533	0.008379	10.87038	125.1522	50.26582	70.21364	-0.93355	0.33967	-0.30229	8.278606	81.14734	-102983
103	2.053953	0.000488	0.003906	0.006569	19.42617	102.8515	31.12734	97.34977	0.467888	0.582119	0.690433	9.659626	63.86758	-103518
47	2.018409	0.881602	0.002424	0.007629	8.919677	107.0969	58.42011	60.26377	-0.69068	0.511201	-0.60901	8.988797	53.08618	-104257
52	2.020356	0.688252	0.00316	0.006058	6.38042	125.6631	55.43247	98.81852	-0.73703	0.229198	0.51244	9.617446	49.10062	-104398
90	2.05705	0.629419	0.003458	0.005277	16.54465	117.9802	42.54685	76.68749	-0.81164	0.806054	-0.76602	9.839767	81.1061	-104419
69	2.090011	0.207702	0.002224	0.007594	12.99062	142.9995	60.91901	76.32142	-0.35833	0.900477	-0.7841	8.970156	96.60489	-104440
104	2.127336	0.109139	0.003842	0.007279	19.04227	104.044	50.29052	94.60996	-0.94362	0.241262	0.305569	8.229633	44.74694	-105077
23	2.020612	0.370541	0.003307	0.008296	10.90526	120.3293	36.60443	77.80568	-0.82906	0.915472	0.538086	6.252438	43.35441	-105211
96	2.112495	0.317641	0.002584	0.009498	8.092198	116.4095	53.11965	88.18363	-0.76637	0.527598	-0.70711	9.348413	72.67551	-105441
112	2.035176	0.416786	0.004514	0.008743	11.40729	143.1047	49.82954	89.57306	-0.37336	0.665457	-0.17484	5.91191	99.07352	-105442
71	2.100652	0.380635	0.003757	0.009741	18.10519	112.118	34.16456	82.35656	-0.70802	0.717632	-0.26715	8.129121	62.91417	-105742
57	2.031295	0.533677	0.004168	0.008259	11.82692	135.1426	66.14856	98.01043	-0.56402	0.372292	-0.20266	7.197071	59.9731	-105767
32	2.060149	0.331779	0.004204	0.00807	5.719453	117.4741	34.16142	90.77095	-0.10611	0.459664	0.646122	8.378958	45.4442	-105805
5	2.050677	0.895073	0.004858	0.006785	16.8897	142.6959	34.32577	67.09194	-0.00189	0.478894	0.038926	9.354766	46.79537	-106104
128	2.013671	0.729183	0.004584	0.009946	15.99176	135.4208	68.43355	86.13641	-0.45441	0.086353	0.407096	5.792383	79.15446	-106438
1	2.088437	0.393597	0.003568	0.005972	18.99053	143.9463	41.25723	70.28267	-0.80912	0.074047	-0.82906	9.615336	59.36576	-106460
74	2.143592	0.211086	0.004688	0.005783	13.72389	112.883	38.34627	98.38507	-0.35873	0.90252	-0.88312	8.328421	91.81074	-106569
55	2.106556	0.719978	0.004513	0.009465	19.78883	123.988	50.51588	82.91346	-0.40567	0.924321	0.131101	8.947177	47.26836	-107114
117	2.070363	0.235098	0.003739	0.005559	12.04053	109.9328	44.8797	73.21628	-0.28474	0.983985	-0.34071	5.26969	70.23034	-107167
46	2.097166	0.749424	0.004886	0.009943	19.78753	144.5984	66.03364	91.53935	-0.82363	0.582683	-0.48499	7.156432	79.12365	-107519
81	2.079108	0.864217	0.003992	0.008029	18.68723	143.0276	43.41716	73.10446	0.25346	0.881235	0.435753	7.241257	70.60641	-107666
129	2.100762	0.73248	0.004563	0.0074	6.525551	135.5978	38.11004	97.81458	-0.69172	0.700914	-0.57905	7.862117	91.89882	-107741
95	2.058956	0.449014	0.003616	0.006139	18.42952	149.0572	52.1753	92.02732	-0.95615	-0.2499	-0.84693	7.68604	57.76814	-108096
80	2.066477	0.309842	0.004854	0.008366	15.91913	121.7657	63.37137	89.73483	0.905114	0.156144	-0.75114	7.980592	80.06278	-108506

68	2.583476	0.099466	0.004492	0.007706	18.98193	135.441	58.86893	73.73977	-0.76443	0.86344	0.503857	8.771704	45.56822	-108681
59	2.931535	0.083873	0.002309	0.008721	11.5723	133.8605	38.39039	82.16089	-0.61306	0.602711	-0.18799	9.587231	79.10229	-108685
97	2.269258	0.423014	0.003536	0.009453	14.82459	130.5069	30.56941	70.44886	-0.56296	0.81368	-0.48028	9.046072	87.69512	-108777
11	2.080493	0.256317	0.003059	0.005792	18.14914	148.5723	42.05858	66.44267	0.704687	0.480922	-0.48216	8.863331	51.78706	-109236
122	2.824067	0.342779	0.002655	0.008468	9.990188	139.4382	43.39173	69.66529	-0.94267	0.321081	-0.27537	9.493347	68.29748	-109366
50	2.807033	0.360011	0.003663	0.009869	7.819497	145.4596	61.91362	87.6739	-0.95233	0.969013	0.468225	9.432686	98.07431	-109600
2	2.95162	0.345994	0.004981	0.009788	17.87066	148.9177	69.71726	81.26392	-0.25727	0.872034	-0.21405	9.670043	76.96708	-109943
0	2.97382	0.193668	0.002835	0.007426	10.56615	142.8392	40.98742	85.95776	-0.83898	0.27774	-0.32107	7.417191	88.23619	-110019
29	2.124177	0.560751	0.004038	0.007953	13.31317	138.4685	35.03789	97.26631	-0.96541	0.773379	0.634695	5.652966	84.84751	-110190
109	2.97134	0.321366	0.00219	0.00738	18.3464	144.8382	51.87376	80.16281	-0.89409	0.790055	0.123131	8.429261	84.76132	-110284
73	2.061204	0.550111	0.004373	0.008167	16.01193	106.5205	50.15202	84.90211	-0.61766	-0.27303	-0.43019	7.201459	77.53363	-110443
77	2.142575	0.964847	0.003958	0.006805	16.36834	141.9965	30.62015	97.31441	-0.99639	0.614905	0.170991	7.225547	49.92397	-110573
107	2.881213	0.108586	0.004376	0.008114	7.066421	137.1367	64.23886	98.65935	-0.75475	0.142069	-0.82615	7.263328	56.22484	-110845
92	2.064417	0.317946	0.002163	0.00603	10.38246	118.4181	40.51256	61.8906	-0.38818	0.542506	0.738604	5.431713	60.09626	-110967
101	2.601019	0.981148	0.004454	0.009741	15.27172	112.5546	58.95101	85.09291	-0.713	0.902175	-0.55519	8.501359	75.51498	-111070
19	2.165054	0.231234	0.003613	0.007564	14.00193	144.8674	36.59126	95.60853	-0.89997	-0.75849	-0.17091	9.946097	60.78688	-111173
45	2.492369	0.271797	0.003927	0.006508	9.370295	128.9368	44.22139	74.95126	-0.76702	0.586383	0.410836	9.430362	82.05107	-111260
85	2.14503	0.964359	0.004254	0.007196	7.495626	128.2828	53.31018	60.77243	-0.64519	0.487109	-0.3196	7.208312	44.30162	-111339
125	2.691845	0.976452	0.004095	0.009296	8.412357	107.1634	60.03495	78.74517	-0.97437	0.498331	-0.91286	9.097397	57.60471	-111358
105	2.882876	0.410217	0.004118	0.009613	13.75692	142.1561	36.58044	62.05478	-0.26397	0.621126	-0.56303	8.375492	89.41132	-111916
16	2.064063	0.423307	0.002418	0.008651	5.475844	147.5578	43.98015	93.85679	-0.52144	-0.69524	-0.33686	7.608338	71.58191	-111928
93	2.226584	0.38459	0.003704	0.009976	10.9914	107.9557	30.39198	98.95269	-0.08749	0.623094	-0.18667	6.614988	62.74742	-112085
60	2.897333	0.332138	0.002633	0.009098	8.254404	108.1523	43.08468	63.11844	-0.2669	0.673722	-0.26938	7.743914	62.20641	-112926
39	2.999798	0.109307	0.003717	0.005008	5.605536	139.5233	69.85466	85.69346	0.076862	0.408866	-0.25053	9.912738	46.30146	-112964
48	2.86708	0.290721	0.003746	0.009494	19.23782	130.8843	43.70377	96.24725	-0.16699	0.529895	0.083681	9.249521	94.32237	-112985
124	2.836573	0.392396	0.003886	0.0053	9.408194	149.3912	58.57925	96.34791	-0.88749	0.490615	0.618454	9.739957	54.69656	-113011
127	2.52002	0.494668	0.002432	0.009545	12.43233	130.3103	35.30059	67.51353	-0.9702	0.456651	0.914413	9.229922	65.7886	-113093
6	2.488034	0.069032	0.002154	0.007517	9.655335	113.6708	30.43631	80.28442	-0.0019	0.225439	-0.56361	9.23739	85.5013	-113350
100	2.324975	0.266047	0.002497	0.006881	19.28839	125.6674	62.67653	66.62434	-0.99666	-0.13909	0.970491	9.678665	44.85066	-113723
13	2.611617	0.910633	0.002136	0.008472	12.37147	122.6552	54.29203	84.45688	-0.61804	0.978429	-0.26953	7.88776	48.25494	-114321
21	2.288059	0.33997	0.003738	0.005884	11.57757	108.5859	56.14344	95.31701	-0.09596	0.087432	-0.34627	8.84919	43.57045	-114804
34	2.628698	0.745741	0.002891	0.007499	12.59507	130.1018	55.51597	87.10276	-0.17795	0.712379	-0.95877	8.351084	98.79496	-115460
26	2.873858	0.586672	0.003078	0.006074	13.22397	144.1373	60.01965	84.29255	-0.69194	0.274487	-0.54138	9.358836	72.7133	-115853
115	2.919151	0.279192	0.00465	0.009453	7.382794	134.9458	39.18651	96.73078	-0.6729	-0.97154	0.246304	7.534141	56.29626	-118101
62	2.645301	0.732117	0.003321	0.009376	15.30329	144.4833	36.58305	73.18407	-0.26932	-0.2783	-0.71305	6.674194	44.63043	-120128
36	2.771994	0.313139	0.002203	0.00795	10.72501	100.5513	63.23813	77.76672	-0.08045	-0.67145	0.048401	9.987711	68.49605	-120669
3	2.050907	0.074004	0.002422	0.0097	5.974312	107.7606	36.42226	66.31029	-0.48395	0.654801	-0.60588	6.126989	53.55859	FAILED
4	2.05228	0.007339	0.002134	0.008224	11.94296	124.1769	55.98165	66.48189	-0.34754	-0.16307	-0.2112	5.65981	54.1719	FAILED
7	2.094108	0.109848	0.002487	0.007306	8.354892	143.237	37.93247	86.42043	-0.9465	0.698864	-0.50781	6.340434	50.34646	FAILED
8	2.159733	0.035425	0.002529	0.006492	14.00942	100.3083	35.70561	84.94713	-0.31393	0.669868	0.638042	8.524859	97.10389	FAILED
9	2.071913	0.032062	0.002081	0.006003	14.14777	131.4817	47.19368	70.70016	-0.01718	0.999867	-0.26989	8.70735	41.31043	FAILED
12	2.089592	0.065915	0.002907	0.007193	6.857984	144.7101	57.10159	70.99235	-0.67226	0.352283	0.272952	5.01917	54.98647	FAILED
14	2.097479	0.04215	0.003265	0.009203	10.61346	108.1666	43.25188	80.47019	-0.73145	0.827299	-0.98162	5.969012	81.42551	FAILED
15	2.25849	0.086684	0.004637	0.009418	14.89686	146.2391	68.81697	91.24841	-0.37456	0.888559	-0.74013	9.161424	67.82877	FAILED

18	2.772732	0.169543	0.003876	0.007851	18.62232	112.6958	46.69628	93.90249	-0.88728	0.909742	-0.28023	6.438428	95.583	FAILED
20	2.289735	0.045509	0.002375	0.007389	19.27815	100.8011	44.62666	82.38927	-0.24092	-0.49449	-0.75915	9.149064	81.01452	FAILED
25	2.040026	0.064104	0.003002	0.006001	15.17118	133.1834	49.05861	95.47636	-0.86691	0.787662	0.025106	8.862661	54.30698	FAILED
28	2.05382	0.093481	0.002081	0.009593	11.98832	143.6985	67.34662	78.45668	-0.3315	-0.43675	-0.74276	9.472983	49.79434	FAILED
30	2.002702	0.097599	0.003667	0.009262	16.07581	144.4357	51.01734	84.90216	-0.98322	0.855115	0.635755	7.630204	91.99637	FAILED
31	2.801364	0.074311	0.002712	0.007338	9.494184	122.1896	60.06629	72.24522	-0.3929	0.90086	0.506196	8.306711	91.93764	FAILED
33	2.189027	0.050168	0.002927	0.009091	14.83478	138.2908	66.81656	85.43041	-0.23225	0.73816	-0.9312	6.279871	91.84853	FAILED
37	2.153252	0.036306	0.003249	0.008952	12.65898	138.1438	69.66009	88.25197	-0.08194	-0.27425	-0.82072	8.850886	43.35346	FAILED
38	2.755966	0.021074	0.004767	0.007259	19.72869	119.4849	44.62611	82.19828	-0.95597	0.533395	-0.20888	9.369299	66.92202	FAILED
40	2.911252	0.008394	0.00464	0.009493	17.25575	128.6625	57.272	76.94253	0.430583	0.454682	-0.26431	5.8532	52.38156	FAILED
42	2.085674	0.122338	0.004125	0.009743	12.70861	142.4622	64.54324	85.79147	-0.45112	0.608213	0.346529	5.164304	98.78577	FAILED
43	2.033842	0.213132	0.002138	0.008355	11.73458	142.4285	59.08091	90.34158	-0.59906	0.984129	-0.54771	6.839031	87.47645	FAILED
44	2.001705	0.054454	0.004961	0.00593	11.3266	117.4867	69.1447	97.9668	-0.85849	0.738601	-0.29353	9.898232	74.77779	FAILED
49	2.124402	0.055895	0.002795	0.005418	19.61831	129.0766	68.4905	69.45838	-0.4911	-0.42081	0.650046	6.902984	51.80187	FAILED
51	2.042458	0.012846	0.003477	0.007712	7.175458	148.9436	68.26987	75.74699	-0.87901	0.954842	0.137287	7.54912	48.2858	FAILED
53	2.005037	0.130327	0.003328	0.009035	17.55171	139.406	69.34497	84.00318	-0.90695	0.590139	-0.70552	9.914518	48.55276	FAILED
56	2.352439	0.142663	0.003231	0.006994	19.38516	119.292	31.68866	93.36134	-0.97776	0.671217	0.505735	8.770239	91.46719	FAILED
58	2.113802	0.165588	0.004171	0.00991	10.92035	135.2095	65.55156	97.299	-0.09468	0.738261	0.167821	8.689755	47.38587	FAILED
61	2.311667	0.005435	0.00462	0.007243	16.24752	148.4434	60.17063	74.76163	0.149152	0.923338	0.24553	8.377548	85.89436	FAILED
63	2.055988	0.014627	0.003079	0.008297	7.042075	131.1893	37.59057	66.33624	-0.08748	0.984468	0.977257	8.820005	44.15889	FAILED
64	2.161231	0.049115	0.002416	0.007224	8.577951	129.3348	60.57991	87.35854	0.025817	0.40897	-0.41911	5.593482	43.15531	FAILED
65	2.182724	0.068893	0.002769	0.008631	15.64599	120.8009	61.83913	93.18112	0.131823	0.605633	-0.9751	8.979868	89.60455	FAILED
66	2.015213	0.180353	0.003346	0.008341	14.96893	127.9714	59.20482	88.56704	0.661934	0.404105	-0.05293	6.203773	45.70086	FAILED
67	2.128193	0.15076	0.004486	0.009804	18.4587	126.3754	50.46133	68.28926	0.432113	0.654844	-0.27727	5.522999	76.44808	FAILED
70	2.031208	0.092951	0.003387	0.006484	8.467784	139.6689	42.07425	81.03382	-0.93813	0.055689	-0.86506	5.921028	99.27499	FAILED
72	2.185582	0.117214	0.004848	0.007312	10.37854	139.8039	69.13573	67.83016	-0.56102	0.518742	-0.99043	8.946482	94.10683	FAILED
75	2.087518	0.129001	0.002461	0.006399	14.42171	120.7735	69.18014	88.72703	-0.67877	0.024102	0.235776	8.63435	51.7024	FAILED
76	2.031358	0.237895	0.004948	0.009462	10.09516	136.8594	51.16146	77.74461	-0.70818	0.927692	-0.94834	9.345564	60.81446	FAILED
78	2.062992	0.202516	0.002233	0.009692	18.38291	132.2018	56.11939	93.70682	-0.18833	0.729565	0.143373	5.946863	77.92862	FAILED
79	2.099632	0.066914	0.004128	0.006003	10.43741	125.6764	31.90092	88.98292	-0.65061	0.543	-0.51655	9.532594	92.69423	FAILED
82	2.056744	0.128091	0.002444	0.008136	14.57907	149.2603	33.74733	60.18525	-0.31641	-0.76486	0.158729	6.997579	92.81665	FAILED
83	2.063834	0.002944	0.003256	0.009313	19.80194	140.3154	36.62525	81.95026	-0.99472	0.691777	-0.64664	5.210628	53.01187	FAILED
84	2.015845	0.010168	0.004446	0.009933	16.59966	149.0812	56.62118	91.39539	-0.96479	0.175982	-0.90211	9.796568	40.05214	FAILED
86	2.044648	0.208221	0.003319	0.007637	9.011311	109.135	64.62658	87.70453	-0.82687	0.918333	-0.83558	5.98496	96.27788	FAILED
87	2.094138	0.068121	0.004543	0.007771	10.54065	125.2464	33.05033	68.75655	-0.3625	0.057153	0.834465	7.480034	70.91911	FAILED
88	2.197474	0.163626	0.002207	0.007765	11.13022	123.3438	49.41188	82.82507	-0.85837	0.70672	-0.20257	7.55262	86.35757	FAILED
89	2.027814	0.25529	0.003204	0.008125	8.997606	129.1763	32.40491	96.08466	-0.51797	0.788006	-0.6194	7.303975	46.64087	FAILED
91	2.077985	0.019437	0.003676	0.008246	5.577685	144.4788	39.10019	85.11691	-0.96545	0.208828	-0.50971	5.534185	73.66058	FAILED
94	2.036503	0.00211	0.003817	0.009692	7.411343	135.6039	66.14553	63.05272	-0.98528	0.759458	-0.55997	8.565018	63.2432	FAILED
98	2.035453	0.185459	0.004945	0.00725	8.647146	133.7981	59.33346	80.17791	-0.51525	0.509634	-0.9139	5.191787	73.32091	FAILED
99	2.139822	0.096743	0.003798	0.009971	16.34302	112.0444	41.23736	99.49463	-0.20869	0.300584	-0.85564	8.479853	62.73241	FAILED
102	2.037868	0.159436	0.004518	0.009165	7.622013	135.5052	68.92229	64.65227	-0.66549	0.619232	0.348288	5.344626	49.37595	FAILED
106	2.109385	0.032619	0.00318	0.006296	7.89015	140.6494	46.71363	72.73519	0.33191	-0.62839	-0.33265	9.33727	73.00527	FAILED
108	2.070443	0.022775	0.004113	0.007132	9.31922	111.2695	40.33315	86.99134	-0.51584	-0.7302	0.780753	8.968642	54.78648	FAILED

110	2.279263	0.090268	0.004383	0.009267	16.45292	106.8025	37.75229	98.13299	-0.31002	0.723268	-0.92382	8.472544	77.93766	FAILED
111	2.124556	0.052926	0.003658	0.00895	13.72756	137.4267	38.09451	75.67283	-0.3547	0.464091	0.482822	8.359412	96.58085	FAILED
113	2.880966	0.097821	0.003099	0.008293	7.560044	112.5101	54.1695	92.4302	-0.75527	0.98096	0.165945	9.41692	53.83132	FAILED
114	2.074921	0.032824	0.002298	0.009366	15.91176	138.4439	34.32683	78.58217	-0.61084	0.403201	-0.84929	9.899393	66.50538	FAILED
116	2.574337	0.173832	0.002009	0.005674	9.095003	112.941	59.25878	99.72044	-0.78488	0.415625	-0.4191	8.798947	55.88947	FAILED
118	2.048547	0.188035	0.004547	0.00763	15.82866	139.1427	36.37894	85.88782	0.275996	0.438024	-0.6795	7.940653	51.96716	FAILED
119	2.097884	0.026792	0.004788	0.00702	11.20599	144.2193	52.56404	75.63597	-0.21947	0.546538	0.720165	6.901445	44.34301	FAILED
121	2.038245	0.037834	0.002331	0.007909	17.20347	102.5018	56.47802	89.35523	-0.70384	0.906933	0.681533	5.751378	45.86774	FAILED
123	2.359959	0.010109	0.004397	0.009556	16.56983	123.3937	68.12972	83.19441	-0.20501	0.939344	-0.26696	8.332017	60.95441	FAILED
126	2.114491	0.086541	0.00267	0.009092	5.483569	121.6482	59.4401	76.04739	-0.49807	0.455902	-0.97126	9.228307	82.4398	FAILED